Lecture Notes in Physics

741

Markus Kuster
Georg Raffelt
Berta Beltrán
Editors

Axions

Theory, Cosmology, and Experimental Searches

Springer

Lecture Notes in Physics

The Lecture Notes in Physics

The series Lecture Notes in Physics (LNP), founded in 1969, reports new developments in physics research and teaching – quickly and informally, but with a high quality and the explicit aim to summarize and communicate current knowledge in an accessible way. Books published in this series are conceived as bridging material between advanced graduate textbooks and the forefront of research and to serve three purposes:

- to be a compact and modern up-to-date source of reference on a well-defined topic
- to serve as an accessible introduction to the field to postgraduate students and nonspecialist researchers from related areas
- to be a source of advanced teaching material for specialized seminars, courses and schools

Both monographs and multi-author volumes will be considered for publication. Edited volumes should, however, consist of a very limited number of contributions only. Proceedings will not be considered for LNP.

Volumes published in LNP are disseminated both in print and in electronic formats, the electronic archive being available at springerlink.com. The series content is indexed, abstracted and referenced by many abstracting and information services, bibliographic networks, subscription agencies, library networks, and consortia.

Proposals should be sent to a member of the Editorial Board, or directly to the managing editor at Springer:

Christian Caron
Springer Heidelberg
Physics Editorial Department I
Tiergartenstrasse 17
69121 Heidelberg / Germany
christian.caron@springer.com

M. Kuster
G. Raffelt
B. Beltrán (Eds.)

Axions

Theory, Cosmology, and Experimental Searches

Springer

Markus Kuster
TU Darmstadt
Institut für Kernphysik
Schloßgartenstr. 9
64289 Darmstadt, Germany
markus.kuster@cern.ch

Berta Beltrán
University of Alberta
11322-89 Av
Edmonton, AB, Canada
T6G 2G7
bbeltran@phys.ualberta.ca

Georg Raffelt
Max-Planck-Institut für Physik
(Werner-Heisenberg-Institut)
Föhringer Ring 6
80805 München, Germany
raffelt@mppmu.mpg.de

M. Kuster et al. (Eds.), *Axions: Theory, Cosmology, and Experimental Searches*, Lect. Notes Phys. 741 (Springer, Berlin Heidelberg 2008), DOI 10.1007/ 978-3-540-73518-2

ISBN: 978-3-540-73517-5 e-ISBN: 978-3-540-73518-2

Lecture Notes in Physics ISSN: 0075-8450

Library of Congress Control Number: 2007936166

Cover design: eStudio Calamar S.L., F. Steinen-Broo, Pau/Girona, Spain

Printed on acid-free paper

9 8 7 6 5 4 3 2 1

springer.com

Emilio Zavattini, born on March 14th, 1927, in Rimini, Italy, distinguished physicist and source of many fertile ideas in our field, passed away on January 9th, 2007.

He will be remembered by all those who had the privilege of working with him, especially the younger generation researchers, for his keen insights and for his ability to critically question all ideas, including his own. This was a peculiar tract of his style which rendered him unique. While holding discussions with him, one was never afraid of expressing a scientific opinion, however trivial or unfounded, and he would always correct mistakes without causing embarrassment.

His early work in the field of strong and weak interactions, especially using muons, conducted at CERN and at other institutions worldwide, represents an outstanding achievement in physics. His deep interest in the structure of vacuum began with the spectroscopy of muonic atoms and led him to formulate the ideas at the basis of current searches for nonlinear effects in Maxwell's equations due to vacuum polarization, and for other new interactions at low energy scales.

This quest is still open and is being carried out today by a growing community of physicists. Many of the members of this community have been trained by him and all remember him fondly for all that he had been able to give.

Preface

Axion physics started in 1977 when Roberto Peccei and Helen Quinn proposed their solution to the strong CP problem by postulating a new U(1) symmetry. The strong CP problem is a "blemish" of the standard model of particle physics which is one of the most profound and successful theories in modern physics that has been verified by numerous experiments to very high accuracy. Associated with the Peccei-Quinn symmetry is a light and weakly-interacting particle that was named by Frank Wilczek based on experience from day-to-day life: *I named them after a laundry detergent, since they clean up a problem with an axial current* (Frank Wilczek, Nobel lecture 2004). So far the axion has remained elusive for over 30 years of intensive research, and none of the axion searches, based on either astrophysical observations or pure laboratory based experiments, was able to yield a positive signature for the axion or an axion-like particle.

The motivation of this book is to provide a starting point for graduate students and senior scientists in the field of axions and axion-like particles. We give a broad overview on the theoretical motivation of axions and axion-like particles, their implication for cosmology and astrophysics, their role as a well-motivated dark-matter candidate, and experimental axion searches. Most of this book is based on lectures given at the 1st Joint ILIAS-CERN-CAST axion training in Geneva at CERN in November 2005. Of course, the experiments and theoretical works are by far too numerous to be completely covered in a volume of lecture notes like this.

We are indebted to many people who have contributed directly or indirectly to finalize this book and to make the axion lecture series possible. Our special thanks go to the lecturers who have delivered stimulating written versions of their presentations and who have helped patiently during the preparation of the final text. We are grateful to our colleagues of the CAST collaboration and numerous helpers whose assistance was crucial, especially for the organization of the lecture series and for the day-to-day running of the meeting. We owe special thanks to Konstantin Zioutas for his support, who right from the conception of the first idea was convinced that the time was ripe for a lecture series on axion-related physics.

We thank the network on direct dark matter detection of the ILIAS integrating activity of the European Union (contract number: RII3-CT-2003-506222) for support and CERN for hosting the meeting.

Kingston, Darmstadt, München, February 2007

Berta Beltrán, Markus Kuster, and Georg Raffelt

Contents

Part I

Axion Theory

1 The Strong CP Problem and Axions

Roberto D. Peccei

Department of Physics and Astronomy, UCLA, Los Angeles, CA 90095, USA
peccei@physics.ucla.edu

Abstract. I describe how the QCD vacuum structure, necessary to resolve the $U(1)_A$ problem, predicts the presence of a P, T, and CP violating term proportional to the vacuum angle $\bar{\theta}$. To agree with experimental bounds, however, this parameter must be very small ($\bar{\theta} \lesssim 10^{-9}$). After briefly discussing some other possible solutions to this, so-called, strong CP problem, I concentrate on the chiral solution proposed by Peccei and Quinn which has associated with it a light pseudoscalar particle, the axion. I discuss in detail the properties and dynamics of axions, focusing particularly on invisible axion models where axions are very light, very weakly coupled, and very long-lived. Astrophysical and cosmological bounds on invisible axions are also briefly touched upon.

1.1 The $U(1)_A$ Problem and Its Resolution

In the 1970s the strong interactions had a puzzling problem, which became particularly clear with the development of quantum chromodynamics (QCD). The QCD Lagrangian for N flavors in the limit of vanishing quark masses $m_f \to 0$ has a large global symmetry: $U(N)_V \times U(N)_A$. As $m_u, m_d \ll \Lambda_{\rm QCD}$, we know that, at least for these quarks, the limit of sending the quark masses to zero is sensible. Thus, one would expect the strong interactions to be approximately $U(2)_V \times U(2)_A$ invariant.

What one finds experimentally is that, indeed, the vector symmetry corresponding to isospin times baryon number, $U(2)_V = SU(2)_I \times U(1)_B$, is a good approximate symmetry of nature, as manifested by the appearance of nucleon and pion multiplets in the spectrum of hadrons. For axial symmetries, however, things are different. Dynamically, quark condensates $\langle \bar{u}u \rangle = \langle \bar{d}d \rangle \neq 0$ form, breaking down the axial symmetry spontaneously. So one does not expect approximate mixed parity multiplets in the hadronic spectrum, but vestiges of the four Nambu-Goldstone bosons associated with the breakdown of $U(2)_A$. Although pions are light, $m_\pi \simeq 0$, there are no signs of another light state in the hadronic spectrum, as $m_\eta^2 \gg m_\pi^2$. Weinberg [1] dubbed this the $U(1)_A$ problem and suggested that, somehow, there was no $U(1)_A$ symmetry in the strong interactions.

The resolution of the $U(1)_A$ problem came through the realization by 't Hooft [2, 3] that the QCD vacuum has a more complicated structure. The more complex nature of the QCD vacuum, in effect, makes $U(1)_A$ not

R.D. Peccei: *The Strong CP Problem and Axions*, Lect. Notes Phys. **741**, 3–17 (2008)
DOI 10.1007/978-3-540-73518-2_1

a true symmetry of QCD, even though it is an apparent symmetry of the QCD Lagrangian in the limit of vanishing quark masses. However, associated with this more complicated QCD vacuum there is a phase parameter θ, and only if this parameter is very small, CP is not very badly broken in the strong interactions. So the solution of the $U(1)_A$ problem begets a different problem: why is CP not badly broken in QCD? This is known as the strong CP problem.

A possible resolution of the $U(1)_A$ problem seems to be provided by the chiral anomaly for axial currents [4, 5, 6]. The divergence of the axial current J_5^μ associated with $U(1)_A$ gets quantum corrections from the triangle graph which connects it to two gluon fields with quarks going around the loop. This anomaly gives a non-zero divergence for J_5^μ

$$\partial_\mu J_5^\mu = \frac{g_s^2 N}{32\pi^2}\, G_a^{\mu\nu}\tilde{G}_{a\mu\nu} \ , \tag{1.1}$$

where $\tilde{G}_{a\mu\nu} = \frac{1}{2}\varepsilon_{\mu\nu\alpha\beta}G_a^{\alpha\beta}$. Hence, in the massless quark limit, although formally QCD is invariant under a $U(1)_A$ transformation,

$$q_f \to \mathrm{e}^{\mathrm{i}\alpha\gamma_5/2} q_f \ , \tag{1.2}$$

the chiral anomaly affects the action:

$$\delta W = \alpha \int \mathrm{d}^4x\, \partial_\mu J_5^\mu = \alpha\, \frac{g_s^2 N}{32\pi^2} \int \mathrm{d}^4x\, G_a^{\mu\nu}\tilde{G}_{a\mu\nu} \ . \tag{1.3}$$

However, matters are not that simple! The pseudoscalar density entering in the anomaly is, in fact, a total divergence [7]:

$$G_a^{\mu\nu}\tilde{G}_{a\mu\nu} = \partial_\mu K^\mu \ , \tag{1.4}$$

where

$$K^\mu = \varepsilon^{\mu\alpha\beta\gamma} A_{a\alpha}\left(G_{a\beta\gamma} - \frac{g_s}{3}\, f_{abc} A_{b\beta} A_{c\gamma}\right) \ . \tag{1.5}$$

Because of these identities δW is a pure surface integral

$$\delta W = \alpha\, \frac{g_s^2 N}{32\pi^2} \int \mathrm{d}^4x\, \partial_\mu K^\mu = \alpha\, \frac{g_s^2 N}{32\pi^2} \int \mathrm{d}\sigma_\mu K^\mu \ . \tag{1.6}$$

Hence, using the naive boundary condition that $A_a^\mu = 0$ at spatial infinity, one has $\int \mathrm{d}\sigma_\mu K^\mu = 0$ and $U(1)_A$ appears to be a symmetry again. What 't Hooft [2, 3] showed, however, is that the correct boundary condition to use is that A_a^μ should be a pure gauge field at spatial infinity, i.e., either $A_a^\mu = 0$ or a gauge transformation of 0. It turns out that, with these boundary conditions, there are gauge configurations for which $\int \mathrm{d}\sigma_\mu K^\mu \neq 0$ and thus $U(1)_A$ is not a symmetry of QCD.

This is most easily understood by working in the A_a^0 gauge. Studying $SU(2)$ QCD for simplicity, in this gauge [8], one has only spatial gauge fields A_a^i. Under a gauge transformation these fields transform as

$$\frac{1}{2}\,\tau_a A_a^i \equiv A^i \to \Omega A^i \Omega^{-1} + \frac{\mathrm{i}}{g_\mathrm{s}}\,\nabla^i \Omega \Omega^{-1}\,. \tag{1.7}$$

Thus, vacuum configurations either vanish or have the form $\mathrm{i}g_\mathrm{s}^{-1}\nabla^i\Omega\Omega^{-1}$. In the $A_a^0 = 0$ gauge, one can further classify these vacuum configurations by how Ω goes to unity as $\mathbf{r} \to \infty$:

$$\Omega_n \to \mathrm{e}^{\mathrm{i}2\pi n} \quad \text{as} \quad \mathbf{r} \to \infty \quad \text{with} \quad n = 0, \pm 1, \pm 2, \ldots\,. \tag{1.8}$$

The integer n (the winding number) is related to the Jacobian of an $S_3 \to S_3$ map and is given by [9]

$$n = \frac{\mathrm{i}g_\mathrm{s}^3}{24\pi^2}\int \mathrm{d}^3 r\,\mathrm{Tr}\left(\varepsilon_{ijk} A_n^i A_n^j A_n^k\right)\,. \tag{1.9}$$

This expression is closely related to the Bardeen current K^μ. Indeed, in the $A_a^0 = 0$ gauge, only $K^0 \neq 0$ and one finds for pure gauge fields

$$K^0 = -\frac{g_\mathrm{s}}{3}\,\varepsilon_{ijk}\varepsilon_{abc} A_a^i A_b^j A_c^k = \frac{4}{3}\,\mathrm{i}g_\mathrm{s}\varepsilon_{ijk}\,\mathrm{Tr}\left(A^i A^j A^k\right)\,. \tag{1.10}$$

The true vacuum is a superposition of these, so-called, n-vacua and is called the θ-vacuum

$$|\theta\rangle = \sum_n \mathrm{e}^{-\mathrm{i}n\theta}|n\rangle\,. \tag{1.11}$$

It is easy to see that in the vacuum to vacuum transition amplitude there are transitions with $\int \mathrm{d}\sigma_\mu K^\mu \neq 0$. Indeed,

$$n|_{t=+\infty} - n|_{t=-\infty} = \frac{g_\mathrm{s}^2}{32\pi^2}\int \mathrm{d}\sigma_\mu K^\mu\Big|_{t=-\infty}^{t=+\infty}\,. \tag{1.12}$$

Using (1.12), in detail one can write for the vacuum to vacuum transition amplitude

$${}_+\langle\theta|\theta\rangle_- = \sum_{m,n} \mathrm{e}^{\mathrm{i}m\theta}\mathrm{e}^{-\mathrm{i}n\theta}\,{}_+\langle m|n\rangle_- = \sum_\nu \mathrm{e}^{\mathrm{i}\nu\theta}\sum_n {}_+\langle n+\nu|n\rangle_-\,. \tag{1.13}$$

It is easy to see that the difference in winding numbers ν is given by

$$\nu = \frac{g_\mathrm{s}^2}{32\pi^2}\int \mathrm{d}\sigma_\mu K^\mu\Big|_{t=-\infty}^{t=+\infty} = \frac{g_\mathrm{s}^2}{32\pi^2}\int \mathrm{d}^4 x\, G_a^{\mu\nu}\tilde{G}_{a\mu\nu}\,. \tag{1.14}$$

Using the usual path integral representation for the vacuum to vacuum amplitude ${}_+\langle\theta|\theta\rangle_-$, one finds that

$${}_+\langle\theta|\theta\rangle_- = \sum_\nu \int \delta A\,\mathrm{e}^{\mathrm{i}S_\mathrm{eff}[A]}\,\delta\left(\nu - \frac{g_\mathrm{s}^2}{32\pi^2}\int \mathrm{d}^4 x\, G_a^{\mu\nu}\tilde{G}_{a\mu\nu}\right)\,, \tag{1.15}$$

where

$$S_{\rm eff}[A] = S_{\rm QCD}[A] + \theta \frac{g_{\rm s}^2}{32\pi^2} \int {\rm d}^4x \, G_a^{\mu\nu} \tilde{G}_{a\mu\nu} \; . \tag{1.16}$$

The resolution of the $U(1)_A$ problem, by recognizing the complicated nature of the QCD vacuum, effectively adds an extra term to the QCD Lagrangian

$$L_\theta = \theta \, \frac{g_{\rm s}^2}{32\pi^2} \, G_a^{\mu\nu} \tilde{G}_{a\mu\nu} \; . \tag{1.17}$$

This term violates parity and time reversal invariance but conserves charge conjugation invariance, so it violates CP. It induces a neutron electric dipole moment of order [10, 11]

$${\rm d}_n \simeq \frac{e \, \theta \, m_q}{m_N^2} \; . \tag{1.18}$$

The strong experimental bound $|{\rm d}_n| < 3 \times 10^{-26} \, e \, {\rm cm}$ [12] implies $\theta \lesssim 10^{-9}$. Why this should be so, is known as the **strong CP problem**.

This problem is actually worse if one considers the effect of chiral transformations on the θ-vacuum. Chiral transformations, because of the anomaly, actually can change the θ-vacuum [13]

$${\rm e}^{{\rm i}\alpha Q_5} |\theta\rangle = |\theta + \alpha\rangle \; . \tag{1.19}$$

If, besides QCD, one includes the weak interactions, the quark mass matrix is in general complex

$$L_{\rm mass} = \bar{q}_{iR} M_{ij} q_{jL} + {\rm h.c.} \tag{1.20}$$

To go to a physical basis, one must diagonalize this mass matrix and when one does so, in general, one performs a chiral transformation that changes θ by $\arg\det M$. So, in the full theory, the coefficient of the $G\tilde{G}$ term is

$$\bar{\theta} = \theta + \arg\det M \; . \tag{1.21}$$

The strong CP problem is why is this $\bar{\theta}$ angle, coming from the strong and weak interactions, so small?

1.2 Approaches to the Strong CP Problem

There are three possible "solutions" to the strong CP problem:

(i) Unconventional dynamics
(ii) Spontaneously broken CP
(iii) An additional chiral symmetry

However, in my opinion, only the third of these is a viable solution. Of course, it might be possible that, as a result of some anthropic reasons, $\bar{\theta}$ just turns out to be of order 10^{-10}, but I doubt it, as a Universe where CP is violated strongly seems as viable as one where it is not (private communication by F. Wilczek).

Appealing to unconventional dynamics is also not very believable. Attempts have been made to suggest that the boundary conditions that give rise to the θ-vacuum are an artifact [14], but then what is the solution to the $U(1)_A$ problem? Other approaches try to use the periodicity of vacuum energy $E(\theta) \sim \cos\theta$ to deduce that θ vanishes [15], but fail to motivate the minimization of the vacuum energy.

The second possibility of spontaneously broken CP is more interesting. Obviously, if CP is a symmetry of nature, which is spontaneously broken, then one can set $\theta = 0$ at the Lagrangian level. However, if CP is spontaneously broken θ gets induced back at the loop level. To get $\theta < 10^{-9}$, one needs, in general, to ensure that θ vanishes also at the 1-loop level. Although models exist where this is accomplished [16, 17, 18], theories with spontaneously broken CP need complex Higgs vacuum expectation values (VEVs), leading to difficulties with flavour changing neutral currents (FCNC) and domain walls [19] and one must introduce recondite physics [20, 21, 22, 23] to avoid these problems. In my view, however, the biggest drawback for this "solution" to the strong CP problem is that experimental data are in excellent agreement with the Cabibbo-Kobayashi-Maskawa model (CKM model) – a model where CP is explicitly, not spontaneously, broken.

Introducing an additional chiral symmetry is a very natural solution for the strong CP problem, as this chiral symmetry, effectively, rotates the θ-vacua away. Two suggestions have been made for this chiral symmetry:

(i) The up-quark has no mass, $m_u = 0$ [24]
(ii) The Standard Model has an additional global $U(1)$ chiral symmetry [25, 26]

The first possibility is disfavored by a standard current algebra analysis [27] that shows that all data are consistent with a non-zero mass for the up-quark. Furthermore, it is difficult to understand what would be the origin of this chiral symmetry, which asks effectively that $\arg\det M = 0$.

1.3 $U(1)_{\mathrm{PQ}}$ and Axions

Introducing a global chiral $U(1)$ symmetry [25, 26] – which has become known as a $U(1)_{\mathrm{PQ}}$ symmetry – provides perhaps the most cogent solution to the strong CP problem. This symmetry is necessarily spontaneously broken, and its introduction into the theory effectively replaces the static CP-violating angle $\bar{\theta}$ with a dynamical CP-conserving field – the axion. The axion is the Nambu-Goldstone boson of the broken $U(1)_{\mathrm{PQ}}$ symmetry [28, 29]. As a result, under a $U(1)_{\mathrm{PQ}}$ transformation, the axion field $a(x)$ translates to

$$a(x) \to a(x) + \alpha f_a \ , \tag{1.22}$$

where f_a is the order parameter associated with the breaking of $U(1)_{\rm PQ}$.

Formally, to make the Lagrangian of the Standard Model $U(1)_{\rm PQ}$ invariant, this Lagrangian must be augmented by axion interactions:

$$L_{\rm total} = L_{\rm SM} + \bar\theta\, \frac{g_{\rm s}^2}{32\pi^2}\, G_b^{\mu\nu} \tilde G_{b\mu\nu} - \frac{1}{2}\, \partial_\mu a\, \partial^\mu a + L_{\rm int}[\partial^\mu a/f_a, \Psi] + \xi\, \frac{a}{f_a}\, \frac{g_{\rm s}^2}{32\pi^2} G_b^{\mu\nu} \tilde G_{b\mu\nu} \ . \tag{1.23}$$

The last term above is needed to ensure that the $U(1)_{\rm PQ}$ current indeed has a chiral anomaly

$$\partial_\mu J^\mu_{\rm PQ} = \xi\, \frac{g_{\rm s}^2}{32\pi^2}\, G_b^{\mu\nu} \tilde G_{b\mu\nu} \ . \tag{1.24}$$

This term also represents an effective potential for the axion field, and its minimum occurs at $\langle a\rangle = -\bar\theta\, f_a/\xi$:

$$\left\langle \frac{\partial V_{\rm eff}}{\partial a} \right\rangle = -\frac{\xi}{f_a}\, \frac{g_{\rm s}^2}{32\pi^2}\, \left\langle G_b^{\mu\nu} \tilde G_{b\mu\nu} \right\rangle \Big|_{\langle a\rangle = -\bar\theta\, f_a/\xi} = 0 \ . \tag{1.25}$$

As at the minimum the $\bar\theta$-term is canceled out, this provides a dynamical solution to the strong CP problem [25, 26].

It is easy to understand the physics of the Peccei-Quinn solution to the strong CP problem. If one neglects the effects of QCD, then the extra $U(1)_{\rm PQ}$ symmetry allows all values for $\langle a\rangle$ to exist:

$$0 \le \xi\, \frac{\langle a\rangle}{f_a} \le 2\pi \ . \tag{1.26}$$

However, including the effects of the QCD anomaly serves to generate a potential for the axion field that is periodic in the effective vacuum angle $\bar\theta + \langle a\rangle \xi/f_a$:

$$V_{\rm eff} \sim \cos\left(\bar\theta + \xi\, \frac{\langle a\rangle}{f_a}\right) \ . \tag{1.27}$$

Minimizing this potential with respect to $\langle a\rangle$ gives the PQ solution:

$$\langle a\rangle = -\frac{f_a}{\xi}\, \bar\theta \ . \tag{1.28}$$

Obviously, the Lagrangian (1.23) written in terms of $a_{\rm phys} = a - \langle a\rangle$ no longer has a CP-violating $\bar\theta$-term.

Expanding $V_{\rm eff}$ at the minimum gives the axion a mass

$$m_a^2 = \left\langle \frac{\partial^2 V_{\rm eff}}{\partial a^2} \right\rangle = -\frac{\xi}{f_a}\, \frac{g_{\rm s}^2}{32\pi^2}\, \frac{\partial}{\partial a} \left\langle G_b^{\mu\nu} \tilde G_{b\mu\nu} \right\rangle \Big|_{\langle a\rangle = -\bar\theta\, f_a/\xi} \ . \tag{1.29}$$

The calculation of the axion mass was first done explicitly using current algebra techniques by Bardeen and Tye [30]. Here I will give an effective Lagrangian derivation [31] of m_a, as this technique also gives readily the couplings of axions to matter.

1.4 Axion Dynamics

In the original Peccei-Quinn model, the $U(1)_{\rm PQ}$ symmetry breakdown coincided with that of electroweak breaking $f_a = v_{\rm F}$, with $v_{\rm F} \simeq 250\,{\rm GeV}$. However, this is not necessary. If $f_a \gg v_{\rm F}$ then the axion is very light, very weakly coupled, and very long-lived. Models where this occurs have become known as invisible axion models.

It is useful to derive first the properties of weak-scale axions and then generalize the discussion to invisible axion models. To make the Standard Model (SM) invariant under a $U(1)_{\rm PQ}$ transformation, one must introduce two Higgs fields to absorb independent chiral transformations of the up- and down-quarks (and leptons). The relevant Yukawa interactions involving these Higgs fields in the SM are

$$L_{\rm Yukawa} = \Gamma^u_{ij} \bar{Q}_{Li} \Phi_1 u_{Rj} + \Gamma^{\rm d}_{ij} \bar{Q}_{Li} \Phi_2 {\rm d}_{Rj} + \Gamma^\ell_{ij} \bar{L}_{Li} \Phi_2 \ell_{Rj} + {\rm h.c.} \tag{1.30}$$

Defining $x = v_2/v_1$ and $v_{\rm F} = \sqrt{v_1^2 + v_2^2}$, the axion is the common phase field in Φ_1 and Φ_2, which is orthogonal to the weak hypercharge:

$$\Phi_1 = \frac{v_1}{\sqrt{2}} {\rm e}^{{\rm i}ax/v_{\rm F}} \begin{pmatrix} 1 \\ 0 \end{pmatrix} \quad \text{and} \quad \Phi_2 = \frac{v_2}{\sqrt{2}} {\rm e}^{{\rm i}a/xv_{\rm F}} \begin{pmatrix} 0 \\ 1 \end{pmatrix} . \tag{1.31}$$

From the above, it is clear that $L_{\rm Yukawa}$ is invariant under the $U(1)_{\rm PQ}$ transformation

$$\begin{aligned} a &\to a + \alpha v_{\rm F} , \\ u_{Rj} &\to {\rm e}^{-{\rm i}\alpha x} u_{Rj} , \\ {\rm d}_{Rj} &\to {\rm e}^{-{\rm i}\alpha/x} {\rm d}_{Rj} , \\ \ell_{Rj} &\to {\rm e}^{-{\rm i}\alpha/x} \ell_{Rj} . \end{aligned} \tag{1.32}$$

Let us focus on the quark pieces. The symmetry current for $U(1)_{\rm PQ}$,

$$J^\mu_{\rm PQ} = -v_{\rm F} \partial^\mu a + x \sum_i \bar{u}_{iR} \gamma^\mu u_{iR} + \frac{1}{x} \sum_i \bar{\rm d}_{iR} \gamma^\mu {\rm d}_{iR} , \tag{1.33}$$

identifies the anomaly coefficient ξ in (1.23) as

$$\xi = \frac{N}{2} \left(x + \frac{1}{x} \right) = N_g \left(x + \frac{1}{x} \right) . \tag{1.34}$$

To compute the axion mass, it is useful to separate the effects of the axion interactions with the light quarks from the rest. These interactions can be deduced from the underlying theory by constructing an appropriate effective chiral Lagrangian. The effects of the heavy quarks essentially can then be accounted for through their contribution to the chiral anomaly of $J^\mu_{\rm PQ}$.

For the two light quarks, as usual [27], one introduces a 2×2 matrix of Nambu-Goldstone fields

$$\Sigma = \exp\left(\mathrm{i}\,\frac{\boldsymbol{\tau}\cdot\boldsymbol{\pi}+\eta}{f_\pi}\right)\ , \tag{1.35}$$

where f_π is the pion decay constant. Then the meson sector of the light-quark theory, neglecting the effect of the Yukawa interactions, is embodied in the $U(2)_V \times U(2)_A$ invariant effective Lagrangian

$$L_{\rm chiral} = -\frac{f_\pi^2}{4}\,{\rm Tr}\left(\partial_\mu \Sigma\,\partial^\mu \Sigma^\dagger\right)\ . \tag{1.36}$$

To $L_{\rm chiral}$ one must add $U(2)_V \times U(2)_A$ breaking terms which mimic the $U(1)_{\rm PQ}$ invariant Yukawa interactions of the u- and d-quarks. This is accomplished by the Lagrangian

$$L_{\rm mass} = \frac{1}{2}\left(f_\pi m_\pi^0\right)^2 {\rm Tr}\left[\Sigma A M + (\Sigma A M)^\dagger\right]\ , \tag{1.37}$$

where

$$A = \begin{pmatrix} \mathrm{e}^{-\mathrm{i}ax/v_{\rm F}} & 0 \\ 0 & \mathrm{e}^{-\mathrm{i}a/xv_{\rm F}} \end{pmatrix} \quad \text{and} \quad M = \begin{pmatrix} \frac{m_u}{m_u+m_d} & 0 \\ 0 & \frac{m_d}{m_u+m_d} \end{pmatrix}\ . \tag{1.38}$$

Note that the invariance of $L_{\rm mass}$ under $U(1)_{\rm PQ}$ requires that Σ transform as

$$\Sigma \to \Sigma \begin{pmatrix} \mathrm{e}^{\mathrm{i}\alpha x} & 0 \\ 0 & \mathrm{e}^{\mathrm{i}\alpha/x} \end{pmatrix}\ . \tag{1.39}$$

$L_{\rm mass}$, however, only gives part of the physics associated with the symmetry breakdown of $U(2)_A$. In fact, the quadratic terms in $L_{\rm mass}$ involving neutral fields

$$L_{\rm mass}^{(2)} = -\frac{\left(m_\pi^0\right)^2}{2}\left[\frac{m_u}{m_u+m_d}\left(\pi^0+\eta-\frac{xf_\pi}{v_{\rm F}}\,a\right)^2 + \frac{m_d}{m_u+m_d}\left(\eta-\pi^0-\frac{f_\pi}{xv_{\rm F}}\,a\right)^2\right] \tag{1.40}$$

give

$$\frac{m_\eta^2}{m_\pi^2} = \frac{m_d}{m_u} \simeq 1.6 \tag{1.41}$$

which contradicts experiment. Indeed, if $L_{\rm mass}$ was all that there was, we would have recreated in the effective Lagrangian language the $U(1)_A$ problem! Furthermore, with only this term the axion is still massless.

The resolution of the $U(1)_A$ problem in the effective Lagrangian theory is achieved by adding a further mass term that takes account of the anomaly

in both $U(1)_A$ and $U(1)_{\rm PQ}$. This mass term gives the η the right mass and produces a mass for the axion. It is easy to convince oneself that such a term has the form [31]

$$L_{\rm anomaly} = -\frac{\left(m_\eta^0\right)^2}{2}\left[\eta + \frac{f_\pi}{v_{\rm F}}\,\frac{(N_g-1)(x+1/x)}{2}\,a\right]^2 , \tag{1.42}$$

where $(m_\eta^0)^2 \simeq m_\eta^2 \gg m_\pi^2$. The coefficient in front of the axion field in $L_{\rm anomaly}$ reflects the relative strength of the couplings of the axion and the η to $G\tilde{G}$ as the result of the anomalies in $U(1)_{\rm PQ}$ and $U(1)_A$. Naively, the ratio of these couplings is just $f_\pi/2v_{\rm F}\xi$. However, the reason that $N_g - 1$ appears in the above, rather than N_g, is that $L_{\rm mass}$ already includes the light quark interactions of axions, so only the contribution of heavy quarks to the PQ anomaly should be taken into account in $L_{\rm anomaly}$.

Diagonalization of the quadratic terms in $L_{\rm mass}$ and $L_{\rm anomaly}$ gives both the axion mass and the parameters for axion-pion and axion-eta mixing for the PQ model. It is convenient to define

$$\bar{m}_a = m_\pi\,\frac{f_\pi}{v_{\rm F}}\,\frac{\sqrt{m_u m_d}}{m_u + m_d} \simeq 25\,{\rm keV} . \tag{1.43}$$

Then one finds

$$m_a = \lambda_m \bar{m}_a , \quad \xi_{a\pi} = \lambda_3\,\frac{f_\pi}{v_{\rm F}} , \quad \xi_{a\eta} = \lambda_0\,\frac{f_\pi}{v_{\rm F}} , \tag{1.44}$$

where

$$\begin{aligned}
\lambda_m &= N_g\left(x + \frac{1}{x}\right) , \\
\lambda_3 &= \frac{1}{2}\left[\left(x - \frac{1}{x}\right) - N_g\left(x + \frac{1}{x}\right)\frac{m_d - m_u}{m_u + m_d}\right] , \\
\lambda_0 &= \frac{1}{2}\,(1 - N_g)\left(x + \frac{1}{x}\right) .
\end{aligned} \tag{1.45}$$

In addition to the three parameters above, all axion models are characterized also by how the axion couples to two photons. Writing the interaction Lagrangian describing this coupling as

$$L_{a\gamma\gamma} = \frac{\alpha}{4\pi}\,K_{a\gamma\gamma}\frac{a_{\rm phys}}{f_a}\,F^{\mu\nu}\tilde{F}_{\mu\nu} , \tag{1.46}$$

one needs to find the coupling $K_{a\gamma\gamma}$ for the PQ model. This coupling follows from the electromagnetic anomaly of the PQ current

$$\partial_\mu J^\mu_{\rm PQ} = \frac{\alpha}{4\pi}\,\xi_\gamma F_{\mu\nu}\tilde{F}^{\mu\nu} . \tag{1.47}$$

Here ξ_γ gets contributions from both quarks and leptons, and one finds

$$\xi_\gamma = N_g \left\{ \left[3 \left(\tfrac{2}{3}\right)^2 \right] x + \left[3 \left(-\tfrac{1}{3}\right)^2 + (-1)^2 \right] \frac{1}{x} \right\}$$
$$= \frac{4}{3} N_g \left(x + \frac{1}{x} \right) . \tag{1.48}$$

As before, in computing $K_{a\gamma\gamma}$, one must separate out the light quark contribution of the axion in the anomaly, so that $\xi_\gamma^{\rm eff} = \frac{4}{3} N_g (x + 1/x) - \frac{4}{3} x - \frac{1}{3} \frac{1}{x}$, and add back the axion to two-photon contribution that arises from the coupling of the π^0 and η to two photons, via axion-pion and axion-eta mixing: $\lambda_3 + \frac{5}{3}\lambda_0$. This then gives

$$K_{a\gamma\gamma} = N_g \left(x + \frac{1}{x} \right) \frac{m_u}{m_u + m_d} . \tag{1.49}$$

1.5 Invisible Axion Models

The original PQ model [25, 26], where $f_a = v_{\rm F}$, was long ago ruled out by experiment. For example, one can estimate the branching ratio (BR) [31]

$$\text{BR}\left(K^+ \to \pi^+ + a\right) \simeq 3 \times 10^{-5} \lambda_0^2 = 3 \times 10^{-5} \left(x + 1/x\right)^2 \tag{1.50}$$

which is well above the bounds obtained at the National Laboratory for High Energy Physics in Japan (KEK) [32] $\text{BR}(K^+ \to \pi^+ + \text{nothing}) < 3.8 \times 10^{-8}$. However, invisible axion models, where $f_a \gg v_{\rm F}$, are still viable.

Invisible axion models introduce scalar fields that carry PQ charge but are $SU(2) \times U(1)$ singlets. As a result, it is possible that the VEVs of these fields have a scale much larger than the one set by the weak interactions. Basically, two types of models have been proposed. The first of these models, due to Kim [33] and Shifman, Vainshtein and Zakharov [34] (the, so-called, KSVZ model), introduces a scalar field σ with $f_a = \langle \sigma \rangle \gg v_{\rm F}$ and a super-heavy quark Q with $M_Q \sim f_a$ as the only fields carrying PQ charge. The second of these models, due to Dine, Fischler and Srednicki [35] and Zhitnisky [36] (the, so-called, DFSZ model), adds to the original PQ model a scalar field ϕ that carries PQ charge and $f_a = \langle \phi \rangle \gg v_{\rm F}$.

It is straightforward to repeat the calculations we just did above for these models, to get the axion mass and couplings. I will do this explicitly here for the KSVZ model, because it is simple and illustrates well what we just did and will just quote the results for the DFSZ model. By construction, the KSVZ axion does not interact with leptons and it only interacts with light quarks as the result of the strong and electromagnetic anomalies

$$L_{\rm axion}^{\rm KSVZ} = \frac{a}{f_a} \left(\frac{g_{\rm s}^2}{32\pi^2} G_b^{\mu\nu} \tilde{G}_{b\mu\nu} + 3 e_Q^2 \frac{\alpha}{4\pi} F^{\mu\nu} \tilde{F}_{\mu\nu} \right) , \tag{1.51}$$

where e_Q is the electromagnetic charge of the super-heavy quark Q.

As in the KSVZ model the ordinary Higgs do not carry PQ charge, the only interactions of the axion with the light-quark sector come from the effective anomaly mass term, which is given here by

$$L_{\text{anomaly}} = -\frac{\left(m_\eta^0\right)^2}{2}\left(\eta + \frac{f_\pi}{2f_a}\,a\right)^2 . \tag{1.52}$$

To the above, one must add the standard quadratic term coming from the light quarks

$$L_{\text{mass}}^{(2)} = -\frac{\left(m_\pi^0\right)^2}{2}\left[\frac{m_u}{m_u+m_d}\left(\pi^0+\eta\right)^2 + \frac{m_d}{m_u+m_d}\left(\eta-\pi^0\right)^2\right] . \tag{1.53}$$

Diagonalizing L_{anomaly} and $L_{\text{mass}}^{(2)}$ gives

$$m_a = \frac{v_{\text{F}}}{f_a}\,\bar{m}_a \equiv \lambda_m\,\frac{v_{\text{F}}}{f_a}\,\bar{m}_a\ , \quad \xi_{a\pi} = \lambda_3\,\frac{f_\pi}{f_a}\ , \quad \xi_{a\eta} = \lambda_0\,\frac{f_\pi}{f_a}\ , \tag{1.54}$$

where for the KSVZ model these parameters are

$$\lambda_m = 1\ , \quad \lambda_3 = -\frac{m_d-m_u}{2\,(m_u+m_d)}\ , \quad \lambda_0 = -\frac{1}{2}\ . \tag{1.55}$$

Note that, numerically, in the KSVZ model the axion mass is given by the formula

$$m_a = \frac{v_{\text{F}}}{f_a}\,\bar{m}_a \simeq 6.3\,\text{eV}\left(\frac{10^6\,\text{GeV}}{f_a}\right) . \tag{1.56}$$

The calculation of $K_{a\gamma\gamma}$ in this model is equally straightforward. To the contribution of the super-heavy quark in the electromagnetic anomaly, $3e_Q^2$, one must add that coming from the mixing of the axion with the π^0 and the η, i.e., $\lambda_3 + \frac{5}{3}\lambda_0$. This gives, finally,

$$K_{a\gamma\gamma} = 3e_Q^2 - \frac{4m_d+m_u}{3\,(m_u+m_d)}\ . \tag{1.57}$$

I will not go through the analogous calculation for the DFSZ model but just quote the results. For this model, it proves convenient to define

$$X_1 = \frac{2v_2^2}{v_{\text{F}}^2} \quad \text{and} \quad X_2 = \frac{2v_1^2}{v_{\text{F}}^2}\ , \tag{1.58}$$

where $v_{\text{F}} = \sqrt{v_1^2+v_2^2}$ and v_1 and v_2 are the two Higgs VEVs. Furthermore, if one rescales $f_a \to f_a/2N_g$, the axion mass in the DFSZ model is given by

(1.56), the same equation as for the KSVZ model, corresponding to $\lambda_m = 1$. With this rescaling understood, one then finds

$$\lambda_3 = \frac{1}{2}\left(\frac{X_1 - X_2}{2N_g} - \frac{m_d - m_u}{m_d + m_u}\right) , \quad \lambda_0 = \frac{1 - N_g}{2N_g} , \tag{1.59}$$

and

$$K_{a\gamma\gamma} = \frac{4}{3} - \frac{4m_d + m_u}{3\,(m_d + m_u)} . \tag{1.60}$$

Although the KSVZ and DFSZ axions are very light, very weakly coupled, and very long-lived, they are not totally invisible. I will not describe in detail how these "invisible" axions affect astrophysics and cosmology, as others will do so in this volume. However, in an attempt to make this brief precis on the strong CP problem and axions self-contained, I will add a few comments on the bounds one derives for invisible axions.

Astrophysics gives bounds on the axion mass as axion emission, through Compton production, $\gamma e \to ae$, and the Primakoff process, causes energy loss in stars [37]. The energy loss is inversely proportional to f_a^2 and hence proportional to m_a^2. Thus axions must be light enough, so as not to affect stellar evolution. This is not the only way in which one obtains an upper bound on m_a. For instance, another bound on m_a comes from SN 1987A, as axion emission through the process $NN \to NNa$ in the core collapse affects the neutrino signal [38]. Typical bounds (Sect. 2.6) obtained from astrophysics require axions to be lighter than

$$m_a < 1 \text{ to } 10^{-3}\,\text{eV} . \tag{1.61}$$

Remarkably, cosmology gives a lower bound on the axion mass (and an upper bound on f_a) [39, 40, 41]. The physics connected with this bound is simple to understand. When the Universe goes through the PQ phase transition at $T \sim f_a \gg \Lambda_{\rm QCD}$, the QCD anomaly is ineffective. As a result, early in the Universe $\langle a_{\rm phys}\rangle$ is arbitrary. Eventually, when the Universe cools down to temperatures of order $T \sim \Lambda_{\rm QCD}$, the axion acquires a mass and $\langle a_{\rm phys}\rangle \to 0$. The PQ mechanism through which this happens, however, is not an instantaneous process and $\langle a_{\rm phys}\rangle$ oscillates to its final value. These coherent $\mathbf{p}_a = 0$ axion oscillations contribute to the Universe's energy density and axions act as cold dark matter. The energy density contained in axion oscillations is proportional to f_a and thus bounds on the energy density of cold dark matter in the Universe provide an upper bound on f_a (and a lower bound on m_a).

I quote the result of a recent calculation by Fox, Pierce and Thomas [42] of the contribution to the Universe's energy density due to axions:

$$\Omega_a h^2 = 0.5\left(\frac{f_a/\xi}{10^{12}\,\text{GeV}}\right)^{7/6}\left[\theta_{\rm i}^2 + (\sigma_\theta)^2\right]\gamma . \tag{1.62}$$

Here ξ is the coefficient of the PQ anomaly and, with the way we defined f_a, $\xi = 1$ for both the KSVZ and DFSZ models. The angle $\theta_{\rm i}$ is the misalignment

value for $\langle a_{\rm phys}\rangle/f_a$, and σ_θ is its mean-squared fluctuation. Finally, γ is a possible dilution factor for the energy density produced by axion oscillations.

One can use the recent WMAP bound on cold dark matter [43] to bound

$$\Omega_a h^2 < 0.12\,. \tag{1.63}$$

Assuming no dilution ($\gamma = 1$) and using for $\theta_{\rm i}$ an average misalignment angle $\theta_{\rm i}^2 = \pi^2/3$ and neglecting its fluctuations, the WMAP data give the following cosmological bound for the PQ scale:

$$f_a < 3\times 10^{11}\,{\rm GeV} \quad \text{or} \quad m_a > 2\times 10^{-5}\,{\rm eV}\,. \tag{1.64}$$

1.6 Concluding Remarks

My conclusions are rather simple and telegraphic. In my view, after more than 25 years, the preferred solution to the strong CP problem still remains the idea that the Standard Model has an additional $U(1)_{\rm PQ}$ symmetry. Such a solution, necessarily, predicts the existence of a concomitant axion. Although Fermi-scale axions have been ruled out, invisible axion models are still viable and axion oscillations toward its minimum could account for the dark matter in the Universe. This is an exciting possibility. However, no totally compelling invisible axion models exist, and there are no strong arguments to believe that f_a takes precisely the value needed for axions to be the dark matter in the Universe. Nevertheless, it is encouraging that experimentalists are actively searching for signals of invisible axions.

Acknowledgments

I thank Markus Kuster for organizing this very nice workshop. Part of the material presented here is derived from my lectures [44] at the KOSEF-JSPS Winter School on Recent Developments in Particle and Nuclear Theory, Seoul, Korea (1996). This work was supported in part by the Department of Energy under Contract No. FG03-91ER40662, Task C.

References

1. Weinberg, S.: The U(1) problem. Phys. Rev. D 11, 3583 (1975) 3
2. 't Hooft, G.: Symmetry breaking through Bell-Jackiw anomalies. Phys. Rev. Lett. 37, 8 (1976) 3, 4
3. 't Hooft, G.: Computation of the quantum effects due to a four-dimensional pseudoparticle. Phys. Rev. D **14**, 3432 (1976); (E) ibid. D **18**, 2199 (1978) 3, 4
4. Adler, S.L.: Axial vector vertex in spinor electrodynamics. Phys. Rev. **177**, 2426 (1969) 4

5. Bell, J.S., Jackiw, R.: A PCAC puzzle: $\pi^0 \to \gamma\gamma$ in the sigma model. Nuovo Cim. A **60**, 47 (1969) 4
6. Bardeen, W.A.: Anomalous Ward identities in spinor field theories. Phys. Rev. **184**, 1848 (1969) 4
7. Bardeen, W.A.: Anomalous currents in gauge field theories. Nucl. Phys. B **75**, 246 (1974) 4
8. Callan, C.G., Dashen, R.F., Gross, D.J.: The structure of the gauge theory vacuum. Phys. Lett. B **63**, 334 (1976) 5
9. Crewther, R.J.: Effects of topological charge in gauge theories. Acta Phys. Austriaca Suppl. **19**, 47 (1978) 5
10. Baluni, V.: CP violating effects in QCD. Phys. Rev. D **19**, 2227 (1979) 6
11. Crewther, R.J., Di Vecchia, P., Veneziano G., Witten, E.: Chiral estimate of the electric dipole moment of the neutron in quantum chromodynamics. Phys. Lett. B **88**, 123 (1979); (E) ibid. B **91**, 487 (1980) 6
12. Baker, C.A., et al.: An improved experimental limit on the electric dipole moment of the neutron. Phys. Rev. Lett. **97**, 131801 (2006) [hep-ex/0602020] 6
13. Jackiw, R., Rebbi, C.: Vacuum periodicity in a Yang-Mills quantum theory. Phys. Rev. Lett. **37**, 172 (1976) 6
14. Khlebnikov, S.Y., Shaposhnikov, M.E.: Extra space-time dimensions: Towards a solution to the strong CP problem. Phys. Lett. B **203**, 121 (1988) 7
15. Schierholz, G.: Towards a dynamical solution of the strong CP problem. Nucl. Phys. Proc. Suppl. **37A**, 203 (1994) [hep-lat/9403012] 7
16. Bég, M.A.B., Tsao, H.S.B.: Strong P, T noninvariances in a superweak theory. Phys. Rev. Lett. **41**, 278 (1978) 7
17. Georgi, H.: A model of soft CP violation. Hadronic J. **1**, 155 (1978) 7
18. Mohapatra, R.N., Senjanović, G.: Natural suppression of strong P and T noninvariance. Phys. Lett. B **79**, 283 (1978) 7
19. Zeldovich, Y.B., Kobzarev, I.Y., Okun, L.B.: Cosmological consequences of the spontaneous breakdown of discrete symmetry. Zh. Eksp. Teor. Fiz. **67**, 3 (1974) [Sov. Phys. JETP **40**, 1 (1974)] 7
20. Barr, S.M.: A natural class of non-Peccei-Quinn models. Phys. Rev. D **30**, 1805 (1984) 7
21. Barr, S.M.: A survey of a new class of models of CP violation. Phys. Rev. D **34**, 1567 (1986) 7
22. Nelson, A.E.: Naturally weak CP violation. Phys. Lett. B **136**, 387 (1984) 7
23. Nelson, A.E.: Calculation of $\bar{\theta}$. Phys. Lett. B **143**, 165 (1984) 7
24. Kaplan, D.B., Manohar, A.V.: Current mass ratios of the light quarks. Phys. Rev. Lett. **56**, 2004 (1986) 7
25. Peccei, R.D., Quinn, H.R.: CP conservation in the presence of instantons. Phys. Rev. Lett. **38**, 1440 (1977) 7, 8, 12
26. Peccei, R.D., Quinn, H.R.: Constraints imposed by CP conservation in the presence of instantons. Phys. Rev. D **16**, 1791 (1977) 7, 8, 12
27. Gasser, J., Leutwyler, H.: Quark masses. Phys. Rept. **87**, 77 (1982) 7, 10
28. Weinberg, S.: A new light boson?. Phys. Rev. Lett. **40**, 223 (1978) 7
29. Wilczek, F.: Problem of strong P and T invariance in the presence of instantons. Phys. Rev. Lett. **40**, 279 (1978) 7
30. Bardeen, W.A., Tye, S.H., Vermaseren, J.A.M.: Phenomenology of the new light Higgs boson search. Phys. Lett. B **76**, 580 (1978) 8
31. Bardeen, W.A., Peccei, R.D., Yanagida, T.: Constraints on variant axion models. Nucl. Phys. B **279**, 401 (1987) 8, 11, 12

32. Asano, Y., et al.: Search for a rare decay mode $K^+ \to \pi^+ \nu\bar{\nu}$ and axion. Phys. Lett. B **107**, 159 (1981) 12
33. Kim, J.E.: Weak interaction singlet and strong CP invariance. Phys. Rev. Lett. **43**, 103 (1979) 12
34. Shifman, M.A., Vainshtein, A.I., Zakharov, V.I.: Can confinement ensure natural CP invariance of strong interactions?. Nucl. Phys. B **166**, 493 (1980) 12
35. Dine, M., Fischler, W., Srednicki, M.: A simple solution to the strong CP problem with a harmless axion. Phys. Lett. B **104**, 199 (1981) 12
36. Zhitnitsky, A.R.: On possible suppression of the axion hadron interactions. Sov. J. Nucl. Phys. **31**, 260 (1980) [Yad. Fiz. **31**, 497 (1980)] 12
37. Raffelt, G.G.: Stars as Laboratories for Fundamental Physics. Chicago University Press, Chicago (1996) 14
38. Turner, M.S.: Windows on the axion. Phys. Rept. **197**, 67 (1990) 14
39. Preskill, J., Wise, M.B., Wilczek, F.: Cosmology of the invisible axion. Phys. Lett. B **120**, 127 (1983) 14
40. Abbott, L.F., Sikivie, P.: A cosmological bound on the invisible axion. Phys. Lett. B **120**, 133 (1983) 14
41. Dine, M., Fischler, W.: The not-so-harmless axion. Phys. Lett. B **120**, 137 (1983) 14
42. Fox, P., Pierce, A., Thomas, S.D.: Probing a QCD string axion with precision cosmological measurements. [hep-th/0409059] 14
43. Spergel, D.N., et al.: Wilkinson Microwave Anisotropy Probe (WMAP) three year results: Implications for cosmology. Astrophys. J. Suppl. **170**, 377 (2007) [astro-ph/0603449] 15
44. Peccei, R.D.: J. Korean Phys. Soc. **29**, S199 (1996) [hep-ph/9606475] 15

2 Axion Cosmology

Pierre Sikivie

[1] Department of Physics, University of Florida, Gainesville, FL 32611, USA
[2] Theoretical Physics Division, CERN, CH-1211 Genève 23, Switzerland
sikivie@phys.ufl.edu

Abstract. The cosmological properties of axions are reviewed. We discuss the axions produced by thermal processes in the early universe, the evolution of the average axion field between the Peccei-Quinn and QCD phase-transitions, the domain-wall problem and its possible resolutions, the population of cold axions produced by vacuum realignment, string decay and domain wall decay, and, finally, axion miniclusters and axion isocurvature perturbations.

For background information on the strong CP problem and on laboratory and astrophysical axion constraints, the reader is referred to Chaps. 1 and 3. In this chapter, we will be concerned only with the cosmological properties of axions. We merely mention that different authors may use different definitions of the axion decay constant f_a. We define normalization by the action density for QCD plus an axion

$$L_{\rm QCD+a} = -\frac{1}{4}G^b_{\mu\nu}G^{b\mu\nu} + \frac{1}{2}\partial_\mu a\,\partial^\mu a + \sum_q \bar{q}\,(i\gamma^\mu\partial_\mu - m_q)\,q + \frac{g_s^2}{32\,\pi^2}\left(\theta + \frac{a}{f_a}\right)G^b_{\mu\nu}\tilde{G}^{b\mu\nu}\ , \quad (2.1)$$

where a is the axion field before mixing with the η and π^0 mesons. Equation (2.1) uses standard notation for the chromomagnetic field strength tensor G, the strong coupling constant $g_{\rm s}$, and the quark fields q. The axion mass, after mixing with the η and π^0 mesons, is given in terms of f_a by

$$m_a \simeq 6\,\mu{\rm eV}\left(\frac{10^{12}\,{\rm GeV}}{f_a}\right)\ . \quad (2.2)$$

The axion-decay constant is related to the magnitude v_a of the vacuum expectation value that breaks the $U(1)_{\rm PQ}$ symmetry by $f_a = v_a/N$. N is an integer characterizing the color anomaly of $U(1)_{\rm PQ}$, and $N = 6$ in the original Peccei-Quinn-Weinberg-Wilczek axion model. All axion couplings are inversely proportional to f_a.

P. Sikivie: *Axion Cosmology*, Lect. Notes Phys. **741**, 19–50 (2008)
DOI 10.1007/978-3-540-73518-2_2

2.1 Thermal Axions

Axions are created and annihilated during interactions among particles in the primordial soup. Let us call the population of axions established as a result of such processes "thermal axions", to distinguish them from the population of "cold axions" which we discuss later. The number density $n_a^{\rm th}(t)$ of thermal axions solves the Boltzmann equation [1]

$$\frac{{\rm d}n_a^{\rm th}}{{\rm d}t} + 3Hn_a^{\rm th} = \Gamma\left(n_a^{\rm eq} - n_a^{\rm th}\right) \ , \tag{2.3}$$

where

$$\Gamma = \sum_i n_i \langle \sigma_i v \rangle \tag{2.4}$$

is the rate at which axions are created and annihilated. $H(t)$ is the Hubble expansion rate and

$$n_a^{\rm eq} = \frac{\zeta(3)}{\pi^2}\, T^3 \tag{2.5}$$

is the number density of axions at thermal equilibrium, where $\zeta(3) = 1.202\ldots$ is the Riemann zeta function of argument 3. In (2.4), the sum is over processes of the type $a + i \leftrightarrow 1 + 2$, where 1 and 2 are other particle species, n_i is the number density of particle species i, σ_i is the corresponding cross section, and $\langle \ldots \rangle$ indicates averaging over the momentum distributions of the particles involved.

Unless unusual events are taking place, $T \propto R^{-1}$ where $R(t)$ is the scale factor, and (2.5) implies, therefore,

$$\frac{{\rm d}n_a^{\rm eq}}{{\rm d}t} + 3Hn_a^{\rm eq} = 0 \ . \tag{2.6}$$

Combining (2.6) and (2.3), one obtains

$$\frac{\rm d}{{\rm d}t}\left[R^3(n_a^{\rm th} - n_a^{\rm eq})\right] = -\Gamma R^3\left(n_a^{\rm th} - n_a^{\rm eq}\right) \ . \tag{2.7}$$

This equation implies that a thermal distribution of axions is approached exponentially fast whenever the condition

$$\Gamma > H \tag{2.8}$$

is satisfied. So, we have a thermal population of axions today, provided the inequality (2.8) prevailed for a few expansion times at some point in the early universe and the thermal population of axions thus established did not subsequently get diluted away by inflation or some other cause of huge entropy release.

The least model-dependent processes for thermalizing axions in the early universe are (a) $a + q(\bar{q}) \leftrightarrow g + q(\bar{q})$, (b) $a + g \leftrightarrow q + \bar{q}$, and (c) $a + g \leftrightarrow g + g$.

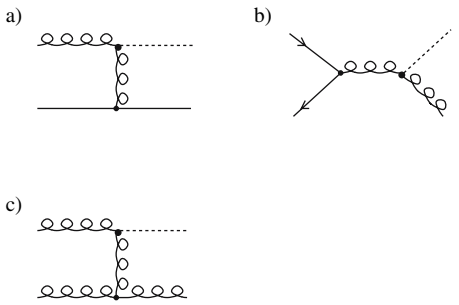

Fig. 2.1. Processes which produce thermal axions in the early universe

The corresponding diagrams are shown in Fig. 2.1. These processes involve only the coupling of the axion to gluons, present in any axion model, and the coupling of quarks to gluons.

A detailed treatment is provided in [2]. We give only a rough estimate here. The processes of Fig. 2.1 have cross sections of order

$$\sigma \sim \frac{\alpha_{\rm s}^3}{8\pi^2}\,\frac{1}{f_a^2}\,, \tag{2.9}$$

where $\alpha_s = g_s^2/4\pi$. At temperatures $T > 1\,\text{TeV}$, the densities of quarks, antiquarks, and gluons are

$$n_q = n_{\bar q} = 27\,\frac{\zeta(3)}{\pi^2}\,T^3 \quad \text{and} \quad n_g = 16\,\frac{\zeta(3)}{\pi^2}\,T^3\,. \tag{2.10}$$

The Hubble rate is given by the Friedmann equation

$$H^2 = \frac{8\pi\,G}{3}\,\varrho = \frac{8\pi\,G}{3}\,\left[\mathcal{N}_b(T) + \frac{7}{8}\,\mathcal{N}_f(T)\right]\,\frac{\pi^2}{30}\,T^4\,, \tag{2.11}$$

where $\mathcal{N}_b(T)$ and $\mathcal{N}_f(T)$ are, respectively, the total effective number of bosonic and fermionic spin degrees of freedom at temperature T. For $T > 1\,\text{TeV}$,

$$\mathcal{N} \equiv \mathcal{N}_b + \frac{7}{8}\,\mathcal{N}_f = 107.75 \tag{2.12}$$

if we assume no new degrees of freedom other than those of the Standard Model plus an axion. Combining everything and setting $\alpha_{\rm s} \simeq 0.03$, one finds

$$\sum_{i=1}^{3}\,\frac{n_i\langle\sigma_i v\rangle}{H} \sim 2\left(\frac{10^{12}\,\text{GeV}}{f_a}\right)^2\,\frac{T}{10^{12}\,\text{GeV}}\,. \tag{2.13}$$

Thus we find that the processes of Fig. 2.1 keep axions in thermal equilibrium with the primordial soup until the temperature

$$T_{\rm D} \sim 5 \times 10^{11}\,{\rm GeV} \left(\frac{f_a}{10^{12}\,{\rm GeV}}\right)^2 . \tag{2.14}$$

Note that the calculation is not valid when $T \gtrsim v_a = N f_a$, as the PQ symmetry is restored then. In particular, in view of (2.14), the processes under consideration produce a population of thermal axions only if $f_a \lesssim 2N\,10^{12}\,{\rm GeV}$.

We will see in Sect. 2.4 that f_a has to be less than approximately $10^{12}\,{\rm GeV}$ to avoid overclosing the universe with cold axions. That bound suggests that the processes of Fig. 2.1 do produce a population of thermal axions. We should keep in mind, however, that this thermal axion population may be wiped out by a period of inflation with reheat temperature less than $T_{\rm D}$. So it is interesting to search for processes that may re-establish a thermal axion population later on. We briefly discuss two such possibilities.

First we consider the Compton-like scattering process $Q + g \leftrightarrow Q + a$, where Q may be a known quark or a new heavy quark. There are related processes in which the gluon is replaced by a photon or Z-boson, and/or the quark is replaced by a lepton. However $Q + g \leftrightarrow Q + a$ is the least model-dependent among the Compton-like processes because, in every axion model, there is at least one colored fermion Q that carries PQ charge and hence to which the axion couples. The cross section is

$$\sigma_Q \sim \frac{\alpha_s}{v_a^2} \times \begin{cases} (m_Q/T)^2 & \text{for } T > m_Q\ , \\ 1 & \text{for } T < m_Q\ . \end{cases} \tag{2.15}$$

The relevant regime is when $T > m_Q$ as the Q number density is Boltzmann suppressed for $T < m_Q$. Using $\alpha_s = 0.05$ and $\mathcal{N} = 107.75$, we have

$$\frac{n_Q \langle \sigma_Q v \rangle}{H} \sim \frac{m_Q^2}{T\,(2 \times 10^7\,{\rm GeV})} \left(\frac{10^{12}\,{\rm GeV}}{v_a}\right)^2 \tag{2.16}$$

for $T > m_Q$. So this process produces a population of thermal axions provided

$$m_Q \gtrsim 2 \times 10^7\,{\rm GeV} \left(\frac{v_a}{10^{12}\,{\rm GeV}}\right)^2 . \tag{2.17}$$

The axions decouple then at a temperature $T_{\rm D} \sim m_Q$.

Let us also consider the process $\pi + \pi \leftrightarrow \pi + a$. As the axion necessarily mixes with the π^0, this process is model-independent as well. It occurs at $T \sim 200\,{\rm MeV}$, after the QCD phase-transition but before the pions have annihilated. The cross section is of order

$$\sigma_\pi \sim f_a^{-2} . \tag{2.18}$$

Using $\mathcal{N} = 17.25$, we find

$$\frac{n_\pi \langle \sigma_\pi v \rangle}{H} \sim \left(\frac{3 \times 10^8\,{\rm GeV}}{f_a}\right)^2 \tag{2.19}$$

at $T \sim m_\pi$. The $\pi + \pi \leftrightarrow \pi + a$ process has the advantage of occurring very late so that any thermal axion population it establishes cannot be wiped out by inflation – inflation occurring that late would also wipe out the baryons. However, (2.19) indicates that it is ineffective unless the bound $f_a > 10^9\,\mathrm{GeV}$ from SN 1987A is saturated.

We have seen that, under a broad set of circumstances, a population of relic thermal axions is produced. For $f_a > 10^9\,\mathrm{GeV}$, the axion lifetime exceeds by many orders of magnitude the age of the universe. Between their last decoupling, at temperature T_D, and today, the thermal axion population is merely diluted and redshifted by the expansion of the universe. Their present number density is

$$n_a^\mathrm{th}(t_0) = \frac{\zeta(3)}{\pi^2}\, T_\mathrm{D}^3 \left(\frac{R_\mathrm{D}}{R_0}\right)^3 , \tag{2.20}$$

where R_D/R_0 is the ratio of scale factors between the time t_D of decoupling and today. Their average momentum is

$$\left\langle p_a^\mathrm{th}(t_0)\right\rangle = \frac{\pi^4}{30\zeta(3)}\, T_\mathrm{D}\, \frac{R_\mathrm{D}}{R_0} = 2.701\, T_\mathrm{D}\, \frac{R_\mathrm{D}}{R_0} . \tag{2.21}$$

If $\left\langle p_a^\mathrm{th}(t_0)\right\rangle \gg m_a$, the energy distribution is thermal with temperature

$$T_{a0} = T_\mathrm{D}\, \frac{R_\mathrm{D}}{R_0} . \tag{2.22}$$

If there is neither inflation nor any other form of entropy release, from t_D until the present, T_{a0} is related to the present cosmic microwave background temperature $T_{\gamma 0} = 2.735\,\mathrm{K}$ by the conservation of entropy. As electron-positron annihilation occurs after neutrino decoupling, one finds

$$T_{a0} = \left(\frac{10.75}{\mathcal{N}_\mathrm{D}}\, \frac{4}{11}\right)^{1/3} T_{\gamma 0} = 0.905\,\mathrm{K} \left(\frac{106.75}{\mathcal{N}_\mathrm{D}}\right)^{1/3} . \tag{2.23}$$

The average momentum of relic thermal axions is

$$\left\langle p_a^\mathrm{th}(t_0)\right\rangle = 2.1 \times 10^{-4}\,\mathrm{eV} \left(\frac{106.75}{\mathcal{N}_\mathrm{D}}\right)^{1/3} , \tag{2.24}$$

and their number density is

$$n_a^\mathrm{th}(t_0) = 7.5\,\mathrm{cm}^{-3}\, \frac{106.75}{\mathcal{N}_\mathrm{D}} . \tag{2.25}$$

2.2 Axion Field Evolution

The thermal axions discussed in the previous section are quantum fluctuations about the average background value of the axion field. The evolution

of the average axion field, from the moment $U(1)_{\rm PQ}$ gets spontaneously broken during the PQ phase-transition to the moment the axion acquires mass during the QCD phase-transition, is the topic of this section.

The $U(1)_{\rm PQ}$ symmetry gets spontaneously broken at a critical temperature $T_{\rm PQ} \sim v_a$, where v_a is the vacuum expectation value of a complex field $\phi(x)$. The action density for this field is of the form

$$L_\phi = \frac{1}{2}\,\partial_\mu\phi^\dagger\,\partial^\mu\phi - \frac{\lambda}{4}\,\left(\phi^\dagger\phi - v_a^2\right)^2 + \dots\ , \tag{2.26}$$

where the dots represent interactions with other fields in the theory. At $T > T_{\rm PQ}$, the free energy has its minimum at $\phi = 0$. At $T < T_{\rm PQ}$, the minimum is a circle, the radius of which quickly approaches v_a as T decreases. Afterwards

$$\langle\phi(x)\rangle = v_a\,{\rm e}^{{\rm i}a(x)/v_a}\ , \tag{2.27}$$

where $a(x)$ is the axion field before mixing with the π^0 and η mesons. The field $a(x)$ has random initial conditions. In particular, at two points outside each other's causal horizon, the values of $a(x)$ are completely uncorrelated.

It is well-known that the size of the causal horizon is hugely modified during cosmological inflation. Without inflation, the size of the causal horizon is of order t, the age of the universe. But, during an inflationary epoch, the causal horizon grows exponentially fast and becomes enormous compared to t. There are two cases to consider.

- **Case 1:** Inflation occurs with reheat temperature smaller than $T_{\rm PQ}$, and the axion field is homogenized over enormous distances. The subsequent evolution of this zero-momentum mode is relatively simple.
- **Case 2:** Inflation occurs with reheat temperature larger than $T_{\rm PQ}$. In addition to the zero mode, the axion field has non-zero modes and carries strings and domain walls as topological defects.

The early universe is assumed to be homogeneous and isotropic. Its curvature is negligible. The space-time metric can therefore be written in the Robertson-Walker form

$$-\,{\rm d}s^2 = {\rm d}t^2 - R(t)^2\,{\rm d}\mathbf{x}\cdot{\rm d}\mathbf{x}\ , \tag{2.28}$$

where the $\mathbf{x}$ are co-moving spatial coordinates and $R(t)$ is the scale factor. The equation of motion for $a(x)$ in this space-time is

$$D_\mu\partial^\mu a(x) + V_a'[a(x)] = \left(\partial_t^2 + 3\,\frac{\dot R}{R}\,\partial_t - \frac{1}{R^2}\,\nabla_{\mathbf{x}}^2\right)\,a(x) + V_a'[a(x)] = 0\ , \tag{2.29}$$

where V_a is the effective potential for the axion field and prime indicates a derivative with respect to a. V_a results from non-perturbative QCD effects associated with instantons [3, 4]. They break the $U(1)_{\rm PQ}$ symmetry down to a $Z(N)$ discrete subgroup [5]. $V_a(a)$ is therefore periodic with period $\Delta a = 2\pi\,v_a/N = 2\pi f_a$. We may write such a potential qualitatively as

$$V_a = f_a^2\, m_a^2(t)\, [1 - \cos\,(a/f_a)]\ , \tag{2.30}$$

where the axion mass $m_a(t) = m_a[T(t)]$ is a function of temperature and hence of time. Equation (2.27) implies that the axion field has a range $0 \leq a \leq 2\pi v_a$. Hence there are N degenerate vacua. The discrete degeneracy implies the existence of domain walls, which will be discussed in Sect. 2.3.

Substituting (2.30) into (2.29), the equation of motion becomes

$$\left(\partial_t^2 + 3\,\frac{\dot{R}}{R}\,\partial_t - \frac{1}{R^2}\,\nabla_{\mathbf{x}}^2\right)\, a(x)\, m_a^2(t)\, f_a \sin\left(\frac{a(x)}{f_a}\right) = 0\ . \tag{2.31}$$

The non-perturbative QCD effects associated with instantons have amplitudes proportional to

$$\mathrm{e}^{-2\pi/\alpha_s(T)} \simeq \left(\frac{\Lambda_{\mathrm{QCD}}}{T}\right)^{11-2N_f/3}\ , \tag{2.32}$$

where N_f is the number of quark flavors with mass less than T. Equation (2.32) implies that the axion mass is strongly suppressed at temperatures that are large compared to the QCD scale but turns on rather abruptly when the temperature approaches Λ_{QCD}.

Because the first three terms in (2.31) are proportional to t^{-2}, the axion mass is unimportant in the evolution of the axion field until $m_a(t)$ becomes of order t^{-1}. Let us define a critical time t_1 by

$$m_a(t_1)\, t_1 = 1\ . \tag{2.33}$$

The axion mass effectively turns on at t_1. From a calculation of the effects [6, 7, 8] of QCD instantons at high temperature [9] one obtains

$$m_a(T) \simeq 4 \times 10^{-9}\,\mathrm{eV}\,\left(\frac{10^{12}\,\mathrm{GeV}}{f_a}\right)\left(\frac{\mathrm{GeV}}{T}\right)^4\ , \tag{2.34}$$

when T is near 1 GeV. The relation between T and t follows from (2.11) and $H = 1/2t$. The total effective number $\mathcal{N}$ of thermal spin degrees of freedom is changing near 1 GeV temperature from a value near 60, valid above the quark-hadron phase transition, to a value of order 30 below that transition. Using $\mathcal{N} \simeq 60$, one has

$$m_a(t) \simeq 0.7 \times 10^{20}\,\mathrm{s}^{-1}\,\left(\frac{t}{1\,\mathrm{s}}\right)^2\left(\frac{10^{12}\,\mathrm{GeV}}{f_a}\right)\ , \tag{2.35}$$

which implies

$$t_1 \simeq 2 \times 10^{-7}\,\mathrm{s}\,\left(\frac{f_a}{10^{12}\,\mathrm{GeV}}\right)^{1/3}\ . \tag{2.36}$$

The corresponding temperature is

$$T_1 \simeq 1\,\mathrm{GeV}\left(\frac{10^{12}\,\mathrm{GeV}}{f_a}\right)^{1/6} . \tag{2.37}$$

Equation (2.35) implies $\mathrm{d}\ln[m_a(t)]/\mathrm{d}t < m_a(t)$ after t_1. So, at least for a short while below 1 GeV, as long as (2.34) remains valid, the axion mass changes adiabatically. The number of axions is the adiabatic invariant. Conservation of the number of axions after t_1 allows us to estimate the energy density of axions today from an estimate of their number density at t_1. When the temperature drops well below 1 GeV, the dilute instanton gas calculations that yield (2.34) are no longer reliable. Complicated things happen such as the confinement and chiral symmetry-breaking phase-transitions. However, because $m_a \gg H$ then, it is reasonable to expect the number of axions to be conserved, at least in order of magnitude.

2.2.1 Zero Mode

In case 1, where inflation occurs after the PQ phase-transition, the axion field is homogenized over enormous distances. Equation (2.31) becomes [6, 7, 8]

$$\left(\frac{\mathrm{d}^2}{\mathrm{d}t^2} + \frac{3}{2t}\frac{\mathrm{d}}{\mathrm{d}t}\right) a(t) + m_a^2(t)\, f_a \sin\left(\frac{a(t)}{f_a}\right) = 0 , \tag{2.38}$$

where we used $R(t) \propto t^{1/2}$. For $t \ll t_1$, we may neglect m_a. The solution is then

$$a(t) = a_0 + a_{1/2}\, t^{-1/2} , \tag{2.39}$$

where a_0 and $a_{1/2}$ are constants. Equation (2.39) implies that the expansion of the universe slows the axion field down to a constant value.

When t approaches t_1, the axion field starts oscillating in response to the turn-on of the axion mass. We will assume that the initial value of a is sufficiently small that $f_a \sin(a/f_a) \simeq a$. Let us define ψ by

$$a(t) \equiv t^{-3/4}\psi(t) . \tag{2.40}$$

The equation for $\psi(t)$ is

$$\left[\frac{\mathrm{d}^2}{\mathrm{d}t^2} + \omega^2(t)\right] \psi(t) = 0 , \tag{2.41}$$

where

$$\omega^2(t) = m_a^2(t) + \frac{3}{16\, t^2} . \tag{2.42}$$

For $t > t_1$, we have $\mathrm{d}\ln\omega/\mathrm{d}t \ll \omega \simeq m_a$. That regime is characterized by the adiabatic invariant $\psi_0^2(t)\,\omega(t)$, where $\psi_0(t)$ is the changing oscillation amplitude of $\psi(t)$. We have, therefore,

$$\psi(t) \simeq \frac{C}{\sqrt{m_a(t)}} \cos\left[\int^t \mathrm{d}t'\, \omega(t')\right] , \tag{2.43}$$

where C is a constant. Hence

$$a(t) = A(t)\, \cos\left[\int^t \mathrm{d}t' \omega(t')\right] , \tag{2.44}$$

with

$$A(t) = \frac{C}{\sqrt{m_a(t)}}\, t^{-3/4} . \tag{2.45}$$

Hence, during the adiabatic regime,

$$A^2(t)\, m_a(t) \propto t^{-3/2} \propto R(t)^{-3} . \tag{2.46}$$

The zero-momentum mode of the axion field has energy density $\varrho_a = \frac{1}{2}\, m_a^2\, A^2$ and describes a coherent state of axions at rest with number density $n_a = \frac{1}{2}\, m_a A^2$. Equation (2.46) states, therefore, that the number of zero-momentum axions per co-moving volume is conserved. The result holds as long as the changes in the axion mass are adiabatic.

We estimate the number density of axions in the zero-momentum mode at late times later by saying that the axion field has a random initial value $a(t_1) = f_a \alpha_1$ and evolves according to (2.44) and (2.45) for $t > t_1$, where α_1 is called the "initial misalignment angle." As the effective potential for a is periodic with period $2\pi f_a$, the relevant range of α_1 values is $-\pi$ to $+\pi$. The number density of zero-momentum axions at time t_1 is then [6, 7, 8]

$$n_a^{\mathrm{vac},0}(t_1) \sim \frac{1}{2}\, m_a(t_1)\, a^2(t_1) = \frac{f_a^2}{2t_1}\, \alpha_1^2 , \tag{2.47}$$

where we used (2.33). We will use (2.47) in Sect. 2.4 to estimate the zero-mode contribution to the cosmological energy density of cold axions.

A more precise treatment would solve (2.38) for $t \sim t_1$, e.g. by numerical integration, to obtain the exact interpolation between the sudden ($t < t_1$) and adiabatic ($t > t_1$) regimes. An additional improvement is to solve (2.38) without linearizing the sine function, thus allowing large values of α_1. Although these improvements are desirable, they would still leave the number of axions unknown in case 1 because the initial misalignment angle α_1 is unknown. In case 2, the zero-mode contribution to the axion number density is also given by (2.47), but the misalignment angle α_1 varies randomly from one horizon to the next.

2.2.2 Non-Zero Modes

In case 2, where there is no inflation after the PQ phase-transition, the axion field is spatially varying. Axion strings are present as topological defects, and non-zero momentum modes of the axion field are excited. We first consider

a region of the universe that happens to be free of strings. Strings will be added in the next subsection.

The axion field satisfies (2.31). We neglect the axion mass until $t \sim t_1$. The solution of (2.31) is a linear superposition of eigenmodes with definite co-moving wavevector $\mathbf{k}$:

$$a(\mathbf{x},t) = \int \mathrm{d}^3\mathbf{k}\, a(\mathbf{k},t)\, \mathrm{e}^{\mathrm{i}\mathbf{k}\cdot\mathbf{x}} \,, \tag{2.48}$$

where $a(\mathbf{k},t)$ satisfies

$$\left(\partial_t^2 + \frac{3}{2t}\,\partial_t + \frac{k^2}{R^2}\right) a(\mathbf{k},t) = 0 \,. \tag{2.49}$$

Equations (2.28) and (2.48) imply that the wavelength $\lambda(t) = 2\pi R(t)/k$ of each mode is stretched by the Hubble expansion. There are two qualitatively different regimes in the evolution of a mode, depending on whether its wavelength is outside $[\lambda(t) > t]$ or inside $[\lambda(t) < t]$ the horizon.

For $\lambda(t) \gg t$, only the first two terms in (2.49) are important and the most general solution is

$$a(\mathbf{k},t) = a_0(\mathbf{k}) + a_{-1/2}(\mathbf{k})\, t^{-1/2} \,. \tag{2.50}$$

Thus, for wavelengths larger than the horizon, each mode goes to a constant; the axion field is "frozen by causality".

For $\lambda(t) \ll t$, let $a(\mathbf{k},t) = R^{-3/2}(t)\,\psi(\mathbf{k},t)$. Equation (2.49) becomes

$$\left[\partial_t^2 + \omega^2(t)\right]\, \psi(\mathbf{k},t) = 0 \,, \tag{2.51}$$

where

$$\omega^2(t) = \frac{k^2}{R^2(t)} + \frac{3}{16\,t^2} \simeq \frac{k^2}{R^2(t)} \,. \tag{2.52}$$

As $\mathrm{d}\ln\omega/\mathrm{d}t \ll \omega$, this regime is again characterized by the adiabatic invariant $\psi_0^2(\mathbf{k},t)\,\omega(t)$, where $\psi_0(\mathbf{k},t)$ is the oscillation amplitude of $\psi(\mathbf{k},t)$. Hence the most general solution is

$$a(\mathbf{k},t) = \frac{C}{R(t)}\, \cos\left[\int^t \mathrm{d}t'\omega(t')\right] \,, \tag{2.53}$$

where C is a constant. The energy density and the number density behave, respectively, as $\varrho_{a,\mathbf{k}} \sim C^2\omega^2 R^{-2}(t) \propto R^{-4}(t)$ and $n_{a,\mathbf{k}} \sim \omega^{-1}\varrho_{a,\mathbf{k}} \propto R^{-3}(t)$, indicating that the number of axions in each mode is conserved. This is as expected because the expansion of the universe is adiabatic for modes with $\lambda(t)\,t \ll 1$.

Let us call $\mathrm{d}n_a(\omega,t)/\mathrm{d}\omega$ the number density, in physical and frequency space, of axions with wavelength $\lambda = 2\pi/\omega$, for $\omega > t^{-1}$. The axion number density in physical space is thus

$$n_a(t) = \int_{t^{-1}} \mathrm{d}\omega \, \frac{\mathrm{d}n_a}{\mathrm{d}\omega}(\omega, t) \, , \tag{2.54}$$

whereas the axion energy density is

$$\varrho_a(t) = \int_{t^{-1}} \mathrm{d}\omega \, \omega \, \frac{\mathrm{d}n_a}{\mathrm{d}\omega}(\omega, t) \, . \tag{2.55}$$

Under the Hubble expansion, axion energies redshift according to $\omega' = \omega \, (R/R')$ and volume elements expand according to $\Delta V' = \Delta V \, (R'/R)^3$, whereas the number of axions is conserved mode by mode. Hence

$$\frac{\mathrm{d}n_a}{\mathrm{d}\omega}(\omega, t) = \left(\frac{R'}{R} \right)^2 \frac{\mathrm{d}n_a}{\mathrm{d}\omega}(\omega \, R/R', t') \, . \tag{2.56}$$

Moreover, the size of $\mathrm{d}n_a/\mathrm{d}\omega$ for $\omega \sim t^{-1}$ is determined in order of magnitude by the fact that the axion field typically varies by $v_a = N f_a$ from one horizon to the next. Thus

$$\omega \, \frac{\mathrm{d}n_a}{\mathrm{d}\omega}(\omega, t) \, \Delta\omega \Big|_{\omega \sim \Delta\omega \sim t^{-1}} \sim \frac{\mathrm{d}n_a}{\mathrm{d}\omega}(t^{-1}, t) \, t^{-2} \sim \frac{1}{2} \, (\boldsymbol{\nabla} a)^2 \sim \frac{1}{2} \, \frac{N^2 f_a^2}{t^2} \, . \tag{2.57}$$

From (2.56), (2.57) and $R \propto t^{1/2}$, we have [10]

$$\frac{\mathrm{d}n_a}{\mathrm{d}\omega}(\omega, t) \sim \frac{N^2 f_a^2}{2 t^2 \omega^2} \, . \tag{2.58}$$

This equation holds until the axion acquires mass during the QCD phase-transition.

2.2.3 Strings

In case 2, axion strings are present as topological defects in the axion field from the PQ to the QCD phase-transitions [11]. The energy per unit length of an axion string is

$$\mu = \pi v_a^2 \ln(v_a L) \, . \tag{2.59}$$

L is an infra-red cutoff, which in practice equals the distance to the nearest neighbor string. Because they are strongly coupled to the axion field, the strings decay very efficiently into axions. We will see that practically all axions produced by string-decay are non-relativistic after t_1. Because each such axion contributes m_a to the present energy density, it is important to evaluate the *number* density of axions emitted in string-decay. This is our main goal in this subsection.

At a given time t, there is at least on the order of one string per horizon. Indeed the axion field is completely uncorrelated over distances larger than t. Hence there is non-zero probability that the random values of $a(\mathbf{x}, t)$ wander from zero to $2\pi \, v_a$ along a closed path in physical space, if that closed path

has size larger than t. When this is the case, a string perforates the surface subtended by the closed path.

At first, the strings are stuck in the primordial plasma and are stretched by the Hubble expansion. During that time, because $R(t) \propto t^{1/2}$, the density of strings grows to be much larger than one per horizon. However, expansion dilutes the plasma, and at some point, the strings become unstuck. The temperature at which strings start to move freely is of order [12]

$$T_* \sim 2 \times 10^7 \,\mathrm{GeV} \left(\frac{f_a}{10^{12}\,\mathrm{GeV}} \right)^2 . \tag{2.60}$$

Below T_*, there is a network of axion strings moving at relativistic speeds. Axions are radiated very efficiently by collapsing string loops and by oscillating wiggles on long strings. By definition, long strings stretch across horizons. They move and intersect one another. When strings intersect, there is a high probability of reconnection, i.e., of rerouting of the topological flux [13]. Because of such "intercommuting," long strings produce loops which then collapse freely. In view of this efficient decay mechanism, the average density of long strings is expected to be of order the minimum consistent with causality, namely, one long string per horizon. Hence the energy density in long strings is

$$\varrho_{\mathrm{str}}(t) = \xi \, \frac{\tau}{t^2} \simeq \xi \, \pi \, \frac{(f_a N)^2}{t^2} \, \ln(v_a t) \, , \tag{2.61}$$

where ξ is a parameter of order one.

The equations governing the number density $n_a^{\mathrm{str}}(t)$ of axions radiated by axion strings are [12]

$$\frac{\mathrm{d}\varrho_{\mathrm{str}}}{\mathrm{d}t} = -2H\varrho_{\mathrm{str}} - \frac{\mathrm{d}\varrho_{\mathrm{str}\to a}}{\mathrm{d}t} \tag{2.62}$$

and

$$\frac{\mathrm{d}n_a^{\mathrm{str}}}{\mathrm{d}t} = -3Hn_a^{\mathrm{str}} + \frac{1}{\omega(t)} \frac{\mathrm{d}\varrho_{\mathrm{str}\to a}}{\mathrm{d}t} \tag{2.63}$$

where $\omega(t)$ is defined by

$$\frac{1}{\omega(t)} = \left(\frac{\mathrm{d}\varrho_{\mathrm{str}\to a}}{\mathrm{d}t} \right)^{-1} \int \frac{\mathrm{d}k}{k} \, \frac{\mathrm{d}^2\varrho_{\mathrm{str}\to a}}{\mathrm{d}t \, \mathrm{d}k} \, , \tag{2.64}$$

where $k = |\mathbf{k}|$. Here, $\mathrm{d}\varrho_{\mathrm{str}\to a}(t)/\mathrm{d}t$ is the rate at which energy density gets converted from strings to axions at time t, and $\mathrm{d}^2\varrho_{\mathrm{str}\to a}(t,k)/\mathrm{d}t\,\mathrm{d}k$ is the spectrum of the axions produced. Therefore, $\omega(t)$ is the average energy of axions radiated in string-decay processes at time t. The term $-2H\varrho_{\mathrm{str}} = +H\varrho_{\mathrm{str}} - 3H\varrho_{\mathrm{str}}$ in (2.62) takes account of the fact that the Hubble expansion both stretches ($+H\varrho_{\mathrm{str}}$) and dilutes ($-3H\varrho_{\mathrm{str}}$) long strings. Integrating (2.61)–(2.63), setting $H = 1/2t$, and neglecting terms of order one versus terms of order $\ln(v_a t)$, one obtains

$$n_a^{\rm str}(t) \simeq \frac{\xi\pi f_a^2 N^2}{t^{3/2}} \int_{t_{\rm PQ}}^{t} {\rm d}t' \, \frac{\ln(v_a t')}{t'^{\,3/2}\omega(t')} \,, \tag{2.65}$$

where $t_{\rm PQ}$ is the time of the PQ transition.

To obtain $n_a^{\rm str}(t)$, we need to know $\omega(t)$, the average energy of axions radiated at time t. If $\omega(t)$ is large, the number of radiated axions is small, and vice versa. Axions are radiated by wiggles on long strings and by collapsing string loops. Consider a process that starts at $t_{\rm in}$ and ends at $t_{\rm fin}$ and converts an amount of energy E from strings to axions. The times $t_{\rm in}$ and $t_{\rm fin}$ are both taken to be of order t. It is useful to define the quantity [14]

$$N_{\rm ax}(t) \equiv \int {\rm d}k \, \frac{{\rm d}E}{{\rm d}k}(t) \, \frac{1}{k} \,, \tag{2.66}$$

where k is the wavevector and ${\rm d}E/{\rm d}k$ is the wavevector spectrum of the a field. At the start ($t = t_{\rm in}$), only strings contribute to the integral in (2.66). At the end ($t = t_{\rm fin}$), only axions contribute. In between, both axions and strings contribute. The number of axions radiated is $N_a = N_{\rm ax}(t_{\rm fin})$, and their average energy is $\omega = E/N_a$. The energy stored in strings has the spectrum ${\rm d}E/{\rm d}k \propto k^{-1}$ for $k_{\rm min} < k < k_{\rm max}$ where $k_{\rm max}$ is of order v_a and $k_{\rm min}$ of order $2\pi/L \sim 2\pi/t$. If $\ell \equiv E/\mu$ is the length of string converted to axions, we have

$$N_{\rm ax}(t_{\rm in}) = \frac{E}{\ln(t v_a)\, k_{\rm min}} \,. \tag{2.67}$$

Hence

$$\omega^{-1} = \frac{r}{\ln(v_a t)\, k_{\rm min}} \,, \tag{2.68}$$

where r is the relative change in $N_{\rm ax}(t)$ during the process in question,

$$r \equiv \frac{N_{\rm ax}(t_{\rm fin})}{N_{\rm ax}(t_{\rm in})} \,. \tag{2.69}$$

$L \simeq 2\pi/k_{\rm min}$ is the loop size in the case of collapsing loops and the wiggle wavelength in the case of bent strings. L is at most of order t but may be substantially smaller if the string network has a lot of small-scale structures. To parameterize our ignorance in this matter, we define χ such that the suitably averaged $k_{\rm min} \equiv \chi\, 2\pi/t$. Combining (2.65) and (2.68) we find

$$n_a^{\rm str}(t) \simeq \frac{\xi \bar{r} N^2}{\chi} \, \frac{f_a^2}{t} \,, \tag{2.70}$$

where $\bar{r}$ is the weighted average of r over the various processes that convert strings to axions. One can show [31] that the population of axions that were radiated between $t_{\rm PQ}$ and t have a spectrum ${\rm d}n_a/{\rm d}k \propto k^{-2}$ for $t^{-1} \lesssim k \lesssim (t_{\rm PQ} t)^{-1/2}$, irrespective of the shape of ${\rm d}^2\varrho_{{\rm str}\to a}/{\rm d}t\,{\rm d}k$, provided $t \gg t_{\rm PQ}$.

At time t_1, each string becomes the edge of N domain walls, and the process of axion radiation by strings stops. Since their momenta are of order

t_1^{-1} at time t_1, the axions radiated by strings become non-relativistic soon after they acquire mass. We discuss the string-decay contribution to the axion energy density in Sect. 2.4. For the moment we turn our attention to the domain walls that appear at t_1 in case 2.

2.3 The Domain-Wall Problem

Axion models have an exact, spontaneously broken, discrete $Z(N)$ symmetry. $Z(N)$ is the subgroup of $U(1)_{\rm PQ}$ that does not get broken by non-perturbative QCD effects [5]. The spontaneously broken $Z(N)$ symmetry implies an N fold degeneracy of the vacuum. The N vacua are at equidistant points on the circle at the bottom of the "Mexican hat" potential for the Peccei-Quinn field ϕ. An axion domain wall is the minimum-energy field configuration that interpolates between neighboring vacua. Note that there are axion domain walls even when $N = 1$. In this case, both sides of the domain wall are in the same vacuum (indeed there is only one vacuum) but the interpolating field configuration winds around the bottom of the Mexican hat potential once. The properties of walls in $N = 1$ models are for most purposes identical to those of walls in $N \geq 2$ models. The only seemingly important difference is that the walls of $N = 1$ models are quantum-mechanically unstable. Even so, their decay-rate per unit surface and time is exponentially small and negligible in the context of our discussion.

When the axion mass turns on, at time t_1, each axion string becomes the edge of N domain walls. The domain walls produce a cosmological disaster unless there is inflation after the PQ phase-transition (case 1) or unless $N = 1$. Indeed, let us consider the implications of case 2 if $N \geq 2$. Since there are two or more exactly degenerate vacua and they have identical properties, the vacua chosen at points outside each other's causal horizon are independent of one another. Hence there is at least on the order of one domain wall per causal horizon at any given time. In case 2, the size of the causal horizon is of order t, the age of the universe. Thus the energy density in domain walls is

$$\varrho_{\rm w}(t) \gtrsim \frac{\sigma}{t} \,, \tag{2.71}$$

where σ is the wall energy per unit surface, given by [5, 15]

$$\sigma \simeq 9 f_a^2 m_a \simeq 5.5 \times 10^{10}\,{\rm GeV}^3 \left(\frac{f_a}{10^{12}\,{\rm GeV}}\right) \,. \tag{2.72}$$

The energy density in axion domain walls today ($t_0 \simeq 14\,{\rm Gyr}$)

$$\varrho_{\rm w}(t_0) \gtrsim \frac{\sigma}{t_0} \simeq 2 \times 10^{-14}\,{\rm g\,cm}^{-3} \left(\frac{f_a}{10^{12}\,{\rm GeV}}\right) \tag{2.73}$$

would exceed by many orders of magnitude the critical energy density, of order $10^{-29}\,\mathrm{g\,cm^{-3}}$, for closing the universe. This would be grossly inconsistent with observation. Let us see what would happen.

Let t_w be the age of the universe when the domain walls start to dominate the energy density. The condition $H^2 \sim 8\pi G\varrho_\mathrm{w}/3$ and (2.71) imply

$$t_\mathrm{w} \lesssim \frac{3}{32\pi G\sigma} \simeq 53\,\mathrm{s}\left(\frac{10^{12}\,\mathrm{GeV}}{f_a}\right) . \tag{2.74}$$

Domain walls are gravitationally repulsive [16, 17, 18]. They accelerate away from each other with acceleration $2\pi G\sigma$ and, after a time of order $(2\pi G\sigma)^{-1}$, recede at the speed of light. By averaging over volumes containing many cells separated by walls, the equation of state of a wall dominated universe is

$$p_\mathrm{w} = -\frac{2}{3}\,\varrho_\mathrm{w} . \tag{2.75}$$

Conservation of energy

$$\mathrm{d}\left(\varrho_\mathrm{w}R^3\right) = -p_\mathrm{w}\mathrm{d}\left(R^3\right) , \tag{2.76}$$

where R is the scale factor, then implies $\varrho_\mathrm{w} \propto R^{-1}$. This scaling-law and the Friedmann equation

$$H^2 = \left(\frac{\dot{R}}{R}\right)^2 = \frac{8\pi G}{3}\,\varrho_\mathrm{w} \tag{2.77}$$

imply that a domain-wall-dominated universe expands according to

$$R \propto t^2 . \tag{2.78}$$

The domain-wall-dominated universe has an accelerated expansion.

One may be tempted to attribute the present-day accelerated expansion of the universe [19, 20] to domain walls. However, a domain-wall-dominated universe is far less homogeneous than today's. It would be divided into cells separated by rapidly expanding walls. Inside each cell, concentrated near the cell's center, would be a clump of matter and radiation with total energy of order

$$M \sim \varrho(t_\mathrm{w})\,t_\mathrm{w}^3 \sim 10^{11}\,M_\odot\left(\frac{m_a}{\mathrm{eV}}\right) . \tag{2.79}$$

One cannot identify these clumps with galaxies because neighboring clumps are receding from one another at close to the speed of light.

There are three solutions to the axion domain-wall problem. The first solution is to have inflation with reheating temperature less than the PQ phase-transition temperature, i.e., postulate case 1. The axion field is then homogenized by inflation, and there are no strings or domain walls. The second solution is to postulate $N = 1$. The third solution is to postulate a small explicit breaking of the $Z(N)$ symmetry. The viability of the second and third solutions is less obvious. We will discuss them in succession.

2.3.1 $N = 1$

The above arguments, showing the existence of a domain-wall problem, are valid only when the vacuum is multiply degenerate. They do not apply to the $N = 1$ case. On the other hand, as $N = 1$ models contain domain walls too, it is not immediately clear that they are free of difficulties. However, $N = 1$ is a solution [11, 21, 22], as we now discuss.

In the circumstances under consideration (case 2), axion strings are present in the early universe from the time of the PQ phase-transition to that of the QCD phase-transition. At temperature T_1 each string becomes the boundary of a single domain wall. To see what the network of walls bounded by strings looks like, a cross section of a finite but statistically significant volume of the universe near time t_1 was simulated [22, 10]. The simulation shows that there are no infinite domain walls that are not cut up by any string. The reason for this is easily understood. An extended domain wall has some probability to be cut up by a string in each successive horizon it traverses. The probability that no string is encountered after traveling a distance l along the wall decreases exponentially with l.

The question now is: what happens to the network of walls bounded by strings? The walls are transparent to the thermalized particles in the primordial soup, whose typical momentum is of order 1 GeV, but have a large reflection coefficient for non-relativistic axions such as the cold axions that were produced by vacuum realignment and wall-decay [15]. The drag on the motion of the walls that results from their reflecting cold axions is important at time t_1 but turns off soon afterwards as the cold axions are diluted by the expansion of the universe [10]. The wall energy per unit surface $\sigma(t) \simeq 8 m_a(t) f_a^2$ is time-dependent. [Equation (2.72) is for zero temperature.] The string at the boundary of a wall is embedded into the wall. Hence its infra-red cutoff L, in the sense of (2.59), is of order m_a^{-1}, the wall thickness [5]. The energy per unit length of such string is therefore

$$\mu \simeq \pi f_a^2 \ln(f_a/m_a) \; . \tag{2.80}$$

The surface energy E_σ of a typical (size $\sim t_1$) piece of wall bounded by a string is $\sigma(t)\, t_1^2$ whereas the energy in the boundary is $E_\mu \sim \mu\, t_1$. There is a critical time t_2 when the ratio

$$\frac{E_\sigma(t)}{E_\mu} \sim \frac{8\, m_a(t)\, t_1}{\pi \ln(f_a/m_a)} \tag{2.81}$$

is of order one. Using (2.35) and (2.36), one estimates

$$\begin{aligned} t_2 &\simeq 10^{-6}\,\mathrm{s} \left(\frac{f_a}{10^{12}\,\mathrm{GeV}} \right)^{1/3} , \\ T_2 &\simeq 600\,\mathrm{MeV} \left(\frac{10^{12}\,\mathrm{GeV}}{f_a} \right)^{1/6} . \end{aligned} \tag{2.82}$$

After t_2, the dynamics of the walls bounded by string is dominated by the energy in the walls, whereas, before t_2, it is dominated by the energy in the string. A string attached to a wall is pulled by the wall's tension. For a straight string and flat wall, the acceleration is

$$a_{\rm s}(t) = \frac{\sigma(t)}{\mu} \simeq \frac{8\, m_a(t)}{\pi \ln(f_a/m_a)} \simeq \frac{m_a(t)}{23} \simeq \frac{1}{t_1}\, \frac{m_a(t)}{m_a(t_2)} \ . \tag{2.83}$$

Therefore, after t_2, each string typically accelerates to relativistic speeds, in the direction of the wall to which it is attached, in less than a Hubble time. The string will then unzip the wall, releasing the stored energy in the form of barely relativistic axions. We will estimate in Sect. 2.4.3 how much do walls bounded by string contribute to the present cosmological axion energy density.

A very small portion of the domain-wall energy density is in walls that are not bounded by string and that form closed surfaces such as spheres or torii [10, 22]. Such closed walls do not decay by the process just described. Instead, they oscillate and emit gravitational waves [11]. Using the quadrupole formula, we may estimate the gravitational-wave power emitted by a closed wall of size ℓ oscillating with frequency $\omega \sim \ell^{-1}$ as

$$P \sim -\frac{{\rm d}(\sigma \ell^2)}{{\rm d}t} \sim G\, (\sigma \ell^4)^2 \omega^6 \sim G\, \sigma^2 \ell^2 \ . \tag{2.84}$$

This result implies the lifetime

$$\tau_{\rm grav} \sim (G\sigma)^{-1} \simeq 2 \times 10^3\, {\rm s} \left(\frac{10^{12}\, {\rm GeV}}{f_a} \right) \ , \tag{2.85}$$

independently of size.

2.3.2 Small Breaking of the PQ Symmetry

A third solution to the domain-wall problem is to postulate a small explicit breaking of the $Z(N)$ symmetry and hence of the PQ symmetry [5]. The symmetry breaking must lift completely the degeneracy of the vacuum and be large enough so that the unique true vacuum takes over before the walls dominate the energy density. On the other hand, it must be small enough so that the PQ mechanism still works. This solution does not appear very attractive, and we will see below that there is little room in parameter space for it to occur, but it is a logical possibility.

To get rid of the walls, we add to the RHS of (2.26) a tiny $U(1)_{\rm PQ}$ breaking term that lifts the vacuum degeneracy completely, e.g.

$$\delta V = -\xi \, \left(\phi\, {\rm e}^{-{\rm i}\delta} + {\rm h.c.} \right) \ . \tag{2.86}$$

To add such a term by hand to an axion model seems rather unnatural. However, it is conceivable that a small $U(1)_{\rm PQ}$-breaking term is in fact a

natural property of the ultimate theory. This would be the case, for example, if the low energy effective theory at some energy scale has an automatic PQ symmetry that is broken in the full theory. Be that as it may, (2.86) yields a small correction to the effective potential for the axion field of

$$\delta V_a = -2v_a\xi\,\cos\left(\frac{a}{v_a}-\delta\right)\,. \tag{2.87}$$

The unique true vacuum is the one for which $|\delta - a/v_a|$ is smallest. Its energy density is lowered by an amount of order ξv_a relative to the other now quasi-vacua. As a result, the walls at the boundary of a region in the true vacuum are subject to an outward pressure of order ξv_a. As the walls are typically a distance t apart, the volume energy $\xi\, v_a\, t^3$ associated with the lifting of the vacuum degeneracy grows more rapidly than the energy σt^2 in the walls. At a time $\tau \sim \sigma/\xi v_a$, the pressure favoring the true vacuum starts to dominate the wall dynamics and the true vacuum takes over, i.e., the walls disappear. The energy stored in the network of walls and strings decays into gravitational waves [10]. The true vacuum must take over before the walls dominate the energy density. Using (2.74), we obtain

$$\tau \sim \frac{\sigma}{\xi v_a} \lesssim 10^2\,\mathrm{s}\,\left(\frac{10^{12}\,\mathrm{GeV}}{f_a}\right)\,. \tag{2.88}$$

On the other hand ξ is bounded from above by the requirement that δV does not upset the PQ mechanism. δV shifts the minimum of the effective potential for the axion field, inducing $\bar\theta \sim \xi/m_a^2 f_a$. The requirement $\bar\theta < 10^{-10}$ implies

$$\tau \gtrsim \frac{10\,\mathrm{s}}{N}\,\left(\frac{f_a}{10^{12}\,\mathrm{GeV}}\right)\,. \tag{2.89}$$

These equations indicate that there is little room in parameter space for this solution to the axion domain-wall problem, but it is not ruled out.

2.4 Cold Axions

We now turn to estimating the cosmological energy density in cold axions and their velocity dispersion. In the previous two sections, we identified several sources for cold axions, i.e., vacuum realignment for the zero-momentum and higher-momentum modes, string decay, and domain-wall decay. In case 1, only the contribution from vacuum realignment with zero momentum is present. In case 2, all sources contribute.

2.4.1 Vacuum Realignment

Zero-Momentum Mode

Let us start with case 1 where the universe was homogenized by inflation after the PQ phase-transition and that is easiest to analyze. The axion number

density at time t_1 is given by (2.47) in terms of the initial vacuum misalignment angle α_1 that has the same value everywhere. We saw in Sect. 2.2 that, barring any sudden changes in the axion mass during the chiral symmetry-breaking phase-transition, the number of axions is an adiabatic invariant after t_1. Hence, the axion density from the vacuum realignment zero mode at a later time t is

$$n_a^{\mathrm{vac},0}(t) \sim \frac{f_a^2}{2t_1}\,\alpha_1^2\,\left(\frac{R_1}{R}\right)^3 , \tag{2.90}$$

where R_1/R is the ratio of scale factors between t_1 and t. Thus, we find

$$\varrho_a^{\mathrm{vac},0}(t_0) \sim \frac{m_a f_a^2}{2t_1}\,\alpha_1^2\,\left(\frac{R_1}{R_0}\right)^3 \tag{2.91}$$

for the axion energy density today.

In case 2, the initial misalignment angle α_1 is different from one QCD horizon to the next. As the average of α_1^2 over many QCD horizons is of order one, we have

$$\varrho_a^{\mathrm{vac},0}(t_0) \sim \frac{m_a f_a^2}{2t_1}\,\left(\frac{R_1}{R_0}\right)^3 . \tag{2.92}$$

However in case 2, there are additional contributions.

Higher-Momentum Modes

In case 2, the axion field is not constant even within each horizon volume. It has wiggles inherited from earlier epochs when the horizon was smaller and the axion field was inhomogeneous on correspondingly shorter scales. The associated density of axions in physical and frequency space is given in (2.58). Integrating over $\omega > t_1^{-1}$, we find the contribution from vacuum realignment involving higher-momentum modes

$$n_a^{\mathrm{vac},1}(t_1) \sim \frac{N^2 f_a^2}{2t_1} . \tag{2.93}$$

Almost all these axions are non-relativistic after t_1. Hence

$$\varrho_a^{\mathrm{vac},1}(t_0) \sim \frac{m_a N^2 f_a^2}{2t_1}\,\left(\frac{R_1}{R_0}\right)^3 . \tag{2.94}$$

Note that, except for the factor N^2, the contributions from the zero- and higher-momentum modes are similar.

2.4.2 String Decay

The evolution of axion strings between the PQ and QCD phase-transitions was discussed in Sect. 2.2.3. The number density of axions emitted in string

decay is given by (2.70) in terms of the quantities ξ, $\bar{r}$, and χ that we introduced to parameterize our ignorance of various aspects of string evolution and decay.

Because their spectrum $\mathrm{d}n_a/\mathrm{d}k \propto k^{-2}$ in the range $t^{-1} \lesssim k \lesssim (t_{\rm PQ}t)^{-1/2}$, the bulk of axions emitted in string-decay have momenta of order t_1^{-1} at time t_1 and become non-relativistic soon after they acquire mass. Therefore, the string-decay contribution to the axion energy density today is

$$\varrho_a^{\rm str}(t_0) = m_a n_a^{\rm str}(t_1) \left(\frac{R_1}{R_0}\right)^3 \simeq m_a \, \frac{\xi \, \bar{r}}{\chi} \, \frac{N^2 f_a^2}{t_1} \left(\frac{R_1}{R_0}\right)^3 . \tag{2.95}$$

We now discuss the factors on the right hand side (RHS) of this equation that are specific to the string-decay contribution.

The parameter ξ determines the density of the string network (2.61) with $\xi = 1$ corresponding to a density of one long string per horizon. In [14] it was argued that $\xi \simeq 1$ because global strings can decay efficiently into axions, and, therefore, the number density of long strings should be close to the minimum consistent with causality. A numerical simulation of global string networks in an expanding universe [23] found that indeed $\xi \simeq 1$. So there appear to be good grounds for using $\xi \simeq 1$.

The parameter χ defines the low-wavevector edge of the $\mathrm{d}n_a/\mathrm{d}k \propto k^{-2}$ spectrum through $k_{\rm min} \equiv \chi \, 2\pi/t$. The parameters χ and ξ are related as the average interstring distance controls both. On dimensional grounds, $\chi \propto \xi^{1/2}$. So the effect of small-scale structure in the axion string network partially cancels out in the RHS of (2.95). We expect χ to be of order one, but the uncertainty on this is at least a factor two.

The parameter $\bar{r}$ defines the average energy of the axions emitted in string-decay through (2.68) and (2.69). It is the unknown on which most of the debate has focused in the past. Two basic scenarios have been put forth, which we call A and B. The question is: what is the spectrum of axions radiated by strings? The main source is closed loops of size $L \sim t$. Scenario A postulates that a bent string or closed loop oscillates many times, with period of order L, before it has released its excess energy and that the spectrum of radiated axions is concentrated near $2\pi/L$. In that case, one has $\bar{r} \sim \ln(v_a t_1) \simeq 67$. Scenario B postulates that the bent string or closed loop releases its excess energy very quickly and that the spectrum of radiated axions is $\mathrm{d}E/\mathrm{d}k \propto k^{-1}$ with a high-frequency cutoff of order $2\pi v_a$ and a low-frequency cutoff of order $2\pi L$. In scenario B, the initial and final spectra $\mathrm{d}E/\mathrm{d}k$ of the energy stored in the axion field are qualitatively the same and hence $\bar{r} \sim 1$. In scenario A, the string-decay contribution dominates over the vacuum-realignment contribution by the factor $\ln(v_a t_1)$, whereas in scenario B the contributions from string-decay and vacuum-realignment have the same order of magnitude.

Many authors [24, 25, 26, 27, 28, 29, 30] have argued in favor of scenario A, adopting the point of view that global strings are similar to local

strings and their coupling to the axion field can be treated perturbatively. My collaborators and I [12, 14] have argued in support of scenario B, emphasizing that the dynamics of global strings is dominated by the energy stored in the axion field and there is no reason to believe that this energy would behave in the same way as the energy stored in the string core. The numerical simulations of the motion and decay of axion strings in [14, 31] give strong support to scenario B. These simulations are of oscillating strings with ends held fixed, of collapsing circular loops and non-circular closed loops with angular momentum. Over the range of $\ln(v_a L)$ accessible with present technology, $2.5 \lesssim \ln(v_a L) \lesssim 5.0$, it was found that $\bar{r} \simeq 0.8$ for closed loops and $\bar{r} \simeq 1.07$ for oscillating strings with ends held fixed. No dependence of $\bar{r}$ on $\ln(v_a L)$ was found for closed loops, and for bent strings with ends held fixed, $\bar{r}$ was found to slightly *decrease* with increasing $\ln(v_a L)$, whereas scenario A predicts $\bar{r}$ to be proportional to $\ln(v_a L)$.

2.4.3 Wall Decay

The final contribution to the cold axion cosmological energy density in case 2 is from the decay into non-relativistic axions of axion walls bounded by string. We assume here that $N = 1$. Indeed, if $N > 1$, the domain-wall problem is presumably solved by introducing a small breaking of the PQ symmetry, as described in Sect. 2.3.2. In that case, the axion walls decay predominantly into gravitational radiation [10].

Let t_3 be the time when the decay effectively takes place and $\gamma \equiv \omega'/m_a(t_3)$ the average Lorentz γ factor of the axions produced, where ω' is their average energy. The density of walls at time t_1 was estimated to be of order 0.7 per horizon volume [10]. Hence the average energy density in walls is

$$\varrho_{\rm wd}(t) \sim 0.7\,\frac{\sigma(t)}{t_1}\left(\frac{R_1}{R}\right)^3 \sim 0.7 \times 8 \times m_a(t)\,\frac{f_a^2}{t_1}\left(\frac{R_1}{R}\right)^3 \tag{2.96}$$

between t_1 and t_3. We assume that the energy in walls simply scales as $\sigma(t)$. After time t_3, the number density of axions produced in the decay of walls bounded by strings is of order

$$n_a^{\rm wd}(t) \sim \frac{\varrho_{\rm wd}(t_3)}{\omega'}\left(\frac{R_3}{R}\right)^3 \sim \frac{6}{\gamma}\,\frac{f_a^2}{t_1}\left(\frac{R_1}{R}\right)^3 . \tag{2.97}$$

Note that the dependence on t_3 drops out of our estimate of $n_a^{\rm wd}$. In the simulations of the motion and decay of walls bounded by string [10], it was found that $\gamma \simeq 7$ for $\ln(v_a/m_a) \sim 4.6$ but γ increases approximately linearly with $\ln(\lambda^{1/2} v_a/m_a)$. If this behavior is extrapolated all the way to $\ln(\lambda^{1/2} v_a/m_a) \simeq 60$, which is the value in axion models of interest, then $\gamma \simeq 60$. In that case the contribution from wall decay is subdominant relative to those from vacuum realignment and string decay.

2.4.4 Cosmological Cold-Axion Energy Density

To estimate the cosmological energy density of cold axions in case 2, we neglect the contribution from wall decay and assume that scenario B is correct for the string contribution. By adding the RHS of (2.92), (2.94) and (2.95) with $N = \bar{r} = \xi = \chi = 1$, we find

$$\varrho_a(t_0) \sim 2\,\frac{f_a^2}{t_1}\,\left(\frac{R_1}{R_0}\right)^3 m_a\ . \tag{2.98}$$

Equation (2.91) gives the cosmological cold-axion energy density in case 1. To determine the ratio of scale factors R_1/R_0, we assume conservation of entropy from time t_1 until the present. The number $\mathcal{N}_1$ of effective thermal degrees of freedom at time t_1 is of order 60. Keeping in mind that neutrinos decouple before electron-positron annihilation, one finds

$$\left(\frac{R_1}{R_0}\right)^3 \simeq 0.063\,\left(\frac{T_{\gamma,0}}{T_1}\right)^3\ . \tag{2.99}$$

Combining (2.36), (2.91),(2.98) and (2.99), and dividing by the critical density $\varrho_{\rm crit} = 3H_0^2/8\pi G$, we find

$$\Omega_a \sim \left(\frac{f_a}{10^{12}\,\text{GeV}}\right)^{7/6}\left(\frac{0.7}{h}\right)^2 \times \begin{cases} 0.15\,\alpha_1^2 & \text{for Case 1,} \\ 0.7 & \text{for Case 2,} \end{cases} \tag{2.100}$$

where h is defined as usual by $H_0 = h\,100\,\text{km}\,\text{s}^{-1}\,\text{Mpc}^{-1}$.

Equations (2.100) are subject to uncertainty from many sources, apart from the uncertainty about the contribution from string-decay. The axion energy density may be diluted by the entropy release from heavy particles which decouple before the QCD epoch but decay afterwards [32, 33, 34], or by the entropy release associated with a first order QCD phase-transition. On the other hand, if the QCD phase-transition is first order [35, 36, 37, 38], an abrupt change of the axion mass at the transition may increase Ω_a. A model has been put forth [39] in which the axion decay constant f_a is time-dependent, the value $f_a(t_1)$ during the QCD phase-transition being much smaller than the value f_a today. This yields a suppression of the cosmological axion energy density by a factor $[f_a(t_1)/f_a]^2$ compared to the usual case. Finally, it has been proposed that the axion density is diluted by "coherent de-excitation," i.e., adiabatic level crossing of $m_a(t)$ with the mass of some other pseudo-Nambu-Goldstone boson which mixes with the axion [40].

2.4.5 Velocity Dispersions

The axions produced by vacuum realignment, string decay, and wall decay all have extremely small velocity dispersion today. In case 1, where the axions are produced in a zero-momentum state, the velocity dispersion is zero.

(This ignores the small quantum-mechanical fluctuations created during the inflationary epoch, which will be discussed in Sect. 2.6.)

In case 2, we distinguish two sub-populations of cold axions, pop. I and pop. II, with the second kind having velocity dispersion larger than the first typically by a factor 10^3 to 10^4. The pop. I axions are those produced by vacuum realignment or string decay and which escaped being hit by moving domain walls. They have a typical momentum $p_{\rm I}(t_1) \sim t_1^{-1}$ at time t_1 because they are associated with axion field configurations that are inhomogeneous on the horizon scale at that time. Their velocity dispersion is of order

$$\beta_{\rm I}(t) \sim \frac{1}{m_a t_1}\left(\frac{R_1}{R}\right) \simeq 3\times 10^{-17}\left(\frac{10^{-5}\,{\rm eV}}{m_a}\right)^{5/6}\frac{R_0}{R}\,. \tag{2.101}$$

The corresponding effective T is of order $0.5\times 10^{-34}\,{\rm K}\,(10^{-5}\,{\rm eV}/m_a)^{2/3}$ today. This is very cold, indeed!

Pop. II are axions produced in the decay of domain walls and axions that were hit by moving domain walls. Axions produced in the decay of domain walls have typical momentum $p_{\rm II}(t_3) \sim \gamma\, m_a(t_3)$ at time t_3 when the walls effectively decay. Their velocity dispersion is therefore of order

$$\beta_{\rm II}(t) \sim \gamma\,\frac{m_a(t_3)}{m_a}\,\frac{R_3}{R} \simeq 10^{-13}\,q\left(\frac{10^{-5}\,{\rm eV}}{m_a}\right)^{1/6}\frac{R_0}{R}\,, \tag{2.102}$$

where $q \equiv \gamma\,[m_a(t_3)/m_a](R_3/R_1)$ parameterizes our ignorance of the wall decay process. We expect q to be of order one but with very large uncertainties. There is however a lower bound on q that follows from the fact that the time t_3 when the walls effectively decay must be after t_2 when the energy density in walls starts to exceed the energy density in strings. Using (2.82), we have

$$q = \frac{\gamma\, m_a(t_3)}{m_a}\,\frac{R_3}{R_1} > \frac{\gamma\, m_a(t_2)}{m_a}\,\frac{R_2}{R_1} \simeq \frac{\gamma}{130}\left(\frac{10^{-5}\,{\rm eV}}{m_a}\right)^{2/3}\,. \tag{2.103}$$

As computer simulations suggest γ is of order 60, pop. II axions have much larger velocity dispersion than pop. I, by a factor of 10^3 or more. Whereas pop. II axions are relativistic or near-relativistic at the end of the QCD phase-transition, pop. I axions are definitely non-relativistic at that time as $m_a \gg t_1^{-1}$. The axions that were produced by vacuum-realignment or string-decay, but were hit by relativistically moving walls at some time between t_1 and t_3 should be included in pop. II as they are relativistic just after getting hit. The next section will highlight the differences in the behaviors of the two populations of cold axions.

The very low velocity dispersion of cold axions and their extremely weak couplings imply that these particles behave as collisionless cold dark matter (CDM). CDM particles lie at all times on a 3-dim hypersurface in 6-dim phase-space [41, 42]. As a result, CDM forms discrete flows and caustics. The

number of discrete flows at a given physical location is the number of times the 3-dim hypersurface covers physical space at that location. At the boundaries between regions with differing number of flows, the 3-dim hypersurface is tangent to velocity space. The dark matter density is very large on these surfaces, which are called caustics. The density diverges at the caustics in the limit of zero velocity dispersion.

2.5 Axion Miniclusters

If there is no inflation after the PQ phase-transition (case 2); the initial misalignment angle α_1 changes by $\mathcal{O}(1)$ from one QCD time horizon to the next. Hence, the fluid of cold axions produced by vacuum realignment is inhomogeneous with $\delta\varrho_a/\varrho_a = \mathcal{O}(1)$ at the time of the QCD phase-transition. As will be shown shortly, the streaming length of pop. I axions is too short for these inhomogeneities to get erased by free streaming before the time $t_{\rm eq}$ of equality between matter and radiation, when density perturbations start to grow in earnest by gravitational instability. At time $t_{\rm eq}$, the $\delta\varrho_a/\varrho_a = \mathcal{O}(1)$ inhomogeneities in the axion fluid promptly form gravitationally bound objects, called axion miniclusters [10, 43, 44, 45]. Their properties are of concern to experimentalists attempting the direct detection of dark matter axions on Earth. Indeed, those experiments would become even more challenging, if most of the cold axions condense into miniclusters and they withstand tidal disruption afterwards. Of course, these issues only arise in case 2. There are no axion miniclusters in case 1.

As described above, there are two populations of cold axions with velocity dispersions given by (2.101) and (2.102) respectively. Both populations are inhomogeneous at the time of the QCD phase-transition. The free-streaming length from time t_1 to $t_{\rm eq}$ is

$$\ell_{\rm f} = R(t_{\rm eq}) \int_{t_1}^{t_{\rm eq}} {\rm d}t \, \frac{\beta(t)}{R(t)} \simeq \beta(t_1) \, (t_1 t_{\rm eq})^{1/2} \, \ln\left(\frac{t_{\rm eq}}{t_1}\right) . \qquad (2.104)$$

The time of equality and the corresponding temperature are, respectively, $t_{\rm eq} \simeq 2.3 \times 10^{12}\,{\rm s}$ and $T_{\rm eq} \simeq 0.77\,{\rm eV}$. The free-streaming length should be compared with the size

$$\ell_{\rm mc} \sim t_1 \, \frac{R_{\rm eq}}{R_1} \simeq (t_1 t_{\rm eq})^{1/2} \simeq 2 \times 10^{13}\,{\rm cm} \left(\frac{10^{-5}\,{\rm eV}}{m_a}\right)^{1/6} \qquad (2.105)$$

of axion inhomogeneities at $t_{\rm eq}$. Using (2.101) we find for pop. I

$$\frac{\ell_{\rm f,I}}{\ell_{\rm mc}} \simeq \frac{1}{t_1 m_a} \ln\left(\frac{t_{\rm eq}}{t_1}\right) \simeq 2 \times 10^{-2} \left(\frac{10^{-5}\,{\rm eV}}{m_a}\right)^{2/3} . \qquad (2.106)$$

Hence, in the axion mass range of interest, pop. I axions do not homogenize. At $t_{\rm eq}$ most pop. I axions condense into miniclusters. The typical size of axion miniclusters is $\ell_{\rm mc}$, and their typical mass is [10, 45]

$$M_{\rm mc} \sim \eta\, \varrho_a(t_{\rm eq})\, \ell_{\rm mc}^3 \sim \eta\, 5 \times 10^{-13}\, M_\odot \left(\frac{10^{-5}\,{\rm eV}}{m_a}\right)^{5/3} , \tag{2.107}$$

where η is the fraction of cold axions that are pop. I. We assume that all pop. I axions condense into miniclusters and use (2.100, Case 2) to estimate $\varrho_a(t_{\rm eq})$.

Using (2.102), we find for pop. II

$$\frac{\ell_{\rm f,II}}{\ell_{\rm mc}} \sim q\, \ln\left(\frac{t_{\rm eq}}{t_3}\right) \simeq 42\, q\, . \tag{2.108}$$

Using (2.103) and assuming the range $\gamma \sim 7$–60, suggested by the numerical simulations [10], we conclude that pop. II axions do homogenize and hence the axion energy density has a smooth component at $t_{\rm eq}$.

However, pop. II axions may get gravitationally bound to miniclusters later on. It seems rather difficult to model this process reliably. A discussion is given in [10]. It is concluded there that the accretion of pop. II axions results in miniclusters that have an inner core of pop. I axions with density of order $10^{-18}\,{\rm g\,cm^{-3}}$ and a fluffy envelope of pop. II axions with density of order $10^{-25}\,{\rm g\,cm^{-3}}$.

When a minicluster falls onto a galaxy, tidal forces are apt to destroy it. If a minicluster falls through the inner parts of the Galaxy ($r < 10\,{\rm kpc}$), where the density is of order $10^{-24}\,{\rm g\,cm^{-3}}$, its fluffy envelope of pop. II axions will likely be pulled off immediately. This is helpful for direct searches of dark matter axions on Earth as it implies that a smooth component of dark-matter axions with density of order the halo density permeates us whether or not there is inflation after the PQ phase-transition. Even the central cores of pop. I axions may eventually get destroyed. When a minicluster passes by an object of mass M with impact parameter b and velocity v, the internal energy per unit mass ΔE given to the minicluster by the tidal gravitational forces from that object is of order [43]

$$\Delta E \sim \frac{G^2 M^2 \ell_{\rm mc}^2}{b^4 \beta^2} , \tag{2.109}$$

whereas the binding energy per unit mass of the minicluster $E \sim G\varrho_{\rm mc}\ell_{\rm mc}^2$. If the minicluster travels a length $L = \beta\, t$ through a region where objects of mass M have density n, the relative increase in internal energy is

$$\frac{\Delta E}{E} \sim \frac{G\varrho_M^2 t^2}{\varrho_{\rm mc}} , \tag{2.110}$$

where $\varrho_M = Mn$. Equation (2.110) follows from the fact that ΔE is dominated by the closest encounter and the latter has impact parameter $b_{\rm min}$ given by $\pi b_{\rm min}^2 nL = \mathcal{O}(1)$. Note that $\Delta E/E$ is independent of M. A minicluster inner core that has spent most of its life in the central part of our galaxy only barely survived as $\Delta E/E \sim 10^{-2}$ in that case.

The direct encounter of a minicluster with Earth would be rare, happening only every 10^4 years or so. The encounter would last for about 3 days during which the local axion density would increase by a factor of order 10^6.

2.6 Axion Isocurvature Perturbations

We now turn to isocurvature perturbations [32, 46, 47, 48, 49, 50] produced if inflation occurs after the PQ phase-transition and derive the constraints on axion parameters from the absence of isocurvature fluctuations in cosmic microwave background radiation (CMBR) observations.

If the reheat temperature after inflation is less than the temperature $T_{\rm PQ}$ at which $U(1)_{\rm PQ}$ is restored (case 1), the axion field is present during inflation and is subject to quantum-mechanical fluctuations, just like the inflaton. In fact, since the axion field is massless and weakly-coupled like the inflaton, it has the same fluctuation spectrum [51, 52, 53, 54]

$$P_a(k) = \int \frac{{\rm d}^3\mathbf{x}}{(2\pi)^3}\, \langle \delta a(\mathbf{x},t)\, \delta a(\mathbf{x}',t)\rangle\, {\rm e}^{-{\rm i}\mathbf{k}\cdot(\mathbf{x}-\mathbf{x}')} = \left(\frac{H_{\rm I}}{2\pi}\right)^2 \frac{2\pi^2}{k^3}\,, \qquad (2.111)$$

where $H_{\rm I}$ is the expansion rate during inflation. As before, $\mathbf{x}$ are co-moving spatial coordinates. The axion fluctuations described by (2.111) are commonly written in shorthand notation as $\delta a = H_{\rm I}/2\pi$. The fluctuation in each axion field mode is "frozen in" after $R(t)/k$ exceeds the horizon length $H_{\rm I}^{-1}$.

We do not consider here the possibility of fluctuations in the axion decay constant f_a during inflation. Such fluctuations are discussed in [55, 56, 57, 58].

At the start of the QCD phase-transition, the local value of the axion field $a(\mathbf{x},t)$ determines the local number density of cold axions produced by the vacuum realignment mechanism [see (2.47)],

$$n_a(\mathbf{x},t_1) = \frac{f_a^2}{2t_1}\,\alpha(\mathbf{x},t_1)^2 \qquad (2.112)$$

where $\alpha(\mathbf{x},t_1) = a(\mathbf{x},t_1)/f_a$ is the misalignment angle. The fluctuations in the axion field produce perturbations in the cold axion density

$$\frac{\delta n_a^{\rm iso}}{n_a} = \frac{2\delta a}{a_1} = \frac{H_{\rm I}}{\pi f_a \alpha_1}\,, \qquad (2.113)$$

where $a_1 = a(t_1) = f_a\alpha_1$ is the value of the axion field at the start of the QCD phase-transition, common to our entire visible universe. These perturbations obey

$$\delta\varrho_a^{\rm iso}(t_1) = -\delta\varrho_{\rm rad}^{\rm iso}(t_1) \tag{2.114}$$

as the vacuum-realignment mechanism converts energy stored in the quark-gluon plasma into axion rest mass energy. In contrast, the density perturbations produced by the fluctuations in the inflaton field [54, 59, 60, 61, 62] satisfy

$$\frac{\delta\varrho_{\rm matter}}{\varrho_{\rm matter}} = \frac{3}{4}\,\frac{\delta\varrho_{\rm rad}}{\varrho_{\rm rad}}\ . \tag{2.115}$$

Density perturbations that satisfy (2.115) are called "adiabatic," whereas that do not satisfy (2.115) are called "isocurvature". Isocurvature perturbations, such as the density perturbations of (2.114), make a different imprint on the cosmic microwave background than do adiabatic ones. The CMBR observations are consistent with pure adiabatic perturbations. This places a constraint on axion models if the PQ phase-transition occurs before inflation.

Before we derive this constraint, two comments are in order. The first is that if the PQ transition occurs *after* inflation, axion models still predict isocurvature perturbations, but not on length scales relevant to CMBR observations. Indeed, we saw in the previous section that in this case (case 2), the axion field fluctuates by order f_a from one QCD horizon to the next. Those fluctuations produce isocurvature perturbations on the scale of the QCD horizon, which is much smaller than the length scales observed in the CMBR. Their main phenomenological implication is the axion miniclusters, which were discussed in Sect. 2.5. The second comment is that, if the PQ phase-transition occurs before inflation (case 1), the density perturbations in the cold axion fluid have both adiabatic and isocurvature components. The adiabatic perturbations, $\delta\varrho_a^{\rm ad}/3\varrho_a = \delta\varrho_{\rm rad}^{\rm ad}/4\varrho_{\rm rad} = \delta T/T$, are produced by the quantum-mechanical fluctuations of the inflaton field during inflation, whereas the isocurvature perturbations are produced by the quantum-mechanical fluctuations of the axion field during that same epoch. The adiabatic and axion isocurvature components are uncorrelated.

The upper bound from CMBR observations and large-scale structure data on the fraction of CDM perturbations that are isocurvature is of order 30% in amplitude (10% in the power spectrum) [63, 64, 65, 66, 67, 68]. Allowing for the possibility that only part of the cold dark matter is axions, the bound on isocurvature perturbations implies

$$\frac{\delta\varrho_a^{\rm iso}}{\varrho_{\rm CDM}} = \frac{\delta\varrho_a^{\rm iso}}{\varrho_a}\,\frac{\varrho_a}{\varrho_{\rm CDM}} = \frac{H_{\rm I}}{\pi f_a \alpha_1}\,\frac{\Omega_a}{\Omega_{\rm CDM}} < 0.3\,\frac{\delta\varrho_{\rm m}}{\varrho_{\rm m}}\ , \tag{2.116}$$

where we used (2.113). Here, $\delta\varrho_{\rm m}/\varrho_{\rm m}$ is the amplitude of the primordial spectrum of matter perturbations. It is related to the amplitude of low multipole CMBR anisotropies through the Sachs-Wolfe effect [69, 70, 71]. The observations imply $\delta\varrho_{\rm m}/\varrho_{\rm m} \simeq 4.6\times 10^{-5}$ [72].

In terms of α_1, the cold axion energy density is given by (2.100). We rewrite that equation here, assuming $h \simeq 0.7$,

$$\Omega_a \simeq 0.15 \left(\frac{f_a}{10^{12}\,\mathrm{GeV}}\right)^{7/6} \alpha_1^2 \,. \tag{2.117}$$

It has been remarked by many authors, starting with S.-Y. Pi [73], that it is possible for f_a to be much larger than $10^{12}\,\mathrm{GeV}$ because α_1 may be accidentally small in our visible universe. The requirement that $\Omega_a < \Omega_{\mathrm{CDM}} = 0.22$ implies

$$\left|\frac{\alpha_1}{\pi}\right| < 0.4 \left(\frac{10^{12}\,\mathrm{GeV}}{f_a}\right)^{7/12} \,. \tag{2.118}$$

Since $-\pi < \alpha_1 < +\pi$ is the a-priori range of α_1 and no particular value is preferred over any other, $|\alpha_1/\pi|$ may be taken to be the "probability" that the initial misalignment angle has magnitude less than $|\alpha_1|$. (Strictly speaking, the word probability is not appropriate here as there is only one universe in which α_1 may be measured.) If $|\alpha_1/\pi| = 2 \times 10^{-3}$, for example, f_a may be as large as $10^{16}\,\mathrm{GeV}$, which is often thought to be the "grand unification scale".

The presence of isocurvature perturbations constrains the small α_1 scenario in two ways [50]. First, it makes it impossible to have α_1 arbitrarily small. Using (2.111), one can show that the fluctuations in the axion field cause the latter to perform a random walk [74] characterized by the property

$$\frac{1}{V}\int_V \mathrm{d}^3\mathbf{x} \left\langle [\delta a(\mathbf{x},t) - \delta a(\mathbf{0},t)]^2 \right\rangle = 4\pi H_{\mathrm{I}}^2 \ln(Rk_{\mathrm{max}}) \,. \tag{2.119}$$

The integral is over a sphere of volume $V = 4\pi R^3/3$ centered at $\mathbf{x} = \mathbf{0}$ and k_{max} is a cutoff on the wavevector spectrum. a_1^2 cannot be smaller than the RHS of (2.119) with R equal to the size of the present universe and k_{max} equal to the Hubble rate at the QCD time, redshifted down to the present. As $\Omega_a < 0.22$, this implies a bound on H_{I}. Translated to a bound on the scale of inflation Λ_{I}, defined by $H_{\mathrm{I}}^2 = 8\pi G \Lambda_{\mathrm{I}}^4/3$, it is

$$\Lambda_{\mathrm{I}} < 5 \times 10^{14}\,\mathrm{GeV} \left(\frac{f_a}{10^{12}\,\mathrm{GeV}}\right)^{5/24} \,. \tag{2.120}$$

Second, one must require axion isocurvature perturbations to be consistent with CMBR observations. Combining (2.116) and (2.117), and setting $\Omega_{\mathrm{CDM}} = 0.22$, $\delta\varrho_{\mathrm{m}}/\varrho_{\mathrm{m}} = 4.6 \times 10^{-5}$, one obtains

$$\Lambda_{\mathrm{I}} < 10^{13}\,\mathrm{GeV}\, \Omega_a^{-1/4} \left(\frac{f_a}{10^{12}\,\mathrm{GeV}}\right)^{5/24} \,. \tag{2.121}$$

Let us keep in mind that the bounds (2.120) and (2.121) pertain only if the reheat temperature $T_{\mathrm{RH}} < T_{\mathrm{PQ}}$. One may, for example, have $\Omega_a = 0.22$, $f_a \simeq 10^{12}\,\mathrm{GeV}$, and $\Lambda_{\mathrm{I}} \simeq 10^{16}\,\mathrm{GeV}$, provided $T_{\mathrm{RH}} \gtrsim 10^{12}\,\mathrm{GeV}$, which is possible if reheating is efficient enough.

Acknowledgments

It is a pleasure to thank Maria Beltrán, Juan García-Bellido, Julien Lesgourgues, David Lyth, Michael Turner and Richard Woodard for enlightening discussions. This work was supported in part by the U.S. Department of Energy under grant number DE-FG02-97ER41029.

References

1. Kolb, E.W., Turner, M.S.: The Early Universe. Addison-Wesley, Redwood City, USA (1990) 20
2. Massó, E., Rota, F., Zsembinszki, G.: On axion thermalization in the early universe. Phys. Rev. D **66**, 023004 (2002) [hep-ph/0203221] 21
3. 't Hooft, G.: Symmetry breaking through Bell-Jackiw anomalies. Phys. Rev. Lett. **37**, 8 (1976) 24
4. 't Hooft, G.: Computation of the quantum effects due to a four-dimensional pseudoparticle. Phys. Rev. D **14**, 3432 (1976); (E) ibid. **18**, 2199 (1978) 24
5. Sikivie, P.: Of axions, domain walls and the early universe. Phys. Rev. Lett. **48**, 1156 (1982) 24, 32, 34, 35
6. Preskill, J., Wise, M.B., Wilczek, F.: Cosmology of the invisible axion. Phys. Lett. B **120**, 127 (1983) 25, 26, 27
7. Abbott, L.F., Sikivie, P.: A cosmological bound on the invisible axion. Phys. Lett. B **120**, 133 (1983) 25, 26, 27
8. Dine, M., Fischler, W.: The not-so-harmless axion. Phys. Lett. B **120**, 137 (1983) 25, 26, 27
9. Gross, D.J., Pisarski, R.D., Yaffe, L.G.: QCD and instantons at finite temperature. Rev. Mod. Phys. **53**, 43 (1981) 25
10. Chang, S., Hagmann, C., Sikivie, P.: Studies of the motion and decay of axion walls bounded by strings. Phys. Rev. D **59**, 023505 (1999) [hep-ph/9807374] 29, 34, 35, 36,
11. Vilenkin, A., Everett, A.E., Cosmic strings and domain walls in models with Goldstone and pseudo-Goldstone bosons. Phys. Rev. Lett. **48**, 1867 (1982) 29, 34, 35
12. Harari, D., Sikivie, P.: On the evolution of global strings in the early universe. Phys. Lett. B **195**, 361 (1987) 30, 39
13. Shellard, E.P.S.: Cosmic string interactions. Nucl. Phys. B **283**, 624 (1987) 30
14. Hagmann, C., Sikivie, P.: Computer simulations of the motion and decay of global strings. Nucl. Phys. B **363**, 247 (1991) 31, 38, 39
15. Huang, M.C., Sikivie, P.: The structure of axionic domain walls. Phys. Rev. D **32**, 1560 (1985) 32, 34
16. Vilenkin, A.: Gravitational field of vacuum domain walls and strings. Phys. Rev. D **23**, 852 (1981) 33
17. Ipser, J., Sikivie, P.: The gravitationally repulsive domain wall. Phys. Rev. D **30**, 712 (1984) 33
18. Vilenkin, A., Gravitational field of vacuum domain walls. Phys. Lett. B **133**, 177 (1983) 33
19. Perlmutter, S., et al.: (Supernova Cosmology Project Collaboration): Measurements of Ω and Λ from 42 high-redshift supernovae. Astrophys. J. **517**, 565 (1999) [astro-ph/9812133] 33

20. Riess, A.G., et al.: (Supernova Search Team Collaboration): Observational evidence from supernovae for an accelerating universe and a cosmological constant. Astron. J. **116**, 1009 (1998) [astro-ph/9805201] 33
21. Lazarides, G., Shafi, Q.: Axion models with no domain wall problem. Phys. Lett. B **115**, 21 (1982) 34
22. Sikivie, P.: Axions in cosmology. In: Proc. Gif-sur-Yvette Summer School, September 6–10, 1982, published by the Institut National de Physique Nucleaire et de Physique des Particules (1983) 34, 35
23. Yamaguchi, M., Kawasaki, M., Yokoyama, J.: Evolution of axionic strings and spectrum of axions radiated from them. Phys. Rev. Lett. **82**, 4578 (1999) [hep-ph/9811311] 38
24. Davis, R.L.: Goldstone bosons in string models of galaxy formation. Phys. Rev. D **32**, 3172 (1985) 38
25. Davis, R.L.: Cosmic axions from cosmic strings. Phys. Lett. B **180**, 225 (1986) 38
26. Vilenkin, A., Vachaspati, T.: Radiation of Goldstone bosons from cosmic strings. Phys. Rev. D **35**, 1138 (1987) 38
27. Davis, R.L., Shellard, E.P.S.: Do axions need inflation? Nucl. Phys. B **324**, 167 (1989) 38
28. Dabholkar, A., Quashnock, J.M.: Pinning down the axion. Nucl. Phys. B **333**, 815 (1990) 38
29. Battye, R.A., Shellard, E.P.S.: Global string radiation. Nucl. Phys. B **423**, 260 (1994) [astro-ph/9311017] 38
30. Battye, R.A., Shellard, E.P.S.: Axion string constraints. Phys. Rev. Lett. **73**, 2954 (1994); (E) ibid. **76**, 2203 (1996) [astro-ph/9403018] 38
31. Hagmann, C., Chang, S., Sikivie, P.: Axion radiation from strings. Phys. Rev. D **63**, 125018 (2001) [hep-ph/0012361] 31, 39
32. Steinhardt, P.J., Turner, M.S.: Saving the invisible axion. Phys. Lett. B **129**, 51 (1983) 40, 44
33. Lazarides, G., Panagiotakopoulos, C., Shafi, Q.: Relaxing the cosmological bound on axions. Phys. Lett. B **192**, 323 (1987) 40
34. Lazarides, G., Schaefer, R.K., Seckel, D., Shafi, Q.: Dilution of cosmological axions by entropy production. Nucl. Phys. B **346**, 193 (1990) 40
35. Unruh, W.G., Wald, R.M.: On damping mechanisms for coherent oscillations of axions. Phys. Rev. D **32**, 831 (1985) 40
36. Turner, M.S.: Quantitative analysis of the thermal damping of coherent axion oscillations. Phys. Rev. D **32**, 843 (1985) 40
37. DeGrand, T.A., Kephart, T.W., Weiler, T.J.: Invisible axions and the QCD phase transition in the early universe. Phys. Rev. D **33**, 910 (1986) 40
38. Hindmarsh, M.: Axions and the QCD phase transition. Phys. Rev. D **45**, 1130 (1992) 40
39. Kaplan, D.B., Zurek, K.M.: Exotic axions. Phys. Rev. Lett. **96**, 041301 (2006) [hep-ph/0507236] 40
40. Hill, C.T., Ross, G.G.: Models and new phenomenological implications of a class of pseudo-Goldstone bosons. Nucl. Phys. B **311**, 253 (1988) 40
41. Sikivie, P., Ipser, J.R.: Phase-space structure of cold dark matter halos. Phys. Lett. B **291**, 288 (1992) 41
42. Natarajan, A., Sikivie, P.: Robustness of discrete flows and caustics in cold dark matter cosmology. Phys. Rev. D **72**, 083513 (2005) [astro-ph/0508049] and references therein 41

43. Hogan, C.J., Rees, M.J.: Axion miniclusters. Phys. Lett. B **205**, 228 (1988) 42, 43
44. Kolb, E.W., Tkachev, I.I.: Axion miniclusters and Bose stars. Phys. Rev. Lett. **71**, 3051 (1993) [hep-ph/9303313] 42
45. Kolb, E.W., Tkachev, I.I.: Femtolensing and picolensing by axion miniclusters. Astrophys. J. **460**, L25 (1996) [astro-ph/9510043] 42, 43
46. Axenides, M., Brandenberger, R.H., Turner, M.S.: Development of axion perturbations in an axion dominated universe. Phys. Lett. B **126**, 178 (1983) 44
47. Linde, A.D.: Generation of isothermal density perturbations in the inflationary universe. Phys. Lett. B **158**, 375 (1985) 44
48. Seckel, D., Turner, M.S.: Isothermal density perturbations in an axion dominated inflationary universe. Phys. Rev. D **32**, 3178 (1985) 44
49. Lyth, D.H.: A limit on the inflationary energy density from axion isocurvature fluctuations. Phys. Lett. B **236**, 408 (1990) 44
50. Turner, M.S., Wilczek, F.: Inflationary axion cosmology. Phys. Rev. Lett. **66**, 5 (1991) 44, 46
51. Birrell, N.D., Davies, P.C.W.: Quantum Field Theory in Curved Space-Time. Cambridge University Press, Cambridge, England (1982) 44
52. Ford, L.H., Vilenkin, A.: Quantum radiation by moving mirrors. Phys. Rev. D **25**, 2569 (1982) 44
53. Linde, A.D.: A new inflationary universe scenario: A possible solution of the horizon, flatness, homogeneity, isotropy and primordial monopole problems. Phys. Lett. B **108**, 389 (1982) 44
54. Starobinsky, A.A.: Dynamics of phase transition in the new inflationary universe scenario and generation of perturbations. Phys. Lett. B **117**, 175 (1982) 44, 45
55. Linde, A.D.: Axions in inflationary cosmology. Phys. Lett. B **259**, 38 (1991) 44
56. Lyth, D.H.: Axions and inflation: Sitting in the vacuum. Phys. Rev. D **45**, 3394 (1992) 44
57. Lyth, D.H., Stewart, E.D.: Constraining the inflationary energy scale from axion cosmology. Phys. Lett. B **283**, 189 (1992) 44
58. Lyth, D.H., Stewart, E.D.: Axions and inflation: String formation during inflation. Phys. Rev. D **46**, 532 (1992) 44
59. Mukhanov, V.F., Chibisov, G.V.: Quantum fluctuation and nonsingular universe. Pisma Zh. Eksp. Teor. Fiz. **33**, 549 (1981) [JETP Lett. **33**, 532 (1981)] 45
60. Hawking, S.W.: The development of irregularities in a single bubble inflationary universe. Phys. Lett. B **115**, 295 (1982) 45
61. Guth, A.H., Pi, S.-Y.: Fluctuations in the new inflationary universe. Phys. Rev. Lett. **49**, 1110 (1982) 45
62. Bardeen, J.M., Steinhardt, P.J., Turner, M.S.: Spontaneous creation of almost scale-free density perturbations in an inflationary universe. Phys. Rev. D **28**, 679 (1983) 45
63. Peiris, H.V., et al.: First year Wilkinson Microwave Anisotropy Probe (WMAP) observations: Implications for inflation. Astrophys. J. Suppl. **148**, 213 (2003) [astro-ph/0302225] 45
64. Valiviita, J., Muhonen, V.: Correlated adiabatic and isocurvature CMB fluctuations in the wake of WMAP. Phys. Rev. Lett. **91**, 131302 (2003) [astro-ph/0304175] 45

65. Crotty, P., García-Bellido, J., Lesgourgues, J., Riazuelo, A.: Bounds on isocurvature perturbations from CMB and LSS data. Phys. Rev. Lett. **91**, 171301 (2003) [astro-ph/0306286] 45
66. Beltrán, M., García-Bellido, J., Lesgourgues, J.: Isocurvature bounds on axions revisited. Phys. Rev. D 75, 103507 (2007). [hep-ph/0606107] 45
67. Bean, R., Dunkley, J., Pierpaoli, E.: Constraining isocurvature initial conditions with WMAP 3-year data. Phys. Rev. D **74**, 063503 (2006) [astro-ph/0606685], and references therein 45
68. Trotta, R.: The isocurvature fraction after WMAP 3-year data. Mon. Not. Roy. Astron. Soc. Lett. 375, L26 (2007). [astro-ph/0608116] 45
69. Sachs, R.K., Wolfe, A.M.: Perturbations of a cosmological model and angular variations of the microwave background. Astrophys. J. **147**, 73 (1967) 45
70. Peebles, P.J.E.: Large-scale background temperature and mass fluctuations due to scale-invariant primeval perturbations, Astrophys. J. **263**, L1 (1982) 45
71. Abbott, L.F., Wise, M.B.: Large-scale anisotropy of the microwave background and the amplitude of energy density fluctuations in the early universe. Astrophys. J. **282**, L47 (1984) 45
72. Dodelson, S.: Modern Cosmology. Academic Press, San Diago, USA (2003) 45
73. Pi, S.-Y.: Inflation without tears. Phys. Rev. Lett. **52**, 1725 (1984) 46
74. Linde, A.D., Lyth, D.H.: Axionic domain wall production during inflation. Phys. Lett. B **246**, 353 (1990) 46

3 Astrophysical Axion Bounds

Georg G. Raffelt

Max-Planck-Institut für Physik (Werner-Heisenberg-Institut), Föhringer Ring 6, 80805 München, Germany
raffelt@mppmu.mpg.de

Abstract. Axion emission by hot and dense plasmas is a new energy-loss channel for stars. Observable consequences include a modification of the solar sound-speed profile, an increase of the solar neutrino flux, a reduction of the helium-burning lifetime of globular-cluster stars, accelerated white-dwarf cooling, and a reduction of the supernova SN 1987A neutrino burst duration. I review and update these arguments and summarize the resulting axion constraints.

3.1 Introduction

The "outer space" of astrophysics and cosmology provides a natural laboratory for the "inner space" of elementary particle physics. Usually, one may first think of the early universe or perhaps high-energy cosmic rays for arguments in favor of or against a new particle-physics model. However, in the case of axions, the low energies available in stars are well suited for very sensitive tests.

The basic idea is very simple. Stars are powerful sources of weakly interacting particles such as neutrinos, gravitons, hypothetical axions, and other new particles that can be produced by nuclear reactions or by thermal processes in the stellar interior. Even when this particle flux cannot be directly measured, the properties of stars themselves would change if they lost too much energy into a new channel. This "energy-loss argument" has been widely used to constrain a long list of particle properties; see [1, 2, 3, 4, 5, 6, 7] for early examples and [8, 9, 10, 11, 12] for extensive reviews. I summarize here the main arguments that have been put forward, the observational evidence, and the resulting constraints for "invisible axions".

To this end, I review in Sect. 3.2 the axion interactions with photons and fermions. In Sect. 3.3, I consider the Sun as an axion source, notably by the Primakoff process, and review limits on the axion-photon interaction strength by helioseismology, the measured neutrino flux, and the CAST experiment. In Sects. 3.4, 3.5, and 3.6, I review axion limits from globular-cluster stars, white-dwarf cooling, and supernova SN 1987A, respectively. I summarize these constraints in Sect. 3.7 in juxtaposition with cosmological arguments.

G.G. Raffelt: *Astrophysical Axion Bounds*, Lect. Notes Phys. **741**, 51–71 (2008)
DOI 10.1007/978-3-540-73518-2_3

3.2 Axion Interactions

The particle-physics motivation for "invisible" axions and their main properties were introduced in Chap. 1 of this volume. Before turning to their role in stars, we briefly review the phenomenological properties of these pseudo Nambu-Goldstone bosons of the Peccei-Quinn (PQ) symmetry. The mass and interaction strength with ordinary particles are approximately given in terms of the relevant π^0 properties, scaled with f_π/f_a where $f_\pi = 92\,\mathrm{MeV}$ is the pion decay constant and f_a is the PQ scale or axion decay constant. The normalization of f_a is defined by the axion-gluon interaction

$$L_{a\gamma\gamma} = \frac{g_{\rm s}^2}{32\,\pi^2}\,\frac{a}{f_a}\,G^b_{\mu\nu}\tilde{G}^{b\mu\nu}\ , \tag{3.1}$$

where a is the axion field, G the gluon field-strength tensor, $\tilde{G}$ its dual, and b a color index. Color anomaly factors have been absorbed in this definition of f_a, which is the quantity that is relevant for all low-energy phenomena [13].

The PQ symmetry is explicitly broken at low energies and axions acquire a small mass. Unless there are non-QCD contributions, perhaps from Planck-scale physics [14, 15], the mass is

$$m_a = \frac{z^{1/2}}{1+z}\,\frac{f_\pi m_\pi}{f_a} = \frac{6.0\,\mathrm{eV}}{f_a/10^6\,\mathrm{GeV}}\ , \tag{3.2}$$

where $z = m_u/m_d$ is the up/down quark mass ratio. We will follow the previous axion literature and usually assume the canonical value $z = 0.56$ [16, 17], although it could vary in the range $z = 0.3$–0.6 [12].

Another generic property of axions is their two-photon interaction that plays a key role for most searches,

$$L_{a\gamma\gamma} = \frac{g_{a\gamma\gamma}}{4}\,F_{\mu\nu}\tilde{F}^{\mu\nu}a = -g_{a\gamma\gamma}\,\mathbf{E}\cdot\mathbf{B}\,a\ . \tag{3.3}$$

Here, F is the electromagnetic field-strength tensor, $\tilde{F}$ its dual, and $\mathbf{E}$ and $\mathbf{B}$ the electric and magnetic fields, respectively. The coupling constant is

$$g_{a\gamma\gamma} = \frac{\alpha}{2\pi f_a}\left(\frac{E}{N} - \frac{2}{3}\,\frac{4+z}{1+z}\right) = \frac{\alpha}{2\pi}\left(\frac{E}{N} - \frac{2}{3}\,\frac{4+z}{1+z}\right)\frac{1+z}{z^{1/2}}\,\frac{m_a}{m_\pi f_\pi}\ , \tag{3.4}$$

where E and N, respectively, are the electromagnetic and color anomaly of the axial current associated with the axion field. $E/N = 0$ in the Kim-Shifman-Vainshtein-Zakharov (KSVZ) model [18, 19], whereas $E/N = 8/3$ in grand unified models, e.g., the Dine-Fischler-Srednicki-Zhitnitskii (DFSZ) model [20, 21]. While these cases are often used as generic examples, in general E/N is not known so that for fixed f_a a broad range of $g_{a\gamma\gamma}$ values is possible [22]. Still, barring fine-tuned cancelations, $g_{a\gamma\gamma}$ scales from the corresponding pion interaction by virtue of the relation (3.4). Taking the

model-dependent factors to be of order unity, this relation defines the "axion line" in the m_a–$g_{a\gamma\gamma}$ plane.

Axions or axion-like particles with a two-photon vertex decay into two photons with a rate

$$\begin{aligned}\Gamma_{a\to\gamma\gamma} &= \frac{g_{a\gamma\gamma}^2 m_a^3}{64\,\pi} = \frac{\alpha^2}{256\,\pi^3}\left[\left(\frac{E}{N}-\frac{2}{3}\,\frac{4+z}{1+z}\right)\frac{1+z}{z^{1/2}}\right]^2 \frac{m_a^5}{m_\pi^2 f_\pi^2} \\ &= 1.1\times 10^{-24}\,\mathrm{s}^{-1}\left(\frac{m_a}{\mathrm{eV}}\right)^5, \end{aligned} \tag{3.5}$$

where the first expression is for general pseudoscalars, the second applies specifically to axions, and the numerical one assumes $z = 0.56$ and the hadronic case $E/N = 0$. Comparison with the age of the universe of $4.3\times 10^{17}\,\mathrm{s}$ reveals that axions decay on a cosmic time scale if $m_a \gtrsim 20\,\mathrm{eV}$.

The interaction with fermions j has a derivative structure so that it is invariant under $a \to a + a_0$ as behooves a Nambu-Goldstone boson,

$$L_{ajj} = \frac{C_j}{2f_a}\,\bar\Psi_j\gamma^\mu\gamma_5\Psi_j\partial_\mu a \quad \text{or} \quad -\mathrm{i}\,\frac{C_j m_j}{f_a}\,\bar\Psi_j\gamma_5\Psi_j a\,. \tag{3.6}$$

Here, Ψ_j is the fermion field, m_j its mass, and C_j a model-dependent numerical coefficient. The combination $g_{ajj} \equiv C_j m_j/f_a$ plays the role of a Yukawa coupling and $\alpha_{ajj} \equiv g_{ajj}^2/4\pi$ that of a "fine-structure constant". The pseudoscalar form is usually equivalent to the derivative structure, but one has to be careful in processes where two Nambu-Goldstone bosons are attached to one fermion line, for example, an axion and a pion attached to a nucleon in the context of axion emission by nucleon bremsstrahlung [23, 24].

In hadronic models such as KSVZ [18, 19], axions do not couple to ordinary quarks and leptons at tree level, whereas in the DFSZ model [20, 21]

$$C_e = \frac{\cos^2\beta}{3}\,. \tag{3.7}$$

Here, $\cot\beta$ is the ratio of two Higgs vacuum expectation values of this model.

For nucleons, the dimensionless couplings $C_{n,p}$ are related by generalized Goldberger-Treiman relations to nucleon axial-vector current matrix elements,

$$\begin{aligned} C_p &= (C_u-\eta)\,\Delta u + (C_d-\eta z)\,\Delta\mathrm{d} + (C_s-\eta w)\,\Delta s\,, \\ C_n &= (C_u-\eta)\,\Delta\mathrm{d} + (C_d-\eta z)\,\Delta u + (C_s-\eta w)\,\Delta s\,. \end{aligned} \tag{3.8}$$

Here, $\eta = (1+z+w)^{-1}$ with $z = m_u/m_d$ and $w = m_u/m_s \ll z$. The quantities Δq represent the axial-vector current couplings to the proton, $\Delta q\, S_\mu = \langle p|\bar q\gamma_\mu\gamma_5 q|p\rangle$ where S_μ is the proton spin.

Neutron beta decay and strong isospin symmetry tell us that $\Delta u - \Delta\mathrm{d} = F + D = 1.267 \pm 0.0035$, whereas hyperon decays and flavor SU(3) symmetry imply $\Delta u + \Delta\mathrm{d} - 2\Delta s = 3F - D = 0.585 \pm 0.025$. Recent determinations

of the strange-quark contribution are $\Delta s = -0.08 \pm 0.01_{\rm stat} \pm 0.05_{\rm syst}$ from the COMPASS experiment [25] and $\Delta s = -0.085 \pm 0.008_{\rm exp} \pm 0.013_{\rm theor} \pm 0.009_{\rm evol}$ from HERMES [26], in agreement with each other and with an early estimate of $\Delta s = -0.11 \pm 0.03$ [27]. We thus adopt the estimates

$$\begin{aligned} \Delta u &= +0.841 \pm 0.020\,, \\ \Delta {\rm d} &= -0.426 \pm 0.020\,, \\ \Delta s &= -0.085 \pm 0.015\,, \end{aligned} \tag{3.9}$$

that are very similar to previous values used in the axion literature.

The uncertainty of the axion-nucleon couplings is dominated by the large uncertainty of $z = 0.3$–0.6 that was mentioned above. For hadronic axions we have $C_{u,d,s} = 0$ so that $C_p = -0.55$ and $C_n = +0.14$ for $z = 0.3$ and $C_p = -0.37$ and $C_n = -0.05$ for $z = 0.6$. Therefore, while it is well possible that $C_n = 0$, C_p does not vanish within the plausible z range. In the DFSZ model we have $C_u = \frac{1}{3}\sin^2\beta$ and $C_d = \frac{1}{3}\cos^2\beta$. Even with the large allowed z range, C_n and C_p never vanish simultaneously. An extreme case is $\cos^2\beta = 0$ where $C_p = 0$ for $z = 0.3$, but in this case $C_n = -0.27$.

3.3 The Sun as an Axion Source

3.3.1 Axion Flux from the Primakoff Process

The Sun would be a powerful axion source. This flux can be searched directly, notably by the CAST experiment. Its sensitivity is competitive with the globular-cluster limits (Sect. 3.4) for hadronic models. In this case, the dominant emission process is the Primakoff effect [28], i.e., particles with a two-photon vertex transform into photons in external electric or magnetic fields. Therefore, stars produce axions from thermal photons in the fluctuating electromagnetic fields of the stellar plasma [6].

Calculating the solar axion flux is straightforward except for the proper inclusion of screening effects [29, 30]. The transition rate for a photon of energy E into an axion of the same energy (recoil effects are neglected) [31] is

$$\Gamma_{\gamma\to a} = \frac{g_{a\gamma\gamma}^2 T \kappa_{\rm s}^2}{32\pi}\left[\left(1+\frac{\kappa_{\rm s}^2}{4E^2}\right)\ln\left(1+\frac{4E^2}{\kappa_{\rm s}^2}\right)-1\right], \tag{3.10}$$

where T is the temperature (natural units with $\hbar = c = k_{\rm B} = 1$ are used). The screening scale in the Debye-Hückel approximation is

$$\kappa_{\rm s}^2 = \frac{4\pi\alpha}{T}\left(n_e + \sum_{\rm nuclei} Z_j^2 n_j\right), \tag{3.11}$$

where n_e is the electron density and n_j the density of the j-th ion of charge Z_j. Near the solar center $\kappa_{\rm s} \approx 9\,{\rm keV}$. Note that $(\kappa_{\rm s}/T)^2 \approx 12$ is nearly

constant throughout the Sun whereas it is about 2.5 throughout the core of a low-mass helium-burning star.

Ignoring the plasma frequency for the initial-state photons, the energy-loss rate per unit volume is [10, 31]

$$Q = \frac{g_{a\gamma\gamma}^2 T^7}{4\pi} F \,, \tag{3.12}$$

where F is a numerical factor of order unity. For $(\kappa_{\rm s}/T)^2 = 2.5$ and 12 one finds $F = 0.98$ and 1.84, respectively.

Integrating over a standard solar model, one finds an axion flux at Earth that is well approximated by (E in keV)

$$\frac{{\rm d}\Phi_a}{{\rm d}E} = g_{10}^2 \; 6.0 \times 10^{10}\,{\rm cm}^{-2}\,{\rm s}^{-1}\,{\rm keV}^{-1}\,E^{2.481}\,{\rm e}^{-E/1.205} \,, \tag{3.13}$$

where $g_{10} = g_{a\gamma\gamma}/(10^{-10}\,{\rm GeV}^{-1})$. The integrated flux parameters are

$$\begin{aligned} \Phi_a &= g_{10}^2\, 3.75 \times 10^{11}\,{\rm cm}^{-2}\,{\rm s}^{-1} \,, \\ L_a &= g_{10}^2\, 1.85 \times 10^{-3} L_\odot \,. \end{aligned} \tag{3.14}$$

The maximum of the distribution is at 3.0 keV, and the average energy is 4.2 keV.

3.3.2 Solar Age

The properties of the Sun itself constrain this flux. The axion losses lead to an enhanced consumption of nuclear fuel. The standard Sun is halfway through its hydrogen-burning phase so that the solar axion luminosity should not exceed its photon luminosity $L_\odot$.

As an example let us recall that a magnetically-induced vacuum dichroism observed by the PVLAS experiment [32], if interpreted in terms of an axion-like particle (ALP), requires [32, 33] $g_{a\gamma\gamma} = 2$–$5 \times 10^{-6}\,{\rm GeV}^{-1}$ and $m_a =$ 1–1.5 meV. With this coupling strength, the Sun's ALP luminosity would exceed $L_\odot$ by a factor of a million and thus it could live only for about 1000 years. Perhaps this problem can be circumvented, but it is noteworthy that even a crude astrophysical argument severely constrains the particle interpretation of the PVLAS signature.

3.3.3 Helioseismology

For a more refined constraint, we note that a model of the present-day Sun, with the integrated effect of axion losses taken into account, would differ from a standard solar model. The modified sound-speed profile can be diagnosed by helioseismology, providing a conservative limit [34]

$$g_{a\gamma\gamma} \lesssim 1 \times 10^{-9}\,\mathrm{GeV}^{-1}\,, \tag{3.15}$$

corresponding to $L_a \lesssim 0.20\,L_\odot$. More recent determinations of the solar metal abundances have diminished the agreement between standard solar models and helioseismology [35], but these modifications do not change the limit (3.15).

3.3.4 Solar Neutrino Flux

The energy loss by solar axion emission requires enhanced nuclear burning and thus a somewhat increased temperature in the Sun. Self-consistent solar models with axion losses reveal that $g_{a\gamma\gamma} = 4.5 \times 10^{-10}\,\mathrm{GeV}^{-1}$ implies a 20% increase of the solar ^{8}B neutrino flux [34]. For $g_{a\gamma\gamma} = 10 \times 10^{-10}\,\mathrm{GeV}^{-1}$ the increase would be a factor of 2.4.

The measured all-flavor ^{8}B neutrino flux is $4.94 \times 10^6\,\mathrm{cm}^{-2}\,\mathrm{s}^{-1}$ with an uncertainty of about 8.8% [36, 37]. The old standard solar model predictions were about 5.7–5.9 in the same units, whereas the new metal abundances imply 4.5–4.6, each time with a 16% "theoretical 1σ error" [35]. Therefore, the measured neutrino fluxes imply a limit

$$g_{a\gamma\gamma} \lesssim 5 \times 10^{-10}\,\mathrm{GeV}^{-1}\,, \tag{3.16}$$

corresponding to $L_a \lesssim 0.04\,L_\odot$. A more precise limit with a realistic error budget would require self-consistent solar models on a finer spacing of $g_{a\gamma\gamma}$.

3.3.5 Searches for Solar Axions

The solar axion flux can be searched with the inverse Primakoff process where axions convert to photons in a macroscopic B field, the "axion helioscope" technique [38]. One would look at the Sun through a "magnetic telescope" and place an X-ray detector at the far end. The conversion can be coherent over a large propagation distance and is then pictured as a particle oscillation effect [39].

Early helioscope searches were performed in Brookhaven [40] and Tokyo [41, 42]. Solar axions could also transform in electric crystal fields, but the limits obtained by SOLAX [43], COSME [44], and DAMA [45] are less restrictive and require a solar axion luminosity exceeding (3.15) and (3.16), i.e., these limits are not self-consistent.

The first helioscope that can actually reach the "axion line" is the CERN Axion Solar Telescope (CAST). The non-observation of a signal above background leads to a constraint [46]

$$g_{a\gamma\gamma} < 1.16 \times 10^{-10}\,\mathrm{GeV}^{-1} \quad (95\%\ \mathrm{CL}) \qquad \text{for} \quad m_a \lesssim 0.02\,\mathrm{eV}\,. \tag{3.17}$$

For larger masses, the axion-photon transition is suppressed by the energy-momentum mismatch between particles of different mass. The full rate can

be restored in a narrow range of masses by providing the photons with a refractive mass in the presence of a low-Z gas [47], a method that was already used in the Tokyo experiment [42] and is also used in the ongoing CAST Phase II. CAST is foreseen to reach eventually $m_a \lesssim 1\,\mathrm{eV}$.

3.3.6 Do Axions Escape from the Sun?

CAST can detect axions only if they actually escape from the Sun. Their mean free path (mfp) against the Primakoff process is the inverse of (3.10). For 4 keV axions with $T \approx 1.3\,\mathrm{keV}$ and $\kappa_\mathrm{s} \approx 9\,\mathrm{keV}$ at the solar center we find $\lambda_a \approx g_{10}^{-2}\, 6 \times 10^{24}\,\mathrm{cm} \approx g_{10}^{-2}\, 8 \times 10^{13}\, R_\odot$ or about 10^{-3} of the radius of the visible universe. Therefore, $g_{a\gamma\gamma}$ would have to be more than 10^7 times larger than the CAST limit for axions to be re-absorbed in the Sun.

Even in this extreme case they are not harmless because they would carry the bulk of the energy flux that otherwise is carried by photons. The mfp of low-mass particles in the trapping regime should be shorter than that of photons (about 10 cm near the solar center) to avoid a dramatic modification of the solar structure [48]. This requirement is so extreme that for anything similar to axions, the possibility of re-absorption is not a serious possibility.

3.4 Globular-Cluster Stars

3.4.1 Helium-Burning Lifetime and the Axion-Photon Interaction

A restrictive limit on $g_{a\gamma\gamma}$ arises from globular-cluster stars. A globular cluster is a gravitationally bound system of stars that formed at the same time and thus differ primarily in their mass. A globular cluster provides a homogeneous population of stars, allowing for detailed tests of stellar-evolution theory. The stars surviving since formation have masses somewhat below $1\,M_\odot$. In a color-magnitude diagram (Fig. 3.1), where one plots essentially the surface brightness vs. the surface temperature, stars appear in characteristic loci, allowing one to identify their state of evolution.

The stars on the horizontal branch (HB) have reached helium burning, where their core (about $0.5\,M_\odot$) generates energy by fusing helium to carbon and oxygen with a core-averaged energy release of about $80\,\mathrm{erg\,g^{-1}\,s^{-1}}$. A typical density is $10^4\,\mathrm{g\,cm^{-3}}$, and a typical temperature $10^8\,\mathrm{K}$. The Primakoff energy-loss rate (3.12) implies that the energy-loss rate per unit mass, $\varepsilon = Q/\varrho$, is proportional to T^7/ϱ. Averaged over a typical HB-star core one finds $\langle (T/10^8\,\mathrm{K})^7\,(10^4\,\mathrm{g\,cm^{-3}}/\varrho)\rangle \approx 0.3$. Therfore, the core-averaged energy-loss rate is about $g_{10}^2\,30\,\mathrm{erg\,g^{-1}\,s^{-1}}$. The main effect would be accelerated consumption of helium and thus a reduction of the HB lifetime by a factor $80/(80 + 30\,g_{10}^2)$, i.e., by about 30% for $g_{10} = 1$.

The HB lifetime can be measured relative to the red-giant evolutionary time scale by comparing the number of HB stars with the number of RGB

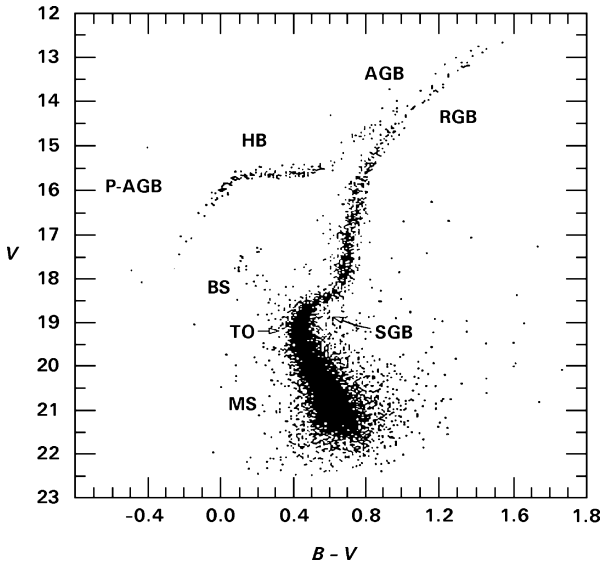

Fig. 3.1. Color-magnitude diagram for the globular cluster M3, based on 10,637 stars [50]. Vertically is the brightness in the visual (V) band, horizontally the difference between B (blue) and V brightness, i.e., a measure of the color and thus surface temperature, where blue (hot) stars lie toward the left. The classification for the evolutionary phases is as follows [51]. MS (main sequence): core hydrogen burning. BS (blue stragglers). TO (main-sequence turnoff): central hydrogen is exhausted. SGB (subgiant branch): hydrogen burning in a thick shell. RGB (red-giant branch): hydrogen burning in a thin shell with a growing core until helium ignites. HB (horizontal branch): helium burning in the core and hydrogen burning in a shell. AGB (asymptotic giant branch): helium and hydrogen shell burning. P-AGB (post-asymptotic giant branch): final evolution from the AGB to the white-dwarf stage

stars that are brighter than the HB. Number counts in 15 globular clusters [49] show that this number ratio agrees with expectations within 20–40% in any one cluster, where the error is mostly statistical because typically only about 100 HB stars were present in the fields of view used. Compounding the results of all 15 clusters, the helium-burning lifetime agrees with expectations within about 10% [10, 11]. Of course, with modern data these results could likely be improved. Either way, a reasonably conservative limit is

$$g_{a\gamma\gamma} < 10^{-10}\,\mathrm{GeV}^{-1}\,. \tag{3.18}$$

It is comparable to the CAST limit (3.17), but applies for higher masses. The relevant temperature is about 10 keV so that significant threshold effects begin only at about $m_a \gtrsim 30\,\mathrm{keV}$. For QCD axions, the coupling increases with mass so that the limit applies to even larger masses.

In the helium-burning core, convection and semi-convection dredges helium to the burning site so that 25–30% of all helium is burnt during the HB phase. Therefore, while the standard theoretical predictions depend on a phenomenological treatment of convection, there is limited room for additional energy supply, even if the treatment of convection were grossly incorrect.

3.4.2 Helium Ignition and the Axion-Electron Interaction

RGB stars have a degenerate helium core with a typical density $10^6\,\mathrm{g\,cm^{-3}}$ and $T \approx 10^8\,\mathrm{K}$. Helium ignites at a critical combination of ϱ and T. Therefore, helium ignition can be delayed by axion cooling. This implies that the core grows more massive before helium ignites. One consequence is that the RGB will extend to brighter stars, i.e., the brightness of the brightest red giant in a given globular cluster signifies the core mass at helium ignition. Detailed studies reveal that the core mass at helium ignition agrees with theoretical expectations within 5–10% [10, 52, 53, 54, 55]. In turn, this implies that a novel energy-loss rate at $T = 10^8\,\mathrm{K}$ and an average density $\langle\varrho\rangle = 2 \times 10^5\,\mathrm{g\,cm^{-3}}$ should not exceed about $10\,\mathrm{erg\,g^{-1}\,s^{-1}}$. At these conditions the standard neutrino emission is about $4\,\mathrm{erg\,g^{-1}\,s^{-1}}$.

The helium-burning lifetime is useful to constrain the axion-photon interaction because the Primakoff rate is suppressed in the degenerate red-giant cores and thus is more effective in HB stars. The helium-ignition argument, on the other hand, is useful when the emission rate is larger on the RGB than on the HB as for bremsstrahlung $e + Ze \to Ze + e + a$. For the conditions in a red-giant core one finds $\varepsilon_{\mathrm{brems}} \approx \alpha_{aee}\, 2 \times 10^{27}\,\mathrm{erg\,g^{-1}\,s^{-1}}$ [54] so that

$$\alpha_{aee} < 0.5 \times 10^{-26} \quad \text{or} \quad g_{aee} < 3 \times 10^{-13}\,. \tag{3.19}$$

In the DFSZ model this limit corresponds to $f_a/\cos^2\beta > 0.8 \times 10^9\,\mathrm{GeV}$, $m_a < 9\,\mathrm{meV}/\cos^2\beta$, and $g_{a\gamma\gamma}\cos^2\beta < 1.2 \times 10^{-12}\,\mathrm{GeV}^{-1}$.

3.4.3 Asymptotic Giant Branch (AGB) Evolution

For axion-electron interactions near or even below the bound (3.19), the emission will strongly affect the evolutionary behavior of AGB stars [56]. However, these results have not been linked closely enough to observational data to obtain new limits or discover evidence for axion emission.

3.5 White-Dwarf Cooling

The degenerate core of a low-mass red giant before helium ignition is essentially a helium white dwarf. After the HB phase, when helium burning has ended, low-mass stars once more ascend the red-giant branch as "asymptotic giants" (AGB stars). They have a degenerate carbon-oxygen core and helium

burning in a shell. Fast mass loss creates a "planetary nebula" surrounding a compact remnant, a white dwarf, that first cools by neutrino emission and later by surface photon emission.

The observed white-dwarf luminosity function reveals that their cooling speed agrees with expectations, constraining new cooling agents such as axion emission [10, 57, 58, 59]. The resulting limit on the axion-electron coupling of $\alpha_{aee} \lesssim 1 \times 10^{-26}$ is comparable to the globular-cluster limit of (3.19).

The cooling speed of individual white dwarfs can be estimated in some cases where they appear as ZZ Ceti stars, i.e., when they are pulsationally unstable and when the period decrease $\dot{P}/P$ can be measured, a quantity that is sensitive to the cooling speed. A well-studied case is the star G117–B15A. For some time, it seemed to be cooling too fast, an effect that could have been attributed to axion cooling with $\alpha_{aee} = 0.2\text{–}0.8 \times 10^{-26}$ [60]. More recent analyses no longer require a new cooling channel, allowing one to set a limit on axion losses corresponding to[1] [61, 62]

$$\alpha_{aee} < 1.3 \times 10^{-27} \quad \text{or} \quad g_{aee} < 1.3 \times 10^{-13} \tag{3.20}$$

at a statistical 95% CL. In the DFSZ model this implies $m_a < 5\,\mathrm{meV}/\cos^2\beta$. This is the most restrictive limit on the axion-electron interaction.

3.6 Supernova 1987A

3.6.1 Energy-Loss Argument

About two dozen neutrinos from SN 1987A were observed about 20 years ago in several detectors [63]. The total number of events, their energies, and the distribution over several seconds correspond reasonably well to theoretical expectations. In the standard picture [64, 65], the core collapse of a massive star leads to a proto neutron star, a solar-mass object at nuclear density and temperature of several 10 MeV, where even neutrinos are trapped. The long time scale of emission is explained by diffusive neutrino energy transport. The emission of more weakly-interacting particles can be a more efficient energy-loss channel, resulting in a reduced neutrino burst duration. The late-time signal is most sensitive to such losses because the early neutrino emission is powered by accretion and thus not very sensitive to volume losses.

This argument has been applied to many cases, from right-handed neutrinos to Kaluza-Klein gravitons, but axions are the earliest and most widely discussed example [23, 66, 67, 68, 69, 70, 71, 72, 73, 74, 75]. They are emitted by nucleon bremsstrahlung $N + N \to N + N + a$ that depends on the axion-nucleon Yukawa coupling g_{aNN}, here taken to be an average of the

[1] The limit on g_{aee} stated in [61] is an order of magnitude more restrictive, but this is an obvious misprint. Likewise, their stated limit $m_a < 5\,\mathrm{meV}\,\cos^2\beta$ has an incorrect scaling with $\cos^2\beta$.

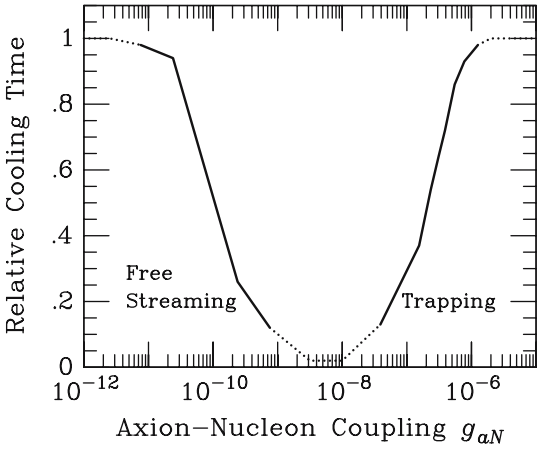

Fig. 3.2. Relative duration of a SN neutrino burst as a function of the axion-nucleon coupling [10]. Freely streaming axions are emitted from the entire core volume, trapped ones from an "axion sphere". The solid line is from numerical calculations [71, 72]. The dotted line is an arbitrary continuation to guide the eye

couplings to neutrons and protons. Figure 3.2 illustrates that axion emission leaves the signal duration unchanged when g_{aNN} is very small. For larger couplings, the signal is shortened until it reaches a minimum, roughly when the axion mfp corresponds to the geometric size of the SN core. For even larger couplings, axions are trapped and are emitted from an "axion sphere". When it moves beyond the neutrino sphere, the signal duration once more remains unaffected.

Of course, such "strongly" interacting axions are not necessarily harmless. They may play an important role during the infall phase. Moreover, in the water Cherenkov detectors that registered the SN 1987A neutrinos, these axions would have interacted with oxygen nuclei, leading to the release of γ rays and causing too many events [76].

However, for axions and other particles, the trapping regime is usually excluded by other arguments so that the free-streaming regime is of greater interest. An approximate analytic constraint on the energy-loss rate is [9]

$$\varepsilon_a \lesssim 1 \times 10^{19}\,\mathrm{erg\,g^{-1}\,s^{-1}}\,, \tag{3.21}$$

to be calculated at $\varrho = 3 \times 10^{14}\,\mathrm{g\,cm^{-3}}$ and $T = 30\,\mathrm{MeV}$. If we take the SN core to have a mass of about $1\,M_\odot = 2 \times 10^{33}\,\mathrm{g}$, this corresponds to an axion luminosity $L_a = \varepsilon_a M_\odot = 2 \times 10^{52}\,\mathrm{erg\,s^{-1}}$. The gravitational binding energy of the neutron star is about $3 \times 10^{53}\,\mathrm{erg}$ and the emission lasts up to 10 s, i.e., axion losses would compete significantly with neutrino emission.

We stress that the criterion (3.21) is not arbitrary, but was distilled from several numerical simulations that consistently showed that the burst duration was roughly halved when the limit (3.21) was saturated [9]. Axion losses

are then not small so that $T = 30\,\mathrm{MeV}$ is not the unperturbed temperature of these models. Different numerical models with different input physics probably have internal temperatures that are more similar once significant axion losses are included. In any event, (3.21) represents quite accurately the results from different simulations.

Recently, self-consistent cooling calculations were performed for Kaluza-Klein gravitons [77], once more confirming (3.21). The neutrino signal duration was directly compared with the data, and the limit, corresponding to (3.21), was found to have a 95% statistical CL.

Of course, this and any other numerical study rely on input physics for which systematic uncertainties are difficult to quantify, notably the nuclear equation of state and the neutrino opacities. In addition, the data are very sparse so that any conclusion based on them suffers from the usual problems of small-number statistics. Therefore, (3.21) should be viewed as a reasonable guide as to where a new energy-loss channel causes a significant tension with the SN 1987A pulse duration.

3.6.2 Axion Emission from a Nuclear Medium

In order to apply (3.21) to axions one needs the emission rate from a hot medium at nuclear density. The main emission process is nucleon bremsstrahlung, $N + N \to N + N + a$, but a reliable calculation of the rate is difficult. Axions couple to the nucleon spin so that bremsstrahlung requires the spin to "jiggle" in a collision, i.e., spin-conserving interactions do not contribute. This leaves the nuclear tensor force that is only crudely modeled by one-pion exchange (OPE). In a dense medium, other problems include the modification of particle masses and couplings as well as many-body and multiple-scattering effects.

One approach to estimate the emission rate relies on linear response theory where emission, absorption, and scattering of neutrinos, axions, and other particles depend only on a few "form factors" of the medium, i.e., the dynamical structure functions [73, 78, 79, 80, 81, 82, 83, 84, 85, 86]. This approach is perturbative to lowest order in the weak interaction between neutrinos (or axions) and nucleons, whereas the interactions among the medium constituents are lumped into the structure functions.

Assuming the medium to consist of one species of non-relativistic nucleons, the relevant quantity is the dynamical spin-density structure function [73]

$$S_\sigma(\omega,\mathbf{k}) = \frac{4}{3n_B}\int_{-\infty}^{+\infty} \mathrm{d}t\, \mathrm{e}^{\mathrm{i}\omega t}\, \langle \boldsymbol{\sigma}(t,\mathbf{k})\cdot\boldsymbol{\sigma}(0,-\mathbf{k})\rangle \ , \tag{3.22}$$

where n_B is the nucleon (baryon) density and $\boldsymbol{\sigma}(t,\mathbf{k})$ the spatial Fourier transform of the nucleon spin-density operator. The basic principles of quantum mechanics imply the detailed-balancing condition

$$S_\sigma(-\omega,\mathbf{k}) = S_\sigma(\omega,\mathbf{k})\,\mathrm{e}^{-\omega/T} \ . \tag{3.23}$$

The structure function obeys the sum rule

$$\int_{-\infty}^{+\infty} \frac{\mathrm{d}\omega}{2\pi}\, S_\sigma(\omega,\mathbf{k}) = 1 + \frac{4}{3n_B} \left\langle \sum_{\substack{i,j=1\\ i\neq j}}^{N_B} \mathbf{s}_i \cdot \mathbf{s}_j \, \cos(\mathbf{k}\cdot\mathbf{r}_{ij}) \right\rangle , \tag{3.24}$$

where $\mathbf{s}_i$ is the spin operator of nucleon i. The f-sum rule includes a factor ω under the integral and establishes a relation to the average nucleon-nucleon spin interaction energy [82]. It is often assumed that the higher sums $\int \mathrm{d}\omega\, \omega^n\, S(\omega,\mathbf{k})$ also exist for all n.

The axion absorption rate and the volume energy-loss rate are given in terms of the structure function as

$$\begin{aligned} \Gamma_a &= \left(\frac{C_N}{2f_a}\right)^2 \frac{n_B}{2}\, \omega\, S_\sigma(\omega,k) \,, \\ Q_a &= \left(\frac{C_N}{2f_a}\right)^2 \frac{n_B}{4\pi^2} \int_0^\infty \mathrm{d}\omega\, \omega^4\, S_\sigma(-\omega,k) \,, \end{aligned} \tag{3.25}$$

where $k = |\mathbf{k}| \approx \omega$ is the modulus of the axion momentum. Neutrino scattering, emission and absorption rates based on the axial vector current are given by similar phase-space integrals.

A reliable expression for $S_\sigma(\omega,k)$ is not available, so we need to use heuristic reasoning. The large nucleon mass compared to the emitted axion energy suggests the use of long-wavelength approximation $S_\sigma(\omega) = \lim_{\mathbf{k}\to 0} S_\sigma(\omega,\mathbf{k})$, i.e., we neglect the momentum transfer to the medium. In this limit (3.22) represents essentially the Fourier transform of the autocorrelation function of a single nucleon spin.

If we picture the nucleon spin as a classical vector that is kicked by a random force, we find [79]

$$S_\sigma^{\mathrm{class}}(\omega) = \frac{\Gamma_\sigma}{\omega^2 + \Gamma_\sigma^2/4} \,, \tag{3.26}$$

where Γ_σ is the spin fluctuation rate. Being a classical result, the quantum-mechanical detailed-balancing property is missing. Overall we thus write

$$S_\sigma(\omega) = \frac{\Gamma_\sigma}{\omega^2 + \Gamma_\sigma^2/4}\, s(\omega/T) \times \begin{cases} 1 & \text{for } \omega \geq 0, \\ \mathrm{e}^{\omega/T} & \text{for } \omega < 0, \end{cases} \tag{3.27}$$

where $s(x)$ is an even function normalized to $s(0) = 1$. The axion emission rate per unit mass, $\varepsilon_a = Q_a/\varrho$, therefore is

$$\varepsilon_a = \left(\frac{C_N}{2f_a}\right)^2 \frac{T^4}{\pi^2 m_N} F = 3.0\times 10^{37}\, \frac{\mathrm{erg}}{\mathrm{g\ s}}\, C_N^2 \left(\frac{\mathrm{GeV}}{f_a}\right)^2 \left(\frac{T}{30\,\mathrm{MeV}}\right)^4 F \,, \tag{3.28}$$

where

$$F = \int_0^\infty \mathrm{d}x \, \frac{x^4 \, \mathrm{e}^{-x}}{4} \, \frac{\Gamma_\sigma/T}{x^2 + (\Gamma_\sigma/2T)^2} \, s(x) \; . \tag{3.29}$$

For $\Gamma_\sigma/T \ll 1$ (dilute medium) assuming $s(x) = 1$, we find $F = \Gamma_\sigma/2T$.

A perturbative calculation, relevant for a dilute medium, using the OPE approximation yields [70, 79]

$$\Gamma_\sigma^{\rm OPE} = 4\pi^{1/2} \alpha_\pi^2 \, \frac{n_B T^{1/2}}{m_N^{5/2}} = 450\,\mathrm{MeV} \, \frac{\varrho}{3{\times}10^{14}\,\mathrm{g\,cm^{-3}}} \left(\frac{T}{30\,\mathrm{MeV}} \right)^{1/2} , \tag{3.30}$$

where $\alpha_\pi = (f 2m_N/m_\pi)^2/4\pi \approx 15$ with $f \approx 1.0$. For soft energies, bremsstrahlung depends only on the on-shell spin-dependent nucleon scattering rate. Based on measured nuclear phase shifts it was argued that the OPE result was an overestimation by about a factor of 4 [75].

Either way, Γ_σ/T is not small compared to unity, but also not very large. A possible range $1 \lesssim \Gamma_\sigma/T \lesssim 10$ appears generous. With $s(x) = 1$, this would imply $F \approx 0.5$ for $\Gamma_\sigma/T = 1$, a maximum of $F \approx 1.35$ near $\Gamma_\sigma/T = 7$ and $F \approx 1.3$ for $\Gamma_\sigma/T = 10$. Of course, $s(x)$ probably decreases with x or else the f-sum and higher sums of $S_\sigma(\omega)$ diverge. On the basis of existing information, one cannot do better than assume F to be a factor of order unity.

The SN 1987A limits are particularly interesting for hadronic axions where the bounds on α_{aee} are moot. Therefore, we use $C_p = -0.4$ and $C_n = 0$. Initially the proton fraction is relatively large so that we use $Y_p = 0.3$ to scale the emission rate to the proton density. With $F = 1$ and $T = 30\,\mathrm{MeV}$ we then find $\varepsilon_a = 1.4 \times 10^{36}\,\mathrm{erg\,g^{-1}\,s^{-1}}$ so that (3.21) implies

$$f_a \gtrsim 4 \times 10^8\,\mathrm{GeV} \qquad \text{and} \qquad m_a \lesssim 16\,\mathrm{meV} \; . \tag{3.31}$$

Despite a lot of effort that has gone into understanding the axion emission rate, these limits remain fairly rough estimates.

3.7 Conclusions

Astrophysics and cosmology provide the most restrictive limits on the axion hypothesis as summarized in Fig. 3.3. Beginning with cosmology, a cold axion population would emerge in the early universe that can make up the dark matter, but the required axion mass involves many uncertainties [87]. Galactic dark matter axions will be searched by the ADMX experiment in the mass range $m_a = 1$–$100\,\mu\mathrm{eV}$ [38, 88, 89, 90].

In addition, a population of hot axions is produced. Before confinement, the relevant processes involve quarks and gluons [91, 92]. Later the most generic process is $\pi + \pi \leftrightarrow \pi + a$ [93]. Axions decouple after the QCD epoch if $f_a \lesssim 3 \times 10^7\,\mathrm{GeV}$ ($m_a \gtrsim 0.2\,\mathrm{eV}$). Some of these hot dark-matter axions would be trapped in galaxies and galaxy clusters. An unsuccesful search for a decay

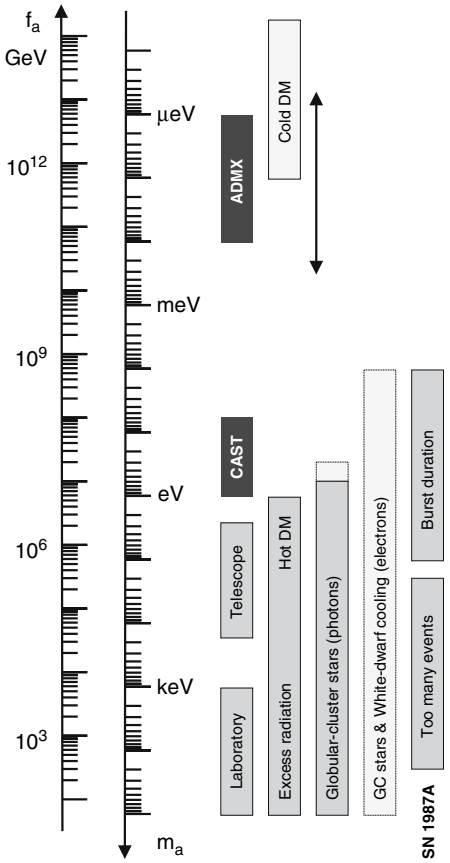

Fig. 3.3. Summary of astrophysical and cosmological axion limits as discussed in the text. The black sensitivity bars indicate the search ranges of the CAST solar axion search and the ADMX search for galactic dark matter axions. Light-grey exclusion bars are very model-dependent

line [94, 95, 96] provides direct limits on a range of axion masses marked "Telescope" in Fig. 3.3. Moreover, the usual structure-formation arguments provide the hot dark-matter limits [97, 98]. Axions decay on a cosmic time scale for $m_a \gtrsim 20\,\mathrm{eV}$. The decay photons would cause a variety of observable consequences [99], seamlessly connecting with the hot dark-matter limit so that cosmology alone rules out axions in the entire mass range $m_a > 1\,\mathrm{eV}$.

Figure 3.3 also shows the stellar-evolution limits discussed in this chapter, notably the globular-cluster limit on the axion-photon coupling. The globular-cluster and white-dwarf limits for DFSZ axions with $\cos^2\beta = 1$ are shown as a light-grey exclusion bar. Even in the DFSZ model, the axion-electron coupling could be accidentally small and at tree level it is entirely absent for

hadronic axions. Therefore, these limits are far less generic than those based on the axion-photon or axion-nucleon interaction.

The requirement that the neutrino signal of SN 1987A was not excessively shortened by axion losses pushes the limits down to $m_a \lesssim 10\,\mathrm{meV}$. However, this limit involves many uncertainties that are difficult to quantify, so it is somewhat schematic. The CAST search for solar axions [46] covers new territory in the parameter plane of m_a and $g_{a\gamma\gamma}$, but a signal would represent a conflict with the SN 1987A limit. While this limit certainly suggests that axions more plausibly have masses relevant for cold dark matter, a single argument, measurement, or observation is never conclusive.

In the DFSZ model, the limits from white-dwarf cooling based on the axion-electron interaction and those from SN 1987A from the axion-nucleon interaction are quite similar. Therefore, axion emission could still play an important role as an energy-loss channel of both SNe and white dwarfs and for other evolved stars, e.g. asymptotic giant stars.

In summary, axions provide a show-case example for the fascinating interplay between astrophysics, cosmology, and particle physics to solve some of the deepest mysteries at the interface between inner space and outer space.

Acknowledgments

Partial support by the Deutsche Forschungsgemeinschaft under grant SFB 375 and the European Union, contract RII3-CT-2004-506222 (ILIAS project), is acknowledged.

References

1. Gamow, G., Schoenberg, M.: The possible role of neutrinos in stellar evolution. Phys. Rev. **58**, 1117 (1940) 51
2. Gamow, G., Schoenberg, M.: Neutrino theory of stellar collapse. Phys. Rev. **59**, 539 (1941) 51
3. Bernstein, J., Ruderman, M., Feinberg, G.: Electromagnetic properties of the neutrino. Phys. Rev. **132**, 1227 (1963) 51
4. Stothers, R.B.: Astrophysical determination of the coupling constant for the electron-neutrino weak interaction. Phys. Rev. Lett. **24**, 538 (1970) 51
5. Sato, K., Sato, H.: Higgs meson emission from a star and a constraint on its mass. Prog. Theor. Phys. **54**, 1564 (1975) 51
6. Dicus, D.A., Kolb, E.W., Teplitz, V.L., Wagoner, R.V.: Astrophysical bounds on the masses of axions and Higgs particles. Phys. Rev. D **18**, 1829 (1978) 51, 54
7. Vysotsky, M.I., Zeldovich, Y.B., Khlopov, M.Y., Chechetkin, V.M.: Some astrophysical limitations on the axion mass. Pisma Zh. Eksp. Teor. Fiz. **27**, 533 (1978) [JEPT Lett. **27**, 502 (1978)] 51
8. Turner, M.S.: Windows on the axion. Phys. Rept. **197**, 67 (1990) 51

9. Raffelt, G.G.: Astrophysical methods to constrain axions and other novel particle phenomena. Phys. Rept. **198**, 1 (1990) 51, 61
10. Raffelt, G.G.: Stars as laboratories for fundamental physics. University of Chicago Press, Chicago (1996) 51, 55, 58, 59, 60, 61
11. Raffelt, G.G.: Particle physics from stars. Ann. Rev. Nucl. Part. Sci. **49**, 163 (1999) [hep-ph/9903472] 51, 58
12. Yao, W.M., et al.: (Particle Data Group), Review of particle physics. J. Phys. G **33**, 1 (2006) 51, 52
13. Georgi, H., Kaplan, D.B., Randall, L.: Manifesting the invisible axion at low energies. Phys. Lett. B **169**, 73 (1986) 52
14. Kamionkowski, M., March-Russell, J.: Planck scale physics and the Peccei-Quinn mechanism. Phys. Lett. B **282**, 137 (1992) [hep-th/9202003] 52
15. Barr, S.M., Seckel, D.: Planck scale corrections to axion models. Phys. Rev. D **46**, 539 (1992) 52
16. Gasser, J., Leutwyler, H.: Quark masses. Phys. Rept. **87**, 77 (1982) 52
17. Leutwyler, H.: The ratios of the light quark masses. Phys. Lett. B **378**, 313 (1996) [hep-ph/9602366] 52
18. Kim, J.E.: Weak interaction singlet and strong CP invariance. Phys. Rev. Lett. **43**, 103 (1979) 52, 53
19. Shifman, M.A., Vainshtein, A.I., Zakharov, V.I.: Can confinement ensure natural CP invariance of strong interactions?. Nucl. Phys. B **166**, 493 (1980) 52, 53
20. Zhitnitsky, A.R.: On possible suppression of the axion hadron interactions. Sov. J. Nucl. Phys. **31**, 260 (1980) [Yad. Fiz. **31**, 497 (1980)] 52, 53
21. Dine, M., Fischler, W., Srednicki, M.: A simple solution to the strong CP problem with a harmless axion. Phys. Lett. B **104**, 199 (1981) 52, 53
22. Cheng, S.L., Geng, C.Q., Ni, W.T.: Axion-photon couplings in invisible axion models. Phys. Rev. D **52**, 3132 (1995) [hep-ph/9506295] 52
23. Raffelt, G., Seckel, D.: Bounds on exotic particle interactions from SN 1987A. Phys. Rev. Lett. **60**, 1793 (1988) 53, 60
24. Carena, M., Peccei, R.D.: The effective Lagrangian for axion emission from SN 1987A. Phys. Rev. D **40**, 652 (1989) 53
25. Alexakhin, V.Y., et al. (COMPASS Collaboration): The deuteron spin-dependent structure function g_1^d and its first moment. Phys. Lett. B **647**, 8 (2007) [hep-ex/0609038] 54
26. Airapetian, A. (HERMES Collaboration): Precise determination of the spin structure function g_1 of the proton, deuteron and neutron. [hep-ex/0609039] 54
27. Ellis, J.R., Karliner, M.: The strange spin of the nucleon. In: Frois, B., Hughes, V.W., De Groot, N. (eds.) The Spin Structure of the Nucleon: International School of Nucleon Structure. Erice, Italy (3–10 August 1995) World Scientific, Singapore (1997) [hep-ph/9601280] 54
28. Primakoff, H.: Photo-production of neutral mesons in nuclear electric fields and the mean life of the neutral meson. Phys. Rev. **81**, 899 (1951) 54
29. Raffelt, G.G.: Astrophysical axion bounds diminished by screening effects. Phys. Rev. D **33**, 897 (1986) 54
30. Altherr, T., Petitgirard, E., del Río Gaztelurrutia, T.: Axion emission from red giants and white dwarfs. Astropart. Phys. **2**, 175 (1994) [hep-ph/9310304] 54
31. Raffelt, G.G.: Plasmon decay into low mass bosons in stars. Phys. Rev. D **37**, 1356 (1988) 54, 55

32. Zavattini, E., et al. (PVLAS Collaboration): Experimental observation of optical rotation generated in vacuum by a magnetic field. Phys. Rev. Lett. **96**, 110406 (2006) [hep-ex/0507107] 55
33. Cameron, R., et al.: Search for nearly massless, weakly coupled particles by optical techniques. Phys. Rev. D **47**, 3707 (1993) 55
34. Schlattl, H., Weiss, A., Raffelt, G.: Helioseismological constraint on solar axion emission. Astropart. Phys. **10**, 353 (1999) [hep-ph/9807476] 55, 56
35. Bahcall, J.N., Serenelli, A.M., Basu, S.: New solar opacities, abundances, helioseismology, and neutrino fluxes. Astrophys. J. **621**, L85 (2005) [astro-ph/0412440] 56
36. Ahmad, Q.R., et al. (SNO Collaboration): Direct evidence for neutrino flavor transformation from neutral-current interactions in the Sudbury Neutrino Observatory. Phys. Rev. Lett. **89**, 011301 (2002) [nucl-ex/0204008] 56
37. Aharmim, B., et al. (SNO Collaboration): Electron energy spectra, fluxes, and day-night asymmetries of B-8 solar neutrinos from the 391-day salt phase SNO data set. Phys. Rev. C **72**, 055502 (2005) [nucl-ex/0502021] 56
38. Sikivie, P.: Experimental tests of the invisible axion. Phys. Rev. Lett. **51**, 1415 (1983); (E) ibid. **52**, 695 (1984) 56, 64
39. Raffelt, G., Stodolsky, L.: Mixing of the photon with low mass particles. Phys. Rev. D **37**, 1237 (1988) 56
40. Lazarus, D.M., Smith, G.C., Cameron, R., Melissinos, A.C., Ruoso, G., Semertzidis, Y.K., Nezrick, F.A.: A search for solar axions. Phys. Rev. Lett. **69**, 2333 (1992) 56
41. Moriyama, S., Minowa, M., Namba, T., Inoue, Y., Takasu, Y., Yamamoto, A.: Direct search for solar axions by using strong magnetic field and x-ray detectors. Phys. Lett. B **434**, 147 (1998) [hep-ex/9805026] 56
42. Inoue, Y., Namba, T., Moriyama, S., Minowa, M., Takasu, Y., Horiuchi, T., Yamamoto, A.: Search for sub-electronvolt solar axions using coherent conversion of axions into photons in magnetic field and gas helium. Phys. Lett. B **536**, 18 (2002) [astro-ph/0204388] 56, 57
43. Avignone, F.T., et al. (SOLAX Collaboration): Experimental search for solar axions via coherent Primakoff conversion in a germanium spectrometer. Phys. Rev. Lett. **81**, 5068 (1998) [astro-ph/9708008] 56
44. Morales, A., et al. (COSME Collaboration): Particle dark matter and solar axion searches with a small germanium detector at the Canfranc underground laboratory. Astropart. Phys. **16**, 325 (2002) [hep-ex/0101037] 56
45. Bernabei, R., et al.: Search for solar axions by Primakoff effect in NaI crystals. Phys. Lett. B **515**, 6 (2001) 56
46. Zioutas, K., et al. (CAST Collaboration): First results from the CERN axion solar telescope (CAST). Phys. Rev. Lett. **94**, 121301 (2005) [hep-ex/0411033] 56, 66
47. van Bibber, K., McIntyre, P.M., Morris, D.E., Raffelt, G.G.: A practical laboratory detector for solar axions. Phys. Rev. D **39**, 2089 (1989) 57
48. Raffelt, G.G., Starkman, G.D.: Stellar energy transfer by keV mass scalars. Phys. Rev. D **40**, 942 (1989) 57
49. Buzzoni, A., Fusi Pecci, F., Buonanno, R., Corsi, C.E.: Helium abundance in globular clusters: the R-method. Astron. Astrophys. **128**, 94 (1983) 58
50. Buonanno, R., Buzzoni, A., Corsi, C.E., Fusi Pecci, F., Sandage, A.R.: High precision photometry of 10000 stars in M3. Mem. Soc. Astron. Ital. **57**, 391 (1986) 58

51. Renzini, A., Fusi Pecci, F.: Tests of evolutionary sequences using color-magnitude diagrams of globular clusters. Annu. Rev. Astron. Astrophys. **26**, 199 (1988) 58
52. Raffelt, G.G.: Core mass at the helium flash from observations and a new bound on neutrino electromagnetic properties. Astrophys. J. **365**, 559 (1990) 59
53. Raffelt, G.G.: New bound on neutrino dipole moments from globular cluster stars. Phys. Rev. Lett. **64**, 2856 (1990) 59
54. Raffelt, G., Weiss, A.: Red giant bound on the axion-electron coupling revisited. Phys. Rev. D **51**, 1495 (1995) [hep-ph/9410205] 59
55. Catelan, M., de Freitas Pacheco, J.A., Horvath, J.E.: The helium-core mass at the helium flash in low-mass red giant stars: Observations and theory. Astrophys. J. **461**, 231 (1996) [astro-ph/9509062] 59
56. Domínguez, I., Straniero, O., Isern, J.: Asymptotic giant branch stars as astroparticle laboratories. Mon. Not. R. Astron. Soc. **306**, L1 (1999) [astro-ph/9905033] 59
57. Raffelt, G.G.: Axion constraints from white dwarf cooling times. Phys. Lett. B **166**, 402 (1986) 60
58. Wang, J.: Constraints of axions from white dwarf cooling. Mod. Phys. Lett. A **7**, 1497 (1992) 60
59. Blinnikov, S.I., Dunina-Barkovskaya, N.V.: The cooling of hot white dwarfs: A theory with non-standard weak interactions and a comparison with observations. Mon. Not. R. Astron. Soc. **266**, 289 (1994) 60
60. Isern, J., Hernanz, M., García-Berro, E.: Axion cooling of white dwarfs. Astrophys. J. **392**, L23 (1992) 60
61. Córsico, A.H., Benvenuto, O.G., Althaus, L.G., Isern, J., García-Berro, E.: The potential of the variable DA white dwarf G117-B15A as a tool for fundamental physics. New Astron. **6**, 197 (2001) [astro-ph/0104103] 60
62. Isern, J., García-Berro, E.: White dwarf stars as particle physics laboratories. Nucl. Phys. Proc. Suppl. **114**, 107 (2003) 60
63. Koshiba, M.: Observational neutrino astrophysics. Phys. Rept. **220**, 229 (1992) 60
64. Burrows, A.: Supernova explosions in the universe. Nature **403**, 727 (2000) 60
65. Woosley, S., Janka, T.: The physics of core-collapse supernovae. Nature Physics **1**, 147 (2005) [astro-ph/0601261] 60
66. Ellis, J.R., Olive, K.A.: Constraints on light particles from supernova 1987A. Phys. Lett. B **193**, 525 (1987) 60
67. Turner, M.S.: Axions from SN 1987A. Phys. Rev. Lett. **60**, 1797 (1988) 60
68. Mayle, R., Wilson, J.R., Ellis, J.R., Olive, K.A., Schramm, D.N., Steigman, G.: Constraints on axions from SN 1987A. Phys. Lett. B **203**, 188 (1988) 60
69. Mayle, R., Wilson, J.R., Ellis, J.R., Olive, K.A., Schramm, D.N., Steigman, G.: Updated constraints on axions from SN 1987A. Phys. Lett. B **219**, 515 (1989) 60
70. Brinkmann, R.P., Turner, M.S.: Numerical rates for nucleon-nucleon axion bremsstrahlung. Phys. Rev. D **38**, 2338 (1988) 60, 64
71. Burrows, A., Turner, M.S., Brinkmann, R.P.: Axions and SN 1987A. Phys. Rev. D **39**, 1020 (1989) 60, 61
72. Burrows, A., Ressell, M.T., Turner, M.S.: Axions and SN 1987A: Axion trapping. Phys. Rev. D **42**, 3297 (1990) 60, 61

73. Janka, H.T., Keil, W., Raffelt, G., Seckel, D.: Nucleon spin fluctuations and the supernova emission of neutrinos and axions. Phys. Rev. Lett. **76**, 2621 (1996) [astro-ph/9507023] 60, 62
74. Keil, W., Janka, H.T., Schramm, D.N., Sigl, G., Turner, M.S., Ellis, J.R.: A fresh look at axions and SN 1987A. Phys. Rev. D **56**, 2419 (1997) [astro-ph/9612222] 60
75. Hanhart, C., Phillips, D.R., Reddy, S.: Neutrino and axion emissivities of neutron stars from nucleon nucleon scattering data. Phys. Lett. B **499**, 9 (2001) [astro-ph/0003445] 60, 64
76. Engel, J., Seckel, D., Hayes, A.C.: Emission and detectability of hadronic axions from SN 1987A. Phys. Rev. Lett. **65**, 960 (1990) 61
77. Hanhart, C., Pons, J.A., Phillips, D.R., Reddy, S.: The likelihood of GODs' existence: Improving the SN 1987A constraint on the size of large compact dimensions. Phys. Lett. B **509**, 1 (2001) [astro-ph/0102063] 62
78. Raffelt, G., Seckel, D.: Multiple scattering suppression of the bremsstrahlung emission of neutrinos and axions in supernovae. Phys. Rev. Lett. **67**, 2605 (1991) 62
79. Raffelt, G., Seckel, D.: A selfconsistent approach to neutral current processes in supernova cores. Phys. Rev. D **52**, 1780 (1995) [astro-ph/9312019] 62, 63, 64
80. Raffelt, G., Seckel, D., Sigl, G.: Supernova neutrino scattering rates reduced by nucleon spin fluctuations: Perturbative limit. Phys. Rev. D **54**, 2784 (1996) [astro-ph/9603044] 62
81. Raffelt, G., Strobel, T.: Reduction of weak interaction rates in neutron stars by nucleon spin fluctuations: Degenerate case. Phys. Rev. D **55**, 523 (1997) [astro-ph/9610193] 62
82. Sigl, G.: Weak interactions in supernova cores and saturation of nucleon spin fluctuations. Phys. Rev. Lett. **76**, 2625 (1996) [astro-ph/9508046] 62, 63
83. Raffelt, G., Sigl, G.: Numerical toy-model calculation of the nucleon spin autocorrelation function in a supernova core. Phys. Rev. D **60**, 023001 (1999) [hep-ph/9808476] 62
84. Yamada, S.: Reduction of neutrino nucleon scattering rate by nucleon nucleon collisions. Nucl. Phys. A **662**, 219 (2000) [astro-ph/9907045] 62
85. Sedrakian, A., Dieperink, A.E.L.: Coherent neutrino radiation in supernovae at two loops. Phys. Rev. D **62**, 083002 (2000) [astro-ph/0002228] 62
86. van Dalen, E.N.E., Dieperink, A.E.L., Tjon, J.A.: Neutrino emission in neutron stars. Phys. Rev. C 67, 065807 (2003) [nucl-th/0303037] 62
87. Sikivie, P.: Axion cosmology. In: Kuster M., Raffelt G., Beltrán B., (eds.) Lecture Notes in Physics, Vol. 741, pp. 51–71. Springer, Heidelberg (2008) [astro-ph/0610440] 64
88. Bradley, R., et al.: Microwave cavity searches for dark-matter axions. Rev. Mod. Phys. **75**, 777 (2003) 64
89. Asztalos, S.J., et al.: An improved RF cavity search for halo axions. Phys. Rev. D **69**, 011101 (2004) [astro-ph/0310042] 64
90. Duffy, L.D., et al.: A high resolution search for dark-matter axions. Phys. Rev. D **74**, 012006 (2006) [astro-ph/0603108] 64
91. Turner, M.S.: Thermal production of not so invisible axions in the early universe. Phys. Rev. Lett. **59**, 2489 (1987); (E) ibid. **60**, 1101 (1988) 64
92. Massó, E., Rota, F., Zsembinszki, G.: On axion thermalization in the early universe. Phys. Rev. D **66**, 023004 (2002) [hep-ph/0203221] 64

93. Chang, S., Choi, K.: Hadronic axion window and the big bang nucleosynthesis. Phys. Lett. B **316**, 51 (1993) [hep-ph/9306216] 64
94. Bershady, M.A., Ressell, M.T., Turner, M.S.: Telescope search for multi-eV axions. Phys. Rev. Lett. **66**, 1398 (1991) 65
95. Ressell, M.T.: Limits to the radiative decay of the axion. Phys. Rev. D **44**, 3001 (1991) 65
96. Grin, D., Covone, G., Kneib, J.P., Kamionkowski, M., Blain, A., Jullo, E.: A telescope search for decaying relic axions. Phys. Rev. D **75**, 105018 (2007) [astro-ph/0611502] 65
97. Hannestad, S., Raffelt, G.: Cosmological mass limits on neutrinos, axions, and other light particles. JCAP 0404, 008 (2004) [hep-ph/0312154] 65
98. Hannestad, S., Mirizzi, A., Raffelt, G.: New cosmological mass limit on thermal relic axions. JCAP 0507, 002 (2005) [hep-ph/0504059] 65
99. Massó, E., Toldra, R.: New constraints on a light spinless particle coupled to photons. Phys. Rev. D **55**, 7967 (1997) [hep-ph/9702275] 65

4 Axions and Large Extra Dimensions

Biljana Lakić, Raul Horvat and Milica Krčmar

Rudjer Bošković Institute, Bijenička cesta 54, 10002 Zagreb, Croatia
Biljana.Lakic@irb.hr

Abstract. Theories including extra space dimensions offer a possible solution to the hierarchy problem of particle physics. An additional effect of these theories is the possibility for axions to propagate in the higher-dimensional space. We explore the potential of the CERN Axion Solar Telescope (CAST) for testing the presence of large extra dimensions.

4.1 Introduction on Extra Dimensions

One of the most puzzling problems in nature is the hierarchy problem of particle physics, i.e., the large separation between the electroweak scale $\sim 10^3\,\mathrm{GeV}$ and the Planck scale $M_{\mathrm{Pl}} = 1.22 \times 10^{19}\,\mathrm{GeV}$. One possible solution is the introduction of n extra space dimensions. Recent theories involve the idea that the standard-model fields are confined to our (3+1)-dimensional subspace (brane) of a higher-dimensional space (bulk), while only gravity may propagate throughout the bulk. The hierarchy is generated by the geometry of the additional dimensions.

While our knowledge of the weak and strong forces extends down to scales of order $10^{-15}\,\mathrm{mm}$, we have almost no knowledge of gravity for distances smaller than roughly a millimeter. It is thus conceivable that at small distances gravity behaves differently from the inverse-square force law. However, gravity obeys Newton's law at distances greater than a millimeter and therefore behaves as if there are only 3 spatial dimensions. There are several different scenarios[1] to achieve this.

1. Arkani-Hamed, Dimopoulos and Dvali (ADD) suggested that the extra dimensions are compactified and the geometry of the space is flat. The hierarchy is generated by a large volume of the extra-dimensional space (large extra dimensions) [2].
2. Randall and Sundrum assumed that the hierarchy is generated by a large curvature of the extra dimensions (warped extra dimensions) [3].

[1] An additional possible scenario is with TeV^{-1} sized extra dimensions [1] which allows also the standard-model particles to propagate in the bulk. This scenario cannot solve the hierarchy problem.

B. Lakić et al.: *Axions and Large Extra Dimensions*, Lect. Notes Phys. **741**, 73–82 (2008)
DOI 10.1007/978-3-540-73518-2_4

It is the relation of these models to the hierarchy which yields testable predictions at the TeV scale.

4.1.1 Large Extra Dimensions

Large extra dimensions aim to stabilize the mass hierarchy by producing the hugeness of the Planck mass M_{Pl} via the relation

$$M_{\mathrm{Pl}}^2 \approx M_D^{n+2} R^n, \tag{4.1}$$

where R is the (common) compactification radius of the extra dimensions and M_D is the fundamental higher-dimensional scale. In this scenario, it is assumed that the extra dimensions are flat and thus of toroidal form. In order to eliminate the hierarchy between the Planck and electroweak scale, M_D should be of order TeV. In this case R ranges from a sub-millimeter to a few fermi for $n = 2$–6. The case of $n = 1$ is excluded since the corresponding compactification radius ($R \approx 10^{11}$ m) is such that deviations from Newton's law could be observed on solar-system scales. Due to the large size of the extra dimensions, the standard-model fields have to be constrained to the brane.

After compactification of the n additional dimensions, all fields propagating in the bulk are decomposed into a complete set of modes, the so-called Kaluza-Klein (KK) tower of states, with mode numbers $\mathbf{k} = (k_1, k_2, \ldots, k_n)$ labeling the KK excitations. The momentum of the bulk field is quantized in the n compactified dimensions, $\mathbf{p}_n^2 = \mathbf{k} \cdot \mathbf{k}/R^2$. For an observer on the brane, each allowed momentum in the compactified volume appears as a KK excitation of the bulk field with mass $m_{\mathbf{k}}^2 = \mathbf{p}_n^2$. The result is a KK tower of states where each KK excitation has identical spin and gauge quantum numbers.

Experimental constraints on the radius of the extra dimensions, for the case of two flat dimensions of equal radii, are given by [4]

- direct tests of Newton's law ($1/r^2 \to 1/r^{2+n}$ for $r < R$)

$$R < 0.15\,\mathrm{mm}\ ,$$

- collider signals (direct production of KK gravitons)

$$R < 210\text{–}610\,\mu\mathrm{m}\ ,$$

- and astrophysics (limits depend on technique and assumption)
  supernova cooling $R < 90\text{–}660\,\mathrm{nm}$
  neutron stars $R < 0.2\text{–}50\,\mathrm{nm}$

4.2 Axions in Large Extra Dimensions

In the ADD model, extra dimensions are felt only by gravity while the standard-model fields are confined to a (3+1)-dimensional subspace of a higher-dimensional space. In addition to gravity, one can assume that fields that are singlets under the standard-model gauge group could also propagate in the higher-dimensional space. As such, one might consider axions.

Axions are hypothetical particles associated with the spontaneously broken Peccei-Quinn (PQ) symmetry that can solve the strong CP problem in QCD [5]. Besides, axions are serious candidates for the dark matter of the Universe. An effective axion Lagrangian is of the form

$$L_{\text{eff}} = L_{\text{QCD}} + \frac{1}{2}\partial_\mu a \partial^\mu a + \xi \frac{g_s^2}{32\pi^2}\frac{a}{f_{\text{PQ}}} G^b_{\mu\nu}\tilde{G}^{b\mu\nu}\,, \tag{4.2}$$

where f_{PQ} is the PQ symmetry breaking scale and ξ is a model-dependent parameter. The axion-photon coupling strength is given by the relation

$$g_{a\gamma\gamma} = \frac{\alpha}{2\pi f_{\text{PQ}}}\left(\frac{E}{N} - 1.93 \pm 0.08\right), \tag{4.3}$$

where E/N is a model-dependent parameter. The mass[2] of the axion m_{PQ} is related to f_{PQ} by

$$m_{\text{PQ}} = 6\,\text{eV}\frac{10^6}{f_{\text{PQ}}/1\,\text{GeV}}\,. \tag{4.4}$$

The most stringent constraints on f_{PQ} (or equivalently on m_{PQ}) are set by astrophysical and cosmological considerations: $10^9\,\text{GeV} \leq f_{\text{PQ}} \leq 10^{12}\,\text{GeV}$.

As already stressed, a singlet higher-dimensional axion field could also propagate into the bulk. Also, according to astrophysical and cosmological considerations, the Peccei-Quinn scale f_{PQ} could be much greater than the fundamental scale M_D. To avoid a new hierarchy problem, axions should propagate in the extra dimensions. Then the higher-dimensional scale $\bar{f}_{\text{PQ}}$ can be lowered by the same mechanism as in the case of gravity

$$f^2_{\text{PQ}} \approx M_S^\delta R^\delta \bar{f}^2_{\text{PQ}}\,, \tag{4.5}$$

where M_S is the string scale, $M_S \sim M_D$. As the phenomenologically allowed region for f_{PQ} is such that $f_{\text{PQ}} \ll M_{\text{Pl}}$, the axion must be restricted to a subspace of the full higher-dimensional space ($\delta < n$), if $\bar{f}_{\text{PQ}}$ is to remain in the TeV range [6]. However, $\delta = n$ is possible for $\bar{f}_{\text{PQ}} \ll$ TeV [7].

Upon compactification of δ additional spatial dimensions, the higher-dimensional axion field is expanded into a Kaluza-Klein tower of states.

[2] It is common in theories with extra dimensions to denote the ordinary 4-dimensional axion mass by m_{PQ}. The axion mass m_a, corresponding to the lowest state in the KK axion tower, does not have to be identical to m_{PQ}.

KK excitations have an almost equidistant mass spacing of order $1/R$. The lowest KK state specifies the coupling strength of each KK state to matter. A source of axions, such as the Sun, will emit all KK states up to the kinematic limit, i.e., axions with masses of some keV. Another interesting feature arising from the higher-dimensional axionic theories is that the axion mass may decouple from the Peccei-Quinn energy scale (in 4-dimensional theories $m_{\rm PQ} \sim 1/f_{\rm PQ}$). In such cases, the axion mass is determined by the compactification radius $m_a \simeq 1/2R$ [6]. This will be shown for the simplest case $\delta = 1$.

In order to obtain an effective 4-dimensional theory, one extra spatial dimension has to be compactified, e.g., on a $\mathbf{Z}_2$ orbifold of radius R where the orbifold action is identified as $y \to -y$. This implies that the axion field will have a Kaluza-Klein decomposition of the form

$$a(x^\mu, y) = \sum_{n=0}^{\infty} a_n(x^\mu) \cos\left(\frac{ny}{R}\right), \tag{4.6}$$

where $a_n(x^\mu)$ are the Kaluza-Klein modes. An effective 4-dimensional Lagrangian is then given by

$$\begin{aligned} L_{\rm eff} = L_{\rm QCD} &+ \frac{1}{2}\sum_{n=0}^{\infty}(\partial_\mu a_n)^2 - \frac{1}{2}\sum_{n=1}^{\infty}\frac{n^2}{R^2}a_n^2 \\ &+ \frac{\xi}{f_{\rm PQ}}\frac{g_s^2}{32\pi}\left(\sum_{n=0}^{\infty} r_n a_n\right) G^b_{\mu\nu}\tilde{G}^{b\mu\nu}\,, \end{aligned} \tag{4.7}$$

where

$$r_n \equiv \begin{cases} 1 & \text{if } n = 0, \\ \sqrt{2} & \text{if } n > 0. \end{cases} \tag{4.8}$$

We can see from (4.7) that the gauge fields couple not to an individual axion mode a_k, but rather to the linear superposition

$$a' \equiv \frac{1}{\sqrt{N}}\sum_{n=0}^{n_{\rm max}} r_n a_n = \frac{1}{\sqrt{N}}\left(a_0 + \sqrt{2}\sum_{n=1}^{n_{\rm max}} a_n\right), \tag{4.9}$$

where

$$N \equiv 1 + 2n_{\rm max}\,, \tag{4.10}$$

and $n_{\rm max}$ is a cutoff, determined according to the underlying mass scale M_S. The Kaluza-Klein axion states have a drastic effect on the axion mass matrix, given by

$$M^2 = m_{\rm PQ}^2 \begin{pmatrix} 1 & \sqrt{2} & \sqrt{2} & \sqrt{2} & \dots \\ \sqrt{2} & 2+y^2 & 2 & 2 & \dots \\ \sqrt{2} & 2 & 2+4y^2 & 2 & \dots \\ \sqrt{2} & 2 & 2 & 2+9y^2 & \dots \\ \vdots & \vdots & \vdots & \vdots & \ddots \end{pmatrix}, \tag{4.11}$$

where we have defined

$$y \equiv \frac{1}{m_{\rm PQ} R} \tag{4.12}$$

as the ratio of the scale of the extra dimension to the 4-dimensional axion mass $m_{\rm PQ}$. The usual Peccei-Quinn case corresponds to the upper-left 1×1 matrix, leading to the result $M^2 = m_{\rm PQ}^2$. Thus, the physical effect of the additional rows and columns is to pull the lowest eigenvalue of this matrix away from $m_{\rm PQ}^2$. The eigenvalues λ of the mass matrix are the solutions to the transcendental equation

$$\pi R \lambda \cot(\pi R \lambda) = \frac{\lambda^2}{m_{\rm PQ}^2}. \tag{4.13}$$

The axion linear superposition can be written as

$$a' \equiv \frac{1}{\sqrt{N}} \sum_n r_n a_n = \frac{1}{\sqrt{N}} \sum_\lambda \frac{\lambda^2}{m_{\rm PQ}^2} A_\lambda \hat{a}_\lambda \ , \tag{4.14}$$

where $\hat{a}_\lambda$ are the normalized mass eigenstates, and A_λ are given by

$$A_\lambda \equiv \frac{\sqrt{2}\, m_{\rm PQ}}{\lambda} \left(\frac{\lambda^2}{m_{\rm PQ}^2} + 1 + \frac{\pi^2}{y^2} \right)^{-1/2} . \tag{4.15}$$

The solutions to the transcendental equation (4.13) for the axion zero mode [6] and the first KK excitation [8] are shown in Fig. 4.1. Let us consider the two limiting cases $m_{\rm PQ} R \ll 1$

$$\lambda_0 \approx m_{\rm PQ}$$
$$\lambda_n \approx \frac{n}{R} \quad \text{with} \quad n = 1, 2, 3, \ldots$$

and $m_{\rm PQ} R \gg 1$

$$\lambda_n \approx \frac{2n+1}{2R} \quad \text{with} \quad n = 0, 1, 2, \ldots \ .$$

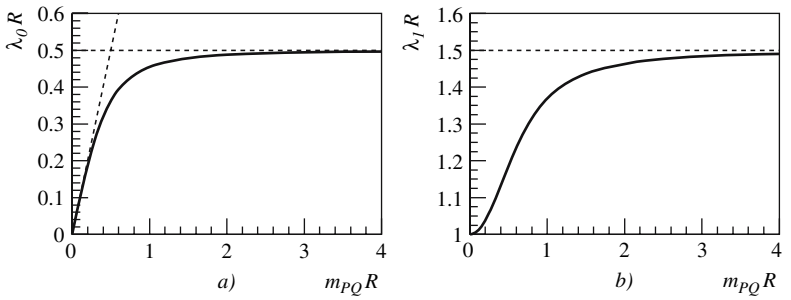

Fig. 4.1. Solutions to the transcendental equation for: (**a**) the axion zero mode; (**b**) the first KK excitation

Two important consequences of (4.13) are:

1. the lightest axion mass eigenvalue is given by

$$m_a \approx \min\left(m_{\rm PQ}, \frac{1}{2R}\right), \text{ and} \tag{4.16}$$

2. the masses of KK excitations are separated by $\approx 1/R$.

From (4.16) we see that for $m_{\rm PQ} \geq \frac{1}{2}R^{-1}$, the Peccei-Quinn scale $f_{\rm PQ}$ decouples from the axion mass. As long as $m_{\rm PQ} \geq \frac{1}{2}R^{-1}$, the axion mass m_a is determined by the radius of the extra space-time dimension, regardless of the specific size of $m_{\rm PQ}$.

4.3 CAST as a Probe of Large Extra Dimensions

4.3.1 CAST Physics

Axions could be produced in the core of the Sun by the Primakoff conversion of thermal photons in the Coulomb fields of nuclei and electrons in the solar plasma. The expected solar axion flux at the Earth has an approximate spectrum [9]

$$\frac{{\rm d}\Phi_a}{{\rm d}E_a} = 4.02\times 10^{10}\left(\frac{g_{a\gamma\gamma}}{10^{-10}\,{\rm GeV}^{-1}}\right)^2 \times \frac{(E_a/{\rm keV})^3}{e^{E_a/1.08\,{\rm keV}}-1}\,{\rm cm}^{-2}\ {\rm s}^{-1}\ {\rm keV}^{-1} \tag{4.17}$$

and an average energy of $\langle E_a\rangle \approx 4.2\,{\rm keV}$. Axions could be back converted into X-rays in laboratory magnetic field [10]. The expected number of X-rays reaching a detector is

$$N_\gamma = \int \frac{{\rm d}\Phi_a}{{\rm d}E_a} P_{a\to\gamma}\, S\, t\, {\rm d}E_a\ , \tag{4.18}$$

where $P_{a\to\gamma}$ is the axion-photon conversion probability, S is the effective area and t is the measurement time. The axion-photon conversion probability in a gas (in vacuum $\Gamma = 0$, $m_\gamma = 0$) is given by the relation

$$P_{a\to\gamma} = \left(\frac{Bg_{a\gamma\gamma}}{2}\right)^2 \frac{1}{q^2+\Gamma^2/4}\left[1+e^{-\Gamma L}-2e^{-\Gamma L/2}\cos(qL)\right]\ , \tag{4.19}$$

where L is the path length, B is the magnetic field and Γ is the inverse absorption length for the X-rays in a gas. The axion-photon momentum transfer q is defined as $q = |(m_\gamma^2 - m^2)/2E_a|$, where m is the axion mass and m_γ is the effective photon mass in a gas (in the case of H_2 and He we have $m_\gamma({\rm eV}) \approx \sqrt{0.02\,P({\rm mbar})/T({\rm K})}$). The coherence condition

$$qL < \pi \Rightarrow \sqrt{m_\gamma^2 - \frac{2\pi E_a}{L}} < m < \sqrt{m_\gamma^2 + \frac{2\pi E_a}{L}} \tag{4.20}$$

restricts the experimental sensitivity to some range of axion masses. For example, the coherence length of $L = 10\,\mathrm{m}$ in vacuum requires $m \leq 0.02\,\mathrm{eV}$ for $E_a = 4.2\,\mathrm{keV}$. For higher axion rest masses, the coherence can be restored for a narrow mass window around $m = m_\gamma$ by the presence of a buffer gas. The CERN Axion Solar Telescope (CAST) experiment [11] is being operated in a scanning mode in which the gas pressure is varied in appropriate steps to cover a range of possible axion masses up to 0.82 eV.

4.3.2 CAST and Large Extra Dimensions

In view of the fact that the CAST experiment is sensitive to axion masses up to $\sim 0.8\,\mathrm{eV}$, it can easily be shown that a possible effect of large extra dimensions can be seen only in the case of $n = 2$ extra dimensions. For the case $n > 2$, the compactification scale $1/R$ becomes greater than the sensitivity region of the CAST experiment and the effect of extra dimensions cannot be observed.

Limits on the Coupling Constant

The total number of X-rays (at the pressure P_i) due to all modes of the KK tower reads for $m_{\mathrm{PQ}}R \ll 1$

$$N_{\gamma i}^{\mathrm{KK}} = \frac{2\pi^{\delta/2}}{\Gamma(\delta/2)} R^\delta \int_0^\infty m^{\delta-1} N_{\gamma i}(m) G(m)\,\mathrm{d}m\,, \tag{4.21}$$

and for the case $m_{\mathrm{PQ}}R \gg 1$

$$N_{\gamma i}^{\mathrm{KK}} = \frac{2\pi^{\delta/2}}{\Gamma(\delta/2)} R^\delta \int_0^\infty m^{\delta-1} N_{\gamma i}(m + 1/2R) G(m + 1/2R)\,\mathrm{d}m\,, \tag{4.22}$$

where $N_{\gamma i}(m)$ is given by

$$N_{\gamma i}(m) = \int \frac{\mathrm{d}\Phi_a(m)}{\mathrm{d}E_a} S t_i P_{a\to\gamma i}(m)\,, \tag{4.23}$$

and the differential axion flux in the case of massive KK axion is given by the relation [7]

$$\frac{\mathrm{d}\Phi_a(m)}{\mathrm{d}E_a} = 4.20 \times 10^{10} \left(\frac{g_{a\gamma\gamma}}{10^{-10}\mathrm{GeV}^{-1}}\right)^2 \times \frac{E_a p^2}{e^{E_a/1.1} - 1}(1 + 0.02m)\ \mathrm{cm}^{-2}\ \mathrm{s}^{-1}\ \mathrm{ke\,V}^{-1}\,. \tag{4.24}$$

The function $G(m)$ is defined as [8]

$$G(m) = \widetilde{m}^4 \left(\widetilde{m}^2 + 1 + \frac{\pi^2}{y^2} \right)^{-2} , \tag{4.25}$$

where $\widetilde{m} \equiv m/m_{\rm PQ}$. The origin of the function $G(m)$ is the mixing between the KK modes entering the KK decomposition of the bulk axion field and the corresponding normalized mass eigenstates. As already shown in (4.7), standard-model fields couple to the linear superposition of KK axion modes. Due to the mixing, this linear superposition rapidly decoheres. Therefore, the subsequent detection of this particular linear combination is strongly suppressed. As a consequence our results reflect a suppressed coupling $g_{a\gamma\gamma} \sim 1/f_{\rm PQ}$. In the absence of the decoherence, photons would be coupled to the linear combination with unsuppressed coupling $1/\bar{f}_{\rm PQ}$.

In order to obtain an upper limit on the coupling constant in the framework of large extra dimensions, we apply the central limit theorem at 3σ level

$$\sum_i N_{\gamma i}^{\rm KK} \leq 3 \sqrt{\sum_i N_{bi}} \, , \tag{4.26}$$

where N_{bi} is the background of the X-ray detector (with numerical values taken from [12]). For the sake of simplicity, it is assumed that all axions have an average energy of 4.2 keV. We take the largest compactification radius of 0.15 mm as set by direct tests of Newton's law. Combining (4.19) with (4.21)–(4.26), we have derived limits on the axion-photon coupling $g_{a\gamma\gamma}$ as a function of the fundamental PQ mass, as shown in Fig. 4.2.

The multiplicity of KK states to which CAST could be sensitive is large ($\sim 10^3$ for $\delta = 1$ and $\sim 10^6$ for $\delta = 2$). Still, one can see from Fig. 4.2 that the upper limit on $g_{a\gamma\gamma}$ is only at most one order of magnitude more stringent than that obtained in conventional theories. This is a result of the fact that CAST is a tuning experiment: for a particular pressure, the coherence condition is satisfied only for a narrow window of axion masses around $m \approx m_{\gamma i}$. Another feature one can observe in Fig. 4.2 is a strong decrease in sensitivity to $g_{a\gamma\gamma}$ for $m_{\rm PQ}R \geq 20$ if $\delta = 2$ and for somewhat lower values if $\delta = 1$. This is a result of the fact that the function $G(m)$ decreases as fast as $1/(m_{\rm PQ}R)^8$ in the regime $m_{\rm PQ}R \gg 1$. In this regime the zero-mode axion mass is determined by the compactification radius, $m_a \approx (1/2)R^{-1} = 6.6 \times 10^{-4}$eV. Contrary to the case of ordinary QCD axions, in theories with large extra dimensions, zero-mode axions with masses outside the favored band arise quite naturally.

Limits on the Compactification Radius

An interesting feature of the CAST experiment is the coherence condition that allows us to detect individual Kaluza-Klein mass states. It is expected

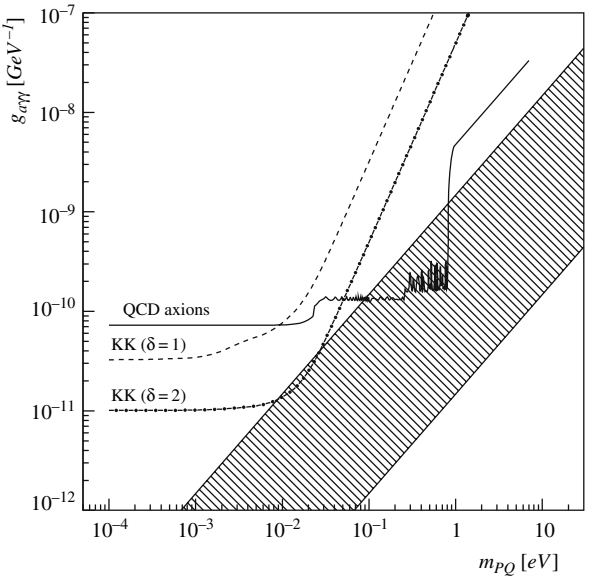

Fig. 4.2. Limits on the axion-photon coupling $g_{a\gamma\gamma}$ as a function of the fundamental PQ mass $m_{\rm PQ}$. The solid line, corresponding to CAST prospects for QCD axions, is obtained using numerical values from [12]. The dashed region represents the theoretically favoured region in axion models in 4 dimensions. The dashed and dot-dashed lines correspond to CAST prospects for KK axions in the case of two extra dimensions ($R = 0.15\,$mm) for $\delta = 1$ and $\delta = 2$, respectively

that more than one axion signal may be observed at different pressures of the gas. Therefore, the detection of the corresponding X-rays at least at two pressures may be the signal for the presence of large extra dimensions. Achievable limits on the compactification radius R depend on the mass of the axion zero mode [8]

1. $m_a = 1/(2R) \;\Rightarrow\; m_1 = 3/(2R) \approx 0.8\,\text{eV} \;\Longrightarrow\; R \approx 370\,\text{nm}$
2. $m_a = m_{\rm PQ} \;\Rightarrow\; m_1 = 1/R \approx 0.8\,\text{eV} \;\Longrightarrow\; R \approx 250\,\text{nm}$

These limits are comparable with the astrophysical limits.

4.4 Conclusion

Theories involving extra dimensions in which gravity propagates offer a possible explanation of the hierarchy problem of particle physics. In addition to gravity, axions too could propagate in the higher-dimensional space. We have explored the potential of the CAST experiment for observing KK axions coming from the solar interior. In theories with two extra dimensions (with $R = 0.15\,$mm), a sensitivity to $g_{a\gamma\gamma}$ improves at most by one order of

magnitude. In addition, the axion mass is decoupled from f_{PQ} and is set by the compactification radius R. We have also demonstrated that the CAST experiment may be sensitive to particular KK axions. Under the requirement to have at least two signals while changing the pressure of the gas, we have found that CAST is capable of probing two large extra dimensions with a compactification radius R down to around 250 nm if $m_{\mathrm{PQ}} < 1/(2R)$ and down to around 370 nm if $m_{\mathrm{PQ}} > 1/(2R)$.

References

1. Antoniadis, I.: A possible new dimension at a few TeV. Phys. Lett. B **246**, 377 (1990) [73]
2. Arkani-Hamed, N., Dimopoulos, S., Dvali, G.: The hierarchy problem and new dimensions at a millimeter. Phys. Lett. B **429**, 263 (1998) [hep-ph/9803315]; Arkani-Hamed, N., Dimopoulos S., Dvali, G.: Phenomenology, astrophysics, and cosmology of theories with submillimeter dimensions and TeV scale quantum gravity. Phys. Rev. D **59**, 086004 (1999) [hep-ph/9807344] [73]
3. Randall, L., Sundrum, R.: Large mass hierarchy from a small extra dimension. Phys. Rev. Lett. **83**, 3370 (1999) [hep-ph/9905221]; Randall, L., Sundrum, R., An alternative to compactification. Phys. Rev. Lett. **83**, 4690 (1999) [hep-ph/9906064] [73]
4. Yao, W.-M., et al. (Particle Data Group): Review of particle physics. J. Phys. G 33, 1 (2006), http://pdg.lbl.gov [74]
5. Peccei, R.D., Quinn, H.R.: CP conservation in the presence of pseudoparticles. Phys. Rev. Lett. **38**, 1440 (1977); Peccei, R.D., Quinn, H.R.: Constraints imposed by CP conservation in the presence of pseudoparticles. Phys. Rev. D **16**, 1791 (1977) [75]
6. Dienes, K.R., Dudas, E., Gherghetta, T.: Invisible axions and large-radius compactifications. Phys. Rev. D 62, 105023 (2000) [hep-ph/9912455] [75, 76, 77]
7. Di Lella, L., Pilaftsis, A., Raffelt G., Zioutas, K.: Search for solar Kaluza-Klein axions in theories of low-scale gravity. Phys. Rev. D **62**, 125011 (2000) [hep-ph/0006327] [75, 79]
8. Horvat, R., Krčmar M., Lakić, B.: CERN axion solar telescope as a probe of large extra dimensions. Phys. Rev. D **69**, 125011 (2004) [astro-ph/0312030] [77, 80, 81]
9. van Bibber, K., McIntyre, P.M., Morris, D.E., Raffelt, G.G.: Design for a practical laboratory detector for solar axions. Phys. Rev. D **39**, 2089 (1989) [78]
10. Sikivie, P.: Experimental tests of the invisible axion. Phys. Rev. Lett. **51**, 1415 (1983); (E) ibid. **52**, 695 (1984) [78]
11. Zioutas K., et al. (CAST Collaboration): First results from the CERN Axion Solar Telescope. Phys. Rev. Lett. **94**, 121301 (2005) [hep-ex/0411033] [79]
12. Zioutas K., et al.: A decommissioned LHC model magnet as an axion telescope. Nucl. Instrum. Methods Phys. Res. A **425**, 480 (1999) [astro-ph/9801176] [80, 81]

5 Axions and Their Relatives

Eduard Massó

Grup de Física Teòrica and Institut de Física d'Altes Energies
Universitat Autònoma de Barcelona, 08193 Bellaterra, Barcelona, Spain
masso@ifae.es

Abstract. A review of the status of axions and axion-like particles is given. Special attention is devoted to the recent results of the PVLAS collaboration, which are in conflict with the CAST data and with the astrophysical constraints. Solutions to the puzzle and the implications for new physics are discussed. The question of axion-like particles being dark matter is also addressed.

5.1 The Axion

In QCD, we can use the gluon field strength G^a to form the operator

$$L_\theta = \bar{\theta}\,\frac{g_s^2}{32\pi^2}\,G_a^{\mu\nu}\tilde{G}_{a\mu\nu}\ , \tag{5.1}$$

that has dimension four and is Lorentz and gauge invariant. We think this operator, named θ-term, should be present in the QCD Lagrangian. In fact, it is thanks to the existence of the term (5.1) that we are able to solve the $U(1)_A$ problem, i.e., why η' is heavy. The introduction of (5.1) in the QCD Lagrangian solves this problem but it introduces a new one: the strong CP problem. The θ-term contributes to some physical observables, e.g., the neutron electric dipole moment d_n. Experimentally, there is a very tight upper limit [1]

$$|\mathrm{d}_n| < 3\times 10^{-26}\, e\,\mathrm{cm}\ , \tag{5.2}$$

which implies the bound

$$\bar{\theta} = |\theta + \arg\det M| \lesssim 10^{-9}\ . \tag{5.3}$$

On the left hand side (LHS) we see the two theoretical contributions to d_n. Apart from the θ-term contribution, there is another related to M, the quark mass matrix. The combination of the LHS is invariant under chiral rotations. On the RHS we see the number coming from the d_n experiments. We do not understand why the combination of the LHS is so tuned that it leads to such a small number. This is the strong CP problem, explained in detail in Chap. 1.

An elegant solution to the strong CP problem was given by Peccei and Quinn [2], based on the hypothesis that there is a new global $U(1)_{\mathrm{PQ}}$ symmetry that is spontaneously broken. How are we going to prove experimentally

E. Massó: *Axions and Their Relatives*, Lect. Notes Phys. **741**, 83–94 (2008)
DOI 10.1007/978-3-540-73518-2_5

that this new symmetry exists? The task indeed seems hard. Fortunately, there is an unavoidable consequence of the Peccei-Quinn solution. The breaking of the $U(1)_{\rm PQ}$ symmetry at an energy scale f_a generates a Goldstone boson, that is called the axion. This fact was realized in [3], where it was noticed that, more correctly, we have a pseudo Goldstone boson, in the sense that the global symmetry has a small explicit breaking due to quantum effects. This means a departure from a completely flat potential for the particle that, in practical terms, endows the axion with a calculable mass

$$m_a = \frac{z^{1/2}}{1+z}\frac{f_\pi m_\pi}{f_a} = 6.3 \text{ eV } \frac{10^6 \,\text{GeV}}{f_a} \,. \tag{5.4}$$

Here we have $z = m_u/m_d$ the up/down quark mass ratio and the pion mass m_π, as well as the pion decay constant $f_\pi = 93\,\text{MeV}$. A consequence of (5.4) is that once we fix the scale f_a, the mass of the axion m_a is no longer a free parameter (and vice versa). The interactions of the axion are model-dependent. We are particularly interested in a coupling that is crucial for the current axion search experiments, namely, the coupling of the axion field a to two photons

$$L_{a\gamma\gamma} = c_\gamma \frac{\alpha}{2\pi\, f_a}\epsilon_{\mu\nu\rho\sigma}F^{\mu\nu}F^{\rho\sigma} = \frac{g_{a\gamma\gamma}}{4}\,F_{\mu\nu}\tilde{F}^{\mu\nu}a = -g_{a\gamma\gamma}\,\mathbf{E}\cdot\mathbf{B}\,a \,, \tag{5.5}$$

where $F_{\mu\nu}$ is the electromagnetic field strength tensor and $\tilde{F}^{\mu\nu}$ its dual, and we have also written the interaction in terms of electric and magnetic fields. The model-dependence is in the parameter c_γ (or equivalently of course in $g_{a\gamma\gamma}$). We can cook up a model with fine-tuned parameters and get a small c_γ, but, in general, c_γ is of order one. For example in the so-called KSVZ axion type or "hadronic axion" [4], where the axion is not coupled to electrons at tree level, we have $c_\gamma = -0.97$. Another example is GUT embedded models like the so-called DFSZ type [5]. For the DFSZ type axion we have $c_\gamma = 0.36$. In summary, we expect $c_\gamma = O(1)$, but we should keep in mind its (weak) model dependence. Other axion interactions are to gluons, which are model-independent, and to matter. All the interactions are inversely proportional to f_a; we can see it explicitly in the $a\gamma\gamma$ case in (5.5), i.e., $g_{a\gamma\gamma} \propto f_a^{-1}$. As we will see, the value of f_a has to be quite large, and a consequence is that the axion is a very weakly interacting particle.

One finds constraints on the axion properties using laboratory experiments as well as using astrophysical and cosmological observations. There are high energy laboratory experiments made in accelerators that lead to $f_a > 10^4\,\text{GeV}$. However, the strongest lower bounds on f_a come from astrophysics. I briefly summarize them here; details can be found in Chap. 3.

Astrophysical limits are based on the idea that a "too" efficient energy drain due to a possible stellar axion emission would change the evolutionary time scale of the star and would be inconsistent with observation. A very stringent limit using these ideas comes from horizontal branch stars in globular clusters. The main source of production is the Primakoff process $\gamma\gamma^* \to a$,

where γ^* corresponds to the electromagnetic field induced by protons and electrons in the stellar plasma. The coupling is restricted to [6]

$$g_{a\gamma\gamma} < 0.6 \times 10^{-10}\,\mathrm{GeV}^{-1} \quad \Rightarrow \quad f_a > 10^7\,\mathrm{GeV}\ . \tag{5.6}$$

However, the most restrictive astrophysical limits come from the analysis of neutrinos from SN 1987A. In the supernova core, the main axion production is by bremsstrahlung in nucleon-nucleon processes. The observed duration of the ν signal constrains the coupling of the axion to nucleons and thus restricts the scale f_a [7]

$$f_a > 6 \times 10^8\,\mathrm{GeV}\ . \tag{5.7}$$

We should point out that when the scale $f_a < 10^5\,\mathrm{GeV}$ the SN constraints are no longer valid because the axions are so strongly coupled to nuclear matter that they are trapped in the SN and do not stream freely from the core. However, for such low values of f_a, the other constraints, like (5.6), are valid. The conclusion is that (5.7) is the lower bound on the Peccei-Quinn scale.

There are also cosmological arguments that put an upper bound to the scale f_a. During the Peccei-Quinn phase transition in the early universe, the axion field is a true Goldstone boson and picks up a vacuum expectation value. In the cooling of the universe the temperatures reach the QCD scale. Then a potential appears that drives the axion field to the CP conserving value. If the axion is too weakly coupled, the oscillation to the true minimum is so slow that the energy of the axion field could be greater than the critical density. This cannot happen of course, and the argument can be used to put an upper bound on f_a. This is the so-called misalignment mechanism for axion production [8]. There are still other mechanisms like axion production from strings, although the studies, that have been done about it, are not consistent among themselves, and there is no clear conclusion about the importance of the axion yield from strings.

5.2 The Axion Relatives

Theories that go beyond the standard model of particle physics have new symmetries, some of them global. Any time one of these global symmetries is spontaneously broken, we get a Goldstone or a pseudo Goldstone boson. An example is family symmetry, which would be related to the number and properties of families (we still do not have an answer to Rabi's question: Who ordered the muon?). The breaking of such a symmetry would give rise to familons. Another example is lepton number symmetry, that would produce majorons. In general, in theories beyond the SU(3)×SU(2)×U(1) standard model, there are quite often light scalar and pseudoscalar particles. We will denote these new hypothetical light particles by ϕ, and refer to them as axion-like particles (ALPs) [9], for both the scalar and pseudoscalar cases. Quite

generally, the new particle ϕ will couple to two photons. In the case that ϕ is a pseudoscalar we have

$$L_{\phi\gamma\gamma} = \frac{1}{8M}\epsilon_{\mu\nu\rho\sigma}F^{\mu\nu}F^{\rho\sigma}\,\phi\,, \tag{5.8}$$

while for a scalar we would have

$$L'_{\phi\gamma\gamma} = \frac{1}{4}g_{\phi\gamma\gamma}F_{\mu\nu}F^{\mu\nu}\,\phi\,. \tag{5.9}$$

For both interaction Lagrangians we have written the coupling as an inverse energy scale M. For a general ALP, there is no relation between mass and couplings, as there is for the axion as we see in (5.4). In analyzing models with an ALP, we will have two independent parameters: the mass m of the light particle and the energy scale M of new physics.

The reason for focusing on the coupling to two photons is that most of the experiments that are searching for axions are based on such a coupling. This means that ALPs might induce a signal in such experiments. Some of the bounds, valid for axions, are valid for an ALP. For example, the bound coming from the analysis of stellar energy losses in horizontal-branch stars of globular clusters is based on the Primakoff production and thus applies. From the upper limit on $g_{a\gamma\gamma}$ shown in (5.6) one gets that

$$M > 10^{10}\,\text{GeV}\,. \tag{5.10}$$

However, there are constraints that cannot be taken without modification. For example, the bound from the SN does not hold in the same way since in the axion model it uses the nucleon-axion coupling. One has to recalculate the SN limit when having only a $\phi\gamma\gamma$ coupling. While in realistic models the ALP usually couples to other particles, to assume that there is only a $\phi\gamma\gamma$ coupling, or that it dominates over other couplings, is a conservative option. The analysis of this scenario has been done in [10], and the conclusion is that the SN bound is looser than the bound given in (5.10). Other constraints on ALPs coupled to photons can be found in [10, 11] and Sect. 9.6.

Reciprocally, there are bounds that have no relevance for the invisible axion model but have their interest for ALPs. Let me mention one example [12]. For very small mass of the ALP, it turns out the emitted ϕ flux could be coherently reconverted to gamma rays in the galactic magnetic field. Measurements on the SN 1987A gamma-ray flux by the gamma-ray spectrometer on the Solar Maximum Mission satellite already imply a bound on the coupling $M > 3\times 10^{11}\,\text{GeV}$, valid for $m < 10^{-9}\,\text{eV}$. It is exciting that the improved generation of satellite-borne detectors, like the project GLAST, would be able to detect a ϕ–γ signal from a nearby supernova, for allowed values of M. Another aspect of interest is the possibility that ALPs could be the dark matter of the universe. We will discuss it in Sect. 5.5. Before finishing the Section, let me remark that another reason to relax the relation (5.4) is that it could be no longer valid even in an axion model where there are contributions to the axion mass from exotic sources [13].

5.3 Searching for ALPs

With the Peccei-Quinn scale f_a pushed towards the high-energy realm, the axion becomes very light and extremely weakly-interacting. The term "invisible axion" was coined, but Sikivie realized that it was not impossible to prove the existence of the axion with feasible experiments [14]. There are several ideas to look for axions, all based on the coherent axion-photon conversion in an external, strong magnetic field. The ideas apply to any light ALP coupled to two photons. Indeed, we can write the pseudoscalar case (5.8) as

$$L_{\phi\gamma\gamma} = g_{\phi\gamma\gamma}\, \mathbf{E}\cdot\mathbf{B}\, \phi\ , \tag{5.11}$$

while for the scalar case (5.9) can be written as

$$L'_{\phi\gamma\gamma} = \frac{1}{2} g_{\phi\gamma\gamma}\, \left(\mathbf{E}^2 - \mathbf{B}^2\right)\, \phi\ . \tag{5.12}$$

Both, (5.11) and (5.12) induce photon-ALP transitions in an external (classical) magnetic field. In (5.11), B plays the role of the external magnetic field, and E describes the photon field that couples to the field ϕ. In (5.12), one of the B is again the external field, while it is now the other B that describes the photon field. The photon-ALP mixing in a magnetic field makes the interaction states $|\phi\rangle$ and $|\gamma\rangle$ different from the propagation states $|\phi'\rangle$ and $|\gamma'\rangle$,

$$|\phi'\rangle = \cos\varphi\, |\phi\rangle - \sin\varphi\, |\gamma\rangle \tag{5.13}$$

$$|\gamma'\rangle = \sin\varphi\, |\phi\rangle + \cos\varphi\, |\gamma\rangle\ . \tag{5.14}$$

The probability P of the ϕ–γ transition always has the suppression factor $1/M^2$. However, the probability P is enhanced when the ϕ–γ conversion in the magnetic field is coherent. A simple way to understand coherence is to describe the photon and the axion as plane waves propagating along a linear path of distance L. The conversion is coherent provided there is overlap of the wave functions across a length L, i.e.,

$$|k_{\gamma'} - k_{\phi'}|\, L < 2\pi\ . \tag{5.15}$$

In the coherent limit, the probability of the conversion is

$$P(\gamma \to \phi) = \frac{1}{4} g^2_{\phi\gamma\gamma}\, B_T^2\, L^2\ . \tag{5.16}$$

Notice that only the transverse magnetic field B_T is effective; this is easily understood from (5.11) and (5.12). We are interested in two methods to search for ALPs that we describe now.

5.3.1 Detection of Solar ALPs

There is a type of experiment, called helioscopy [14], that aims to detect ALPs from the Sun. It is based on the fact that light particles, coupled to photons, would be produced in the interior of the Sun, and subsequently leave it in the form of a continuous flux. From the Earth, we can try to detect this solar flux by looking at ALP back conversion to X-rays in a magnetic field. The reason why the photon is in the X-ray range, is that it carries the typical energies of the photons in the solar interior, namely on the order of keV. There have been several helioscopes working in the last years, but without any doubt CAST has reached an unprecedented level of accuracy. Until now CAST has not observed any signal, and this leads to the bound [15]

$$M > 0.9 \times 10^{10}\,\mathrm{GeV}\ , \tag{5.17}$$

valid for a mass of the light particle $m < 0.02\,\mathrm{eV}$ (see also Chap. 10).

5.3.2 Production and Detection of ALPs in the Laboratory

A helioscope is not precisely a laboratory experiment. Indeed, the assumed source of ALPs is the Sun. There is nothing wrong with this; after all, we are able to detect solar neutrinos that have been produced in the solar interior. But it is desirable to have experiments where the ALP is produced and detected in terrestrial laboratories. An experiment with these characteristics was proposed in [16]. It consists of letting a polarized laser light propagate in a magnetic field. The coupling of the ALP to photons makes the transition $\gamma \to \phi$ possible, with the probability (5.16).

Notice that the absorption is selective. Take the polarization as the direction of the electric field of the laser beam. In the case of a pseudoscalar ϕ, from (5.11) we see that it is the polarization parallel to $\mathbf{B}$ that is absorbed. In the scalar case, (5.12) tells us that it is the polarization perpendicular to $\mathbf{B}$ that decreases. In both cases, the effect is a rotation of the plane of polarization. The selective absorption makes the vacuum dichroic in the presence of a magnetic field.

The PVLAS collaboration has been performing such an experiment [17] (see also Sect. 8.7). They did find a signal of rotation of the plane of the polarization of the laser. Their result can be interpreted in terms of an ALP. It is consistent with a scale

$$M \sim 4 \times 10^{5}\,\mathrm{GeV} \tag{5.18}$$

and with a light particle mass

$$m \sim 10^{-3}\,\mathrm{eV}\ . \tag{5.19}$$

Before discussing this result in the next section in the light of other bounds, I would like to comment on two further related issues. First, there is a second

possible effect when light propagates in a magnetic field, as discussed in [16]. The double virtual conversion $\gamma{-}\phi{-}\gamma$ produces a phase retardation of one of the polarizations. Which polarization is retarded depends on the parity of the particle ϕ. This property manifests as vacuum birefringence, and it seems that there are positive results [18]; we should take them as a preliminary result, but of course confirmation would be most exciting.

A final experiment, I would like to mention, is another (fully contained) laboratory method that could help in clarifying the puzzle we discuss in the next Section. It consists of the remarkable effect of light shining through a wall: in a magnetic field light oscillates into ALPs, these cross a wall, and afterwards they convert back into photons. This type of experiment was already made in [19] with no signal being observed that allowed to put some limits, consistent with (5.18) and (5.19). There are now several proposals for similar experiments that are much more sensitive and that should materialize in one or two years; they are explained in Chap. 10.

5.4 Is it Possible to Evade the Astrophysical Constraints?

We ask this question because the PVLAS results (5.18) and (5.19) strongly contradict the astrophysical limits. So, is there any ALP model where the astrophysical bounds are no longer valid? I will try to convince the reader that the answer to this question is yes. But at the same time I think it is not an easy task. In the literature there are, up to now, only a handful of papers describing models that would be able to evade the astrophysical constraints on ALPs [9, 20, 21]. Hopefully, if the PVLAS results are confirmed, the new physics will be restricted to a few selected models, either one from the list in [9, 20, 21], or a new one. Apart from experiments, more theoretical work along this line is needed!

In this review, I summarize the paraphoton model of [21], where it is assumed that the neutral ϕ particle couples to two photons through a triangle diagram with an internal new fermion f. We require two necessary conditions on the properties of f and the triangle diagram. The new particle f should have a small electric charge on the one hand, as it has to couple to photons, and on the other hand, this charge should decrease very sharply when going from the momentum transfer involved in the PVLAS experiment, $|k^2| \ll \mathrm{O}(\mathrm{keV}^2)$, to the typical momentum transfer in the solar processes, $|k^2| \sim \mathrm{O}(\mathrm{keV}^2)$.

We can meet both conditions in the context of paraphoton models [22, 23] if we introduce a very low energy scale. First, as far as we know, these models are the only ones where the effective electric charge of some particles can naturally be very small. The idea is that particles with a paracharge get an induced electric charge proportional to some small mixing angle ϵ between

photons and paraphotons. To satisfy the second condition, i.e., to get a variation of the effective electric charge with energy, we use a model with two light but massive paraphotons, having the same mixing with the photon. If the fermion f couples to the two paraphotons with opposite paracharge, the resulting effective electric charge for f decreases with energy or temperature T,

$$q_f(T) \approx \frac{\mu^2}{T^2} q_f(0) \ , \tag{5.20}$$

where μ is the mass scale of the paraphoton masses. In (5.20) we have assumed $T \gg \mu$. With the low energy scale $\mu \simeq 10^{-3}$ eV and ϵ such that $q(0)e \simeq 10^{-8}e$, the model is able to accommodate the strength of the PVLAS signal and yet have a very suppressed emission in the Sun. Notice that in this paraphoton model the CAST limit (5.17), which is based on a standard solar ϕ-flux, does not hold. Concerning the nature of ϕ, there are three possibilities:

1. ϕ is a fundamental particle coupled to f,
2. ϕ is an $f\bar{f}$ composite particle, with f and $\bar{f}$ confined by new forces, or
3. ϕ is not really a particle but is positronium-like state. The same way positronium is an e^-e^+ bound state, ϕ is an $f\bar{f}$ bound state.

The PVLAS results have stimulated some new lines of thought. For example, an explanation of the data not in terms of light particles coupled to photons is given in [24] (however, see [25]). Alternatively axion models that could make all observations compatible, are worked out in [26]. Finally, I would like to mention the work in [27], where it is shown that the results from PVLAS and from other related experiments can be used to bound the properties of epsilon-charged particles.

5.5 ALPs as Dark Matter

We have many independent indications of the existence of dark matter (DM): from the local measurements of the galactic rotation curves to the joint fit of the high redshift SN data, X-ray emission of clusters of galaxies and the anisotropies of the Cosmic Microwave Background (CMB). Also, we have several well motivated DM candidates. Only experiments in future will tell us which one is selected, although we should keep in mind that quite possibly there might be several different components contributing to the DM of the universe.

Among the popular candidates for DM we have the axions. With this motivation there are ongoing searches that probe the possible contribution of axions to the galactic DM as described in Chap. 8. In this section I would like to discuss some aspects about the possibility that ALPs might be DM.

A first result is the following. Assume the existence of a light ALP that is coupled *only* to two photons, either (5.8) or (5.9), but *not* to other particles.

In this case, the final result is that the ALP cannot be DM. The reason is that this particle is born thermally. The ALP species was in thermal equilibrium in the early universe thanks to the photon coupling. There is a moment when the expansion rate of the universe is greater than the interaction rate so that the $\phi\gamma\gamma$ coupling is no longer effective to maintain equilibrium. The relic number of ALPs today is less than the number of relic photons today in the CMB. It follows that only when they have masses on the order of the keV, ALPs could, in principle, contribute substantially to the DM. However, with such masses, ALPs are unstable due to the decay $\phi \to \gamma\gamma$. Thus, as we said, the result is negative: an ALP with only a photon coupling cannot be DM.

In fact, leaving apart the DM issue, there are even more restrictions. Consider the region of the parameter space (m, M) that would correspond to a relic density not far from the critical density of the universe if we ignore decays. In the realistic case of decays, the region is excluded by the constraints coming from CMB distortion and He photodissociation [10].

This negative conclusion may be altered in realistic models of ALPs with couplings to matter. In addition, we should take into account the possibility of other mechanisms that generate ALPs in the early universe, as it happens with the axions.

An example of a model with ALPs that are not only coupled to photons and where the ALPs may be DM is presented in [28]. The model describes the effects of a small explicit breaking of a global symmetry, as suggested by gravitational arguments. It has one scalar field transforming under a global U(1) symmetry, and coupled to matter and to gauge bosons. The spontaneous breaking of the explicitly broken symmetry gives rise to a massive pseudo Goldstone boson, i.e, to an ALP. In such a model, one analyzes thermal and non-thermal production of ALPs in the early universe, and performs a systematic study of astrophysical and cosmological constraints on the ALP properties. The conclusion is that for very suppressed explicit breaking the pseudo Goldstone boson is a cold DM candidate [28]. Such a suppression is not unexpected according to some analyses of gravitational symmetry breaking [29].

5.6 Conclusion

The experimental search for light particles coupled to photons, that we call axion-like particles (ALPs), is reaching an unprecedented level of sensitivity. There are already some results (from the PVLAS collaboration) that may be interpreted in terms of ALPs. If confirmed, we have to search for models that make compatible their apparent inconsistency with the sound astrophysical bounds and with other results, for example from the CAST collaboration. We have examined these issues. Also, we have reviewed the possibility that ALPs may contribute to the dark matter present in our universe.

Acknowledgments

I thank B. Beltrán, M. Kuster, T. Papaevengelou, and K. Zioutas for the successful axion meeting they organized at CERN. Also, thanks goes to my colleagues J. Redondo, A. Ringwald, J. Jaeckel, and F. Takahashi for many discussions that have helped me in writing this chapter. Finally, I acknowledge support by the CICYT Research Project FPA2005-05904 and the Departament d'Universitats, Recerca i Societat de la Informació (DURSI), Project 2005SGR00916.

References

1. Baker, C.A., et al.: An improved experimental limit on the electric dipole moment of the neutron. Phys. Rev. Lett. **97**, 131801 (2006) [hep-ex/0602020] 83
2. Peccei, R.D., Quinn, H.R.: CP conservation in the presence of instantons. Phys. Rev. Lett. **38**, 1440 (1977);
   Constraints imposed by CP conservation in the presence of instantons. Phys. Rev. D **16**, 1791 (1977) 83
3. Weinberg, S.: A new light boson?. Phys. Rev. Lett. **40**, 223 (1978);
   Wilczek, F.: Problem of strong P and T invariance in the presence of instantons. Phys. Rev. Lett. **40**, 279 (1978) 84
4. Kim, J.E.: Weak interaction singlet and strong CP invariance. Phys. Rev. Lett. **43**, 103 (1979);
   Shifman, M.A., Vainshtein, A.I., Zakharov, V.I.: Can confinement ensure natural CP invariance of strong interactions?. Nucl. Phys. B **166**, 493 (1980) 84
5. Dine, M., Fischler, W., Srednicki, M.: A simple solution to the strong CP problem with a harmless axion. Phys. Lett. B **104**, 199 (1981);
   Zhitnitsky, A.R.: On possible suppression of the axion hadron interactions. Sov. J. Nucl. Phys. **31**, 260 (1980) [Yad. Fiz. **31**, 497 (1980)] 84
6. Raffelt, G.G.: Stars as Laboratories for Fundamental Physics. Chicago University Press, Chicago (1996) 85
7. Ellis, J.R., Olive, K.A.: Constraints on light particles from supernova 1987A. Phys. Lett. B **193**, 525 (1987);
   Raffelt G., Seckel, D.: Bounds on exotic particle interactions from SN 1987A. Phys. Rev. Lett. **60**, 1793 (1988);
   Turner, M.S.: Axions from SN 1987A. Phys. Rev. Lett. **60**, 1797 (1988) 85
8. Preskill, J., Wise, M.B., Wilczek, F.: Cosmology of the invisible axion. Phys. Lett. B **120**, 127 (1983);
   Abbott, L.F., Sikivie, P.: A cosmological bound on the invisible axion. Phys. Lett. B **120**, 133 (1983);
   Dine, M., Fischler, W.: The not-so-harmless axion. Phys. Lett. B **120**, 137 (1983);
   Turner, M.S.: Cosmic and local mass density of 'invisible' axions. Phys. Rev. D **33**, 889 (1986) 85
9. Jaeckel, J., Massó, E., Redondo, J., Ringwald, A., Takahashi, F.: The need for purely laboratory-based axion-like particle searches. Phys. Rev. D 75, 013004 (2007) [hep-ph/0610203] 85

10. Masso, E., Toldrá, R.: On a light spinless particle coupled to photons. Phys. Rev. D **52**, 1755 (1995) [hep-ph/9503293];
New constraints on a light spinless particle coupled to photons. Phys. Rev. D **55**, 7967 (1997) [hep-ph/9702275] 86, 91
11. Kleban, M., Rabadán, R.: Collider bounds on pseudoscalars coupling to gauge bosons. [hep-ph/0510183] 86
12. Grifols, J.A., Masso, E., Toldra, R.: Gamma rays from SN1987A due to pseudoscalar conversion. Phys. Rev. Lett. **77**, 2372 (1996) [astro-ph/9606028];
Brockway, J.W., Carlson, E.D., Raffelt, G.G.: SN 1987A gamma-ray limits on the conversion of pseudoscalars. Phys. Lett. B **383**, 439 (1996) [astro-ph/9605197] 86
13. Holman, R., Hsu, S.D.H., Kephart, T.W., Kolb, E.W., Watkins, R., Widrow, L.M.: Solutions to the strong CP problem in a world with gravity. Phys. Lett. B **282**, 132 (1992) [hep-ph/9203206];
Kamionkowski, M., March-Russell, J.: Planck scale physics and the Peccei-Quinn mechanism. Phys. Lett. B **282**, 137 (1992) [hep-th/9202003];
Barr, S.M., Seckel, D.: Planck scale corrections to axion models. Phys. Rev. D **46**, 539 (1992) 86
14. Sikivie, P.: Experimental tests of the invisible axion. Phys. Rev. Lett. **51**, 1415 (1983); (E) ibid. **52**, 695 (1984) 87, 88
15. Zioutas, K., et al. (CAST Collaboration): First results from the CERN axion solar telescope (CAST). Phys. Rev. Lett. **94**, 121301 (2005) [hep-ex/0411033] 88
16. Maiani, L., Petronzio, R., Zavattini, E.: Effects of nearly massless, spin zero particles on light propagation in a magnetic field. Phys. Lett. B **175**, 359 (1986) 88, 89
17. Zavattini, E., et al. (PVLAS Collaboration): Experimental observation of optical rotation generated in vacuum by a magnetic field. Phys. Rev. Lett. **96**, 110406 (2006) [hep-ex/0507107] 88
18. Cantatore, G., Gastaldi, U.: private communication 89
19. Cameron, R., et al.: Search for nearly massless, weakly coupled particles by optical techniques. Phys. Rev. D **47**, 3707 (1993) 89
20. Masso, E., Redondo, J.: Evading astrophysical constraints on axion-like particles, JCAP 0509, 015 (2005) [hep-ph/0504202];
Jain, P., Mandal, S.: Evading the astrophysical limits on light pseudoscalars, [astro-ph/0512155]
21. Masso, E., Redondo, J.: Compatibility of CAST search with axion-like interpretation of PVLAS results Phys. Rev. Lett. 97, 151802 (2006) [hep-ph/0606163] 89
22. Okun, L.B.: Limits of electrodynamics: paraphotons?. sov. Phys. JETP **56**, 502 (1982) [Zh. Eksp. Teor. Fiz. **83**, 892 (1982)] 89
23. Holdom, B.: Two U(1)'s and epsilon charge shifts. Phys. Lett. B **166**, 196 (1986);
Searching for epsilon charges and a new U(1). Phys. Lett. B **178**, 65 (1986) 89
24. Mendonça, J.T., Dias de Deus, J., Castelo Ferreira, P.: Higher harmonics in non-linear vacuum from QED effects without low mass intermediate particles. Phys. Rev. Lett. **97**, 100403 (2006) [hep-ph/0606099]; (E) ibid. 97, 269901 (2006) 90
25. Adler, S.L.: Vacuum birefringence in a rotating magnetic field. J. Phys. A **40**, F143 (2007) [hep-ph/0611267] 90

26. Antoniadis, I., Boyarsky, A., Ruchayskiy, O.: Axion alternatives. [hep-ph/0606306] 90
27. Gies, H., Jaeckel, J., Ringwald, A.: Polarized light propagating in a magnetic field as a probe of millicharged fermions. Phys. Rev. Lett. 97, 140402 (2006). [hep-ph/0607118] 90
28. Masso, E., Rota, F., Zsembinszki, G.: Planck-scale effects on global symmetries: Cosmology of pseudo-Goldstone bosons. Phys. Rev. D **70**, 115009 (2004) [hep-ph/0404289] 91
29. Kallosh, R., Linde, A.D., Linde, D.A. Susskind, L.: Gravity and global symmetries. Phys. Rev. D **52**, 912 (1995) [hep-th/9502069] 91

Part II

Observations and Experiments

6 Magnetic and Electric Dipole Moments in Storage Rings

Yannis K. Semertzidis

Physics Department, Brookhaven National Laboratory, Upton,
NY 11973-5000, USA
yannis@bnl.gov

Abstract. Electric and magnetic dipole moments of fundamental particles had a large influence in shaping the standard model in the past and continue to play a significant role at present by restricting the many possible expansions of the standard model. In this chapter I describe, in particular, the present status and prospects of the dipole moments in storage rings experiments, in the context of other significant electric and magnetic dipole moment efforts.

6.1 Dipole Moment Experiments in Storage Rings

It was recognized early that studying the muon anomalous magnetic moment in a storage ring would be a powerful tool for testing the standard model (SM). Every new model had to confront the limits imposed by the apparent agreement of the theory based on the SM and the experimental value of the muon g–2 (Due to quantum field fluctuations the muon spin in a storage ring precesses a little faster than the momentum vector. This difference can be estimated theoretically using all the current knowledge from the SM which can be compared to the experimental results). This approach to physics (precision physics) has not run its natural course. The theory is known well enough that a further improvement of a factor of two in the experimental uncertainty would still be beneficial and would play an important role in our quest for uncovering any new physics. I am going to describe the current state of the experimental approach and the theoretical situation regarding this very beautiful experiment.

The current disagreement between theory and experiment is estimated to be 3.4 times the stated combined uncertainties. Even though this fact is very exciting in its own right it is not the main reason, in my opinion, to support the completion of this experiment. The main reason includes the following three points:

1. The muon g–2 experiment is sensitive to physics at the 100 GeV scale as the W and Z contributions testify to it. This scale is the energy frontier and needs to be fully exploited. Certain speculative models, like e.g. supersymmetry (SUSY), might have even larger contribution enhanced by the $\tan\beta$ parameter (the ratio of the expectation values of the two Higgs doublets) which could take a value up to 50.

Y. K. Semertzidis: *Magnetic and Electric Dipole Moments in Storage Rings*, Lect. Notes Phys. **741**, 97–113 (2008)
DOI 10.1007/978-3-540-73518-2_6

2. The experimental value of the muon g–2 is statistics-limited.
3. The theoretical error in the estimation of the g–2 is smaller than the experimental uncertainty. The main uncertainty in the theory comes from the use of experimental data in e^+e^- colliders and it is highly likely that this error will be further reduced by at least a factor of two (to 0.25 ppm from the present 0.5 ppm) in the near term.

On the other hand, another approach to precision physics that had even more impact on restraining beyond the SM models (BSMM) is the study of the electric dipole moments (EDMs) of fundamental particles. Even though the magnetic dipole moments (MDMs) are allowed by all the relevant symmetries the same is not true for the EDMs. The presence of an EDM in a fundamental particle with spin would require both parity (P) and time (T) reversal symmetry violation. Assuming CPT (with C meaning the charge symmetry) invariance, it would mean that CP symmetry is also violated. The last point is very important as the matter-antimatter asymmetry mystery of our universe requires CP-violation almost 10 orders of magnitude larger than that available from the SM in order to be accommodated. Physics beyond the SM could be the solution to this puzzle and the EDM experiments are one of the best probes for such a scenario.

EDM experiments in storage rings so far have been performed only parasitically [1] and only as a secondary byproduct of another main effort. Our collaboration (see http://www.bnl.gov./edm) made the first extensive study for a dedicated EDM experiment in storage rings. In this paper I will describe the various methods we have seriously considered [2, 3] in proposing to work with before we arrived at the latest resonance EDM method suggested by Yuri Orlov [4].

The sensitivity for new physics of the deuteron EDM at the $10^{-29}\,e\,\mathrm{cm}$ level is at the unprecedented $\sim$1000 TeV energy scale assuming that the CP-violating phase is of the order of 1. If new physics does exist at the LHC energy scale, the sensitivity to the CP-violating phase is at the 10^{-5} rad level, which is also much beyond the LHC planned sensitivity. Both of the above approaches are complementary to the spectrometer experiments at the energy frontier colliders, like LHC (under construction) and ILC (under consideration), and can provide important information at the science frontier.

The muon g–2 concept has been under development for several years now and is ready to go as soon as the funding appears. On the other hand, the deuteron EDM in storage rings is still being optimized and its natural time scales are three years for the muon g–2 and five years for the deuteron EDM experiment.

6.2 Muon g–2

A particle with charge e and mass m moving in a circular path has both an angular momentum $L = mvr$ and a magnetic dipole moment $\mu = IA$, and with a little algebra one can get

$$\boldsymbol{\mu} = \frac{e}{2m}\mathbf{L} \,. \tag{6.1}$$

In quantum mechanics (QM) μ is given by

$$\boldsymbol{\mu} = g\frac{e}{2m}\mathbf{s} \,. \tag{6.2}$$

For a Dirac point-like, spin 1/2 particle, $g = 2$. The definition of the g-factor is

$$g \equiv \left(\frac{\text{magnetic moment}}{e\hbar/2m}\right)\left(\frac{\text{angular momentum}}{\hbar}\right)^{-1} \,. \tag{6.3}$$

The measure of the difference between the mass and charge distributions is g–2; it equals zero when the two distributions are the same all the time.

The state of vacuum in classical physics is empty, but this is not the case in QM. Every possible state comes in and out of existence, violating energy conservation within a time scale allowed by the uncertainty principle. Thus e^+e^-, $\mu^+\mu^-$, photons, hadrons, etc. come in and out of existence with the heavier particles appearing for shorter time than the lighter ones. The same way as in vacuum, real particles continuously create back and forth combinations of virtual particles. Those virtual particles surround the real particle like a "soup" interacting with them. The muons are heavier than the electrons creating an even thicker "soup" of virtual particles than the electrons and interacting with it. It is those interactions, which involve all known forces (save gravity), that the theory can estimate accurately enough so that when compared with the experimental value, one can test the validity of the theoretical estimation. Measuring the g–2 value of a particle is a very sensitive probe of the virtual contributions, and the factor

$$a = \frac{g - -2}{2} \tag{6.4}$$

is called the anomalous magnetic moment. The QM contributions to the anomalous magnetic moment are small, so when the proton ($g_p = +5.586$) and neutron ($g_n = -3.826$) values were measured it became apparent that they are composite particles. The ratio $g_p/g_n = -1.46$, which is close to the predicted $-3/2$, was the first success of the constituent quark model.

Another example is the g_e-2 of the electron, which is sensitive (as far as the experiment concerns) to quantum field fluctuations involving only quantum electrodynamics (QED). The muon g_μ-2 is sensitive to heavier particles compared to the electron, in most cases, by a factor of $(m_\mu/m_e)^2 \approx 40000$. Thus, even though the electron g–2 is known [5] with much higher accuracy than the muon g–2, the muon g–2 is much more sensitive to contributions at the energy frontier than the electron.

6.2.1 Theory of Muon g–2

The theory of muon g–2 is the subject of intense study and is presented in numerous recent publications [6]. In this chapter we will concentrate only on the main elements of it. The theoretical value of the anomalous magnetic moment is the sum of the contributions including QED, strong, and weak interactions, plus any new physics contribution that might be important:

$$a_\mu(\text{theo}) = a_\mu(\text{QED}) + a_\mu(\text{strong}) + a_\mu(\text{weak}) + a_\mu(\text{new physics}) \ , \quad (6.5)$$

with some representative contributions shown in Fig. 6.1. The estimated contributions from QED and weak interactions are

$$a_\mu(\text{QED}) = (116\,584\,719.90 \pm 1.15 \pm 0.08 \pm 0.04) \times 10^{-11}$$

and

$$a_\mu(\text{weak}) = (154 \pm 2 \pm 1) \times 10^{-11} \ ,$$

respectively. The estimations of the QED and weak interactions, even though involved, are based on purely theoretical arguments, and the total error compared to the experimental error is small. The strong interactions' contribution is much harder to estimate based solely on theoretical arguments and the error would be much larger. The graphs in question include the hadronic vacuum polarization, i.e., a muon emits a virtual photon which in turn converts to a virtual hadron-antihadron pair. This Feynman graph cannot be calculated accurately enough from perturbative quantum chromodynamics (pQCD) alone because it invloves low-energy scales. However, as it turns out, experimental data come to the rescue. Through the dispersion relation the real cross section is fundamentally related to the virtual contribution of the hadronic vacuum polarization, as shown in Fig. 6.2. The ratio of cross sections R is measured using e^+e^- collisions as

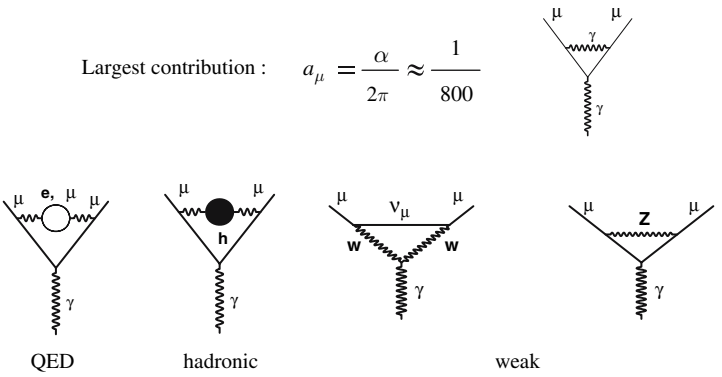

Fig. 6.1. The largest contributions to a_μ from QED, strong, and weak interactions

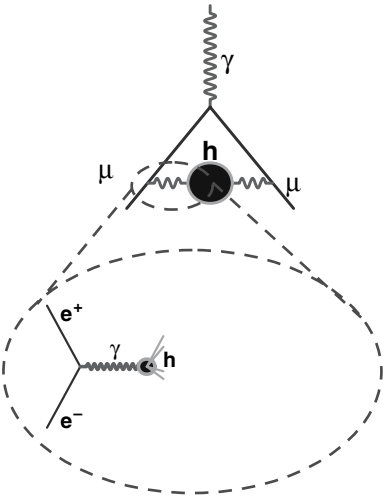

Fig. 6.2. Experimental data involving e^+e^- are used to estimate the hadronic vacuum polarization contribution. The virtual photon between the two muon lines is converted to a hadron-antihadron pair, which, when cut in half, looks like the real cross section of e^+e^- collisions going to hadrons. The two rates are fundamentaly connected via the dispersion relation. The low energy is dominating the contribution to the anomalous magnetic moment

$$R = \frac{\sigma(e^+e^- \to \text{hadrons})}{\sigma(e^+e^- \to \mu^+\mu^-)} \,, \tag{6.6}$$

which is used as input in the estimation of the hadronic contribution to the anomalous magnetic moment of the muon

$$a_\mu(\text{had}, 1) = \left(\frac{am_\mu}{3\pi}\right)^2 \int_{4m_\pi^2}^{\infty} \frac{\mathrm{d}s}{s^2} K(s)R(s) \,, \tag{6.7}$$

with s being the square of the center of mass energy, and $K(s)$ a weight function emphasizing the low energies. The hadronic vacuum polarization contribution is at the 60 ppm level, and therefore, the e^+e^- cross section to hadrons need to be estimated with better than 1% absolute accuracy, which is a daunting task. Many different collaborations have worked for several years on this subject and now seem to be making great progress toward not only achieving this goal but with the prospect of improving it further by another factor of two or so in the near term. Figure 6.3 shows some data from Cryogenic Magnetic Detector-2 (CMD-2), from the Novosibirsk e^+e^- collider. The total theoretical value of the anomalous magnetic moment based on the SM is [6]

$$a_\mu(\text{SM}) = 116\,591\,831\,(82) \times 10^{-11} \,. \tag{6.8}$$

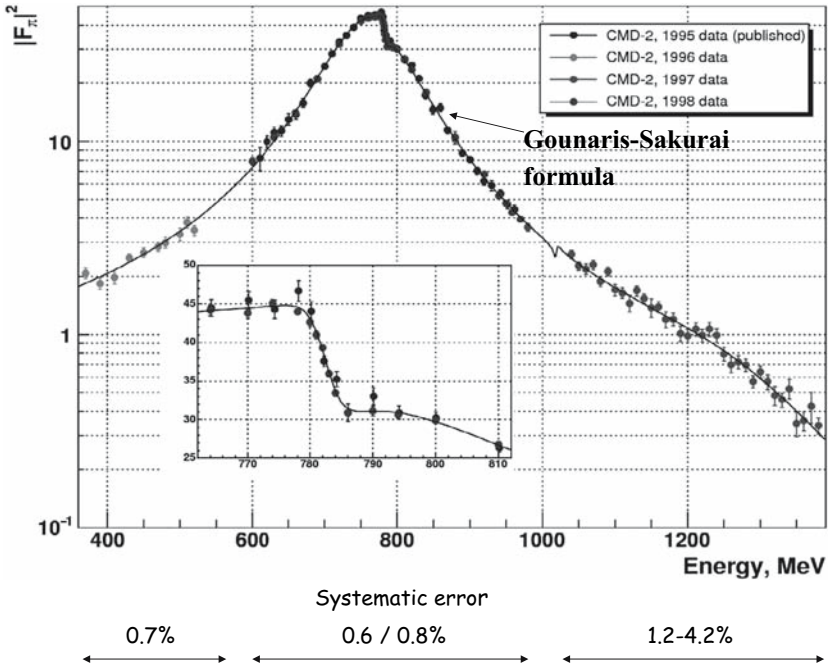

Fig. 6.3. Experimental data from CMD-2 involving e^+e^- together with the fit to the Gounaris-Sakurai formula

6.2.2 The Muon g–2 Experiment

The principle of the muon g–2 experiment is based on the following three points

1. Polarize: using the parity-violating weak decay of pions to a muon and a muon anti-neutrino, one can collect muons of a specific handedness ($\pi^+ \rightarrow \mu^+ + \nu_\mu$). Using 1% of momentum range, we can collect the forward going muons resulting in a muon polarization of over 90%.
2. Interact: precess the horizontally polarized muons in a uniform magnetic field. The muon magnetic moment causes the particles to precess in a magnetic field, very much like a spinning top precessing in the presence of a gravitational field. The spin does not just align itself with the external force because it needs to conserve angular momentum. The spin precession rate is given by $\mathrm{d}\mathbf{s}/\mathrm{d}t = \boldsymbol{\mu} \times \mathbf{B}$, which describes a spin precession in the horizontal plane in the presence of a vertical magnetic field.
3. Analyze: using the parity-violating weak muon decay to an electron and two neutrinos, one can determine the muon spin direction ($\mu^+ \rightarrow e^+ + \bar{\nu}_\mu + \nu_e$). In the muon rest-frame the higher energy positrons are emitted along the muon spin direction. In the lab-frame the highest positron energies are (on average) emitted when the muon spin and the muon mo-

mentum are aligned parallel. The lowest energy electrons, on the other hand, result when the muon spin is anti-parallel to the muon momentum. By measuring the energy and time of the decay positron, we can determine the spin angle *relative* to the muon momentum, i.e., the muon g–2 precession frequency.

The g–2 frequency is given by (when $\beta \cdot E = \beta \cdot B = 0$)

$$\omega_a = \frac{e}{m}\left[aB + \left(a_\mu - \frac{1}{\gamma^2 - 1}\right)\frac{\beta \times E}{c}\right] , \tag{6.9}$$

which for $\gamma = 29.3$ reduces to

$$\omega_a = a\frac{e}{m}B , \tag{6.10}$$

i.e., at the muon energy of 3.1 GeV the electric field does not contribute to the g–2 frequency as at that energy it contributes equally to the spin and momentum vector precessions.

The last muon g–2 experiment took place at Brookhaven National Laboratory using high intensity 24 GeV protons from the alternating gradient synchrotron (AGS). The protons hit an Ni target producing hadrons (mostly pions) which were then directed to a decay channel where the (almost) forward going decay muons were collected and then injected into the muon storage ring, as shown in Fig. 6.4. The momentum acceptance of the muon ring at 3 GeV c^{-1} is $\approx$ 0.6%. Several billion decay positrons (running with μ^+) and electrons (running with μ^-) have been collected. The time spectrum of

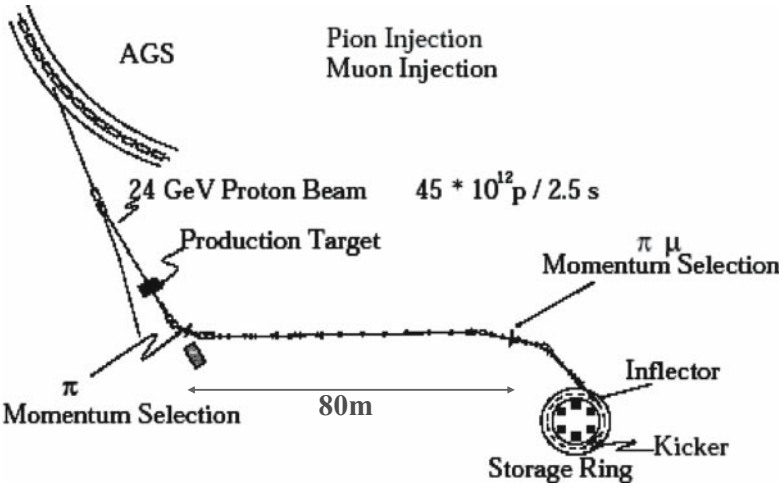

Fig. 6.4. The muon g–2 beam-line at the exit of the AGS ring and before the muon g–2 storage ring

$$dN/dt = N_0 e^{-\frac{t}{\tau}} [1 + A \cos(\omega_a t + \phi_a)]$$

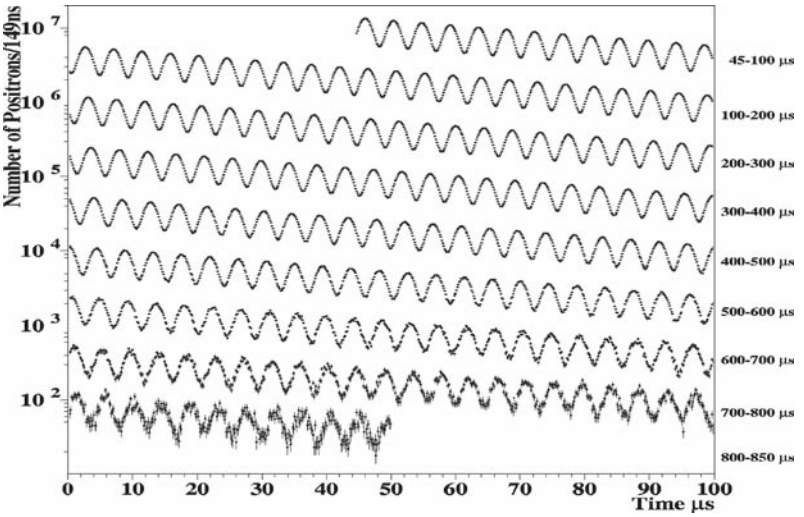

Fig. 6.5. The time spectrum of four Billion detected positrons with energy greater than 2 GeV is shown along with the main function used to fit the same data

some of the positrons collected is shown in Fig. 6.5. The experimental value of the anomalous magnetic moment is

$$a_\mu(\text{exp}) = 116\,592\,080\,(63) \times 10^{-11}\,, \tag{6.11}$$

which includes the ±0.46 ppm statistical error and ±0.28 ppm systematic error (combined in quadrature). This is different from the most recent theoretical value given by (6.8) which is 3.3 times the stated uncertainty.

The Muon g–2 Experiment Upgrade Towards 0.25 ppm

With the realistic prospects of reducing the theoretical error by a factor of two and in view of the tantalizing difference present between theory and experiment, the muon g–2 collaboration has decided to put together a proposal towards reducing the total experimental error by a factor of two. Should the central theoretical and experimental values remain as present, the difference could go to 6–7 standard deviations. The main approach to achieve the experimental error reduction is to

1. Increase the number of stored muons by about a factor of five by making several improvements in both the muon collection channel and improving the injection efficiency into the g–2 ring.

2. Segment the calorimeter detectors to reduce positron overlap and the systematic errors associated with it.
3. Reduce all the systematic errors in both the precession frequency and the knowledge of the magnetic field, based on our previous experience.

The collaboration is confident that such an experiment would be both timely and successful. The BNL program advisory committee (PAC) was of the same opinion and the national high energy physics (HEP) committee (known in short as P5), in charge of listing the physics priorities of the field, has included this experiment in its short list. The committee has decided that in the present funding profile, it is better to wait until 2010 and then decide what to do depending on the physics outcome of the LHC. Even though the muon g–2 collaboration is disappointed by the recommendation to wait, they are delighted by the recognition of the physics potential of the experiment and are seeking alternative solutions to the stalemate.

6.3 Electric Dipole Moments

If a particle with spin should have an EDM, it would have to be proportional to the spin vector as it is the only vector that defines the particle. Then the interaction energy of the EDM in an electric field region would be transformed by the time (T) and parity (P) symmetries in incompatible ways

$$\begin{aligned} H = -\mathrm{d}\boldsymbol{\sigma}\cdot\mathbf{E} &\xrightarrow{T} H = -\mathrm{d}(-\boldsymbol{\sigma})\cdot\mathbf{E} = \mathrm{d}\boldsymbol{\sigma}\cdot\mathbf{E} \\ H = -\mathrm{d}\boldsymbol{\sigma}\cdot\mathbf{E} &\xrightarrow{P} H = -\mathrm{d}\boldsymbol{\sigma}\cdot(-\mathbf{E}) = \mathrm{d}\boldsymbol{\sigma}\cdot\mathbf{E}\,, \end{aligned} \tag{6.12}$$

which can only be true if either d is zero or both P and T symmetries are violated.

Induced EDMs are allowed as they are proportional to the electric field and the interaction energy is proportional to the square of the electric field and hence conserves the above symmetries. EDMs unrelated to a specific spin direction are also allowed (e.g., batteries) and do not contradict the main conclusion stated above.

The violation of T-symmetry also means (assuming CPT conservation) that CP-violation is also present. If EDMs were to be found in the next round of experiments it would provide a new large CP-violation source, much larger than that provided by the SM. This ties up with an interesting observation: the matter–anti-matter imbalance in our universe requires much stronger CP-violation than the SM is able to offer. On top of it many BSMM, like SUSY, contain many CP-violating phases with the current limits set by the EDM experimental limits. Other BSMM include multi-Higgs, Left-Right symmetric, etc. For a recent review on the theory of the EDMs of fundamental particles and their physics reach refer to [7]. Similar to the magnetic dipole moments, the electric dipole moment experimental efforts are based on the following principles:

1. Polarize: A well defined highly polarized state needs to be prepared in high intensity. High intensity (10^{11}–10^{12} deuterons per cycle), with high polarization (80–90%), deuteron beams at the momentum range of $1 - 1.5\,\mathrm{GeV\,c^{-1}}$ are readily available. This technology has been under development for several decades now.
2. Interact: precess the horizontally polarized deuterons in an electric field. The spin precession rate is given by $\mathrm{d}\mathbf{s}/\mathrm{d}t = \mathbf{d} \times \mathbf{E}$, which describes a precession in the vertical plane in the presence of a horizontal electric field.
3. Analyze: Using spin-dependent elastic hadronic cross section, one can deduce the deuteron spin direction as a function of time. In one of the considered schemes the deuterons are allowed to scatter off a carbon target, which serves as the limiting aperture [8], in a controlled way as a function of time. Any vertical polarization shows up as a left-right asymmetry in the detection rate, and any horizontal polarization, as an up–down asymmetry. An EDM signal would be a change in the left-right asymmetry as a function of time.

Early on, it was recognized that placing a charged particle in an electric field would not be the way to a very sensitive experiment as the particle would move under the influence of the electric field and would get lost in the walls of the experimental aperture within a very short time. On the other hand, if a neutral atom is used, the argument went, the total electric field acting on the electron would still be zero as the particle feels no force (it would otherwise move if there was a force acting on it). It was this argument that led the first experimental effort to be focused on the neutron [9]. The obtained limits are very impressive with the latest results [10] giving a limit of $\mathrm{d}_n \leq 3 \times 10^{-26}\,e\,\mathrm{cm}$. This is indeed an impressive limit, corresponding to the Earth's surface being smooth and symmetric to 0.5 μm [11].

In the 1960s it was made clear (first by Schiff himself, even though the Schiff theorem is a misnomer and wrongly reflects that an EDM of a charged particle cannot be measured) [12] that in the presence of forces other than electric, the particle can still be at equilibrium, but the total electric field may not be zero. In fact, in some cases (like in paramagnetic atoms) there might be an enhancement [13] of the total EDM effect by large factors (in case of the ^{205}Tl atom the enhancement factor is estimated to be ~ -585). The ^{199}Hg atom, even though is diamagnetic and does not benefit from an enhancement factor (it actually suffers from a large reduction factor), turns out to be a good system to work with. The limit obtained, which is impressive numerically on its face value, is competitive in its physics reach with the best EDM limits in spite of the large reduction factor due to the coulomb shielding of the nucleus by the atomic electrons. Table 6.1 shows the current status of the experimental limits on the EDMs. Recently major efforts have been launched for studying molecular systems with potentially much larger enhancement factors. The main issue there is to create a well-defined initial

Table 6.1. Current experimental limits on electric dipole moments

Particle	System studied	Limit ($e$cm)
Electron	^{205}Tl atom ($\sim 10^{-24}$) [14]	1.5×10^{-27}
Mercury	^{199}Hg atom [15]	2×10^{-28}
Neutron	Ultra-cold neutrons [10]	3×10^{-26}
Proton	^{199}Hg atom	5×10^{-24}

state with high efficiency so that the statistical accuracy would be adequate. There are three major new initiatives on the neutron EDM front:

1. At PSI, with a goal of $10^{-27}\,e\,$cm. This essentially uses the "old" apparatus of the last neutron EDM experiment [10], with significant improvements. It includes a higher intensity neutron spallation source using the 1 MW proton beam power available at PSI. They expect to start collecting data in 2008.
2. At Grenoble, where the last neutron EDM experimental apparatus [10] is being upgraded. The new experiment is using an ultra cold neutron (UCN) source, SQUIDS as sensors of the magnetic field, higher electric field values, etc. among some of the improvements. The sensitivity goal is $2 \times 10^{-28}\,e\,$cm per year, starting data collection in 2009.
3. At spallation neutron source (SNS) at Oak Ridge National Laboratory in the USA. The goal is $10^{-28}\,e\,$cm using polarized UCN stored in a ^{4}He bath together with polarized ^{3}He. The ^{3}He plays the role of the neutron spin analyzer through the interaction

$$^3\bar{\mathrm{H}}\mathrm{e} + \bar{\mathrm{n}} \rightarrow \mathrm{t} + \mathrm{p}\ , \tag{6.13}$$

where the cross section of the interaction greatly depends on the relative direction of the ^{3}He and the neutron spins. When their spins are opposite, the cross section of the interaction is $\sim 10^4$ barns, whereas when they are parallel, is $< 10^2$ barns providing an excellent contrast.

6.3.1 Hadronic EDMs

QCD CP-violating Parameter θ

The QCD Lagrangian includes a term, which violates

$$L_\theta = \theta \frac{g_\mathrm{s}^2}{32\pi^2} G_a^{\mu\nu} \tilde{G}_{a\mu\nu}\ , \tag{6.14}$$

with the gluon field-strength tensor G and its dual $\tilde{G}$. This term induces a neutron (hadronic) EDM that, using dimensional analysis, is given by

$$\mathrm{d}_n \simeq \theta \frac{e\, m^*}{\Lambda_{\mathrm{QCD}} m_n} \approx \theta \times 6 \times 10^{-17}\, e\,\mathrm{cm}\,, \tag{6.15}$$

where $m^* = m_u m_d/(m_u + m_d)$ is the reduced mass of the up and down quark, and Λ_{QCD} is the QCD energy scale $\sim 1\,\mathrm{GeV}$. A more accurate determination of the neutron EDM is [7]

$$\mathrm{d}_n \approx \theta \times 3.6 \times 10^{-16}\, e\,\mathrm{cm}\,, \tag{6.16}$$

which from the current neutron EDM experimental limit [10] yields $\theta \leq 10^{-10}$. The QCD CP-violating parameter θ contribution to the deuteron EDM is the sum of the nucleon EDMs plus the nuclear CP-violating interaction

$$\mathrm{d}_D \approx \mathrm{d}_n + \mathrm{d}_p + \mathrm{d}_D^{\mathrm{nuclear}}\,, \tag{6.17}$$

which can reliably be estimated, using the simple deuteron wavefunction, [16, 18] to be

$$\mathrm{d}_D \approx -\theta \times 10^{-16}\, e\,\mathrm{cm}\,. \tag{6.18}$$

This implies that $\mathrm{d}_D(\theta)/\mathrm{d}_n(\theta) \approx -1/3$. Therefore, if both the neutron and deuteron EDM are measured, the above equation provides an excellent check as to whether θ is the EDM source.

Supersymmetry

In case supersymmetry (SUSY) exists, where every fermion particle has a bosonic counter-part, then new types of interactions are also present. Some of those interactions are CP-violating and can induce an EDM. In such cases the neutron EDM is estimated [17, 18] to be, in terms of the up and down quark EDMs (d_u and d_d respectively) as well as the quark-color EDMs, d_q^c

$$\mathrm{d}_n \approx 1.4(\mathrm{d}_d - 0.25\mathrm{d}_u) + 0.83e(\mathrm{d}_d^c + \mathrm{d}_u^c) + 0.27e(\mathrm{d}_d^c - \mathrm{d}_u^c)\,, \tag{6.19}$$

whereas the deuteron EDM is estimated to be

$$\mathrm{d}_D \approx (\mathrm{d}_d + \mathrm{d}_u) + 6e(\mathrm{d}_d^c - \mathrm{d}_u^c) - 0.2e(\mathrm{d}_d^c + \mathrm{d}_u^c)\,. \tag{6.20}$$

The last two equations illustrate the advantage of the deuteron over the neutron for the isovector $e(\mathrm{d}_{\mathrm{d}}^c - \mathrm{d}_u^c)$ interaction. The gain in sensitivity by the large factor of 20 is there due to the large $I = 1$ pion-exchange interaction present in the deuteron. Again, it is evident that should both the neutron and deuteron EDMs be observed, their relative strengths will point to their respective sources.

6.3.2 Storage Ring EDM

As EDMs couple only to electric fields one would expect that in a purely magnetic storage ring there is no sensitivity to them. However, in a magnetic storage ring a non-stationary particle experiences an electric field in its own rest-frame equal to $\mathbf{E}^* = \gamma(\mathbf{v} \times \mathbf{B})$. The spin precession due to this electric field is equal to

$$\frac{\mathrm{d}s}{\mathrm{d}t^*} = \mathbf{d} \times \gamma(\mathbf{v} \times \mathbf{B}) \Longrightarrow \frac{\mathrm{d}s}{\mathrm{d}t} = \mathbf{d} \times (\mathbf{v} \times \mathbf{B}) \,. \tag{6.21}$$

For $\mathbf{v} \sim c$ and $B = 1\,\mathrm{T}$ it is equivalent to a spin precession in a $300\,\mathrm{MV\,m^{-1}}$ electric field, which is much higher than it can be achieved in the laboratory.[1] There are three variations of the EDM in storage ring method, each one with different sensitivity and systematic errors.

1. Indirect, parasitic to g–2 measurement where the EDM measurement is a byproduct of another major experimental aim. This is the least sensitive method. The total spin precession angular velocity is given by

$$\boldsymbol{\omega} = \frac{e}{m}\left[a\mathbf{B} + \frac{\eta}{2c}\mathbf{v} \times \mathbf{B}\right] \,, \tag{6.22}$$

   where η is for the EDM similar to what the g-factor is for the magnetic moment. a is the anomalous magnetic moment and c the speed of light. The effect of the EDM is to tilt the total vector relative to the external magnetic field as shown in Fig. 6.6.
2. A dedicated experiment where the EDM is the major goal. In this method a radial electric field is used to almost *freeze* the spin direction along the momentum vector. This is the most sensitive method for short-lived systems or systems where long spin coherence times are not possible. The spin is kept along the momentum vector and the vertical component accumulates for the duration of the storage [3].
3. A dedicated experiment where the spin is allowed to precess with its g–2 frequency but the velocity is modulated in resonance with the g–2 precession. There is a small, non-zero, EDM signal per g–2 oscillation, which can become very large if a very large number of g–2 oscillations could be used. This is the most sensitive method for stable or long-lived particles where very long spin coherence times are also possible. The velocity is modulated with the g–2 frequency, and therefore, the vertical spin does not quite return to its original value but accumulates with time. The change of the particle speed between the two spin directions (parallel and anti-parallel to its momentum) is the reason for the non-cancelation of the induced vertical spin component within one g–2 cycle. The preliminary deuteron EDM lattice currently under consideration is shown in Fig. 6.7.

[1] The rest-frame time $t^* = t/\gamma$, with t the lab-frame time, and hence the absence of the relativistic γ factor from the final equation.

The indirect method (number 1) was used in the muon g–2 experiment, and final results are expected to be published soon. There are two letters of intent (LOI) based on the *frozen* spin method (number 2) that can advance the sensitivity to the muon EDM by several orders of magnitude over the parasitic method. The resonance method (number 3) is currently under an intense development by the Storage Ring EDM collaboration (SREDM).

Why Study the Deuteron EDM?

There are several additional advantages that the deuteron nucleus offers in the study of hadronic EDMs

1. It is complementary to neutron EDM as there are more than one potential EDM sources, and the two systems have very different sensitivity to them. Table 6.2 shows the future plans for hadronic EDM experiments and their *neutron equivalent* [19].
2. Very high intensity polarized deuteron sources (10^{11}–10^{12} particles per cycle) in a well defined state are readily available today. The underlying accelerator techniques have been developed and well understood for the last 50 years.

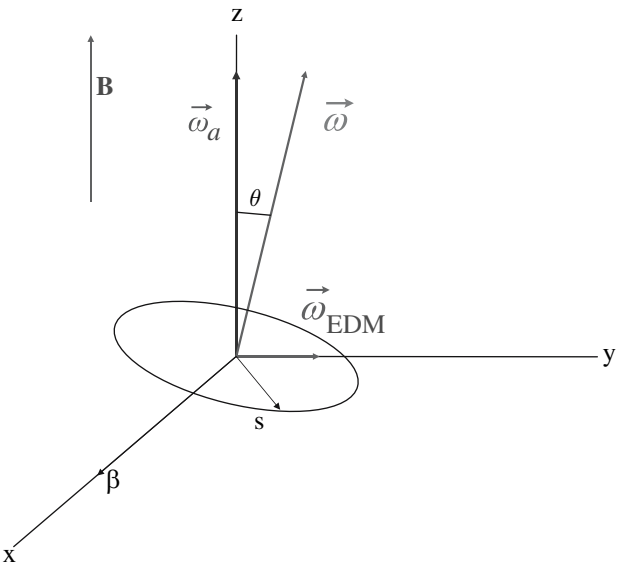

Fig. 6.6. The presence of an EDM causes the tilt of the total precession vector relative to the magnetic field. This method was used to set a limit to the muon EDM in the muon g–2 experiment by investigating the spin precession level as a function of the g–2 phase. The vertical spin component oscillates as the spin rotates due to its g–2 precession, but there is no accumulation with time

Table 6.2. Comparison with other EDM efforts

System	Current Bound (e cm)	Future Goal (e cm)	$\sim$ d_n equivalent ($e$cm)
Neutron	$d_n < 3 \times 10^{-26}$	$\sim 10^{-28}$	$\sim 10^{-28}$
^{199}Hg atom	$d_{Hg} < 2 \times 10^{-28}$	$\sim 2 \times 10^{-29}$	10^{-25}–10^{-26}
^{129}Xe atom	$d_{Xe} < 6 \times 10^{-27}$	$\sim 10^{-30}$–10^{-33}	10^{-26}–10^{-29}
Deuteron	–	10^{-29}	3×10^{-29}–5×10^{-31}

3. Polarimeters with high efficiency and high analyzing power for deuterons in the considered range of 1–1.5 GeV c^{-1} are already developed and understood.

In September 2006 the method was presented to the Brookhaven National Laboratory (BNL) program advisory committee (PAC). The PAC response was enthusiastic and has suggested to perform a series of systematic error studies including not only both beam and spin tracking but also polarime-

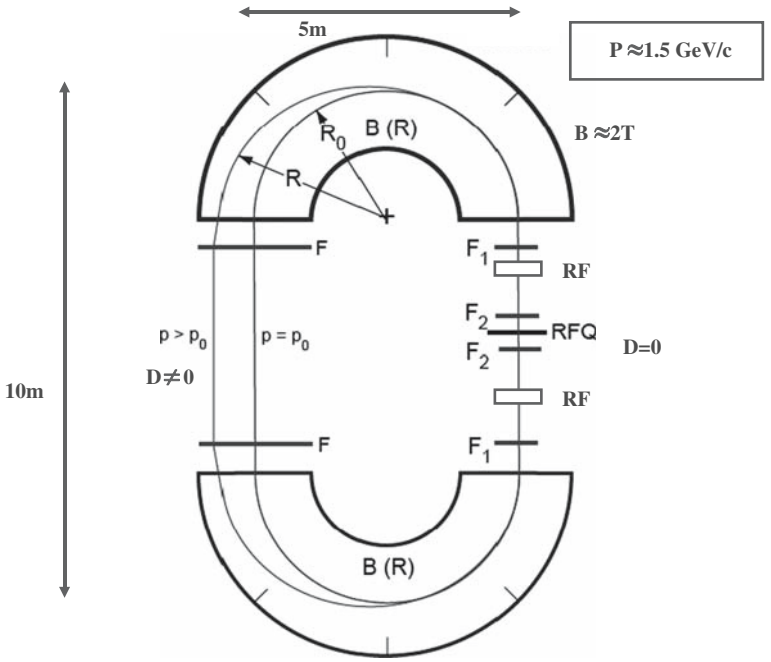

Fig. 6.7. The draft deuteron EDM lattice currently under consideration is shown here. It describes a 5 m by 10 m storage ring with two dipole magnetic field regions, (top/bottom) and a region where the dispersion function (D) is zero (right side) and a region where the dispersion function is non-zero (left side). The location of the RF-cavities and the RF-Quadrupole (RFQ) is on the right side in order to reduce the potential systematic errors

try studies with hardware testing before the final proposal submission. The SREDM collaboration is currently optimizing the ring lattice to increase the statistical sensitivity of the method and minimize the systematic errors. They have also laid out the plans for the testing of the issues regarding the polarimeter. The proposal is expected to be presented to a suitable laboratory before the middle of 2008.

References

1. Bailey, J., et al.: Final report on the CERN muon storage ring including the anomalous magnetic moment and the electric dipole moment of the muon, and a direct test of relativistic time dilation. Nucl. Phys. B **150**, 1 (1979) 98
2. Semertzidis, Y.K., et al.: Sensitive search for a permanent muon electric dipole moment, hep-ph/0012087;
   Semertzidis, Y.K., et al.: A sensitive search for a muon electric dipole moment. Int. J. Mod. Phys. A16S1B 690 (2001) 98
3. Farley, F.J.M., et al.: A new method of measuring electric dipole moments in storage rings. Phys. Rev. Lett. **92**, 052001 (2004) 98, 109
4. Orlov, Y.F., Morse, W.M., Semertzidis, Y.K.: Resonance method of electric-dipole-moment measurements in storage rings. Phys. Rev. Lett. **96**, 214802 (2006) 98
5. Gabrielse, G., et al.: New determination of the fine structure constant from the electron g value and QED. Phys. Rev. Lett. **97**, 030802 (2006) 99
6. Bennett, G.W., et al.: Final report of the muon E821 anomalous magnetic moment measurement at BNL. Phys. Rev. D73 072003 (2006);
   Miller, J.P., de Rafael, E., Roberts, B.L.: Muon (g–2): Experiment and Theory. To be submitted to Reports in Progress in Physics. 100, 101
7. Pospelov, M., Ritz, A.: Electric dipole moments as probes of new physics. Ann. Phys. **318**, 119 (2005) 105, 108
8. Stephenson, E.: private communication;
   Ladygin, V.P., et al.: Analyzing powers for the inclusive reaction of deuterons on carbon at energies between 0.175 and 1.6 GeV. Nucl. Instr. Meth. Phys. Res. A **404**, 129 (1998) 106
9. Purcell, E.M., Ramsey, N.F.: On the possibility of electric dipole moments for elementary particles and nuclei. Phys. Rev. **78**, 807 (1950) 106
10. Baker, C.A., et al.: An improved experimental limit on the electric dipole moment of the neutron. Phys. Rev. Lett. **97**, 131801 (2006) 106, 107, 108
11. Ellis, J.: private communication 106
12. Schiff, L.I.: Measurability of nuclear electric dipole moments. Phys. Rev. **132**, 2194 (1963) 106
13. Sandars, P.G.H.: The electric dipole moment of an atom. Phys. Lett. **14**, 194 (1965);
    Sandars, P.G.H.: Enhancement factor for the electric dipole moment of the valence electron in an alkali atom. Phys. Lett. **22**, 290 (1966) 106
14. Regan, B.C., et al.: New Limit on the electron electric dipole moment. Phys. Rev. Lett. **88**, 071805 (2002) 107

15. Romalis, M., et al.: New limit on the permanent electric dipole moment of ^{199}Hg. Phys. Rev. Lett. **86**, 2505 (2001) 107
16. Khriplovich, I.B., Korkin, R.A.: P and T odd electromagnetic moments of deuteron in chiral limit. Nucl. Phys. A **665**, 365 (2000) [nucl-th/9904081] 108
17. Lebedev, O., et al.: Probing CP violation with the deuteron electric dipole moment. Phys. Rev. D **70**, 016003 (2004) 108
18. Liu, C.P., Timmermans, R.G.E.: P- and T-odd two-nucleon interaction and the deuteron electric dipole moment. Phys. Rev. C **70**, 055501 (2004) [nucl-th/0408060] 108
19. Marciano, W.: private communication 110

7 Photon-Axion Conversion in Intergalactic Magnetic Fields and Cosmological Consequences

Alessandro Mirizzi,[1] Georg G. Raffelt[1] and Pasquale D. Serpico[2]

[1] Max-Planck-Institut für Physik (Werner-Heisenberg-Institut)
Föhringer Ring 6, 80805 München, Germany
raffelt@mppmu.mpg.de
[2] Center for Particle Astrophysics, Fermi National Accelerator Laboratory
Batavia, IL 60510-0500, USA
serpico@fnal.gov

Abstract. Photon-axion conversion induced by intergalactic magnetic fields causes an apparent dimming of distant sources, notably of cosmic distance indicators such as supernovae of type Ia (SNe Ia). We review the impact of this mechanism on the luminosity-redshift relation of SNe Ia, on the dispersion of quasar spectra, and on the spectrum of the cosmic microwave background. The original idea of explaining the apparent dimming of distant SNe Ia without cosmic acceleration is strongly constrained by these arguments. However, the cosmic equation of state extracted from the SN Ia luminosity-redshift relation remains sensitive to this mechanism. For example, it can mimic phantom energy.

7.1 Introduction

The two-photon coupling of axions or axion-like particles allows for transitions between them and photons in external electric or magnetic fields as shown in Fig. 7.1 [1, 2]. This mechanism serves as the basis for the experimental searches for galactic dark matter axions [1, 3] and solar axions [1, 4, 5, 6, 7]. The astrophysical implications of this mechanism have also been widely investigated and reviewed [8, 9]. The phenomenological consequences of an extremely light or massless axion would be particularly interesting in several astrophysical circumstances such as polarization of radio-galaxies [10] and quasars [11], the diffuse X-ray background [12], or ultra-high energy cosmic rays [13, 14].

One intriguing cosmological consequence of this mechanism is photon-axion conversion caused by intergalactic magnetic fields, leading to the dimming of distant light sources, notably of supernovae (SNe) of type Ia that are used as cosmic distance indicators [15]. Observationally, SNe Ia at redshifts, $0.3 \lesssim z \lesssim 1.7$, appear fainter than expected from the luminosity-redshift relation in a decelerating Universe [16, 17, 18], a finding usually interpreted as evidence for acceleration of the cosmic expansion rate and thus for a cosmic equation of state (EoS) that today is dominated by a cosmological constant,

A. Mirizzi et al.: *Photon-Axion Conversion in Intergalactic Magnetic Fields and Cosmological Consequences*, Lect. Notes Phys. **741**, 115–134 (2008)
DOI 10.1007/978-3-540-73518-2_7

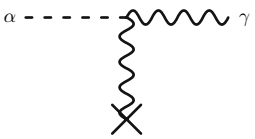

Fig. 7.1. Axion-photon transition in an external electric or magnetic field

a slowly evolving scalar field, or something yet more exotic [19]. The dimming caused by photon-axion conversion could mimic this behavior and thus provide an alternative to the interpretation as cosmic acceleration. Although still requiring some non-standard fluid to fit the flatness of the Universe, this model seemed capable of explaining the SN-dimming through a completely different mechanism.

However, if the light from distant SNe Ia reaches us partially converted to axion-like particles, the same mechanism would affect all distant sources of electromagnetic radiation. Therefore, it appears useful to update the different arguments constraining photon-axion conversion in intergalactic magnetic fields, in particular the constraints arising from spectral distortions of the cosmic microwave background (CMB) and dispersion of quasar (QSO) spectra.

To this end, we begin in Sect. 7.2 with a review of the formalism of photon-axion conversion in magnetic fields. Some technical details are deferred to Appendix A. In Sect. 7.3 we describe how this mechanism affects the SN Ia luminosity-redshift relation and accounts for the observed dimming. In Sect. 7.4 we turn to spectral CMB distortions and in Sect. 7.5 combine these limits with those from the dispersion of QSO spectra. In Sect. 7.6 we describe some additional limits from a violation of the reciprocity relation between the luminosity and angular diameter distances. We conclude in Sect. 7.7 with comments on the viability of the photon-axion conversion mechanism.

7.2 Photon-Axion Conversion

To understand how photon-axion conversion could affect distant sources, we take a closer look at the phenomenon of photon-axion mixing. The Lagrangian (density) describing the photon-axion system is [8]

$$L = L_\gamma + L_a + L_{a\gamma\gamma} \,. \tag{7.1}$$

The QED Lagrangian for photons is

$$L_\gamma = -\frac{1}{4} F_{\mu\nu} F^{\mu\nu} + \frac{\alpha^2}{90 m_e^4} \left[(F_{\mu\nu} F^{\mu\nu})^2 + \frac{7}{4} (F_{\mu\nu} \tilde{F}^{\mu\nu})^2 \right] \,, \tag{7.2}$$

where $F_{\mu\nu}$ is the electromagnetic field-strength tensor, $\tilde{F}_{\mu\nu} = \frac{1}{2} \varepsilon_{\mu\nu\varrho\sigma} F^{\varrho\sigma}$ its dual, α the fine-structure constant, and m_e the electron mass. We always

use natural units with $\hbar = c = k_{\rm B} = 1$. The second term on the RHS is the Euler-Heisenberg effective Lagrangian, describing the one-loop corrections to classical electrodynamics for photon frequencies $\omega \ll m_e$. The Lagrangian for the non-interacting axion field a is

$$L_a = \frac{1}{2}\partial^\mu a\, \partial_\mu a - \frac{1}{2}m^2 a^2 \ . \tag{7.3}$$

A generic feature of axion models is the CP-conserving two-photon coupling, so that the axion-photon interaction is

$$L_{a\gamma\gamma} = -\frac{1}{4}\, g_{a\gamma\gamma} F_{\mu\nu}\tilde{F}^{\mu\nu} a = g_{a\gamma\gamma}\, \mathbf{E}\cdot\mathbf{B}\, a \ , \tag{7.4}$$

where $g_{a\gamma\gamma}$ is the axion-photon coupling with dimension of inverse energy. A crucial consequence of L is that the propagation eigenstates of the photon-axion system differ from the corresponding interaction eigenstates. Hence, interconversion takes place, much in the same way as for massive neutrinos of different flavors. However, as the mixing term $F_{\mu\nu}\tilde{F}^{\mu\nu}a$ involves two photons, one of them must correspond to an external field [1, 2, 8, 20].

Axion-photon oscillations are described by the coupled Klein-Gordon and Maxwell equations implied by these Lagrangians. For very relativistic axions ($m_a \ll \omega$), the short-wavelength approximation can be applied, and the equations of motion reduce to a first-order propagation equation. More specifically, we consider a monochromatic light beam traveling along the z-direction in the presence of an arbitrary magnetic field $\mathbf{B}$. Accordingly, the propagation equation takes the form [2]

$$(\omega - {\rm i}\partial_z + \mathcal{M}) \begin{pmatrix} A_x \\ A_y \\ a \end{pmatrix} = 0 \ , \tag{7.5}$$

where A_x and A_y correspond to the two linear photon polarization states, and ω is the photon or axion energy. The mixing matrix is

$$\mathcal{M} = \begin{pmatrix} \Delta_{xx} & \Delta_{xy} & g_{a\gamma\gamma}B_x/2 \\ \Delta_{yx} & \Delta_{yy} & g_{a\gamma\gamma}B_y/2 \\ g_{a\gamma\gamma}B_x/2 & g_{a\gamma\gamma}B_y/2 & \Delta_a \end{pmatrix} \ , \tag{7.6}$$

where $\Delta_a = -m_a^2/2\omega$. The component of $\mathbf{B}$ parallel to the direction of motion does not induce photon-axion mixing. The terms proportional to B have an evident physical meaning, but the Δ_{ij}-terms ($i, j = x, y$) require some explanation. Generally speaking, they are determined both by the properties of the medium and by the QED vacuum polarization effect. We ignore the latter, being sub-dominant for the problem at hand [21].

For a homogeneous magnetic field, we may choose the y-axis along the projection of $\mathbf{B}$ perpendicular to the z-axis. Correspondingly we have $B_x = 0$, $B_y = |\mathbf{B}_{\rm T}| = B\sin\theta$, $A_x = A_\perp$, and $A_y = A_\parallel$. Equation (7.5) then becomes

$$(\omega - \mathrm{i}\partial_z + \mathcal{M}) \begin{pmatrix} A_\perp \\ A_\parallel \\ a \end{pmatrix} = 0 \,, \tag{7.7}$$

with the mixing matrix

$$\mathcal{M} = \begin{pmatrix} \Delta_\perp & \Delta_{\mathrm{R}} & 0 \\ \Delta_R & \Delta_\parallel & \Delta_{a\gamma} \\ 0 & \Delta_{a\gamma} & \Delta_a \end{pmatrix} \,, \tag{7.8}$$

where

$$\Delta_{a\gamma} = \frac{g_{a\gamma\gamma}}{2} |\mathbf{B}_{\mathrm{T}}| \,, \tag{7.9}$$

$$\Delta_{\parallel,\perp} = \Delta_{\mathrm{pl}} + \Delta^{\mathrm{CM}}_{\parallel,\perp} \,. \tag{7.10}$$

In a plasma, the photons acquire an effective mass given by the plasma frequency $\omega^2_{\mathrm{pl}} = 4\pi\alpha\, n_e/m_e$, with n_e the electron density, leading to

$$\Delta_{\mathrm{pl}} = -\frac{\omega^2_{\mathrm{pl}}}{2\omega} \,. \tag{7.11}$$

Furthermore, the $\Delta^{\mathrm{CM}}_{\parallel,\perp}$ terms describe the Cotton-Mouton effect, i.e., the birefringence of fluids in the presence of a transverse magnetic field where $|\Delta^{\mathrm{CM}}_\parallel - \Delta^{\mathrm{CM}}_\perp| \propto B^2_{\mathrm{T}}$. These terms are of little importance for the following arguments and will thus be neglected. Finally, the Faraday rotation term Δ_{R}, which depends on the energy and the longitudinal component B_z, couples the modes $A_\parallel$ and $A_\perp$. While Faraday rotation is important when analyzing polarized sources of photons, it plays no role in the problem at hand.

With this simplification the $A_\perp$ component decouples, and the propagation equations reduce to a 2-dimensional mixing problem with a purely transverse field $\mathbf{B} = \mathbf{B}_{\mathrm{T}}$

$$(\omega - \mathrm{i}\partial_z + \mathcal{M}_2) \begin{pmatrix} A_\parallel \\ a \end{pmatrix} = 0 \,, \tag{7.12}$$

with a 2-dimensional mixing matrix

$$\mathcal{M}_2 = \begin{pmatrix} \Delta_{\mathrm{pl}} & \Delta_{a\gamma} \\ \Delta_{a\gamma} & \Delta_a \end{pmatrix} \,. \tag{7.13}$$

The solution follows from diagonalization by the rotation angle

$$\vartheta = \frac{1}{2} \arctan\left(\frac{2\Delta_{a\gamma}}{\Delta_{\mathrm{pl}} - \Delta_a} \right) \,. \tag{7.14}$$

In analogy to the neutrino case [22], the probability for a photon emitted in the state $A_\parallel$ to convert into an axion after travelling a distance s is

$$P_0(\gamma \to a) = \left|\langle A_\parallel(0)|a(s)\rangle\right|^2 = \sin^2(2\vartheta)\sin^2(\Delta_{\rm osc}s/2)$$
$$= (\Delta_{a\gamma}s)^2\,\frac{\sin^2(\Delta_{\rm osc}s/2)}{(\Delta_{\rm osc}s/2)^2}\,, \qquad (7.15)$$

where the oscillation wavenumber is given by

$$\Delta_{\rm osc}^2 = (\Delta_{\rm pl} - \Delta_a)^2 + 4\Delta_{a\gamma}^2\,. \qquad (7.16)$$

The conversion probability is energy-independent when $2|\Delta_{a\gamma}| \gg |\Delta_{\rm pl} - \Delta_a|$ or whenever the oscillatory term in (7.15) is small, i.e., $\Delta_{\rm osc}s/2 \ll 1$, implying the limiting behavior $P_0 = (\Delta_{a\gamma}s)^2$.

The propagation over many B-field domains is a truly 3-dimensional problem because different photon polarization states play the role of $A_\parallel$ and $A_\perp$ in different domains. This average is enough to guarantee that the conversion probability over many domains is an incoherent average over magnetic field configurations and photon polarization states. The probability after traveling over a distance $r \gg s$, where s is the domain size, is derived in Appendix A along the lines of [23] and is found to be

$$P_{\gamma\to a}(r) = \frac{1}{3}\left[1 - \exp\left(-\frac{3P_0\,r}{2s}\right)\right]\,, \qquad (7.17)$$

with P_0 given by (7.15). As expected, for $r/s \to \infty$ the conversion probability saturates, so that on average one third of all photons converts to axions.

7.3 Photon-Axion Conversion and Supernova Dimming

7.3.1 Observations

In 1998, two groups using SNe Ia as cosmic distance indicators reported first evidence for a luminosity-redshift relation that indicated that the expansion of the universe was accelerating at that time [16, 17]. The quantity relevant for SN Ia observations is the luminosity distance d_L at redshift z, defined by

$$\mathrm{d}_L^2(z) = \frac{\mathcal{L}}{4\pi\mathcal{F}}\,, \qquad (7.18)$$

where $\mathcal{L}$ is the absolute luminosity of the source and $\mathcal{F}$ is the energy flux arriving at Earth [16, 17]. In Friedmann-Robertson-Walker cosmologies, the luminosity distance at a given redshift z is a function of the Hubble parameter H_0, the matter density $\Omega_{\rm M}$, and the dark energy density Ω_Λ. Usually the data are expressed in terms of magnitudes

$$m = M + 5\log_{10}\left(\frac{d_L}{\rm Mpc}\right) + 25\,, \qquad (7.19)$$

where M is the absolute magnitude, equal to the value that m would have at $\mathrm{d}_L = 10\,\mathrm{pc}$.

Figure 7.2 shows the Hubble diagram for SN Ia samples at low and high z. The distances of high-redshift SNe are, on average, 10–15% larger than those in a low matter density ($\Omega_\mathrm{M} = 0.2$) Universe without dark energy ($\Omega_\Lambda = 0$). Therefore, objects of a fixed intrinsic brightness appear fainter, if the cosmic energy density budget is dominated by dark energy. The best fit of these data supports a Universe composed of a fraction of dark matter $\Omega_\mathrm{M} \simeq 0.3$ and a fraction of dark energy $\Omega_\Lambda \simeq 0.7$.

Dark energy has been associated with vacuum energy or an Einstein cosmological constant resulting in a constant energy density at all times. Defining the equation of state

$$w = \frac{p}{\varrho}\,, \tag{7.20}$$

the cosmological constant is characterized by $p = -\varrho$, i.e., $w = -1$. From the Friedmann equations, any component of the density budget with equation of state $w < -1/3$ causes cosmic acceleration. SN Ia data imply that $w \gtrsim -0.5$ are disfavored, supporting the cosmic acceleration of the Universe [17].

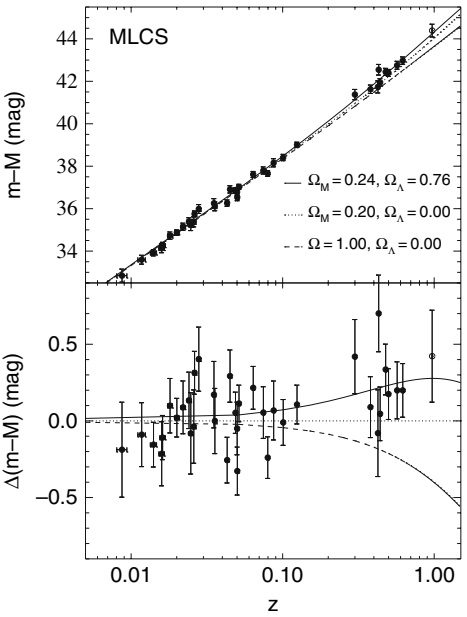

Fig. 7.2. SN Ia Hubble diagram. *Upper panel:* Hubble diagram for low- and high-redshift SN Ia samples. Overplotted are three cosmologies: "low" and "high" Ω_M with $\Omega_\Lambda = 0$ and the best fit for a flat cosmology, $\Omega_\mathrm{M} = 0.24$ and $\Omega_\Lambda = 0.76$. *Lower panel:* Difference between data and models with $\Omega_\mathrm{M} = 0.20$ and $\Omega_\Lambda = 0$ (Figure from [16] with permission)

7.3.2 Interpretation in Terms of Photon-Axion Conversion

To explore the effect of photon-axion conversion on SN-dimming, we recast the relevant physical quantities in terms of natural parameters. The energy of optical photons is a few eV. The strength of widespread, all-pervading B-fields in the intergalactic medium must be less than a few $10^{-9}\,\mathrm{G}$ over coherence lengths s crudely at the Mpc scale, according to the constraint from the Faraday effect of distant radio sources [24]. Along a given line of sight, the number of such domains in our Hubble radius is about $N \approx H_0^{-1}/s \approx 4\times10^3$ for $s \sim 1\,\mathrm{Mpc}$. The mean diffuse intergalactic plasma density is bounded by $n_e \lesssim 2.7\times10^{-7}\,\mathrm{cm}^{-3}$, corresponding to the recent WMAP measurement of the baryon density [25]. Recent results from the CAST experiment [7] give a direct experimental bound on the axion-photon coupling of $g_{a\gamma\gamma} \lesssim 1.16\times10^{-10}\,\mathrm{GeV}^{-1}$, comparable to the long-standing globular-cluster limit [8]. Suitable representations of the mixing parameters are

$$\begin{aligned}
\frac{\Delta_{a\gamma}}{\mathrm{Mpc}^{-1}} &= 0.15\; g_{10}\; B_{\mathrm{nG}}\,,\\
\frac{\Delta_{a}}{\mathrm{Mpc}^{-1}} &= -7.7\times10^{28}\left(\frac{m_a}{1\,\mathrm{eV}}\right)^2\left(\frac{\omega}{1\,\mathrm{eV}}\right)^{-1}\,,\\
\frac{\Delta_{\mathrm{pl}}}{\mathrm{Mpc}^{-1}} &= -11.1\left(\frac{\omega}{1\,\mathrm{eV}}\right)^{-1}\left(\frac{n_e}{10^{-7}\,\mathrm{cm}^{-3}}\right)\,,
\end{aligned} \tag{7.21}$$

where we have introduced $g_{10} = g_{a\gamma\gamma}/10^{-10}\,\mathrm{GeV}^{-1}$ and B_{nG} is the magnetic field strength in nano-Gauss.

The mixing angle defined in (7.14) is too small to yield a significant conversion effect for the allowed range of axion masses because $|\Delta_a| \gg |\Delta_{a\gamma}|$, $|\Delta_{\mathrm{pl}}|$. Therefore, to ensure a sufficiently large mixing angle one has to require nearly massless pseudoscalars, sometimes referred to as "arions" [26, 27]. For such ultra-light axions, a stringent limit from the absence of γ-rays from SN 1987A gives $g_{a\gamma\gamma} \lesssim 1\times10^{-11}\,\mathrm{GeV}^{-1}$ [28] or even $g_{a\gamma\gamma} \lesssim 3\times10^{-12}\,\mathrm{GeV}^{-1}$ [29]. Henceforth we will consider the pseudoscalars to be effectively massless so that our remaining independent parameters are $g_{10}B_{\mathrm{nG}}$ and n_e. Note that m_a only enters the equations via the term $m_a^2 - \omega_{\mathrm{pl}}^2$ so that for tiny but non-vanishing values of m_a, the electron density should be interpreted as $n_{e,\mathrm{eff}} = |n_e - m_a^2 m_e/(4\pi\alpha)|$.

Allowing for the possibility of photon-axion oscillations in intergalactic magnetic fields, the number of photons emitted by the source and thus the flux $\mathcal{F}$ is reduced to the fraction $P_{\gamma\to\gamma} = 1 - P_{\gamma\to a}$. Therefore, the luminosity distance (7.18) becomes

$$\mathrm{d}_L \to \mathrm{d}_L/P_{\gamma\to\gamma}^{1/2}\,, \tag{7.22}$$

and the brightness (7.19)

$$m \to m - \frac{5}{2}\log_{10}(P_{\gamma\to\gamma})\,. \tag{7.23}$$

Distant SNe Ia would eventually saturate ($P_{\gamma\to\gamma} = 2/3$) and hence, would appear $(3/2)^{1/2}$ times farther away than they really are. This corresponds to a maximum dimming of approximately 0.4 mag. Csáki, Kaloper and Terning (CKT I) showed that if photon-axion conversion takes place, this mechanism can reproduce the SN Hubble diagram [15], assuming, for example, a non-standard dark energy component $\Omega_S = 0.7$ with equation of state $w = -1/3$, which does not produce cosmic acceleration (Fig. 7.3).

However, in the model of CKT I, plasma density effects were neglected ($n_e = 0$). Later, it was recognized that the conclusions of CKT I can be significantly modified when the effects of the intergalactic plasma on the photon-axion oscillations are taken into account [21]. In the presence of plasma effects, the probability of oscillation is lower than before and it is no longer achromatic (Fig. 7.4). SN observations require not only dimming, but also that the dimming be achromatic. In fact, SN observations put a constraint on the color excess between the B and V bands,

$$E[B-V] \equiv -2.5\,\log_{10}\left[\frac{F^{\rm o}(B)}{F^{\rm e}(B)}\,\frac{F^{\rm e}(V)}{F^{\rm o}(V)}\right]\,, \tag{7.24}$$

where $F^{\rm o}$ and $F^{\rm e}$ are the observed and emitted flux, respectively. The B and V bands correspond to 0.44 μm and 0.55 μm, respectively. Observations constrain $E[B-V]$ to be lower than 0.03 [17]. This can be translated to

$$P(\gamma\to a)_V\left[\frac{P(\gamma\to a)_B}{P(\gamma\to a)_V} - 1\right] < 0.03\,. \tag{7.25}$$

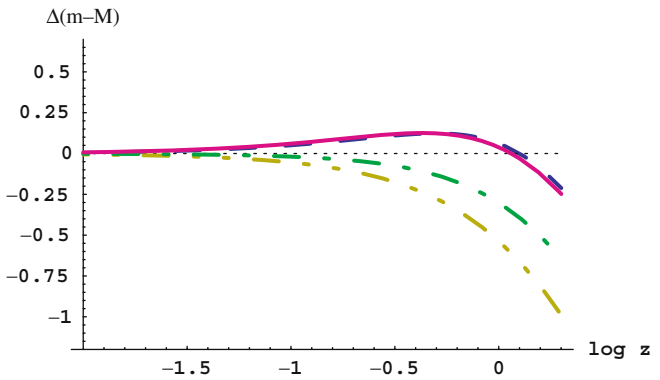

Fig. 7.3. Hubble diagram for SNe Ia for different cosmological models, relative to the curve with $\Omega_{\rm tot} = 0$ (*dotted horizontal line*). The dashed curve is a best fit to the SN data assuming that the Universe is accelerating ($\Omega_{\rm M} = 0.3$, $\Omega_\Lambda = 0.7$); the solid line is the photon-axion oscillation model with $\Omega_{\rm M} = 0.3$ and $\Omega_S = 0.7$, the dot-dashed line is $\Omega_{\rm M} = 0.3$, $\Omega_S = 0.7$ with no oscillation, the dot-dot-dashed line is for $\Omega_{\rm M} = 1$ and again no oscillation (Figure from [15] with permission)

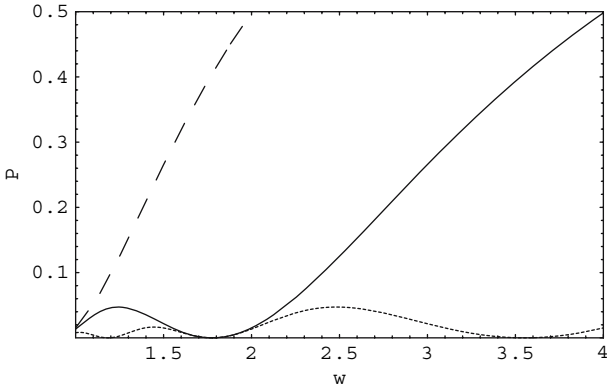

Fig. 7.4. Ratio of the probability of conversion of photons to axions including the effects of the intergalactic plasma ($n_e \approx 10^{-7}\,\mathrm{cm}^{-3}$) and the probability of oscillations when this effect is not considered, as a function of the photon energy ω. The curves are drawn for different size s of the magnetic domains: 0.5 Mpc (*dashed line*), 1 Mpc (*solid line*) and 2 Mpc (dotted line, Figure from [21] with permission)

Therefore, assuming an electron density $n_e \approx n_{\mathrm{baryons}} = n_\gamma \eta \sim 10^{-7}\,\mathrm{cm}^{-3}$, the model is ruled out in most of the parameter space because of either an excessive photon conversion or a chromaticity of the dimming [21]. Only fine-tuned parameters for the statistical properties of the extragalactic magnetic fields would still allow this explanation.

On the other hand, Csáki, Kaloper and Terning [30] (CKT II) criticized the assumed value of n_e as being far too large for most of the intergalactic space, invoking observational hints for a value at least one order of magnitude smaller. As a consequence, for $\omega_{\mathrm{pl}} \lesssim 6 \times 10^{-15}\,\mathrm{eV}$, corresponding to $n_e \lesssim 2.5 \times 10^{-8}\,\mathrm{cm}^{-3}$, one finds $|P_V - P_B| < 0.03$ so that the chromaticity effect disappears very rapidly and becomes undetectable by present observations.

Figure 7.5 shows qualitatively the regions of n_e and $g_{10} B_{\mathrm{nG}}$ relevant for SN dimming at cosmological distances. To this end, we show iso-dimming contours obtained from (7.23) for a photon energy 4.0 eV and a magnetic domain size $s = 1\,\mathrm{Mpc}$. For simplicity, we neglect the redshift evolution of the intergalactic magnetic field B, domain size s, plasma density n_e, and photon frequency ω. Our iso-dimming curves are intended to illustrate the regions where the photon-axion conversion could be relevant. In reality, the dimming should be a more complicated function since the intergalactic medium is expected to be very irregular: there could be voids of low n_e density, but there will also be high-density clumps, sheets, and filaments and these will typically have higher B fields as well. However, the simplifications used here

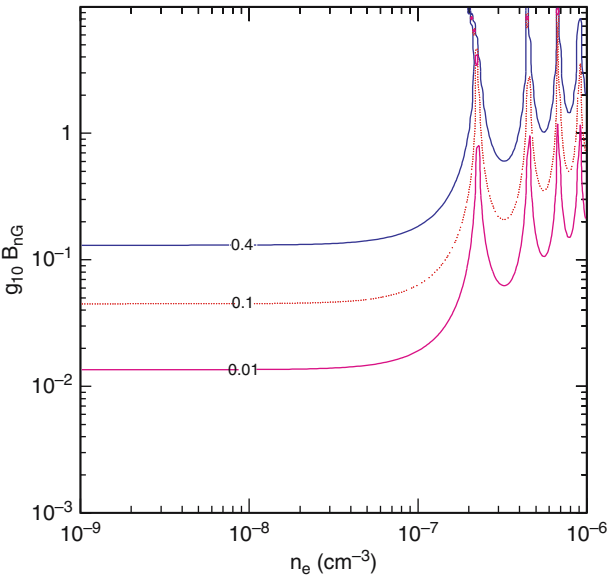

Fig. 7.5. Iso-dimming curves for an attenuation of 0.01, 0.1, and 0.4 magnitudes. The photon energy of 4.0 eV is representative of the B-band. The size of a magnetic domain is $s = 1$ Mpc (Figure from [32] with permission)

are consistent with the ones adopted in CKT II and do not alter our main results.

The iso-dimming contours are horizontal in the low-n_e and low-$g_{10}B_{\rm nG}$ region. They are horizontal for any $g_{10}B_{\rm nG}$ when n_e is sufficiently low. From the discussion in Sect. 7.2, we know that the single-domain probability P_0 of (7.15) is indeed energy-independent when $|\Delta_{\rm osc}s| \ll 1$, i.e., for $|\Delta_{\rm pl}|s/2 \ll 1$ and $|\Delta_{a\gamma}|s \ll 1$. When $n_e \lesssim$ few $10^{-8}\,{\rm cm}^{-3}$ and $g_{10}B_{\rm nG} \lesssim 4$, we do not expect an oscillatory behavior of the probability. This feature is nicely reproduced by our iso-dimming contours. From Fig. 7.5, we also deduce that a significant amount of dimming is possible only for $g_{10}B_{\rm nG} \gtrsim 4 \times 10^{-2}$.

In CKT I, where the effect of n_e was neglected, $m_a \sim 10^{-16}\,{\rm eV}$ was used, corresponding to $n_{e,{\rm eff}} \approx 6 \times 10^{-12}\,{\rm cm}^{-3}$. As noted in CKT II, when plasma effects are taken into account, any value $n_e \lesssim 2.5 \times 10^{-8}\,{\rm cm}^{-3}$ guarantees the required achromaticity of the dimming below the 3% level between the B and V bands. The choice $B_{\rm nG}$ of a few and $g_{10} \approx 0.1$ in CKT I and II falls in the region where the observed SN-dimming could be explained while being marginally compatible with the bounds on the intergalactic B field and on the axion-photon coupling.

7.4 CMB Constraints

If photon-axion conversion over cosmological distances is responsible for the SN Ia dimming, the same phenomenon should also leave an imprint in the CMB. A similar argument was previously considered for photon-graviton conversion [31]. Qualitatively, in the energy-dependent region of $P_{\gamma\to a}$ one expects a rather small effect due to the low energy of CMB photons ($\omega \sim 10^{-4}\,\mathrm{eV}$). However, when accounting for the incoherent integration over many domains crossed by the photon, appreciable spectral distortions may arise in view of the accuracy of the CMB data at the level of one part in 10^4–10^5. For the same reason, in the energy-independent region, at much lower values of n_e than for the SNe Ia, the constraints on $g_{10}B_{\mathrm{nG}}$ are expected to be quite severe. The depletion of CMB photons in the patchy magnetic sky and its effect on the CMB anisotropy pattern have been previously considered [15]. However, more stringent limits come from the distortion of the overall blackbody spectrum [32].

To this end, the COBE/FIRAS data for the experimentally measured spectrum were used, corrected for foregrounds [33]. Note that the new calibration of FIRAS [34] is within the old errors and would not change any of our conclusions. The $N = 43$ data points Φ_i^{exp} at different energies ω_i are obtained by summing the best-fit blackbody spectrum (Fig. 7.6) to the residuals reported in [33]. The experimental errors σ_i and the correlation indices ϱ_{ij} between different energies are also available. In the presence of photon-axion conversion, the original intensity of the "theoretical blackbody" at temperature T

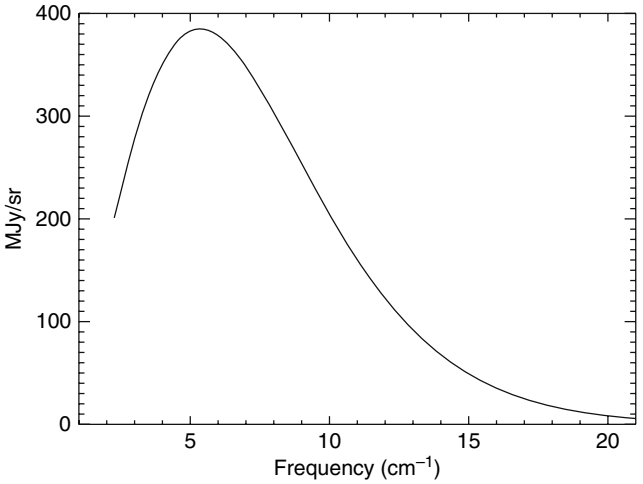

Fig. 7.6. Uniform CMB spectrum and fit to the blackbody spectrum. Uncertainties are a small fraction of the line thickness (Figure from [33] with permission)

$$\Phi^0(\omega, T) = \frac{\omega^3}{2\pi^2}\left[\exp(\omega/T) - 1\right]^{-1} \tag{7.26}$$

would convert to a deformed spectrum that is given by

$$\Phi(\omega, T) = \Phi^0(\omega, T) P_{\gamma\to\gamma}(\omega) \ . \tag{7.27}$$

In [32], we built the reduced chi-squared function

$$\chi^2_\nu(T, \lambda) = \frac{1}{N-1} \sum_{i,j=1}^{N} \Delta\Phi_i (\sigma^2)^{-1}_{ij} \Delta\Phi_j \ , \tag{7.28}$$

where

$$\Delta\Phi_i = \Phi_i^{\rm exp} - \Phi^0(\omega_i, T) P_{\gamma\to\gamma}(\omega_i, \lambda) \tag{7.29}$$

is the i-th residual, and

$$\sigma^2_{ij} = \varrho_{ij} \sigma_i \sigma_j \tag{7.30}$$

is the covariance matrix. We minimize this function with respect to T for each point in the parameter space $\lambda = (n_e, g_{10} B_{\rm nG})$; i.e., T is an empirical parameter determined by the χ^2_ν minimization for each λ rather than being fixed at the standard value $T_0 = 2.725 \pm 0.002$ K [34]. In principle, one should marginalize also over the galactic foreground spectrum [33]. However, this is a subleading effect relative to the spectral deformation caused by the photon-axion conversion.

In Fig. 7.7 we show the exclusion contour in the plane of n_e and $g_{10} B_{\rm nG}$. The region above the continuous curve is the excluded region at 95% CL, i.e., in this region the probability to get larger values of χ^2_ν is lower than 5%. We also show the corresponding 99% CL contour which is very close to the 95% contour so that another regression method and/or exclusion criterion would not change the results very much. Within a factor of a few, the same contours also hold if one varies the domain size s within a factor of 10. Comparing this exclusion plot with the iso-dimming curves of Fig. 7.5, we conclude that the entire region $n_e \lesssim 10^{-9}\,{\rm cm}^{-3}$ is excluded as a leading explanation for SN-dimming.

A few comments are in order. Intergalactic magnetic fields probably are a relatively recent phenomenon in the cosmic history, arising only at redshifts of a few. As a first approximation, we have considered the photon-axion conversion as happening for present ($z = 0$) CMB photons. As $P_{\gamma\to\gamma}$ is an increasing function of the photon energy ω, our approach leads to conservative limits. Moreover, we assumed no correlation between n_e and the intergalactic magnetic field strength. It is, however, physically expected that the fields are positively correlated with the plasma density so that relatively high values of $g_{10} B_{\rm nG}$ should be more likely when n_e is larger. Our constraints in the region of $n_e \gtrsim 10^{-10}\,{\rm cm}^{-3}$ are thus probably tighter than what naively appears.

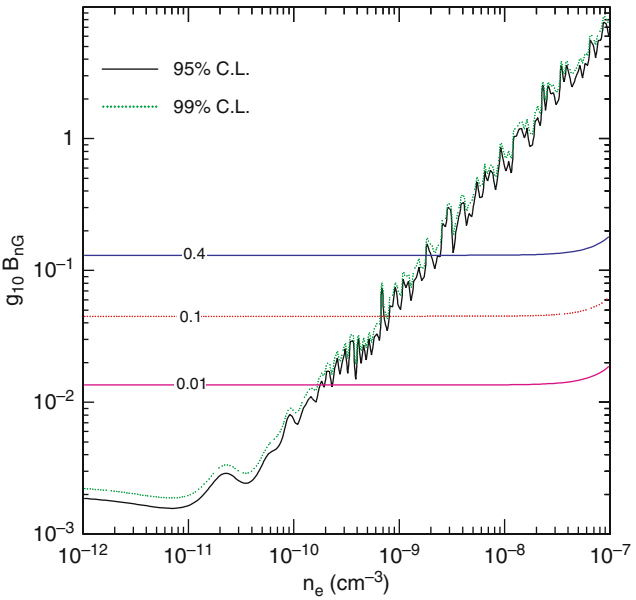

Fig. 7.7. Exclusion plot for axion-photon conversion based on the COBE/FIRAS CMB spectral data. The region above the solid curve is excluded at 95% CL whereas the one above the dotted curve is excluded at 99% CL. The size of each magnetic domain is fixed at $s = 1\,\mathrm{Mpc}$. We also reproduce the iso-dimming contours from Fig. 7.5 (Figure from [32] with permission)

7.5 QSO Constraints

CMB limits are nicely complementary to the ones obtained from the effects of photon-axion conversion on quasar colors and spectra [35]. One effect of photon-axion oscillations is that a dispersion is added to the quasar spectra due to the energy-dependence of the effect. By comparing the dispersion observed in quasar spectra with the dispersion in simulated ones, one can find out whether the model behind each simulation is allowed. The SuperNova Observation Calculator (SNOC) [36] was used [35] to simulate the effects of photon-axion oscillations on quasar observations (Fig. 7.8). If the simulated dispersion is smaller than observed, one cannot exclude the scenario as real quasars have an intrinsic dispersion.

In Fig. 7.9, we superimpose the CMB exclusion contours with the schematic region excluded by quasars[1]. The region to the right of the dot-dashed line is excluded by requiring achromaticity of SN Ia dimming [30]. The

[1] We use the exclusion regions of astro-ph/0410501v1. In the published version [35], corresponding to astro-ph/0410501v2, the iso-dimming curves were erroneously changed. The difference is that in version 1 the angle α in equation (3) of [35] that characterizes the random magnetic field direction was correctly taken in the

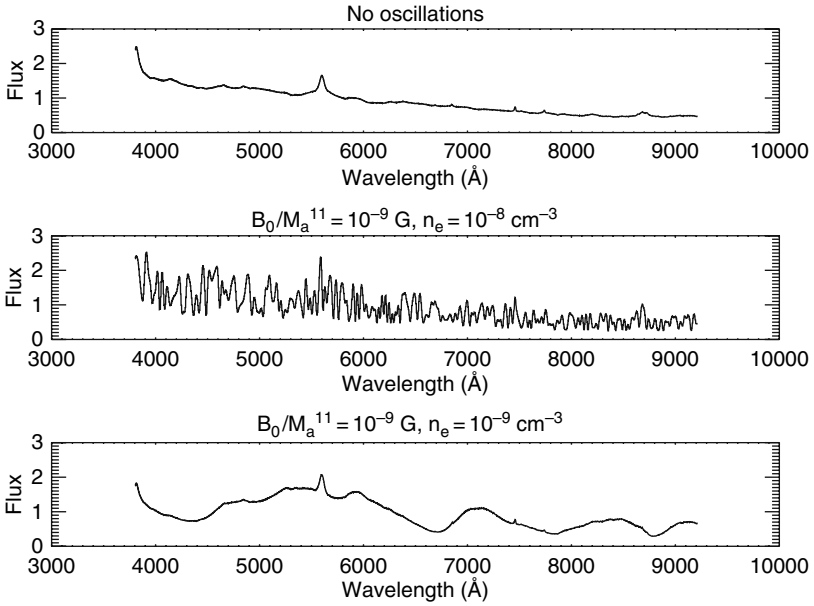

Fig. 7.8. Simulated quasar spectra at $z = 1$ for different photon-axion oscillation scenarios (Figure from [35] with permission)

region inside the dashed lines is excluded by the dispersion in QSO spectra. Moreover, assuming an intrinsic dispersion of 5% in these spectra, the excluded region could be enlarged up to the dotted lines. The CMB argument excludes the region above the solid curve at 95% CL.

A cautionary remark is in order when combining the two constraints. As we have discussed in the previous section, CMB limits on photon-axion conversion are model-independent. On the other hand, the limits placed by the QSO spectra may be subject to loop holes, as they are based on a full correlation between the intergalactic electron density and the magnetic field strength, which is reasonable but not well established observationally.

7.6 Constraints from Angular Diameter Distance

We now turn briefly to two other types of constraints on the photon-axion conversion mechanism. The first is based on angular diameter distance measurements of radio-galaxies. For a source of linear radius r and angular diameter θ, the angular diameter distance is

$$\mathrm{d}_A = \frac{2r}{\theta} \,. \tag{7.31}$$

interval 0–360°, whereas in version 2 it was taken in the interval 0–90° (private communication by the authors).

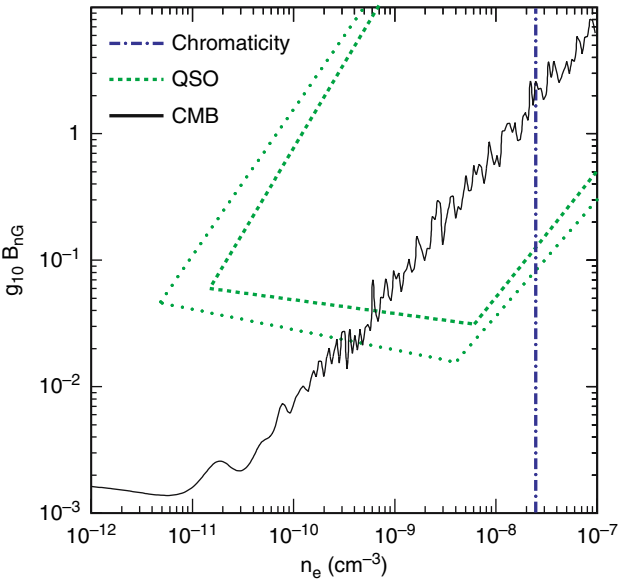

Fig. 7.9. Exclusion plot for photon-axion conversion. The region to the right of the dot-dashed line is excluded by requiring achromaticity of SN Ia dimming. The region inside the dashed lines is excluded by the dispersion in QSO spectra. Assuming an intrinsic dispersion of 5% in QSO spectra, the excluded region could be extended up to the dotted curve. The CMB argument excludes the entire region above the solid curve at 95% CL (Figure from [32] with permission)

In metric theories where photons travel on null geodesics and their number is conserved, the angular distance d_A and the luminosity distance d_L are fundamentally related by the reciprocity relation [37]

$$\mathrm{d}_L(z) = (1+z)^2 \mathrm{d}_A(z)\ . \tag{7.32}$$

Photon-axion conversion in intergalactic magnetic fields would not affect the angular-diameter distance [38, 39] and hence would cause a fundamental asymmetry between measurements of $\mathrm{d}_L(z)$ and $\mathrm{d}_A(z)$.

In a first search for a violation of the reciprocity relation, a joint analysis of high-redshift SNe Ia $[\mathrm{d}_L(z)]$ and radio galaxies $[\mathrm{d}_A(z)]$ was undertaken [38]. The results do not favor the loss of photons and hence disfavor mixing. However, this constraint is less robust than the QSO one because it is affected by possibly large systematic errors that are difficult to quantify [40].

As angular-diameter distance is immune to the loss of photons, the axion-conversion versus accelerating-universe ambiguity in the interpretation can be resolved [41] by combining CMB acoustic peak measurements with the recent detection of baryon oscillations in galaxy power spectra [42]. This

combination excludes a non-accelerating dark-energy species at the 4σ level regardless of the level of the axion coupling.

7.7 Conclusions

We have reviewed the intriguing and phenomenologically rich [43] mechanism of conversion of photons into very low-mass axion-like particles in the presence of intergalactic magnetic fields. We have examined the existing astrophysical and cosmological limits on this model, coming from the distortion of the CMB spectrum, from the quasar dispersion, and from the angular diameter distance, including the baryon oscillations detected in large-scale structure surveys.

In particular, we have shown that the resulting CMB spectral deformation excludes a previously allowed parameter region corresponding to very low densities of the intergalactic medium (IGM). These limits are complementary to the ones derived from QSO dispersion that place serious constraints on the axion-photon conversion mechanism, especially for relatively large densities of the IGM. As a result, it appears that the photon-axion conversion will not play a leading role for the apparent SN Ia dimming.

It may still happen that ultra-light or massless axions play an important cosmological role. For example, it was shown that by adding a photon-axion conversion mechanism on top of a dark-energy model with $w \gtrsim -1$, one can mimic cosmic equations of state as negative as $w \simeq -1.5$ [44]. Although at present there is no need for such an extreme equation of state, it is an interesting possibility to keep in mind, especially as alternative explanations as ghost/phantom fields usually pose a threat to very fundamental concepts in general relativity and quantum field theory.

Acknowledgments

A. Mirizzi and G. Raffelt thank the organizers of the Joint ILIAS-CAST-CERN Axion Training at CERN for their kind hospitality. In Munich, this work was supported, in part, by the Deutsche Forschungsgemeinschaft under grant No. SFB 375 and by the European Union under the ILIAS project, contract No. RII3-CT-2004-506222. A. Mirizzi was supported, in part, by the Istituto Nazionale di Fisica Nucleare (INFN) and by the Ministero dell'Istruzione, Università e Ricerca (MIUR) through the "Astroparticle Physics" research project.

Appendix A: A Photon-Axion Conversion in a Random Background

In the following, we derive (7.17) along the lines of [23]. It is assumed that photons and axions traverse N domains of equal length s. The component of the magnetic field perpendicular to the direction of flight $\mathbf{B}_{\rm T}$ is constant within each domain and of equal strength ($B \equiv |\mathbf{B}_{\rm T}|$) in each domain, but it is assumed to have a random orientation in each cell.

We begin with an initial state that is a coherent superposition of an axion and the two photon states $|A_{1,2}\rangle$ that correspond respectively to photons polarized parallel and perpendicular to the magnetic field in the first domain,

$$\kappa_1(0)|A_1\rangle + \kappa_2(0)|A_2\rangle + \kappa_a(0)|a\rangle \; . \tag{7.33}$$

The initial photon and axion fluxes are

$$I_\gamma(0) \sim |\kappa_1(0)|^2 + |\kappa_2(0)|^2 \; , \tag{7.34}$$

$$I_a(0) \sim |\kappa_a(0)|^2 \; , \tag{7.35}$$

respectively. In the n-th domain the transverse magnetic field $\mathbf{B}_{\rm T}$ is tilted by an angle γ_n compared to the magnetic field in the first domain

$$|A_\parallel^n\rangle = c_n|A_1\rangle + s_n|A_2\rangle \; , \tag{7.36}$$

$$|A_\perp^n\rangle = -s_n|A_1\rangle + c_n|A_2\rangle \; , \tag{7.37}$$

or

$$c_1(z) = c_n\kappa_\parallel^n(z) - s_n\kappa_\perp^n(z) \; , \tag{7.38}$$

$$c_2(z) = s_n\kappa_\parallel^n(z) + c_n\kappa_\perp^n(z) \; , \tag{7.39}$$

where $c_n = \cos\gamma_n$ and $s_n = \sin\gamma_n$. Only photons polarized parallel to the magnetic field mix with axions. The values of the transition elements are equal in each domain as the magnitude of the magnetic field B has been assumed to be the same everywhere. The transition probability P_0 for photon to axion oscillation in one domain is given by (7.15), and the photon survival probability is $1 - P_0$. At the end of the n-th domain, the photon and axion fluxes are

$$I_\gamma(n+1) \sim (1 - P_0c_n^2)|\kappa_1(z_n)|^2 \tag{7.40}$$

$$+(1 - P_0s_n^2)|\kappa_2(z_n)|^2 + P_0|\kappa_a(z_n)|^2 + \cdots \tag{7.41}$$

$$I_a(n+1) \sim P_0c_n^2|\kappa_1(z_n)|^2$$

$$+P_0s_n^2|\kappa_2(z_n)|^2 + (1 - P_0)|\kappa_a(z_n)|^2 + \cdots \tag{7.42}$$

where the dots represent terms that are proportional to c_n, s_n, or c_ns_n. We have defined $z_n = (n-1)s$. The coefficients κ_1, κ_2 and κ_a are taken at the beginning of the n-th domain.

Next, we assume that the transition probability in one domain is small, i.e., $P_0 \ll 1$, and the direction of the magnetic field is random, i.e., γ_n is a random variable so that $\gamma_{n+1} - \gamma_n$ is of order unity. Due to the randomness of the magnetic field, in this limit c_n^2 and s_n^2 can be replaced by their average value 1/2, while the interference terms c_n, s_n and $c_n s_n$ are averaged to zero. Using

$$I_\gamma(n) \sim |\kappa_1(z_n)|^2 + |\kappa_2(z_n)|^2 \,, \tag{7.43}$$

$$I_a \sim |\kappa_a(z_n)|^2 \,, \tag{7.44}$$

one arrives at

$$\begin{aligned} \begin{pmatrix} I_\gamma(n+1) \\ I_a(n+1) \end{pmatrix} &= \begin{pmatrix} 1 - \frac{1}{2}P_0 & P_0 \\ \frac{1}{2}P_0 & 1 - P_0 \end{pmatrix} \begin{pmatrix} I_\gamma(n) \\ I_a(n) \end{pmatrix} \\ &= \frac{1}{3} \begin{pmatrix} 2 + \left(1 - \frac{3}{2}P_0\right)^{n+1} & 2 - 2\left(1 - \frac{3}{2}P_0\right)^{n+1} \\ 1 - \left(1 - \frac{3}{2}P_0\right)^{n+1} & 1 + 2\left(1 - \frac{3}{2}P_0\right)^{n+1} \end{pmatrix} \begin{pmatrix} I_\gamma(0) \\ I_a(0) \end{pmatrix} . \end{aligned} \tag{7.45}$$

As the number of domains is large, one can replace $(1 - 3P_0/2)^{n+1}$ with the limiting function $\exp\left[-3P_0 z/(2s)\right]$ to arrive at the final expressions

$$I_\gamma(z) = I_\gamma(0) - P_{\gamma\to a}[I_\gamma(0) - 2I_a(0)] \,, \tag{7.46}$$

$$I_a(z) = I_a(0) + P_{\gamma\to a}[I_\gamma(0) - 2I_a(0)] \,, \tag{7.47}$$

with

$$P_{\gamma\to a} = \frac{1}{3}\left[1 - \exp\left(-\frac{3P_0 z}{2\,s}\right)\right] . \tag{7.48}$$

References

1. Sikivie, P.: Experimental tests of the 'invisible' axion. Phys. Rev. Lett. **51**, 1415 (1983), (E) ibid. **52**, 695 (1984) 115, 117
2. Raffelt, G., Stodolsky, L.: Mixing of the photon with low mass particles. Phys. Rev. D **37**, 1237 (1988) 115, 117
3. Bradley, R., et al.: Microwave cavity searches for dark-matter axions. Rev. Mod. Phys. **75**, 777 (2003) 115
4. van Bibber, K., McIntyre, P.M., Morris, D.E., Raffelt, G.G.: A practical laboratory detector for solar axions. Phys. Rev. D **39**, 2089 (1989) 115
5. Moriyama, S., Minowa, M., Namba, T., Inoue, Y., Takasu, Y., Yamamoto, A.: Direct search for solar axions by using strong magnetic field and X-ray detectors. Phys. Lett. B **434**, 147 (1998) [hep-ex/9805026] 115
6. Inoue, Y., Namba, T., Moriyama, S., Minowa, M., Takasu, Y., Horiuchi, T., Yamamoto, A.: Search for sub-electronvolt solar axions using coherent conversion of axions into photons in magnetic field and gas helium. Phys. Lett. B **536**, 18 (2002) [astro-ph/0204388] 115
7. Zioutas, K., et al. (CAST Collaboration): First results from the CERN axion solar telescope (CAST). Phys. Rev. Lett. **94**, 121301 (2005) [hep-ex/0411033] 115, 121

8. Raffelt, G.G.: Stars as Laboratories for Fundamental Physics. University of Chicago Press, Chicago (1996) [115, 116, 117, 121]
9. Raffelt, G.G.: Particle physics from stars. Annu. Rev. Nucl. Part. Sci. **49**, 163 (1999) [hep-ph/9903472] [115]
10. Harari, D., Sikivie, P.: Effects of a Nambu-Goldstone boson on the polarization of radio galaxies and the cosmic microwave background. Phys. Lett. B **289**, 67 (1992) [115]
11. Hutsemekers, D., Cabanac, R., Lamy, H., Sluse, D.: Mapping extreme-scale alignments of quasar polarization vectors. Astron. Astrophys. **441**, 915 (2005) [astro-ph/0507274] [115]
12. Krasnikov, S.V.: New astrophysical constraints on the light pseudoscalar photon coupling. Phys. Rev. Lett. **76**, 2633 (1996) [115]
13. Gorbunov, D.S., Raffelt, G.G., Semikoz, D.V.: Axion-like particles as ultrahigh-energy cosmic rays?. Phys. Rev. D **64**, 096005 (2001) [hep-ph/0103175] [115]
14. Csáki, C., Kaloper, N., Peloso, M., Terning, J.: Super-GZK photons from photon axion mixing. JCAP 0305, 005 (2003) [hep-ph/0302030] [115]
15. Csáki, C., Kaloper, N., Terning, J.: (CKT I), Dimming supernovae without cosmic acceleration. Phys. Rev. Lett. **88**, 161302 (2002) [hep-ph/0111311] [115, 122, 125]
16. Riess, A.G., et al. (Supernova Search Team Collaboration): Observational evidence from supernovae for an accelerating universe and a cosmological constant. Astron. J. **116**, 1009 (1998) [astro-ph/9805201] [115, 119, 120]
17. Perlmutter, S., et al. (Supernova Cosmology Project Collaboration): Measurements of Ω and Λ from 42 high-redshift supernovae. Astrophys. J. **517**, 565 (1999) [astro-ph/9812133] [115, 119, 120, 122]
18. Riess, A.G., et al. (Supernova Search Team Collaboration): Type Ia supernova discoveries at $z > 1$ from the Hubble Space Telescope: Evidence for past deceleration and constraints on dark energy evolution. Astrophys. J. **607**, 665 (2004) [astro-ph/0402512] [115]
19. Carroll, S.M.: Why is the universe accelerating? eConf C0307282 (2003) TTH09 [AIP Conf. Proc. **743**, 16 (2005), astro-ph/0310342] [116]
20. Anselm, A.A.: Experimental test for arion $\leftrightarrow$ photon oscillations in a homogeneous constant magnetic field. Phys. Rev. D **37**, 2001 (1988) [117]
21. Deffayet, C., Harari, D., Uzan, J.P., Zaldarriaga, M.: Dimming of supernovae by photon-pseudoscalar conversion and the intergalactic plasma. Phys. Rev. D **66**, 043517 (2002) [hep-ph/0112118] [117, 122, 123]
22. Kuo, T.K., Pantaleone, J.T.: Neutrino oscillations in matter. Rev. Mod. Phys. **61**, 937 (1989) [118]
23. Grossman, Y., Roy, S., Zupan, J.: Effects of initial axion production and photon axion oscillation on type Ia supernova dimming. Phys. Lett. B **543**, 23 (2002) [hep-ph/0204216] [119, 131]
24. Kronberg, P.P.: Extragalactic magnetic fields. Rept. Prog. Phys. **57**, 325 (1994) [121]
25. Spergel, D.N., et al. (WMAP Collaboration): First year Wilkinson Microwave Anisotropy Probe (WMAP) observations: determination of cosmological parameters. Astrophys. J. Suppl. **148**, 175 (2003) [astro-ph/0302209] [121]
26. Anselm, A.A., Uraltsev, N.G.: A second massless axion? Phys. Lett. B **114**, 39 (1982) [121]
27. Anselm, A.A., Uraltsev, N.G.: Long range 'arion' field in the radiofrequency band. Phys. Lett. B **116**, 161 (1982) [121]

28. Brockway, J.W., Carlson, E.D., Raffelt, G.G.: SN 1987A gamma-ray limits on the conversion of pseudoscalars. Phys. Lett. B **383**, 439 (1996) [astro-ph/9605197] 121
29. Grifols, J.A., Massó, E., Toldrà, R.: Gamma rays from SN 1987A due to pseudoscalar conversion. Phys. Rev. Lett. **77**, 2372 (1996) [astro-ph/9606028] 121
30. Csáki, C., Kaloper, N., Terning, J.: (CKT II), Effects of the intergalactic plasma on supernova dimming via photon axion oscillations. Phys. Lett. B **535**, 33 (2002) [hep-ph/0112212] 123, 127
31. Chen, P.: Resonant photon-graviton conversion and cosmic microwave background fluctuations. Phys. Rev. Lett. **74**, 634 (1995); (E) ibid. **74**, 3091 (1995) 125
32. Mirizzi, A., Raffelt, G.G., Serpico, P.D.: Photon axion conversion as a mechanism for supernova dimming: Limits from CMB spectral distortion. Phys. Rev. D **72**, 023501 (2005) [astro-ph/0506078] 124, 125, 126, 127, 129
33. Fixsen, D.J., Cheng, E.S., Gales, J.M., Mather, J.C., Shafer, R.A., Wright, E.L.: The cosmic microwave background spectrum from the full COBE/FIRAS data set. Astrophys. J. **473**, 576 (1996) [astro-ph/9605054] 125, 126
34. Mather, J.C., Fixsen, D.J., Shafer, R.A., Mosier, C., Wilkinson, D.T.: Calibrator design for the COBE far infrared absolute spectrophotometer (FIRAS). Astrophys. J. 512 (1999) 511 [astro-ph/9810373] 125, 126
35. Ostman, L., Mörtsell, E.: Limiting the dimming of distant type Ia supernovae. JCAP 0502, 005 (2005) [astro-ph/0410501] 127, 128
36. Goobar, A., Mörtsell, E., Amanullah, R., Goliath, M., Bergström, L., Dahlen, T.: SNOC: a Monte-Carlo simulation package for high-z supernova observations. Astron. Astrophys. **392**, 757 (2002) [astro-ph/0206409] 127
37. Schneider, P., Ehlers, J., Falco, E.E.: Gravitational lenses. Springer-Verlag, Berlin (1992) 129
38. Bassett, B.A., Kunz, M.: Cosmic acceleration versus axion photon mixing. Astrophys. J. **607**, 661 (2004) [astro-ph/0311495] 129
39. Bassett, B.A., Kunz, M.: Cosmic distance-duality as a probe of exotic physics and acceleration. Phys. Rev. D **69**, 101305 (2004) [astro-ph/0312443] 129
40. Uzan, J.P., Aghanim, N., Mellier, Y.: The distance duality relation from X-ray and Sunyaev-Zel'dovich observations of clusters. Phys. Rev. D **70**, 083533 (2004) [astro-ph/0405620] 129
41. Song, Y.S., Hu, W.: Constraints on supernovae dimming from photon-pseudo scalar coupling. Phys. Rev. D **73**, 023003 (2006) [astro-ph/0508002] 129
42. Eisenstein, D.J., et al.: Detection of the baryon acoustic peak in the large-scale correlation function of SDSS luminous red galaxies. Astrophys. J. **633**, 560 (2005) [astro-ph/0501171] 129
43. Das, S., Jain, P., Ralston, J.P., Saha, R.: Probing dark energy with light: Propagation and spontaneous polarization. JCAP 0506, 002 (2005) [hep-ph/0408198] 130
44. Csáki, C., Kaloper, N., Terning, J.: Exorcising $w < -1$. Annals Phys. **317**, 410 (2005) [astro-ph/0409596] 130

8 Microwave Cavity Searches

Gianpaolo Carosi[1] and Karl van Bibber[2]

Lawrence Livermore National Laboratory, Livermore, CA, 94550, USA
[1] carosi2@llnl.gov
[2] vanbibber1@llnl.gov

Abstract. This chapter will cover the search for dark matter axions based on microwave cavity experiments proposed by Pierre Sikivie. We will start with a brief overview of halo dark matter and the axion as a candidate. The principle of resonant conversion of axions in an external magnetic field will be described as well as practical considerations in optimizing the experiment as a signal-to-noise problem. A major focus of this chapter will be the two complementary strategies for ultra-low noise detection of the microwave photons – the "photon-as-wave" approach (i.e., conventional heterojunction amplifiers and soon to be quantum-limited SQUID devices), and the "photon-as-particle" approach (i.e., Rydberg-atom single-quantum detection). Experimental results will be presented; these experiments have already reached well into the range of sensitivity to exclude plausible axion models, for limited ranges of mass. The chapter will conclude with a discussion of future plans and challenges for the microwave cavity experiment.

8.1 Dark Matter and the Axion

Recent precision measurements of various cosmological parameters have revealed a universe of which only a small fraction can be observed directly. Measurements of deuterium abundances predicted from the theory of big bang nucleosynthesis (BBN) have limited the familiar baryonic matter to a mere 4% of the universe's total energy density [1]. Evidence from the cosmic microwave background, combined with supernovae searches, galaxy surveys, and other measurements lead to the fascinating conclusion that the vast majority of the universe is made of gravitating "dark matter" (26%) and a negative pressure "dark energy" (70%) [2].

Though the evidence for "dark energy" is relatively recent (primarily resting on cosmological supernovae surveys taken over the last decade), the existence of "dark matter" has been known since the early 1930s. It was then that Fritz Zwicky, surveying the Coma cluster, noticed that member galaxies were moving far too quickly to be gravitationaly bound by the luminous matter [3]. Either they were unbound, which meant the cluster should have ripped apart billions of years ago or there was a large amount of unseen "dark matter" keeping the system together. Since those first observations evidence for dark matter has accumulated on scales as small as dwarf galaxies (kiloparsecs) to the size of the observable universe (gigaparsecs) [4, 5].

G. Carosi and K. van Bibber: *Microwave Cavity Searches*, Lect. Notes Phys. **741**, 135–156 (2008)
DOI 10.1007/978-3-540-73518-2_8

Currently, the best dark matter candidates appear to be undiscovered non-baryonic particles left over from the big bang.[1] By definition, they would have only the feeblest interactions with standard-model particles such as baryons, leptons and photons. Studies of structure formation in the universe suggest that the majority of this dark matter is "cold", i.e., non-relativistic at the beginning of galactic formation. As it is collisionless, relativistic dark matter would tend to stream out of initial density perturbations effectively smoothing out the universe before galaxies had a chance to form [10]. The galaxies that we observe today tend to be embedded in large halos of dark matter that extend much further than their luminous boundaries. Measurements of the Milky Way's rotation curves (along with other observables such as microlensing surveys) constrain the density of dark matter near the solar system to roughly $\varrho_{\mathrm{CDM}} \approx 0.45\,\mathrm{GeV\,cm^{-3}}$ [11].

The two most popular dark matter candidates are the general class of Weakly Interacting Massive Particles (WIMPs), one example being the supersymmetric neutralino, and the axion, predicted as a solution to the "Strong CP" problem. Though both particles are well motivated, this discussion will focus exclusively on the axion. As described in Chap. 1, the axion is a light chargeless pseudo-scalar boson (negative parity, spin-zero particle) predicted from the breaking of the Peccei-Quinn symmetry. This symmetry was originally introduced in the late 1970s to explain why charge (C) and parity (P) appear to be conserved in strong interactions, even though the QCD Lagrangian has an explicitly CP-violating term. Experimentally this CP-violating term should have lead to an easily detectable electric dipole moment in the neutron, but none has been observed to very high precision [12].

The key parameter defining most of the axion's characteristics is the spontaneous symmetry breaking (SSB) scale of the Peccei-Quinn symmetry f_a. Both the axion coupling and mass are inversely proportional to f_a with the mass defined as

$$m_a \simeq 6.3\,\mathrm{eV}\left(\frac{10^6\,\mathrm{GeV}}{f_a}\right)\,, \tag{8.1}$$

and the coupling of axions to photons ($g_{a\gamma\gamma}$) expressed as

$$g_{a\gamma\gamma} \equiv \frac{\alpha}{2\pi f_a} C\,, \tag{8.2}$$

where α is the fine structure constant, and C is a dimensionless model-dependent coupling parameter (compare (3.4)). Generally, C is thought to

[1] Even without the limits from Big Bang Nucleosynthesis searches for baryonic dark matter in cold gas clouds [6] or MAssive Compact Halo Objects (MACHOs), like brown dwarfs [7, 8], have not detected nearly enough to account for the majority of dark matter. Attempts to modify the laws of gravity at larger scales have also had difficulties matching observations [9].

be $\sim$0.97 for the class of axions denoted KSVZ (for Kim-Shifman-Vainshtein-Zakharov) and ~ -0.36 for the more pessimistic grand-unification-theory inspired DFSZ (for Dine-Fischler-Srednicki-Zhitnitshii) models [13, 14, 15, 16]. As interactions are proportional to the square of the couplings these values of C tend to constrain the possible axion-to-photon conversion rates to only about an order of magnitude at any particular mass.

Initially f_a was believed to be around the electroweak scale ($f_a \sim 250\,\mathrm{GeV}$) resulting in an axion mass of order 100 keV and couplings strong enough to be seen in accelerators [17, 18]. Searches for axions in particle and nuclear experiments, along with limits from astrophysics, soon lowered its possible mass to $m_a \leq 3 \times 10^{-3}\,\mathrm{eV}$ corresponding to $f_a \geq 10^9\,\mathrm{GeV}$ [19]. As their couplings are inversely proportional to f_a, these low-mass axions were initially thought to be undetectable and were termed "invisible" axions.

From cosmology it was found that a general lower limit as well could be placed on the axion mass. At the time of the big bang, axions would be produced in copious amounts via various mechanisms described in previous chapters. The total contributions to the energy density of the universe from axions created via the vacuum misalignment method can then be expressed as

$$\Omega_a \sim \left(\frac{5\,\mu\mathrm{eV}}{m_a}\right)^{7/6}, \tag{8.3}$$

which puts a lower limit on the axion mass of $m_a \geq 10^{-6}\,\mathrm{eV}$ (any lighter and the axions would overclose the universe, $\Omega_a \geq 1$). Combined with the astrophysical and experimental limits this results in a 3-decade mass range for the axion, from μeV–meV, with the lower masses more likely if the axion is the major component of dark matter. The axions generated in the early universe around the QCD phase transition, when the axion mass turns on, would have momenta $\sim 10^{-8}\,\mathrm{eV\,c^{-1}}$ while the surrounding plasma had a temperature $T \simeq 1\,\mathrm{GeV}$ [19]. Furthermore, such axions are so weakly-coupling that they would never be in thermal equilibrium with anything else. This means they would constitute non-relativistic "cold" dark matter from the moment they appeared and could start to form structures around density perturbations relatively quickly.

Today the axion dark matter in the galaxy would consist of a large halo of particles moving with relative velocities of the order of $10^{-3}c$. It is unclear whether any or all of the axions would be gravitationally thermalized, but, in order for them to be bound in the galaxy, they would have to be moving less than the local escape velocity of $2 \times 10^{-3}c$. It is possible that non-thermalized axions could still be oscillating into and out of the galaxy's gravitational well. These axions would have extraordinarily tiny velocity dispersions (of the order of $10^{-17}c$ [20]), and the differences in velocity from various infalls (first time falling into the galaxy, first time flying out, second time falling in, etc.) would be correlated with the galaxy's development.

8.2 Principles of Microwave Cavity Experiments

Pierre Sikivie was the first to suggest that the "invisible" axion could actually be detected [21]. This possibility rests on the coupling of axions to photons given by

$$L_{a\gamma\gamma} = -g_{a\gamma\gamma}\,\mathbf{E}\cdot\mathbf{B}\,a = -\left(\frac{\alpha}{2\pi f_a}C\right)\mathbf{E}\cdot\mathbf{B}\,a\,, \tag{8.4}$$

where $\mathbf{E}$ and $\mathbf{B}$ are the standard electric and magnetic field of the coupling photons, α is the fine structure constant and C is the model-dependent coefficient mentioned in the previous section [19]. Translating this to a practical experiment Sikivie suggested that axions passing through an electromagnetic cavity permeated with a magnetic field could resonantly convert into photons when the cavity resonant frequency (ω) matched the axion mass (m_a). As the entire mass of the axion would be converted into a photon, a 5 μeV axion at rest would convert to a 1.2 GHz photon, which could be detected with sensitive microwave receivers. The predicted halo axion velocities $\beta \approx 10^{-3}$ would predict a spread in the axion energy, from $E_a = m_a c^2 + \frac{1}{2}m_a c^2\beta^2$, of the order of 10^{-6}. For our example 5 μeV axions, this would translate into a 1.2 kHz upward spread in the frequency of converted photons. The power of axions converting to photons on resonance in a microwave cavity is given by

$$\begin{aligned} P_a &= g_{a\gamma\gamma}^2 V B_0^2 \varrho_a C_{lmn} \frac{1}{m_a} \min\left(Q_L, Q_a\right) \\ &= 0.5\times 10^{-26}\,\mathrm{W}\left(\frac{V}{500\,\mathrm{l}}\right)\left(\frac{B_0}{7\,\mathrm{T}}\right)^2 C \left(\frac{g_\gamma}{0.36}\right)^2 \\ &\quad\times\left(\frac{\varrho_a}{0.5\times 10^{-24}\,\mathrm{g\,cm^{-3}}}\right) \\ &\quad\times\left(\frac{m_a}{2\pi(\mathrm{GHz})}\right)\min\left(Q_L, Q_a\right)\,, \end{aligned} \tag{8.5}$$

where V is the cavity volume, B_0 is the magnetic field, Q_L is the cavity's loaded quality factor (defined as center frequency over frequency bandwidth), $Q_a = 10^6$ is the quality factor of the axion signal (axion energy over spread in energy or $1/\beta^2$), ϱ_a is the axion mass density at the detection point (earth), and C_{lmn} is the form factor for one of the transverse magnetic (TM_{lmn}) cavity modes (see Sect. 8.3.2 for more on cavity modes). This form factor is essentially the normalized overlap integral of the external static magnetic field, $\mathbf{B_0}(\mathbf{x})$, and the oscillating electric field, $\mathbf{E}_\omega(\mathbf{x})e^{i\omega t}$, of that particular cavity mode. It can be determined using

$$C = \frac{\left|\int_V \mathrm{d}^3x \mathbf{E}_\omega\cdot\mathbf{B}_0\right|^2}{\mathbf{B}_0^2 V\int_V \mathrm{d}^3x\epsilon|\mathbf{E}_\omega|^2}\,, \tag{8.6}$$

where ϵ is the dielectric constant in the cavity.

For a cylindrical cavity with a homogeneous longitudinal magnetic field the TM_{010} mode provides the largest form factor ($C_{010} = 0.69$ [19]). Though

model-dependent, equation (8.5) can give an idea of the incredibly small signal, measured in yoctowatts (10^{-24} W), expected from axion-photon conversions in a resonant cavity. This is much smaller than the 2.5×10^{-21} W of power received from the last signal of the Pioneer 10 spacecraft's 7.5 W transmitter in 2002, when it was 12.1 billion kilometers from earth [22].

Currently the axion mass is constrained between a μeV and a meV corresponding to a frequency range for converted photons between 240 MHz and 240 GHz. To maintain the resonant quality of the cavity, however, only a few kHz of bandwidth can be observed at any one time. As a result, the cavity needs to be tunable over a large range of frequencies in order to cover all possible values of the axion mass. This is accomplished using metallic or dielectric tuning rods running the length of the cavity cylinder. Moving the tuning rods from the edge to the center of the cavity shifts the resonant frequency by up to 100 MHz.

Even when the cavity is exactly tuned to the axion mass, detection is possible only if the microwave receiver is sensitive enough to distinguish the axion conversion signal over the background noise from the cavity and the electronics. The signal to noise ratio (SNR) can be calculated from the Dicke radiometer equation [23]

$$\mathrm{SNR} = \frac{P_a}{\bar{P}_N}\sqrt{Bt} = \frac{P_a}{k_\mathrm{B} T_\mathrm{S}}\sqrt{\frac{t}{B}}\,, \tag{8.7}$$

where P_a is the axion conversion power, $\bar{P}_N = k_\mathrm{B} B T_\mathrm{S}$ is the average thermal noise power, B is the bandwidth, T_S is the total system noise temperature (cavity plus electronics), and t is the signal integration time [19]. With the bandwidth of the experiment essentially set by the axion mass and anticipated velocity dispersion ($\beta^2 \sim 10^{-6}$), the SNR can be raised by increasing the signal power ($P_a \propto B_0^2 V$), lowering the noise temperature or integrating for a longer period of time. Increasing the size of the magnetic field or the volume of the cavity to boost the signal power can get prohibitively expensive fairly quickly. Given the large range of possible masses, the integration time needs to remain relatively short (of order 100 seconds for every kHz) in order to scan an appreciable amount in time scales of a year or so. If one chooses a specific SNR that would be acceptable for detection, then a scanning rate can be defined as

$$\begin{aligned}\frac{\mathrm{d}f}{\mathrm{d}t} = \frac{12\,\mathrm{GHz}}{\mathrm{yr}} &\left(\frac{4}{\mathrm{SNR}}\right)^2 \left(\frac{V}{500\,\mathrm{l}}\right) \left(\frac{B_0}{7\ T}\right)^4 \\ &\times C^2 \left(\frac{g_\gamma}{0.36}\right)^4 \left(\frac{\varrho_a}{5\times 10^{-25}}\right)^2 \\ &\times \left(\frac{3K}{T_\mathrm{S}}\right)^2 \left(\frac{f}{\mathrm{GHz}}\right)^2 \frac{Q_\mathrm{L}}{Q_\mathrm{a}}\,. \end{aligned} \tag{8.8}$$

Given that all other parameters are more or less fixed, due to physics and budgetary constraints, the sensitivity of the experiment (both in coupling reach and in scanning speed) can only practically be improved by developing ultra-low-noise microwave receivers. In fact some of the quietest microwave receivers in the world have been developed to detect axions [24].

8.3 Technical Implementation

The first generation of microwave experiments were carried out at Brookhaven National Laboratory (BNL) and at the University of Florida in the mid-1980s [25, 26]. These were proof-of-concept experiments and got within factors of 100–1000 of the sensitivity required to detect plausible dark matter axions (mostly due to their small cavity size and relatively high noise temperatures) [19]. In the early 1990s second generation cavity experiments were developed at Lawrence Livermore National Laboratory (LLNL) in the U.S. and in Kyoto, Japan. Though both used a microwave cavity to convert the axions to photons, they each employed radically different detection techniques. The U.S. experiment focused on improving coherent microwave amplifiers (photons as waves) while the Japan experiment worked to develop a Rydberg-atom single-quantum detector (photons as particles). As the Kyoto experiment is still in the development phase we will save its description for a later section and focus on the U.S. experiment.

A schematic of the LLNL experiment, dubbed the Axion Dark Matter eXperiment (ADMX), can be seen in Fig. 8.1. The experiment consists of a cylindrical copper-plated steel cavity containing two axial tuning rods. These can be moved transversely from the edge of the cavity wall to its center allowing one to perturb the resonant frequency. The cavity itself is located in the bore of a superconducting solenoid providing a strong constant axial magnetic field. The electromagnetic field of the cavity is coupled to low-noise receiver electronics via a small adjustable antenna [19]. These electronics initially amplify the signal using two ultra-low-noise cryogenic amplifiers arranged in series. The signal is then boosted again via a room temperature post-amplifier and injected into a double-heterodyne receiver. The receiver consists of an image reject mixer to reduce the signal frequency from the cavity resonance (hundreds of MHz–GHz) to an intermediate frequency (IF) of 10.7 MHz. A crystal bandpass filter is then employed to reject noise power outside of a 35 kHz window centered at the IF. Finally, the signal is mixed down to almost audio frequencies (35 kHz) and analyzed by fast-Fourier-transform (FFT) electronics that compute a 50 kHz bandwidth centered at 35 kHz. Data is taken every 1 kHz or so by moving the tuning rods to obtain a new resonant TM_{010} mode. In the next few sections, we will expand on some of these components.

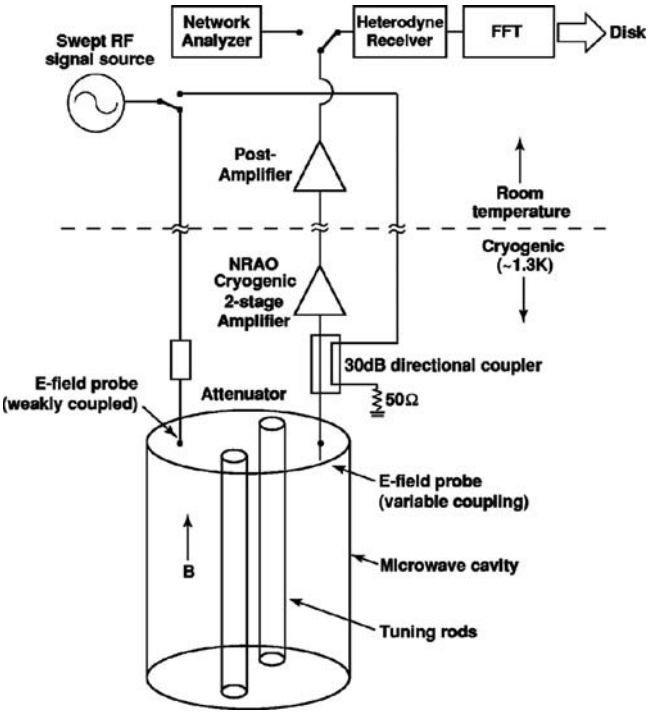

Fig. 8.1. Schematic diagram of ADMX experiment including both the resonant cavity (which sits in the bore of a superconducting solenoid) and receiver electronics chain

8.3.1 The Magnet

The main magnet for ADMX was designed to maximize the $B_0^2 V$ contribution to the signal power (8.5). It was determined that a superconducting solenoid would yield the most cost effective solution and its extremely large inductance (535 Henry) would have the added benefit of keeping the field very stable. The 6 t magnet coil is housed in a 3.6 m tall cryostat (see Fig. 8.2) with an open magnet bore allowing the experimental insert, with the cavity and its liquid helium (LHe) reservoir, to be lowered in. The magnet itself is immersed during operations in a 4.2 K LHe bath in order to keep the niobium-titanium windings superconducting. Generally, the magnet was kept at a field strength of 7.6 T in the solenoid center (falling to approximately 70% strength at the ends), but recently the experiment has been run at fieldstrengths as high as 8.2 T [19].

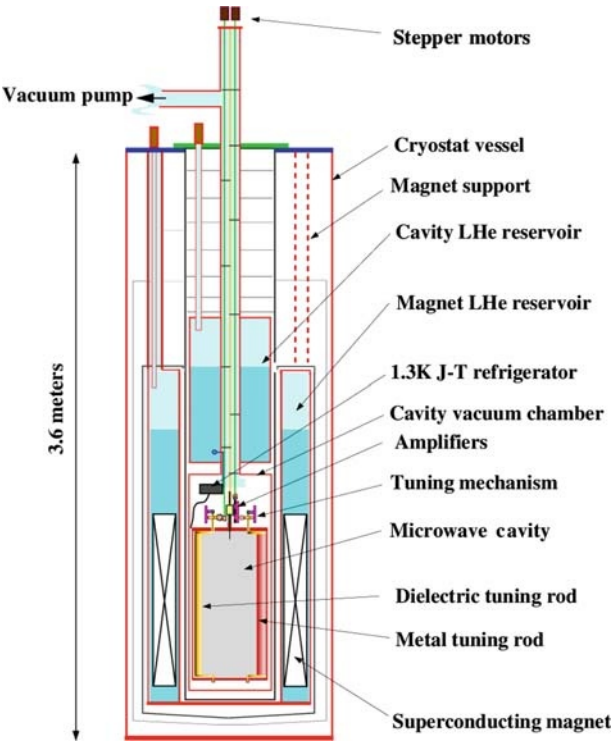

Fig. 8.2. Overview of ADMX hardware including the superconducting magnet and the cavity insert

8.3.2 Microwave Cavities

The ADMX experiment uses cylindrical cavities in order to maximize the axion conversion volume in the solenoid bore. They are made of a copper-plated steel cylinder with capped ends. The electromagnetic field structure inside a cavity can be found by solving the Helmholtz equation

$$\nabla^2\Phi + k^2\Phi = 0\,, \tag{8.9}$$

where the wavenumber k is given by

$$k^2 = \mu\epsilon\omega^2 - \beta^2\,, \tag{8.10}$$

where β is the eigenvalue for the transverse (x, y) component [27]. The cavity modes are the standing wave solutions to (8.9). The boundary conditions of an empty cavity allow only transverse magnetic (TM) modes ($B_z = 0$) and transverse electric (TE) modes ($E_z = 0$). As the TE modes have no axial electric field, one can see from (8.4) that they don't couple at all to axions, and we will ignore them for the moment. The TM_{lmn} modes are three-dimensional standing waves where $l = 0, 1, 2, \ldots$ is the number of azimuthal

nodes, $m = 1, 2, 3, \ldots$ is the number of radial nodes, and $n = 0, 1, 2, \ldots$ is the number of axial nodes. The axions couple most strongly to the lowest order TM_{010} mode.

The resonant frequency of the TM_{010} mode can be shifted by the introduction of metallic or dielectric tuning rods inserted axially into the cavity. Metallic rods raise the cavity resonant frequency the closer they get to the center while dielectric rods lower it. In ADMX these rods are attached to the ends of alumina arms that pivot about axles set in the upper and lower end plates (Fig. 8.3). The axles are rotated via stepper motors mounted at the top of the equipment (see Fig. 8.2) that swing the tuning rods from the cavity edge to the center in a circular arc. The stepper motors are attached to a gear reduction that translates a single step into a 0.15 arcsecond rotation, corresponding to a shift of $\sim$1 kHz at 800 MHz resonant frequency [19].

With the addition of metallic tuning rods, TEM modes ($B_z = E_z = 0$) can also be supported in the cavity. Like the TE modes, they do not couple to the axions but can couple weakly to the vertically mounted receiver antenna (due to imperfections in geometry, etc). Figure 8.4 demonstrates how the various resonant modes shift as a copper tuning rod is moved from near the cavity wall toward the center. The TEM and TE modes are largely unaffected by the change in tuning-rod position while TM modes rise in frequency as one of the copper rods moves toward the cavity center. This leads to regions in which a TM mode crosses a TE or TEM mode (referred to as mode mixing). These mode mixings (illustrated by the *Right* part of Fig. 8.4) introduce

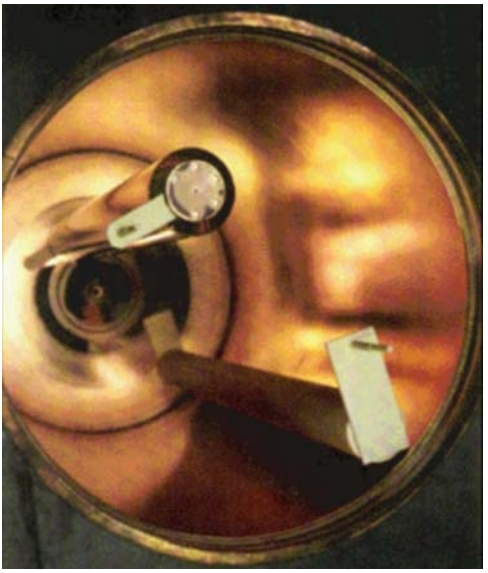

Fig. 8.3. Resonant cavity with the top flange removed. An alumina tuning rod can be seen at the bottom right and a copper tuning rod is in the upper left

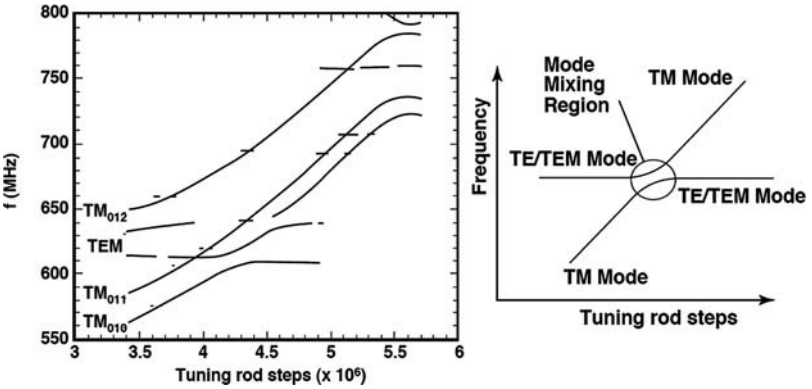

Fig. 8.4. Mode structure of a cavity with two copper tuning rods. **Left**: Frequencies of the resonant modes, measured via a swept RF signal, when one tuning rod is kept at the cavity edge while the other is moved toward the center. **Right**: A sketch of a mode crossing

frequency gaps that cannot be scanned. To address this the cavity was later filled with LHe, which changed the microwave index of refraction to 1.027, thus lowering the mode crossings by 2.7% and allowing the previously unaccessible frequencies to be scanned. Upgrades to the ADMX experiment will use a dry system in which both tuning rods are adjusted to "dance" around the mode crossing without using LHe.

A key feature of the resonant microwave cavity is its quality factor Q, which is a measure of the sharpness of the cavity response to external excitations. It is a dimensionless value that can be defined in a number of ways including as the ratio of the stored energy U to the power loss P_{L} per cycle: $Q = \omega_0 U/P_{\mathrm{L}}$. The quality factor Q of the TM_{010} mode is determined by sweeping a radio frequency (RF) signal through the weakly-coupled antenna in the cavity top plate (see Fig. 8.1). Generally, the unloaded Q of the cavity is $\sim 2 \times 10^5$, which is very near to the theoretical maximum for oxygen-free annealed copper at cryogenic temperatures [19]. During data collection, the insertion depth of the major antenna is adjusted to make sure that it matches the $50\,\Omega$ impedance of the cavity (called critically coupling). When the antenna is critically coupled, half the microwave power in the cavity enters the electronics via the antenna while the other half is dissipated in the cavity walls. Overcoupling the cavity would lower the Q and thus limit the signal enhancement, while undercoupling the cavity would limit the microwave power entering the electronics.

8.3.3 Amplifier and Receiver

After the axion signal has been generated in the cavity and coupled to the major port antenna, it is sent to the cryogenic amplifiers. The design of the

first amplifier is especially important because its noise temperature (along with the cavity's Johnson noise) dominates the rest of the system. This can be illustrated by following a signal from the cavity as it travels through two amplifiers in series. The power contribution from the thermal noise of the cavity at temperature T_c over bandwidth B is given by $P_{nc} = Bk_{\mathrm{B}}T_{\mathrm{c}}$ (where k_{B} is Boltzmann's constant). When this noise passes through the first amplifier, which provides gain G_1, the output includes the boosted cavity noise as well as extra power ($P_{\mathrm{N,A}_1}$) from the amplifier itself. The noise from the amplifier appears as an increase in the temperature of the input source

$$P_1 = G_1 Bk_{\mathrm{B}}T_{\mathrm{c}} + P_{\mathrm{N,A}_1} = G_1 Bk_{\mathrm{B}}(T_{\mathrm{c}} + T_{\mathrm{A}_1}) \; . \tag{8.11}$$

If this boosted noise power (cavity plus first amplifier) is then sent through a second amplifier, with gain G_2 and noise temperature T_{A_2}, the power output becomes

$$P_2 = G_2 P_1 + P_{\mathrm{N,A}_2} = G_2(G_1 Bk_{\mathrm{B}}(T_{\mathrm{c}} + T_{\mathrm{A}_1})) + G_2 Bk_{\mathrm{B}}T_{\mathrm{A}_2} \; . \tag{8.12}$$

The combined noise temperature from the two amplifiers (T_{A}) can be found by matching (8.12) to that of a single amplifier, $P_2 = G_2 G_1 Bk_{\mathrm{B}}(T_{\mathrm{c}} + T_{\mathrm{A}})$, which gives

$$T_{\mathrm{A}} = T_{\mathrm{A}_1} + \frac{T_{\mathrm{A}_2}}{G_1} \; . \tag{8.13}$$

Thus one can see that, because of the gain G_1 of the first stage amplifier, its noise temperature dominates all other amplifiers in the series.

The current first-stage amplifiers used in ADMX are cryogenic heterostructure field-effect transistors (HFETs) developed at the National Radio Astronomy Observatory (NRAO) specifically for the ADMX experiment [19, 28]. In these amplifiers, electrons from an aluminum doped gallium arsenide (GaAs) layer fall into the GaAs two-dimensional quantum well (the FET channel). The FET electrons travel ballistically, with little scattering, thus minimizing electronic noise [29]. Currently electronic noise temperatures of under 2 K have been achieved using the HFETs. In the initial ADMX data runs, now concluded, two HFET amplifiers were used in series, each with approximately 17 dB power gain, leading to a total first-stage power gain of 34 dB. Each amplifier utilized 90 degree hybrids in a balanced configuration in order to minimize input reflections, thus providing a broadband match to the 50Ω cavity impedance (see Fig. 8.5).

Though the amplifiers worked well in the high magnetic field just above the cavity, it was determined during commissioning that they should be oriented such that the magnetic field was parallel to the HFET channel electron flow. This minimized the electron travel path and thus the noise temperature [19].

The signal from the cryogenic amplifiers is carried by coaxial cable to a low-noise room-temperature post-amplifier, which adds an additional 38 dB

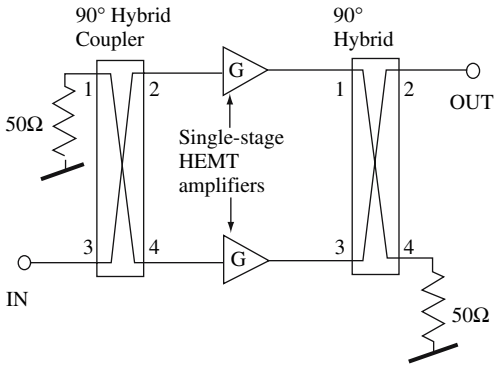

Fig. 8.5. Schematic diagram of a balanced amplifier. Every time the signal crosses through the middle of a hybrid its phase is shifted by 90 degrees. Reflections back to the input destructively interfere while reflections to the upper left constructively interfere and are dumped into a 50 Ω terminator. Signals to the output are both shifted by 90 degrees and thus add constructively

gain between 300 MHz–1 GHz. Though the post-amplifier's noise temperature is 90 K, its contribution relative to the cryogenic amplifiers (with 38 dB initial gain) is only 0.03 K (see (8.13)). After taking into account the various losses, the total gain from the cavity to the post-amplifier output is 69 dB [19].

After initial stages of amplification the signal enters the double-heterodyne receiver (essentially an AM radio). Figure 8.6 is a schematic of the receiver electronics. The first element is an image-reject mixer, which uses a local oscillator to mix the signal down to 10.7 MHz. This intermediate frequency (IF) is then sent through a programmable attenuator (used during room temperature testing so that the receiver electronics are not saturated). An IF amplifier then boosts the signal by another 20 dB before passing it by a weakly coupled signal sampler. The signal then passes through a crystal bandpass filter that suppresses noise outside a 30 kHz bandwidth centered at 10.7 MHz. The signal is then boosted by an additional 20 dB before being

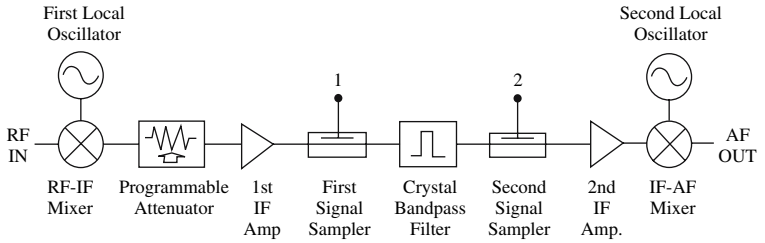

Fig. 8.6. Receiver chain that mixes the signal down from the cavity TM_{010} resonant frequency to 35 kHz

mixed down to 35 kHz. The total amplification of the signal from the cavity is $\sim$106 dB [30].

Once the signal has been mixed down to the 35 kHz center frequency, it is passed off to a commercial FFT spectrum analyzer, and the power spectrum is recorded. The entire receiver, including the filter, is calibrated using a white-noise source at the input. During data collection, the FFT spectrum analyzer takes 8 ms single-sided spectra (the negative and positive frequency components are folded on top of each other). Each spectrum consists of 400 bins with 125 Hz width, spanning a frequency range of 10–60 kHz. After 80 seconds of data recording (with a fixed cavity mode), the 10,000 spectra are averaged together and saved as raw data. This is known as the medium resolution data.

In addition there is a high-resolution channel to search for extremely narrow conversion lines from late infall non-thermal axions (as mentioned at the end of Sect. 8.1). For this channel the 35 kHz signal is passed through a passive LC filter with a 6.5 kHz passband, amplified, and then mixed down to a 5 kHz center frequency. A single spectrum is then obtained by acquiring 2^{20} points in about 53 s and an FFT is performed. This results in about 3.4×10^5 points in the 6.5 kHz passband with a frequency resolution of 19 mHz.

8.4 Data Analysis

The ADMX data analysis is split into medium- and high-resolution channels. The medium-resolution channel is analyzed using two hypotheses. The first is a "single-bin" search motivated by the possibility that some of the axions have not thermalized and therefore, would have negligible velocity dispersion, thus depositing all their power into a single power-spectrum bin. The second hypothesis utilizes a "six-bin" search that assumes that axions have a velocity dispersion of order $10^{-3}c$ or less (axions with velocities greater than $2 \times 10^{-3}c$ would escape the halo). The six-bin search is the most conservative and is valid regardless of whether the halo axions have thermalized or not.

Since each 80 s long medium-resolution spectrum is only shifted by 1 kHz from the previous integration, each frequency will show up in multiple spectra (given the 50 kHz window). As a result each 125 Hz bin is weighted according to where it falls in the cavity response function and co-added to give an effective integration time of $\sim$25 minutes per frequency bin. For the single-bin search, individual 125 Hz bins are selected if they exceed an initial power-level threshold. This is set relatively low, so a large number of bins are usually selected. These bins are then rescanned to achieve a similar signal-to-noise ratio and combined with the first set of data, generating a spectra with higher signal-to-noise ratio. The selection process is then repeated a number of times until persistent candidates are identified. These few survivors are then carefully checked to see whether there are any external sources of interference that could mimic an axion signal. If all candidates turn out to be exterior

radio interference, the excluded axion couplings (assuming a specific dark matter density) can be computed from the near-Gaussian statistics of the single-bin data. For the six-bin search, all six adjacent frequency bins that exceed a set power-threshold are selected from the power spectra. A large number of candidates are then whittled down using the same iterations as in the single-bin analysis. If no candidate survives the excluded axion couplings are computed by Monte Carlo [19].

From the radiometer equation (8.7), it follows that the search sensitivity can be increased if strong, narrow spectral lines exist. The integration times for each tuning rod setting is around 60 s and the resulting Doppler shift from the Earth's rotation leads to a spread of order $\sim$ mHz in a narrow axion signal. Because the actual velocity dispersion of each discrete flow is unknown, multiple resolution searches were performed by combining 19 mHz wide bins. These were referred to as n-bin searches, where $n = 1, 2, 4, 8, 64, 512$ and 4096. Candidate peaks were kept if they were higher than a specified threshold set for that particular n-bin search. These thresholds were $20, 25, 30, 40, 120, 650$ and 4500σ, for increasing order of n. The initial search using the high-resolution analysis took data between 478 and 525 MHz, corresponding to axion masses between 1.98 and 2.17 μeV. This search was made in three steps. First, the entire frequency range was scanned in 1 kHz increments with the candidate axion peaks recorded. Next, multiple time traces were taken of candidate peaks [31]. Finally, persistent peaks were checked by attenuating or disconnecting various diagnostic coaxial cables leading into the cavity (see Fig. 8.1). If the signals were external interference they would decrease in power dramatically, while an axion signal would remain unchanged [19]. Further checks could be done by disconnecting the cavity from the receiver input and replacing it with an antenna to see whether the signal persisted.

If a persistent candidate peak is found that does not have an apparent source from external interference a simple check would be to turn off the magnetic field. If the signal disappears, it would be a strong indication that it was due to axions and not some unknown interference. So far, though, all candidates have been identified with an external source.

8.5 Results

So far no axions have been detected in any experiment. ADMX currently provides the best limits from microwave cavity experiments in the lowest mass range (most plausible if axions are the major component to the dark matter). Both the medium-resolution and the high-resolution data yield exclusion plots in either the coupling strength of the axion (assuming a halo density of $\varrho_{\mathrm{a}} = 0.45\,\mathrm{GeV\,cm^{-3}}$) or in the axion halo density (assuming a specific DFSZ or KSVZ coupling strength). Results from the medium-resolution channel [24] can be seen in Fig. 8.7 and the high-resolution results, in Fig. 8.8 [31]. Both the results are at the 90% confidence level.

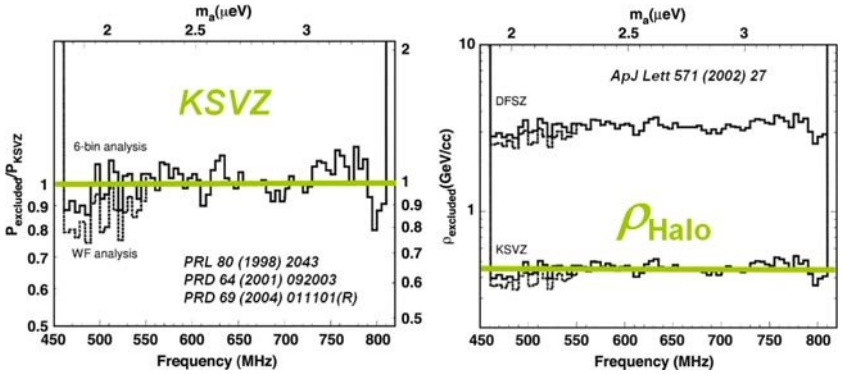

Fig. 8.7. Results from the medium-resolution channel [24]. **Left**: Exclusion plot for the power in a thermalized spectrum assuming a halo density of $\varrho_{\mathrm{a}} = 0.45\,\mathrm{GeV\,cm^{-3}}$. **Right**: The dark matter halo density excluded as axions for two different axion models

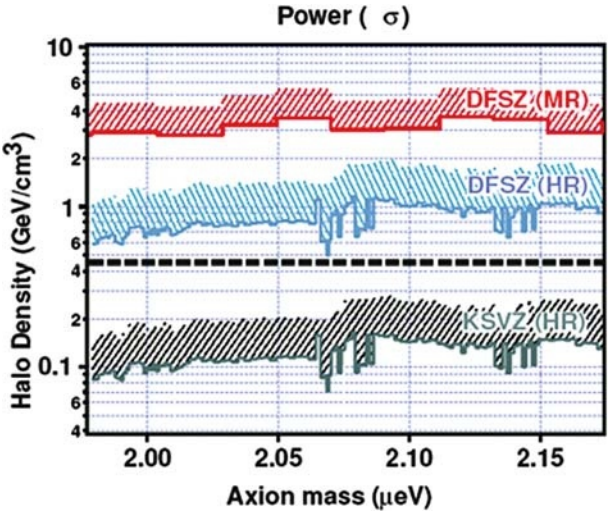

Fig. 8.8. High-resolution limits given different axion couplings [31]. This shows that the current high-resolution channel is sensitive to fractional halo densities ($\approx 30\%$) if the axions couple via the KSVZ model. If they couple via the DFSZ model the experiment is not yet sensitive to the maximum likelihood halo density ($\varrho_{\mathrm{a}} \sim 0.45\,\mathrm{GeV\,cm^{-3}}$), but would be sensitive to a single line with twice that density

8.6 Future Developments

In order to conduct a definitive search for axion dark matter various improvements to the detector technology need to be carry out. Not only do the experiments need to become sensitive enough to detect even the most pessimistic

axion couplings (DFSZ) at fractional halo densities but they must be able to scan relatively quickly over a few decades in mass, up to possibly hundreds of GHz. The sensitivity of the detectors (which is also related to scanning speed) is currently limited by the noise in the cryogenic HFET amplifiers. Even though they have a noise temperature under 2 K, the quantum limit (defined as $T_{\mathrm{Q}} \sim h\nu/k$) is almost two orders of magnitude lower (25 mK at 500 MHz). To get down to, or even past, this quantum limit, two very different technologies are being developed. The first is the implementation of SQUIDs (Superconducting Quantum Interference Devices) as first-stage cryogenic amplifiers. The second uses Rydberg atoms to detect single microwave photons from axion conversions in the cavity.

Though both techniques will lead to vastly more sensitive experiments, they will still be limited in their mass range. Currently all cavity experiments have been limited to the 2–20 μeV range, mostly due to the size of resonant cavities. For a definitive search, the mass range must be increased by a factor of 50, which requires new cavity designs that increase the resonant frequency while maintaining large enough detection volumes. Detectors that work at these higher frequencies also need to be developed.

8.6.1 SQUID Amplifiers

The next generation of the ADMX experiment will use SQUID amplifiers to replace the first-stage HFETs. SQUIDs essentially use a superconducting loop with two parallel Josephson junctions to enclose a total amount of magnetic flux Φ. This includes both a fixed flux supplied by the bias coil and the signal flux supplied by an input coil. The phase difference between the currents on the two sides of the loop are affected by changing Φ resulting in an interference effect similar to the two-slit experiment in optics [27]. Essentially the SQUID will act as flux to voltage transducers as illustrated in Fig. 8.9.

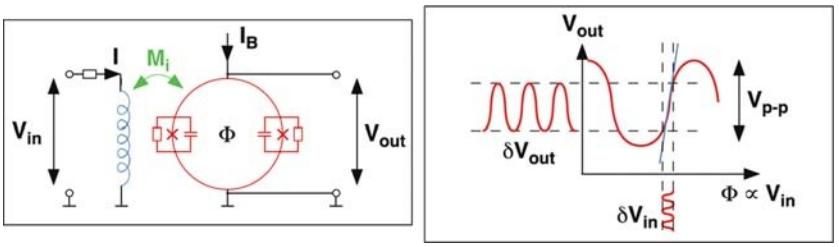

Fig. 8.9. Essentials of a SQUID microwave detector. **Left:** Schematic drawing of the SQUID device coupling to the input signal which is converted into magnetic flux. **Right**: Biasing of the flux allows for amplification

Most SQUIDs are built using the Ketchen and Jaycox design [32], in which the SQUID loop is an open square washer made of niobium (Nb). The loop is closed by a separate Nb electrode connected to the washer opening on either side by a Josephson junction and external shunt resistors. A spiral input coil is placed on top of the washer, separated by a layer of insulation. The original designs in which input signals were coupled into both ends of the coil tended to work only below about 200 MHz due to parasitic capacitance between the coil and the washer at higher frequencies. This was solved by coupling the input signal between one end of the coil and the SQUID washer, which would act as a ground plane to the coil and create a microstrip resonator (see Fig. 8.10). This design has been tested successfully up to 3 GHz [27].

Unlike the HFETs, whose noise temperature bottoms out at just under 2 K regardless of how cold the amplifiers get, the SQUID's noise temperature remains proportional to the physical temperature down to within 50% of the quantum limit. This thermal noise comes from the shunt resistors across the SQUID's Josephson junctions, and future designs that minimize this could push the noise temperature even closer to the quantum limit [29].

Currently the ADMX experiment is in the middle of an upgrade in which SQUIDs will be installed as first stage cryogenic amplifiers. This should cut the combined noise temperature of the cavity and electronics in half, allowing ADMX to become sensitive to half the KSVZ coupling (with the same scanning speed as before). Due to the SQUIDs' sensitivity to magnetic fields, this upgrade includes an entire redesign in which a second superconducting magnet is being installed in order to negate the main magnet's field around the SQUID amplifiers. Data collection is expected to begin in the first half of 2007 and run for about a year. Future implementations of ADMX foresee using these SQUID detectors with a dilution refrigerator to set an operating temperature of ~ 100 mK, allowing sensitivity to DFSZ axion couplings to be achieved with 5 times the scanning rate the current HFETs take to reach KSVZ couplings.

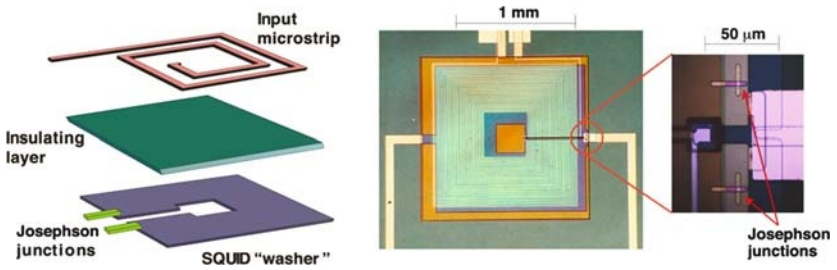

Fig. 8.10. Diagram and picture of a microstrip resonator SQUID to be used in ADMX upgrade

8.6.2 Rydberg-Atom Single-Quantum Detectors

One technique to evade the quantum noise limit is to use Rydberg atoms to detect single photons from the cavity. A Rydberg atom has a single valence electron promoted to a level with a large principal quantum number n. These atoms have energy spectra similar in many respects to hydrogen, and dipole transitions can be chosen anywhere in the microwave spectrum by an appropriate choice of n. The transition energy itself can be finely tuned, by using the Stark effect, to exactly match a desired frequency. That, combined with the Rydberg atom's long lifetime and large dipole-transition probability, makes it an excellent microwave photon detector.

An experimental setup utilizing this technique called CARRACK has been assembled in Kyoto, Japan, and a schematic is given in Fig. 8.11 [19, 33]. The axion conversion cavity is coupled to a second "detection" cavity tuned to the same resonant frequency ν. A laser excites an atomic beam (in this case rubidium) into a Rydberg state ($|0\rangle \rightarrow |n\rangle$), which then traverses the detection cavity. The spacing between the energy levels is adjusted to $h\nu$ using the Stark effect, and microwave photons from the cavity can be efficiently absorbed by the atoms (one photon per atom, $|ns\rangle \rightarrow |np\rangle$). The atomic beam then exits the cavity and is subjected to selective field ionization in which electrons from atoms in the higher energy state ($|np\rangle$) get just enough energy to be stripped off and detected [29].

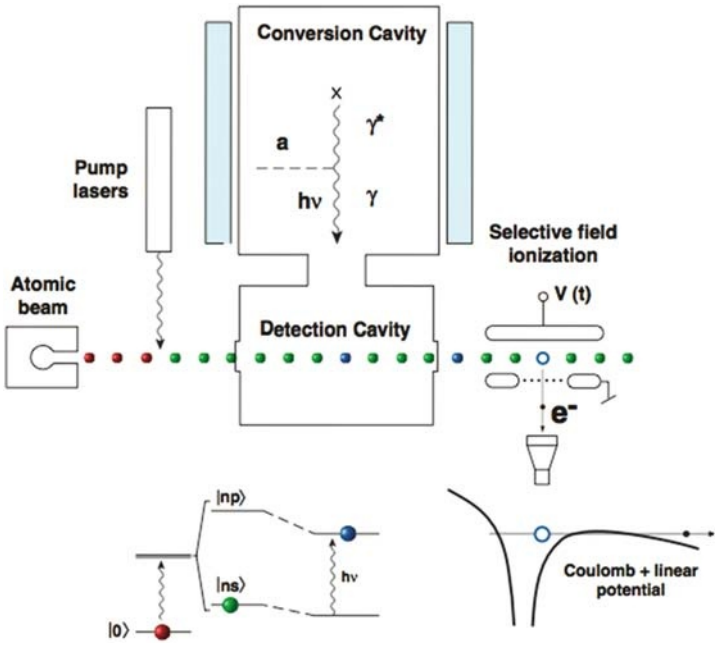

Fig. 8.11. Schematic of single photon microwave detection utilizing Rydberg atoms

Currently, the Kyoto experiment has measured cavity emission at 2527 MHz down to a temperature of 67 mK, a factor of two below the quantum limit at that frequency, and is working to reach the eventual design goal of 10 mK [33]. This would be the point at which the cavity blackbody radiation would become the dominant noise background. One deficiency of the Rydberg-atom technique is that it can't detect structures narrower than the bandpass ($\Delta E/E$) of the cavity (generally $\sim 10^{-5}$). As a result it is insensitive to axion halo models that predict structure down to $\Delta E/E \sim 10^{-11}$, an area which the ADMX high-resolution channel, utilizing microwave amplifiers, can cover. Despite this, Rydberg-atom detectors could become very useful tools for halo axion detection in the near future.

8.6.3 Challenge of Higher Frequencies

Current microwave-cavity technology has only been able to probe the lowest axion mass scale. In order to cover the entire range up to the exclusion limits set by SN 1987a of $m_a \leq 1$meV, new cavity and detection techniques must be investigated that can operate up to the 100 GHz range. The resonant cavity frequency essentially depends on the size of the cavity and the resonant mode used. The TM_{010} mode has by far the largest form factor ($C \sim 0.69$) of any mode, and all other higher-frequency modes have much smaller or identically zero form factors. The single 50 cm diameter cavity used in the initial ADMX experiments had a central resonant frequency (TM_{010}) of 460 MHz, and radial translation of metallic or dielectric tuning rods could only raise or lower that frequency by about $\pm 50\%$ [19]. Smaller cavities could get higher frequencies, but the rate of axion conversions would go down as the cavity volume decreased.

In order to use the full volume of the magnet with smaller cavities, it was determined that multiple cavities could be stacked next to each other and their power combined. As long as the de Broglie wavelength of the axions is larger than the total array, individual cavities tuned to the same frequency can be summed in phase. Typical axion de Broglie wavelengths are $\lambda_{dB} \sim 10$–100 m, which means they drive the ~ 1 m cavity volume coherently. Data recorded using a four-cavity array in ADMX reached KSVZ sensitivity over a small mass range (see Fig. 8.12, [27]). These initial tests had difficulties getting the piezoelectric motors working trouble-free in the magnetic and cryogenic environment. Since those tests, the technology has advanced to the point at which it may be feasible to create larger sets of smaller cavity arrays.

To reach even higher frequencies ideas have been raised to use resonators with periodic arrays of metal posts. Figure 8.12 shows the electric field profile of one possible array using a 19-post hexagonal pattern. Mounting alternating posts from the cavity top and bottom and translating them relative to each other allow the resonant frequency to be adjusted by $\approx 10\%$. The possibility

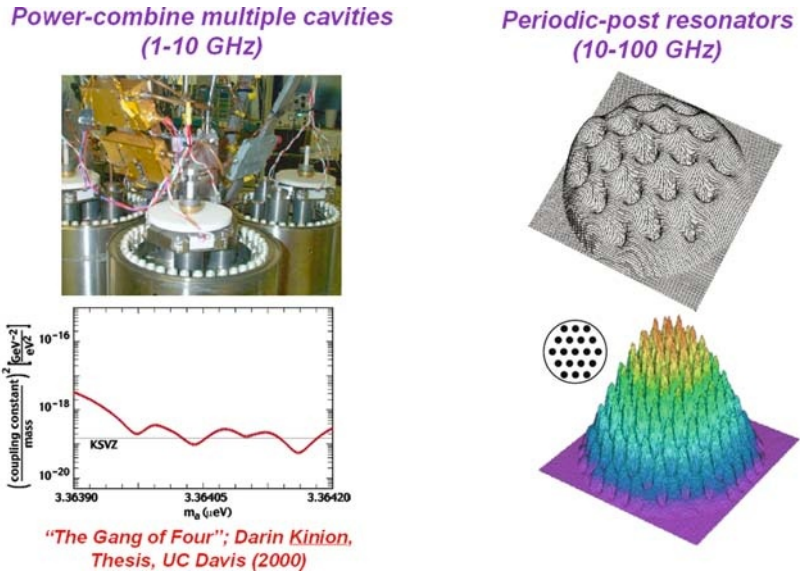

Fig. 8.12. Outline of possible cavity concepts to explore higher axion masses. **Left**: A picture of the four cavity array and its corresponding exclusion plot over the limited mass range it took data. **Right**: Field maps for multiple posts inserted in a cavity

of using such cavities, or other new cavity geometries, is an active area of research and progress needs to be made before the full axion mass range can be explored.

8.7 Summary and Conclusions

Experimentally the axion is a very attractive cold dark matter candidate. Its coupling to photons ($g_{a\gamma\gamma}$) for several different models all fall within about an order of magnitude in strength, and its mass scale is currently confined to a three-decade window. This leaves the axion in a relatively small parameter space, the first two decades of which is within reach of current or near future technology.

The ADMX experiment has already begun to exclude dark matter axions with KSVZ couplings over the lowest masses, and an upgrade to SQUID amplifiers and a dilution refrigerator could make ADMX sensitive to DFSZ axion couplings over the first decade in mass within the next three years. Development of advanced Rydberg-atom detectors, along with higher frequency cavity geometries, could give rise to the possibility of a definitive axion search within a decade. By "definitive" we mean a search that would either detect

axions at even the most pessimistic couplings (DFSZ) at fractional halo densities over the full mass range or rule them out entirely.

It should be noted that if the axion is detected it would not only solve the Strong-CP problem and perhaps the nature of dark matter but could offer a new window into astrophysics, cosmology, and quantum physics. Details of the axion spectrum, especially if fine structure is found, could provide new information on how the Milky Way was formed. The large size of the axions de Broglie wavelength ($\lambda_a \sim 10$–$100\,\mathrm{m}$) could even allow for interesting quantum experiments to be performed at macroscopic scales. All of these tantalizing possibilities, within the reach of current and near future technologies, makes the axion an extremely exciting dark matter candidate to search for.

Acknowledgments

This work was supported by the U.S. Department of Energy under contract W-7405-Eng-48 at Lawrence Livermore National Laboratory.

References

1. Schramm, D.N., Turner, M.S.: Big-bang nucleosynthesis enters the precision era. Rev. Mod. Phys. **70**, 303 (1998) [astro-ph/9706069] 135
2. Tegmark, M., et al. [SDSS Collaboration]: Cosmological parameters from SDSS and WMAP. Phys. Rev. D **69**, 103501 (2004) [astro-ph/0310723] 135
3. Zwicky, F.: On the masses of nebulae and of clusters of nebulae. Helvetica Phys. Acta **2**, 110 (1933) 135
4. Jungman, G., Kamionkowski, M., Griest, K.: Supersymmetric dark matter. Phys. Rept. **267**, 195 (1996) [hep-ph/9506380] 135
5. Spergel, D.N., et al. [WMAP Collaboration]: First year Wilkinson microwave anisotropy probe (WMAP) observations: Determination of cosmological parameters. Astrophys. J. Suppl. **148**, 175 (2003) [astro-ph/0302209] 135
6. De Paolis, F., Ingrosso, G., Jetzer, P., Roncadelli, M.: A case for a baryonic dark halo. Phys. Rev. Lett. **74**, 14 (1995) [astro-ph/9410016] 136
7. Alcock, C., et al. [MACHO Collaboration]: The MACHO project: Microlensing results from 5.7 years of LMC observations. Astrophys. J. **542**, 281 (2000) [astro-ph/0001272] 136
8. Asztalos, S.J., et al.: An improved RF cavity search for halo axions. Phys. Rev. D **69**, 011101 (2004) [astro-ph/0310042] 136
9. Kleyna, J.T., et al.: First clear signatures of an extended dark matter halo in the Draco dwarf spheroidal. Astrophys. J. Lett. **563**, 115 (2001). [astro-ph/0111329] 136
10. Primack, J.R.: Dark matter and structure formation in the universe. In: Proceedings of Midrasha Matematicae in Jerusalem: Winter School in Dynamic Systems (1997), [astro-ph/9707285] 136
11. Gates, E.I., Gyuk, G., Turner, M.S.: The local halo density. Astrophys. J. **449**, L123 (1995) [astro-ph/9505039] 136

12. Baker, C.A., et al.: An improved experimental limit on the electric dipole moment of the neutron. Phys. Rev. Lett. **97**, 131801 (2006) [hep-ex/0602020] 136
13. Kim, J.E.: Weak interaction singlet and strong CP invariance. Phys. Rev. Lett. **43**, 103 (1979) 137
14. Shifman, M.A., Vainshtein, A.I., Zakharov, V.I.: Can confinement ensure natural CP invariance of strong interactions? Nucl. Phys. B **166**, 493 (1980) 137
15. Zhitnitskii, A.R.: On the possible suppression of axion-hadron interactions. Soviet Journal of Nucl. Phys. **31**, 260 (1980) 137
16. Dine, M., Fischler, W., Srednicki, M.: A simple solution to the strong CP problem with a harmless axion. Phys. Lett. B **104**, 199 (1981) 137
17. Weinberg, S.: A new light boson? Phys. Rev. Lett. **40**, 223 (1978) 137
18. Wilczek, F.: Problem of strong P and T invariance in the presence of instantons. Phys. Rev. Lett. **40**, 279 (1978) 137
19. Bradley, R., et al.: Microwave cavity searches for dark-matter axions. Rev. Mod. Phys. **75**, 777 (2003) 137, 138, 139, 140, 141, 143, 144, 145, 146, 148, 152, 153
20. Sikivie, P.: Evidence for ring caustics in the Milky Way. Phys. Lett. B **567**, 1 (2003) [astro-ph/0109296] 137
21. Sikivie, P.: Experimental tests of the 'invisible' axion. Phys. Rev. Lett. **51**, 1415 (1983) [Erratum-ibid. **52**, 695 (1984)] 138
22. Lasher, L.: Pioneer 10 Project Manager, (2005), priv. comm 139
23. Dicke, R.H.: The measurement of thermal radiation at microwave frequencies. Rev. of Sci. Instrum. **17**, 268 (1946) 139
24. Asztalos, S.J., et al.: An improved RF cavity search for halo axions. Phys. Rev. D **69**, 011101 (2004) [astro-ph/0310042] 140, 148, 149
25. De Panfilis, S., et al.: Limits on the abundance and coupling of cosmic axions at $4.5\,\mu\text{eV} < m(a) < 5.0\,\mu\text{eV}$. Phys. Rev. Lett. **59**, 839 (1987) 140
26. Hagmann, C., Sikivie, P., Sullivan, N.S. Tanner, D.B.: Results from a search for cosmic axions. Phys. Rev. D **42**, 1297 (1990) 140
27. Kinion, D.S.: First results from a multiple microwave cavity search for dark matter axions. UMI-30-19020, UC Davis – Physics Department, PhD Thesis (2001), http://www.slac.stanford.edu/spires/find/hep/www?r=umi-30-19020 142, 150, 151, 153
28. Daw, E., Bradley, R.F.: Effects of high magnetic fields on the noise temperature of a heterostructure field-effect transistor low-noise amplifier. J. Appl. Phys. **82**, 1925 (1997) 145
29. van Bibber, K., Rosenberg, L.J.: Ultrasensitive searches for the axion. Phys. Today 59N8 (2006) 30 145, 151, 152
30. Asztalos, S., et al.: Large-scale microwave cavity search for dark-matter axions. Phys. Rev. D **64**, 092003 (2001) 147
31. Duffy, L.D., et al.: A high resolution search for dark-matter axions. Phys. Rev. D **74**, 012006 (2006) [astro-ph/0603108] 148, 149
32. Ketchen, M.B., Jaycox, M.B.: Ultra-low-noise tunnel junction dc SQUID with a tightly coupled planar input coil. Appl. Phys. Lett. **40**, 736 (1982) 151
33. Tada, M., et al.: Single-photon detection of microwave blackbody radiations in a low-temperature resonant-cavity with high Rydberg atoms. Phys. Lett. B **349**, 488 (2006) 152, 153

9 Recent Results from the PVLAS Experiment on the Magnetized Vacuum

Giovanni Cantatore[1] and the PVLAS Collaboration[2]

[1] INFN Sezione di Trieste and University of Trieste
Via A. Valerio 2, 34127 Trieste, Italy
giovanni.cantatore@trieste.infn.it

[2] PVLAS Collaboration: G. Di Domenico, G. Zavattini (INFN Sezione di Ferrara and University of Ferrara, Italy) – R. Cimino (INFN Laboratori Nazionali di Frascati, Frascati, Italy) – U. Gastaldi, G. Ruoso (INFN Laboratori Nazionali di Legnaro, Legnaro, Italy) – S. Carusotto, E. Polacco (INFN Sezione di Pisa and University of Pisa, Italy) – M. Bregant, F. Della Valle, M. Karuza, E. Milotti, G. Raiteri, E. Zavattini (INFN Sezione di Trieste and University of Trieste, Italy)

Abstract. The vacuum element can be used as a target in a photon-photon collider in order to study its properties. Some of these properties are predicted by Quantum Electrodynamics, while additional and unexpected properties might be linked to the existence of yet undiscovered axion-like particles (ALPs) interacting with two photons. In this low energy case (1–2 eV), real photons from a polarized laser beam are scattered off virtual photons provided by a magnetic field. Information on the scattering processes can be obtained by measuring changes in the polarization state of the probe photons. In the PVLAS (Polarizzazione del Vuoto con LASer) experiment, running at the Legnaro Laboratory of the Istituto Nazionale di Fisica Nucleare (INFN), near Padova, Italy, a linearly polarized laser beam is sent through a 5 T strong magnetic field in vacuum, where it is reflected back and forth, by means of a Fabry-Pérot resonator, $\sim 50,000$ times over a distance of 1 m. A heterodyne ellipsometer allows the simultaneous detection of a birefringence and a rotation of the polarization plane. The sensitivity of the instrument allows the detection of rotation or of ellipticity angles of about 10^{-9} rad, in an hour of data taking. The measurement technique employed by PVLAS will be illustrated, and recent results on polarization effects due to the magnetized vacuum will be presented in this chapter. The interpretation of these effects in terms of the production of ALPs will also be discussed. Finally, the realization of a photon-regeneration type experiment will be briefly illustrated.

9.1 Introduction

The idea that vacuum can be considered as a "medium" with dielectric properties is not new [1] and is based on the existence of zero-point fluctuations in the energy of quantum vacuum. Some of these properties are predicted by QED, while additional and unexpected properties might be linked to the existence of yet undiscovered axion-like particles (ALPs) interacting with two photons. Processes such as photon-photon scattering and the Primakoff effect,

G. Cantatore and the PVLAS Collaboration: *Recent Results from the PVLAS Experiment on the Magnetized Vacuum*, Lect. Notes Phys. **741**, 157–197 (2008)
DOI 10.1007/978-3-540-73518-2_9

where light, neutral, scalar, or pseudoscalar particles are produced from an effective two-photon vertex, have been considered in theoretical works [2]. These microscopic processes could contribute to macroscopically observable properties of the vacuum. In particular, it is expected from theoretical arguments that these scattering processes should manifest themselves as optical properties of the vacuum. For instance, in the presence of an external magnetic field, quantum vacuum can behave as an optically anisotropic medium showing selective absorption and selective delay of photons propagating transversely with respect to the field. The selection is according to the polarization of the photons, and if one starts with a linearly polarized light beam, the magnetized vacuum can induce both a linear birefringence (selective delay) and a linear dichroism (selective absorption).

Experimentally observable optical quantities, such as the ellipticity connected to birefringence and the apparent rotation of the polarization plane connected to dichroism, can be cast as functions of the fundamental constants [3] or of the parameters characterizing the particle producing vertices [4]. In such experiments, when optical wavelengths are involved, the magnetically perturbed vacuum can be considered as the target in a low energy photon-photon collider. The observation of magnetically induced vacuum birefringence and dichroism amounts then to a determination of the total photon-photon scattering cross section at low energies and of mass and coupling constant to two photons of the hypothetical particles produced via the Primakoff effect.

The first practical concept to build a suitably sensitive ellipsometer, i.e., an optical instrument capable of detecting minute changes in the polarization state of a light beam, is based on the proposal by Iacopini and Zavattini [3]. This experimental effort was focused on detecting photon-photon scattering as predicted by QED. Later, a pioneering experiment conducted at Brookhaven by the Brookhaven-Fermilab-Rochester-Trieste collaboration (BFRT) attempted also to observe particle production from a two-photon Primakoff process. The Polarizzazione del Vuoto con LASer (PVLAS) experiment builds on this experience, expanding its sensitivity to all possible processes causing macroscopically observable changes in the polarization of a light beam probing the magnetized vacuum [5, 6].

Presently, the PVLAS collaboration is operating a high-sensitivity ($\approx 10^{-7}$ rad $\mathrm{Hz}^{-1/2}$) optical ellipsometer capable of independently detecting both ellipticities and dichroisms, at the INFN Legnaro National Laboratory in Legnaro, Italy. The experiment has a sensitivity of 10^{-9} rad assuming one hour of data-taking time. The polarization effects are induced on a 1064 nm linearly polarized laser beam that passes in a vacuum in the bore of a superconducting 1.1 m long dipole magnet normally operated at a magnetic field of 5.0 T. The heterodyne technique is used to extract low-level and time-varying signals from a large background. A high-finesse ($F \approx 10^5$), high-quality-factor ($Q > 10^{11}$), 6.4 m long Fabry-Pérot (FP) optical resonator enclosing

the interaction region provides amplification of the optical path, while mechanical rotation of the magnet-cryostat assembly gives the time modulation necessary for heterodyne detection.

In Sect. 9.2 we will describe the aim of the experiment and the principle of the measurement, along with the technical challenges to be met, in greater detail. Section 9.3 gives an insight to the actual layout of the apparatus, while in Sect. 9.4 we report on the results obtained from polarization measurements both with gas and with vacuum in the interaction region. We will focus, in particular, on the observation of a rotation signal in vacuum at the frequency expected from the heterodyne detection setup. Finally, a discussion of the result and its possible relevance, along with future perspectives, can be found in Sect. 9.5.

9.2 Aim and Measurement Principle of PVLAS

The Feynman diagrams in Figs. 9.1 and 9.2 show interactions of light with an external electromagnetic field that can be studied with the PVLAS experiment. Figure 9.1 illustrates diagrams of processes possibly contributing to an overall vacuum birefringence effect. The effective Lagrangian for light propagating in vacuum, in the presence of a magnetic field, can be written (to fourth-order approximation and in Gaussian units) as [5]

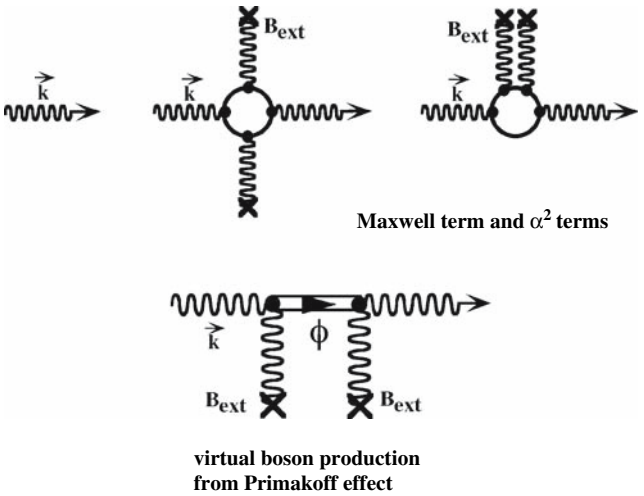

Fig. 9.1. Photon-photon scattering in QED and virtual boson production from Primakoff effect, leading to a vacuum magnetic birefringence (see text)

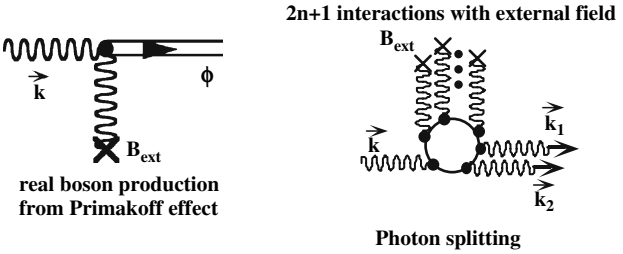

Fig. 9.2. Real boson production from Primakoff effect and photon splitting in QED leading to a vacuum magnetic dichroism (see text)

$$L_0 + L_{e^+e^-} = \frac{\left(E^2 - B^2\right)}{8\pi} + \frac{\alpha^2 \lambda\!\!\!^{-}_e{}^3}{360\pi^2 m_e c^2}\left[4\left(\frac{E^2 - B^2}{2}\right)^2 + 7\left(\mathbf{E}\cdot\mathbf{B}\right)^2\right], \tag{9.1}$$

where L_0 is the classical Maxwell term, and $L_{e^+e^-}$ contains the one loop contributions. Here $\mathbf{E}$ is the electric field of the light beam, $\mathbf{B}$ the external magnetic field (assumed to be sub-critical), α the fine structure constant, m_e the electron mass, and $\lambda\!\!\!^{-}_e = \hbar/m_e c^2$.

The top three diagrams of Fig. 9.1 show a freely propagating photon, corresponding to the Maxwell term of the effective Lagrangian and two possible one-loop contributions, corresponding to photon-photon scattering in QED. The bottom diagram of Fig. 9.1 corresponds to the virtual production of a boson via the Primakoff effect [4, 22]. The effective Lagrangians (in natural units) for the two-photon vertex are, in the case of pseudoscalar and scalar particles

$$L_p = \frac{1}{4M_p}\phi\left(\mathbf{E}\cdot\mathbf{B}\right) \ , \text{ and} \tag{9.2}$$

$$L_s = \frac{1}{4M_s}\sigma\left(E^2 - B^2\right), \tag{9.3}$$

where $M_{p,s}$ is the inverse coupling constant, and ϕ and σ are the pseudoscalar and scalar fields, respectively. Both the QED photon-photon scattering and the virtual Primakoff production illustrated in Fig. 9.1 produce a birefringence. In the first case, only photons polarized parallel to the external magnetic field scatter. They briefly oscillate into massive particles and are delayed with respect to photons polarized normal to the magnetic field. In virtual production, virtual pseudoscalars (scalars) are produced only by photons polarized parallel (normal) to the magnetic field. These photons oscillate into massive particles and are therefore delayed.

Figure 9.2 shows two examples of processes that can contribute to a vacuum magnetic dichroism, which results in an apparent rotation of the polarization plane of linearly polarized light. The diagram on the right hand side of Fig. 9.2 corresponds to real Primakoff production of bosons from a two-photon vertex (see (9.1)) for the corresponding Lagrangian). Here pseudoscalar

(scalar) real particles are produced from photons polarized parallel (normal) to the external magnetic field. These photons disappear from the beam; real production amounts to selective absorption of photons and therefore to a dichroism. The other diagram corresponds to a Photon splitting, in the presence of an external magnetic field, into two lower-energy photons (see S. L. Adler in [1] for a detailed theoretical treatment). Photon splitting also occurs only for a definite polarization direction with respect to the external field. If the apparatus used to detect polarization changes is also selective in energy, then split photons will be undetected and the original photons will appear to have been selectively absorbed, resulting in a dichroism. The PVLAS experiment aims at detecting the macroscopic birefringence and dichroism possibly related to the above processes.

9.2.1 Polarization Measurements

To better understand how the microscopic processes pictured in Figs. 9.1 and 9.2 can connect to polarization changes, let us consider Figs. 9.3 and 9.4, which show the special case realized in the PVLAS experimental setup. Figure 9.3 shows a schematic layout of an optical ellipsometer suitable for static detection of a linear birefringence produced by a physical phenomenon occurring inside the ellipsometer itself. The instrument basically consists of two crossed polarizers and a light detector. An interaction region is enclosed between the two polarizers, and a light beam propagates through the ellipsometer. If no interaction takes place, polarization is unchanged and no light will be detected after the output polarizer. Let us assume that an interaction with the magnetic field between the polarizers changes beam polarization: a polarization component along the output polarizer axis will appear, and some light intensity will be detected exiting the ellipsometer. In the special case shown in Fig. 9.3, the interaction region is a vacuum where a constant and uniform magnetic field is present. Field direction is at an angle with respect to the initial light polarization direction. According to the above discussion, photons polarized parallel to the field will be delayed with respect to those polarized normal to the field, resulting in different refractive indices for the two polarizations, that is a birefringence. Light exiting the interaction region will be elliptically polarized: the tip of the light beam electric vector describes an ellipse in space, and the ratio of the semi-minor to the semi-major axes of this ellipse is called ellipticity. It is clear that the electric vector has acquired a component parallel to the transmission axis of the output polarizer, and therefore some light intensity will be transmitted through it. This intensity depends on the ellipticity angle.

Let us analyze the layout of Fig. 9.3 using the Jones matrix formalism [8]. In this formalism, light electric fields along the chosen x and y directions are represented by (2x2) matrices with complex elements. The physical fields are contained in the real part of the expressions. The Jones matrix representing

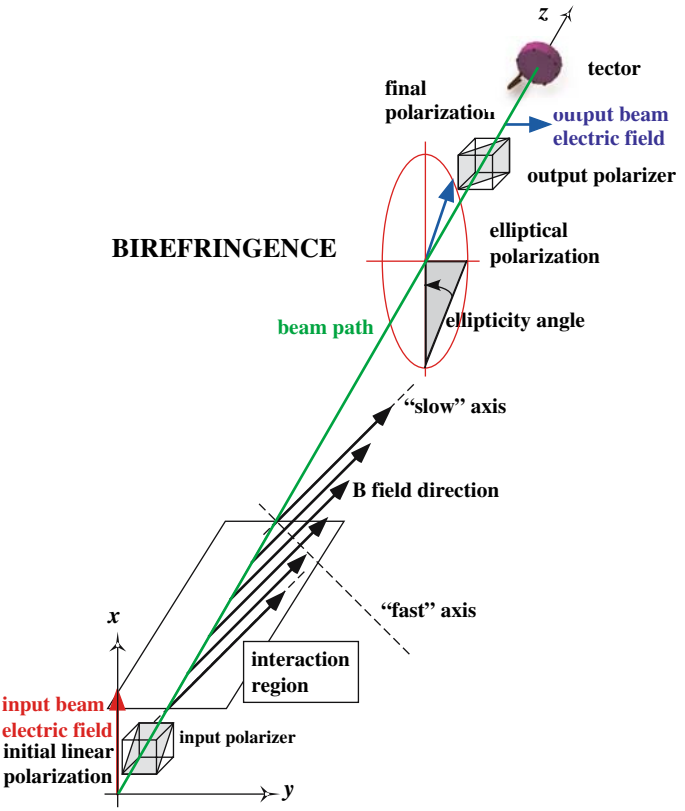

Fig. 9.3. Schematic layout of a simple ellipsometer to detect the selective delay of photons polarized along a transverse external magnetic field (*linear birefringence*). The field action transforms a linearly polarized beam into an elliptically polarized beam (see text)

the input electric field of Fig. 9.3 (which is directed along x) for instance is given by

$$E_{\rm in} = E_0 e^{-{\rm i}\omega t} \begin{pmatrix} 1 \\ 0 \end{pmatrix} , \tag{9.4}$$

where ω is the light angular frequency. The matrices representing the input and the output polarizer (analyzer) are

$$P = \begin{pmatrix} 1 & 0 \\ 0 & 0 \end{pmatrix} \quad A = \begin{pmatrix} 0 & 0 \\ 0 & 1 \end{pmatrix} . \tag{9.5}$$

A birefringent element having its slow axis along some "parallel" direction can be represented by the matrix

$$B_{\parallel,\perp} = \begin{pmatrix} e^{-{\rm i}\delta} & 0 \\ 0 & e^{{\rm i}\delta} \end{pmatrix} , \tag{9.6}$$

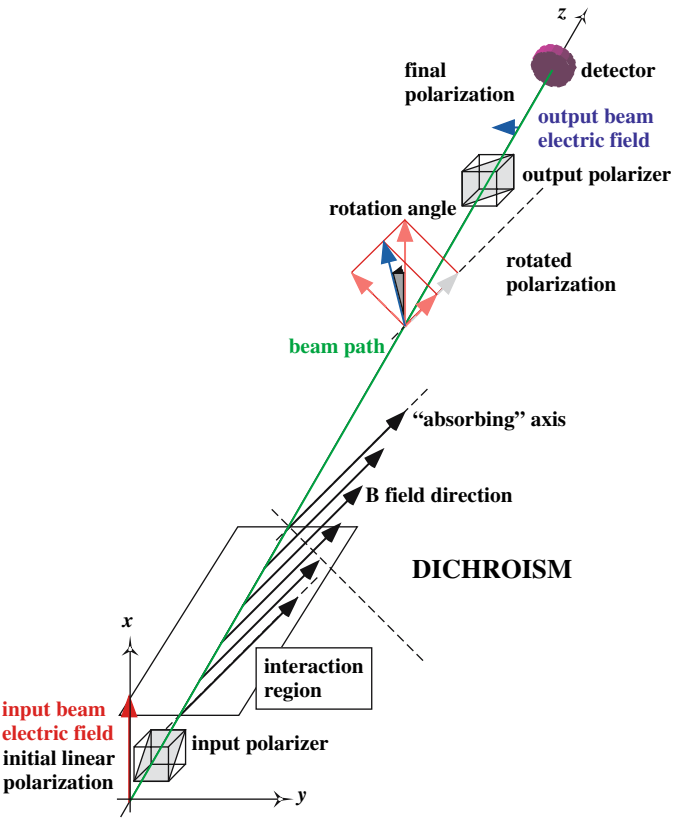

Fig. 9.4. Schematic layout of an ellipsometer to detect selective absorption of photons polarized along a transverse external magnetic field (*linear dichroism*). The dichroism results in an apparent rotation of the polarization plane of a linearly polarized beam (see text)

where the phase delay between the parallel and normal polarizations is 2δ. In terms of the difference of the refractive indices, one writes $2\delta = \left(n_{\parallel} - n_{\perp}\right) 2\pi L/\lambda$, where L is the depth of the birefringent element, and λ is the wavelength of the light. If the birefringent element optical axes are rotated by an angle θ with respect to the axes x and y, the matrix representing the birefringent element (in the rotated reference frame)

$$B_{xy} = \begin{pmatrix} e^{-\mathrm{i}\delta}\cos^2\theta + e^{\mathrm{i}\delta}\sin^2\theta & -\mathrm{i}\sin\sin 2\theta \\ -\mathrm{i}\sin\sin 2\theta & e^{-\mathrm{i}\delta}\sin^2\theta + e^{\mathrm{i}\delta}\cos^2\theta \end{pmatrix} . \tag{9.7}$$

We are now ready to analyze Fig. 9.3. The electric field just before the output polarizer is

$$E_{\mathrm{ell}} = \begin{pmatrix} \cos\delta \\ -\mathrm{i}\sin\delta \end{pmatrix} E_0 e^{-\mathrm{i}\omega t} . \tag{9.8}$$

Assume that $\theta = 45°$ (maximum effect) and that $\delta \ll 1$. It is easy then to see that $E_{\rm ell}$ represents elliptically polarized light with negative ellipticity $\psi = \delta$. After the output polarizer we get

$$E_{\rm out} = AB_{xy}E_{\rm in} = \begin{pmatrix} 0 \\ -\mathrm{i}\sin\delta\sin 2\theta \end{pmatrix} E_0 e^{-\mathrm{i}\omega t} \tag{9.9}$$

and the transmitted intensity is

$$I_{\rm out} = E^*_{\rm out}E_{\rm out} = E_0^2\left(\sin\delta\sin 2\theta\right)^2 \simeq E_0^2\left(\psi\sin 2\theta\right)^2 \ . \tag{9.10}$$

Notice the dependence on twice the angle θ. Figure 9.4 shows a situation analogous to the one pictured in Fig. 9.3, but in this case a selective absorption takes place in the interaction region (linear dichroism). Only photons polarized along the direction of the external field are affected by absorption. Assume that the light electric field amplitude is reduced by a factor q ($q < 1$) by the interaction with the external field (in general, q will be proportional to the length L of the magnetic field region). The Jones matrix representing this selective absorption along a "parallel" direction is then

$$D_{\parallel,\perp} = \begin{pmatrix} q & 0 \\ 0 & 1 \end{pmatrix} \ . \tag{9.11}$$

In the reference system xy of the figure, where the external field is again at an angle θ with respect to the x-axis (the initial polarization direction), this matrix is

$$D_{xy} = \begin{pmatrix} q\cos^2\theta + \sin^2\theta & \frac{q-1}{2}\sin 2\theta \\ \frac{q-1}{2}\sin 2\theta & q\cos^2\theta + \sin^2\theta \end{pmatrix} \ . \tag{9.12}$$

As before, one obtains the electric field amplitude before the output polarizer from

$$E_{\rm rot} = D_{xy}E_{\rm in} = \begin{pmatrix} q\cos^2\theta + \sin^2\theta \\ \frac{q-1}{2}\sin 2\theta \end{pmatrix} E_0 e^{-\mathrm{i}\omega t} \ . \tag{9.13}$$

Assume that $\theta = 45°$ and $1 - q = p \ll 1$; then $E_{\rm rot}$ represents linearly polarized light with its electric vector rotated by an angle

$$\alpha = -\left(\frac{1-q}{2}\right) \ , \tag{9.14}$$

with respect to the initial polarization direction. The electric field at the exit of the analyzer is

$$E_{\rm out} = AD_{xy}E_{\rm in} = \begin{pmatrix} 0 \\ \frac{q-1}{2}\sin 2\theta \end{pmatrix} E_0 e^{-\mathrm{i}\omega t} \tag{9.15}$$

and the corresponding transmitted intensity is

$$I_{\rm out} = E_0^2\left(\frac{q-1}{2}\right)^2 \sin^2 2\theta = E_0^2\alpha^2\sin^2 2\theta \ . \tag{9.16}$$

Again the intensity depends on twice the angle θ. Thus, in principle, a measurement of the ratio of the transmitted to the incident intensity gives either the ellipticity or the rotation angle. In practice, however, we must take into account the fact that actual polarizers are imperfect and that between a crossed pair, with no effect in between, some fraction σ^2 of the incident intensity will always be transmitted. σ^2, called the extinction factor, can be as small as 10^{-8} for very high quality polarizers. If we assume that both an ellipticity $\psi \ll 1$ and a rotation $\alpha \ll 1$ are produced in the interaction region, then it can be shown that the intensity transmitted through the ellipsometer is

$$I_{\mathrm{t}} \simeq I_0 \left(\sigma^2 + \psi^2 + \alpha^2\right) \ . \tag{9.17}$$

It is clear then that ellipticities or rotations smaller that 10^{-4} rad cannot be detected with such a static setup. For instance, from the QED photon-photon scattering we expect an ellipticity angle of about 3×10^{-16} rad for the PVLAS setup (following [5]) for a 1 m long interaction region and $\lambda = 1064$ nm. Direct static detection would be hopeless for such small angles. A great effort in PVLAS has gone into meeting the technical challenge of detecting such tiny angles.

9.2.2 Technical Challenges

Fabry-Pérot Cavity

The amount of induced magnetic birefringence and rotation are proportional to the length of the interaction region. This length can be effectively amplified, with respect to the actual magnet length, by folding the optical path inside the magnetic field zone. This can be acheived by using a resonant optical cavity, called a Fabry-Pérot resonator (FP), which is an interferometer where a monochromatic standing wave is established between two reflective surfaces placed at a distance apart. The wave results from the interference of beams, multiplies reflected from the surfaces, and appears at resonance; that is when the separation distance is an integer multiple of half the wavelength of the light impinging on the resonator. Practical FPs consist of two high-reflectivity mirrors (either plane or concave) at some distance L. High reflectivity is normally obtained by depositing several layers of dielectric material on a transparent substrate. If the layers are properly spaced, constructive interference will cause almost total reflection at normal incidence. Typically a reflectivity $R > 0.9999$ can be achieved with this technique. The device is usually kept at resonance by means of some active feedback system. Figure 9.5 shows a schematic drawing of such a Fabry-Pérot resonator. The FP is characterized by the following three parameters

$$\text{Finesse:} \quad F \simeq \frac{1}{(1-R)^2} \ , \tag{9.18}$$

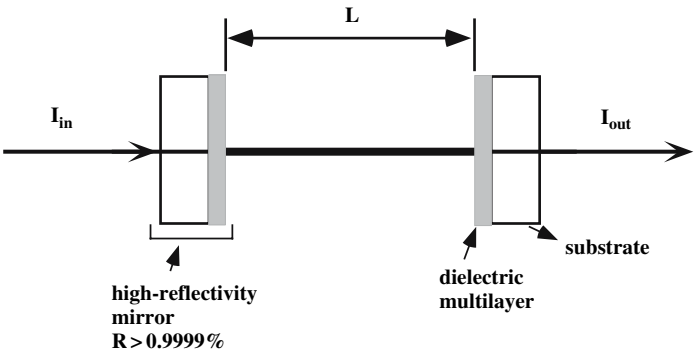

Fig. 9.5. Schematic drawing of a Fabry-Pérot optical resonator based on high-reflectivity multilayer dielectric mirrors

$$\text{Quality Factor:} \quad Q = \frac{2FL}{\lambda} \,, \tag{9.19}$$

$$\text{Photon lifetime:} \quad \tau = \frac{FL}{(\pi c)} \,, \tag{9.20}$$

where λ is the light wavelength, and c is the speed of light. It can be shown that an FP resonator having a finesse F amplifies the optical path length by a factor $N \simeq 2F/\pi$. The PVLAS ellipsometer contains a high-finesse FP resonator, which typically provides amplification factors of the order of $N \sim 50000$. With this amplification, the QED photon-photon scattering expected ellipticity would become about 1.5×10^{-11} rad, still well below static detection capabilities.

Heterodyne Detection

Static detection must then be abandoned in favor of a heterodyne detection scheme. The principle of heterodyne detection is to make the effect to be detected time-varying and to introduce a second similar, and normally larger, time-varying effect called carrier. The effect and the carrier will add resulting in signals at sum and difference frequencies, called beat frequencies. The amplitude of the beat signal will contain the carrier amplitude and will be linear, rather than quadratic, on the signal effect. Figure 9.6 shows a schematic layout of the heterodyne detection principle as applied in PVLAS. Let us first discuss Fig. 9.6 (a), which refers to the measurement of small ellipticities. After passing through the input polarizer, the linearly polarized light beam traverses the magnetic field region where it acquires an ellipticity ψ. This ellipticity is made time-varying by changing the angle θ between the magnetic field and the initial polarization direction (see discussion above). In practice, this is done by mechanically

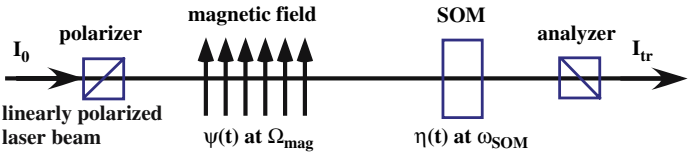

a) heterodyne detection of a small, time-varying, ellipticity ψ

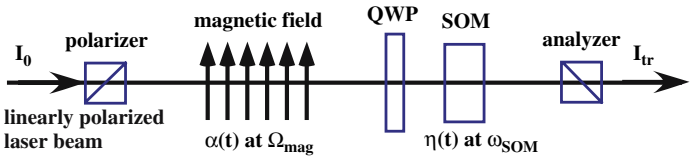

b) heterodyne detection of a small, time-varying, rotation α

Fig. 9.6. Principle of heterodyne detection of small signals: (**a**) birefringence detection (**b**) dichroism detection (see text)

rotating the magnet and keeping the initial polarization fixed in space, so that $\theta(t) = \Omega_{\rm mag} t + \theta_0$. Therefore we get for the time dependence of $\psi(t)$

$$\psi(t) = \psi_0 \sin 2\theta(t) = \psi_0 \cos\left(2\Omega_{\rm mag} t + \theta_{\rm mag}\right) \ . \tag{9.21}$$

Subsequently the light passes through a device called Stress Optical Modulator (SOM) that introduces an additional ellipticity

$$\eta(t) = \eta_0 \cos\left(\omega_{\rm SOM} t + \theta_{\rm SOM}\right) \tag{9.22}$$

where both the modulation frequency $\omega_{\rm SOM}$ and the modulation amplitude η_0 can be chosen. The SOM is based on the birefringence acquired by a piece of optical glass when stressed by external forces [9]. Using the Jones matrix formalism and assuming that $\eta_0, \psi_0 \ll 1$, the intensity transmitted through the ellipsometer of Fig. 9.6 (a) is (I_0 is the intensity after the input polarizer)

$$\begin{aligned}
I_{\rm T} &\approx I_0 \left\{\sigma^2 + \left[\psi(t) + \eta(t)\right]^2\right\} \\
&= I_0 \left\{\sigma^2 + \psi(t)^2 + \eta(t)^2 + 2\psi(t)\eta(t)\right\} \\
&\approx I_0 \left\{\sigma^2 + \eta_0^2 \cos^2\left(\omega_{\rm SOM} t + \theta_{\rm SOM}\right)\right. \\
&\quad \left. + \ 2\eta_0\psi_0 \cos\left(\omega_{\rm SOM} t + \theta_{\rm SOM}\right) \cos\left(2\Omega_{\rm mag} t + \theta_{\rm mag}\right)\right\} \\
&= I_0 \left\{ \left(\sigma^2 + \frac{\eta_0^2}{2}\right) + \frac{\eta_0^2}{2} \cos\left(2\omega_{\rm SOM} t + 2\theta_{\rm SOM}\right)\right. \\
&\quad + \eta_0\psi_0 \ \left[\cos\left(\left(\omega_{\rm SOM} + 2\Omega_{\rm mag}\right) t + 2\left(\theta_{\rm SOM} + \theta_{\rm mag}\right)\right)\right. \\
&\quad \left.\left. + \cos\left(\left(\omega_{\rm SOM} - 2\Omega_{\rm mag}\right) t + 2\left(\theta_{\rm SOM} - \theta_{\rm mag}\right)\right) \ \right] \ \right\} \ .
\end{aligned} \tag{9.23}$$

From the above formula one finds that the ellipticity η_0 to be measured appears at the angular frequencies $\omega_{\rm SOM} \pm 2\Omega_{\rm mag}$, i.e., at two sidebands of the carrier frequency separated by twice the magnet rotation frequency from the carrier. The sidebands amplitude is linear in ψ_0. Thus, compared to static detection, heterodyne detection has two main advantages: signal amplitudes contain ψ_0 rather than its square, and they appear far from the zero frequency, where $1/f$ noise is lower. For instance, if we assume $\psi_0 \sim 1.5 \times 10^{-11}$ rad and $\eta_0 \sim 10^{-3}$ rad, the number to be compared to $\sigma^2 \sim 10^{-8}$ is $\eta_0\psi_0 \sim 1.5 \times 10^{-14}$, rather than $\psi_0^2 \sim 2 \times 10^{-22}$. Furthermore, σ^2 and $\eta_0\psi_0$ appear at different frequencies. Information on the underlying physical processes can be extracted by measuring phase and amplitude of the frequency components of the transmitted intensity.

Let us now turn to the detection of small rotations, as illustrated in Fig. 9.6 b). Here one exploits the fact that a Quarter-Wave Plate[1] (QWP) is able, when properly aligned, to change rotations into ellipticities and vice versa [10]. This fact can also be verified by using the Jones matrix formalism, where a QWP with its slow axis along the x direction (refer to Fig. 9.3 for instance) is represented by

$$\mathrm{QWP}_x = \begin{pmatrix} e^{-\mathrm{i}\pi} & 0 \\ 0 & e^{\mathrm{i}\pi} \end{pmatrix} . \tag{9.24}$$

Thus, if the beam acquires a rotation by traversing the magnetic field region, then after passing through the QWP the acquired rotation has turned into an ellipticity $\psi_\alpha = \alpha$. This ellipticity can beat with the carrier ellipticity η and be detected, in the same manner as a "normal" ellipticity. Without the QWP, the rotation would not beat with the carrier ellipticity and would not be detected, as in the static case. It follows then, that the formula for the transmitted intensity in the case of rotation detection is the same as the above formula for ellipticity detection; one just substitutes ψ with ψ_α. In particular, one must again turn to the sidebands of the carrier frequency. Finally, notice that if the QWP axes are exchanged, by rotating the QWP itself by 90° and orienting the slow axis along y, then ψ_α will change sign. This sign change can be exploited when attempting to identify an observed signal as a "true" rotation.

Rotating Superconducting Magnet

At the end of this section, we briefly discuss the superconducting magnet, the third key element, along with the Fabry-Pérot resonator and the

[1] A Quarter-Wave Plate is a birefringent element which retards one polarization with respect to another by exactly 1/4 of a wave.

heterodyne setup, that enables the PVLAS ellipsometer to detect extremely small magnetically induced rotations and birefringences. The PVLAS magnet is a superconducting dipole with a 1 m long bore housed within a liquid He cryostat having an axial opening at room temperature, corresponding to the magnet bore, through which the light can propagate. The magnet normally operates at 4.2 K and is energized up to 5.0 T. For a detailed description of the magnet-cryostat system and its operation see [7]. The main feature of the cryostat is that it can be filled with liquid He, disconnected from the cryogenic supply, and rotated around its vertical axis. Before rotation, the magnet is energized by means of a power supply, then its coils are short-circuited to enter persistent current mode, and finally it is disconnected from the power supply. A turntable, actuated by a hydraulic motor, supports the cryostat and can rotate it at frequencies of the order of 1 Hz. Figure 9.7 shows a picture, taken during the construction phase of PVLAS, where the cryostat and turntable are visible at the center. Rotation of the cryostat-magnet assembly has the effect of changing the angle between the magnetic field direction and the initial light polarization direction: this is a necessary requirement for heterodyne detection.

Fig. 9.7. View of the cryostat with the magnet inside during assembly. The cryostat is mounted on a turntable fastened to a concrete beam spanning the PVLAS dugout. The turntable is situated below the cryostat. The magnet power supply is the cabinet visible at lower left

9.3 PVLAS Apparatus

The PVLAS apparatus develops vertically starting from a square dugout in the floor of the experimental hall at the Legnaro National Laboratories of INFN, Legnaro (Padova), Italy, as shown in Fig. 9.8. The bottom of the dugout is a concrete slab resting on six 14 m poles sunk in the ground and is separated by a slit from the dugout walls (also made of concrete) and the rest of the experimental hall floor. The bottom of the dugout supports a two-storey, 7.7 m high tower structure, resembling two stacked four legged stools, made of black granite beams. A granite optical bench is positioned at the top of the tower, while a second bench of the same material is at its bottom. The two benches are rigidly coupled via the tower. A reinforced concrete beam

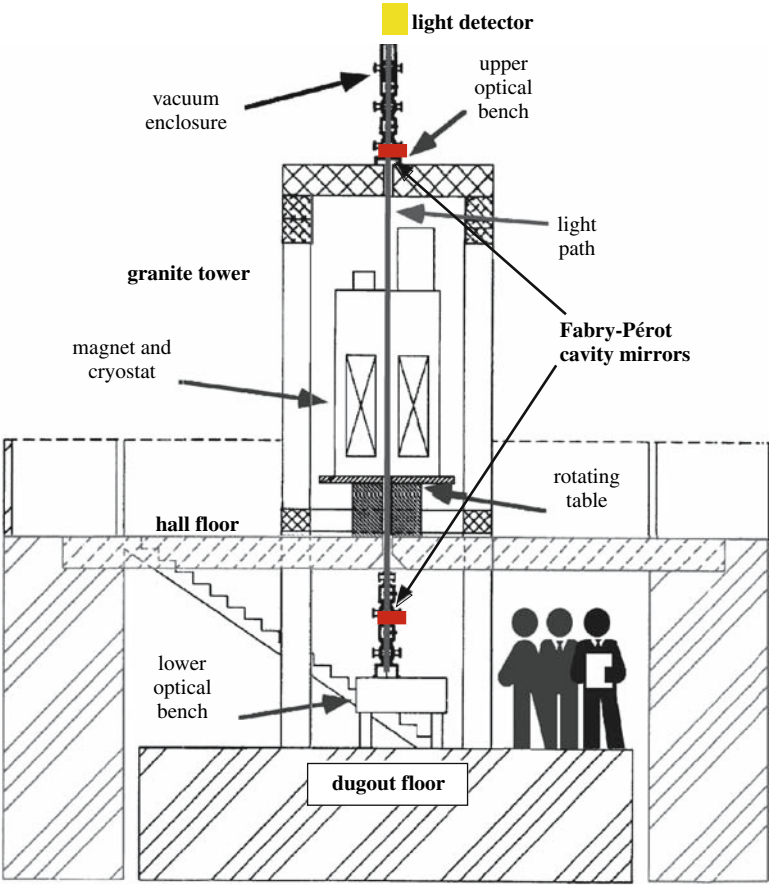

Fig. 9.8. Schematic cross section of the PVLAS apparatus (see text for a detailed explanation). Distance between dugout floor and top of the upper optical bench is 7.7 m

Fig. 9.9. View of the PVLAS granite tower and of its aluminum access structure. The cabinet visible at lower left is the magnet power supply

spans the dugout and passes through the tower (without touching it) for the purpose of supporting the magnet-cryostat-turntable assembly. In this manner, the rotating magnet can be positioned at the center of the tower structure without mechanical contact between the two. Figure 9.9 shows a picture of the PVLAS tower enclosed in the aluminum structure that is used to access various levels of the tower for operating purposes.

9.3.1 Optics Layout

Figure 9.10 shows a schematic layout of the PVLAS apparatus, including a simplified block diagram of the data acquisition system. Light from a Nd:YAG laser emitting at 1064 nm, placed on the lower optical bench, is sent vertically through the warm bore of the rotating cryostat by means of beam splitter (the rest of the injection optics layout is omitted for clarity). The beam then passes a polarizer, which fixes the initial polarization direction and is always kept in the same position during data taking. It subsequently enters the interaction region, where the horizontal rotating field is present, and is reflected back and forth thousands of times between the mirrors of the FP cavity. The actual length of the magnet is 1 m, but the mirrors, due to various mechanical constraints, are 6.4 m apart (see Fig. 9.8). After exiting the cavity, light passes through a QWP and the SOM ellipticity modulator, when measuring rotations, or just the SOM, when measuring birefringencies. An output polarizer (analyzer), crossed with the input polarizer for maximum extinction, transmits the extraordinary ray to a detection photodiode and

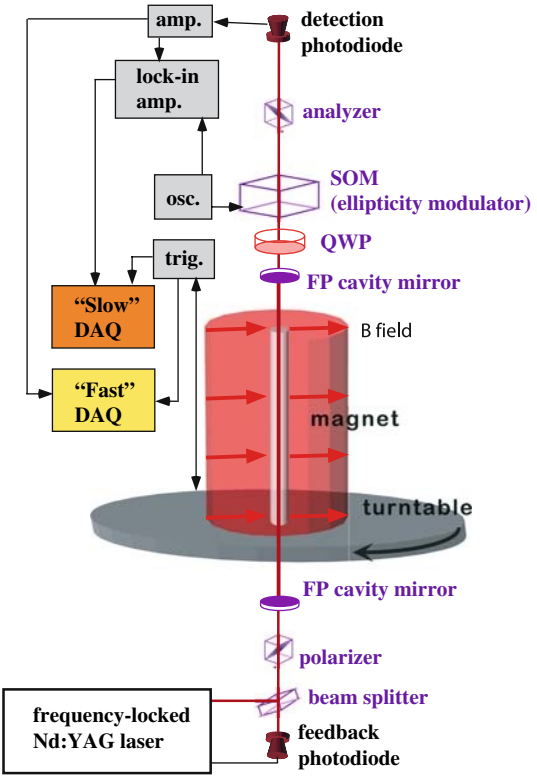

Fig. 9.10. Schematic layout (not to scale) of the PVLAS apparatus (see text)

sends the ordinary ray to a position-sensitive diode (not illustrated) used to monitor beam intensity and beam movements. The detection photodiode produces a current that contains the information on beam interactions.

During data taking, the FP must be kept at resonance. This is done by letting the mirrors float freely (subject to the mechanical rigidity of their mounts) and by adjusting the laser wavelength to follow the mirror separation using a frequency-locking feedback system [11]. This electro-optical feedback uses the light reflected back form the FP cavity to derive a correction signal, which is then applied directly to the internal piezoelectric actuator controlling the laser frequency.

9.3.2 Vacuum System and Gas Line

All the optical elements shown in Fig. 9.10, apart from the initial beam-splitter, must be kept in vacuum. The vacuum system consists basically of two large cylindrical steel chambers, one sitting on the lower optical bench and the other sitting on the upper bench, connected by a quartz tube. The

quartz tube has an outer diameter of 25 mm and passes through the warm bore of the cryostat without touching its walls. It basically defines the geometry of the FP cavity. The lower vacuum chamber contains the initial polarizer and the lower FP mirror. The upper optical chamber contains the upper mirror, the QWP, the SOM modulator, and the analyzer. All these optical elements are fixed to multi-axis movement stages that can be manually actuated without breaking the vacuum. The QWP can also be moved in and out of the beam also without breaking the vacuum.

Each of the two chambers is equipped with a pumping station. Ion pumps are normally used when not running the experiment, and the residual pressure is kept below 10^{-7} mbar. When taking data these pumps are turned off and their magnets are removed in order to eliminate possible couplings between the rotating field and the ion pump permanent magnets. The vacuum is then maintained by means of liquid-nitrogen traps supplemented by Ti sublimation pumps. We can reach a residual pressure in this case that is below 10^{-8} mbar. As it is desirable to use low pressure pure gases to check the ellipsometer operation (see discussion below), the vacuum system is completed by a separately pumped out gas line, which allows insertion of gases, such as He, Ne or N_2, from high purity bottles. Absolute capacitive gauges are used in this case to monitor gas pressure.

9.3.3 Light Detection, Data Acquisition and Data Analysis

Light exiting the ellipsometer after the analyzer leaves the vacuum through a glass window and propagates in air to the detection photodiode. Before impinging on this diode, it passes a spatial filter with a 50 μm pinhole and is focused on the diode's sensitive surface. The detection photodiode produces a current signal that is amplified and converted into a voltage by a transimpedance, high-gain, amplifier (see Fig. 9.3). This voltage constitutes the main signal to be acquired and processed. Data acquisition (DAQ) is split into two channels called "slow" and "fast". Both channels are used to acquire, besides the main signal, several other signals that carry additional information and monitor the functioning of the apparatus.

The "slow" channel is mainly used for on-line display and for diagnostic purposes. It basically consists of a lock-in amplifier referred to the same frequency used to excite the SOM modulator and triggered by a series of signals obtained from the magnet turntable. These triggering signals are generated by a set of 32 marks fixed on the outer circumference of the turntable and read by a photodiode. Each mark corresponds to a given angular position of the turntable. In this way, the phases of all signals are referred to the magnet rotation and are, therefore, absolutely known. As an added advantage, the "slow" acquisition is insensitive to small variations in the magnet rotation frequency (normally around 0.3 Hz). The output of the "slow" channel is a signal demodulated at the SOM frequency. A Fourier spectrum of this signal will show the SOM frequency as the zero frequency, while the sidebands of

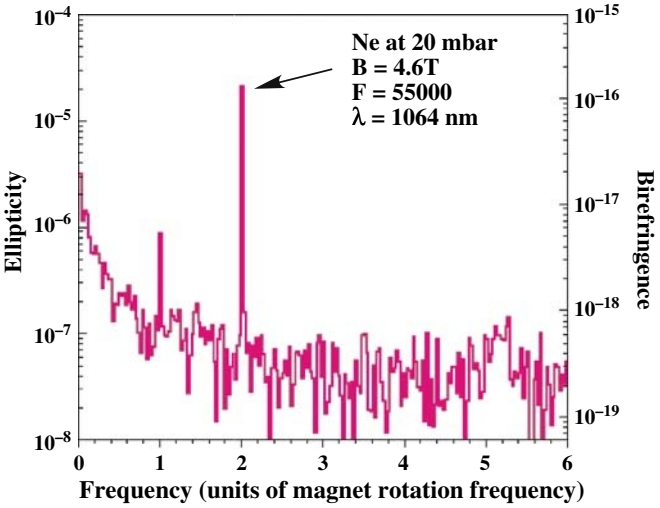

Fig. 9.11. Spectrum of the demodulated ellipsometer signal showing a peak at "2" due to the CME of 20 mbar of Ne (see text)

interest appear as peaks separated from zero by the same sideband-to-carrier frequency distance (see the discussion in Sect. 9.2.2). An example of such a spectrum is shown in Fig. 9.11.

The "fast" channel is essentially a set of ADCs sampling the signal voltage at 8.2 kHz and storing the data on a computer for off-line analysis. The "fast" channel also acquires the trigger signals, and the signal phases can then be reconstructed off-line. Analysis of the "fast" data is based on a multi-parameter fit that determines phase and amplitude of the frequency components of interest contained in the main and in the auxiliary signals. These raw data are then used for further analysis and to generate plots and spectra for visualization. For a more detailed description of the data acquisition system see [12].

9.4 Results

We summarize here a few recent results obtained with the sensitive ellipsometer described in the previous sections [13]. Let us recall that the instrument is capable of detecting both birefringencies and rotations and that switching between birefringence and rotation detection is accomplished by simply inserting a quarter-wave plate in the beam path. The measured sensitivity of the ellipsometer (i.e., the minimum signal amplitude which can be detected in 1 s with a signal-to-noise ratio of 1) is about $10^{-7}\,\mathrm{Hz}^{-1/2}$ for both ellipticities and rotations.

There are three main types of measurements to be discussed: performance tests using the magnetic birefringence effect of test gases (Cotton-Mouton effect), rotation, and birefringence measurements in vacuum. The last type of measurement will be briefly touched upon, but no actual data will be presented.

9.4.1 Performance Tests with CME in Gases

The performance of the PVLAS ellipsometer can be tested and calibrated by exploiting the Cotton-Mouton effect (CME) in gases [16]. In order to do this, a gas, normally He, Ne, or N_2, is inserted at a controlled pressure in the interaction region. The presence of the magnetic field turns the gas into a birefringent medium, and the amount of induced ellipticity is proportional to the square of the magnetic field amplitude and to the gas pressure. As the CME is a known physical effect, the amplitude of the corresponding peak in the detection photodiode signal spectrum must have a precise value which, at least in the case of N_2, is already well established in the literature [17]. The sensitivity of the PVLAS ellipsometer is such that CME peaks appear well above background even for He gas, which has the weakest effect. Furthermore, the phase of the CME peak must have a definite value set by the position of the initial linear polarization of the probe beam with respect to the data acquisition trigger position. This phase is deduced by recalling that the CME signal is maximum when the rotating field is at 45° with respect to the initial polarization vector. The absolute value of this reference phase, 16° in the case of He and Ne, which exhibit positive birefringence, and 196° in the case of N_2, is not essential. It is however important to recognize that any signal detected by the ellipsometer having a physical origin will have a phase near either the Ne phase or the N_2 phase.

Cotton-Mouton Measurements

A typical photodiode current spectrum showing a CME signal can be seen in Fig. 9.11. The spectrum was obtained at a wavelength of 1064 nm with 20 mbar of Ne in the interaction region, a magnetic field strength $B = 4.6$ T, and a finesse $F = 55000$. The detection photodiode signal is demodulated by a lock-in amplifier set at a reference frequency equal to the SOM modulation frequency (506 Hz); therefore, the CME signal appears in the spectrum as a sideband of the zero frequency at twice the chosen magnet rotation frequency (0.33 Hz in this case). Notice that the abscissa axis is in units of the magnet rotation frequency, thus the CME peak appears at the "2" frequency. This last quantity is defined, following [18], as the anisotropy of the index of refraction relative to the directions parallel and normal to the external field $\Delta n = n_{\parallel} - n_{\perp}$. The CME peak Signal-to-Noise Ratio (SNR) can be estimated from Fig. 9.11 to be about 200.

The amplitude response of the PVLAS ellipsometer is then calibrated by repeating the measurement as a function of gas pressure: the slope of the curve thus obtained must give the birefringence value characteristic of the gas in use. Figure 9.12 shows such a curve in the case of Ne. A linear fit to the data is superimposed on the data points. The ordinate axis gives the reduced birefringence, while pressure is given along the abscissa axis. The reduced birefringence is defined as $\Delta n_u^r = \Delta n(1/B[\mathrm{T}])^2 P_{\mathrm{atm}}$ [18], where n is the birefringence, B is the applied field in T, and P_{atm} is the atmospheric pressure.

Phase information from CME measurements is best appreciated on a polar plot. Figure 9.13 shows such a plot, where data points are the amplitude-phase pairs relative to the measured CME peaks of Ne (right side of the plot) and N_2 (left side of the plot) as a function of pressure. Notice how data points for different pressure values align along a straight line pointing to 16° at right and to 196° at left. We call this line the physical axis. The Ne data all lie on the right half of the physical axis with respect to the origin, while the N_2 points all lie on the opposite side. The gas measurements, then, reproduce the expected position of the physical axis as deduced from the geometry of the apparatus (taking into account the direction of the initial polarization). The inset gives an idea of the aspect of the typical spectrum from which each point is obtained. The spectrum in this case is taken from the "fast" DAQ and is not demodulated. Thus CME peaks appear as large sidebands of the SOM-generated carrier peak.

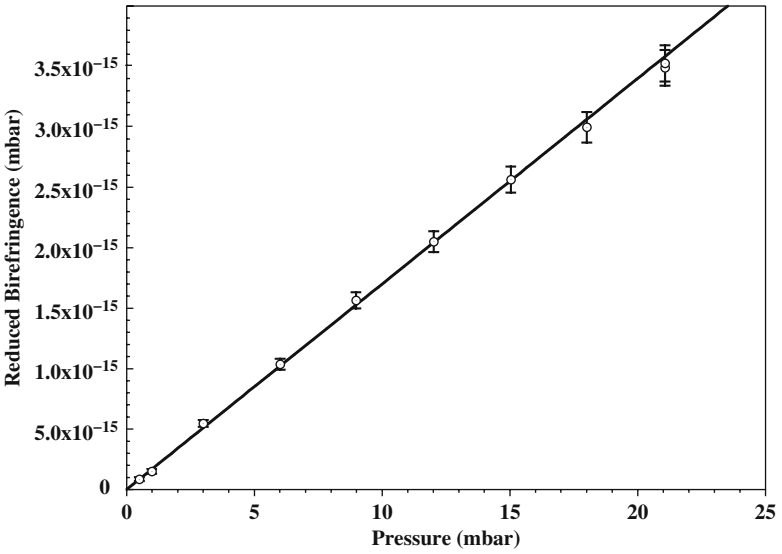

Fig. 9.12. Reduced birefringence due to CME as a function of Ne pressure (see text)

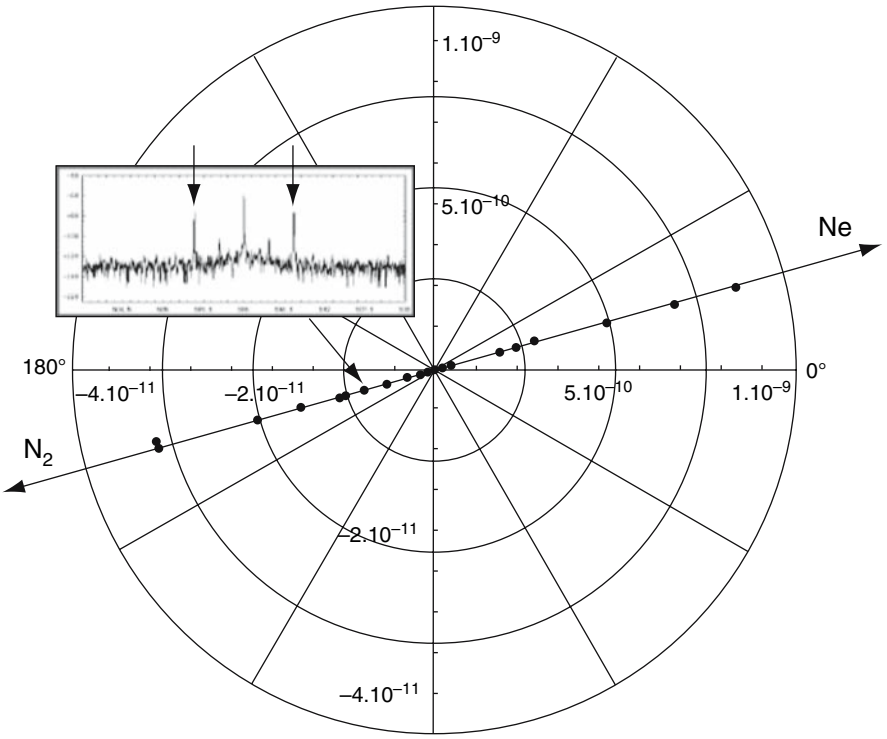

Fig. 9.13. Polar plot of phase and amplitude of CME peaks of Ne and N_2 taken at several pressure values (see text)

Residual Gas Checks

Before discussing vacuum measurements, we must briefly mention the characteristics of the residual gas that is present in the chamber under "vacuum" conditions. Recall here that the typical operating pressure when in vacuum is always below 10^{-7} mbar. Under static conditions, the chamber out-gassing rate is $< 2 \times 10^{-5}$ mbar hour^{-1}. When taking data the composition of the residual gas is monitored by means of two mass spectrometers, placed correspondingly at the upper and lower optic chambers. The main components are H_2, CO, and H_2O. The partial pressure of the worst contaminant, which is CO, is at the level of 1% of the total pressure. The magnetic birefringence of CO is $\Delta n_u = -1.83 \times 10^{-13}$ (at $T \sim 293$ K). Using this value, one finds that the contribution of the residual gas to birefringence measurements is at the level of 10^{-12} in ellipticity (with $B = 5$ T and the total pressure $P = 10^{-7}$ mbar). No contribution is expected from gases to the magnetic field induced rotation in vacuum.

9.4.2 Vacuum Measurements

We will mainly discuss in this section the results form data runs attempting to detect a residual linear rotation of the magnetized vacuum. Let us state at the beginning that, as in the gas case, no rotation of the polarization plane of light propagating in vacuum through the interaction region was expected. The main result to be reported here is the observation of a rotation peak in the spectrum of the photodiode current at the position of the sideband separated by twice the magnet rotation frequency from the carrier SOM frequency (recall that, in order to detect rotations, a QWP is inserted in the beam before the SOM ellipticity modulator). The peak is present when the magnet is energized and the Fabry-Pérot cavity mirrors are present. This is a surprising observation because not only a peak appears where there should be none, but, in addition, the peak exhibits a large amplitude (typically 10^{-7} rad), with an SNR above background ranging from 5 to 20, depending on the particular data run.

We mention also, without however providing evidence in this chapter, that an unexpected ellipticity peak also is observed in all those data runs attempting to detect a residual linear magnetic birefringence of vacuum. As in the rotation case, the ellipticity peak is observed only when the magnetic field is on and the Fabry-Pérot cavity is present. Also, the absolute magnitude of this peak in radians is about the same order of the magnitude of the rotation peak.

Magnetic Rotation of Vacuum

Figure 9.14 shows a sample spectrum of the detection photodiode current signal demodulated by a lock-in amplifier at the frequency of the SOM. The peak of interest thus appears at a frequency distance from the zero frequency equal to twice the rotation frequency of the magnet. In the case shown in Fig. 9.14, the QWP axis was set to the nominal "0" position, the light beam made about 44000 passes in the interaction region, and the residual vacuum pressure was below 10^{-7} mbar. Figure 9.14 (a) gives the observed spectrum when $B = 0$, while Fig. 9.14 (b) shows the spectrum when $B = 5.5$ T. Signal amplitudes in Volts are reported on the ordinate axis, while the abscissa axis gives frequency measured in multiples of the magnet rotation frequency (0.33 Hz in this case). Notice the presence of a peak at the "2" frequency in the spectrum with the magnet on and its corresponding absence in the spectrum with the magnet off. This fact establishes the dependence of the signal on the presence of the magnetic field.

The additional large peak visible at the "1" frequency, that is exactly at the magnet rotation frequency, has been studied separately, and its amplitude and phase were found to be uncorrelated with those of the signal peak. Its most probable origin is a Faraday type rotation generated by residual fringe fields acting on the reflective coatings of the mirrors. Recall that a Faraday

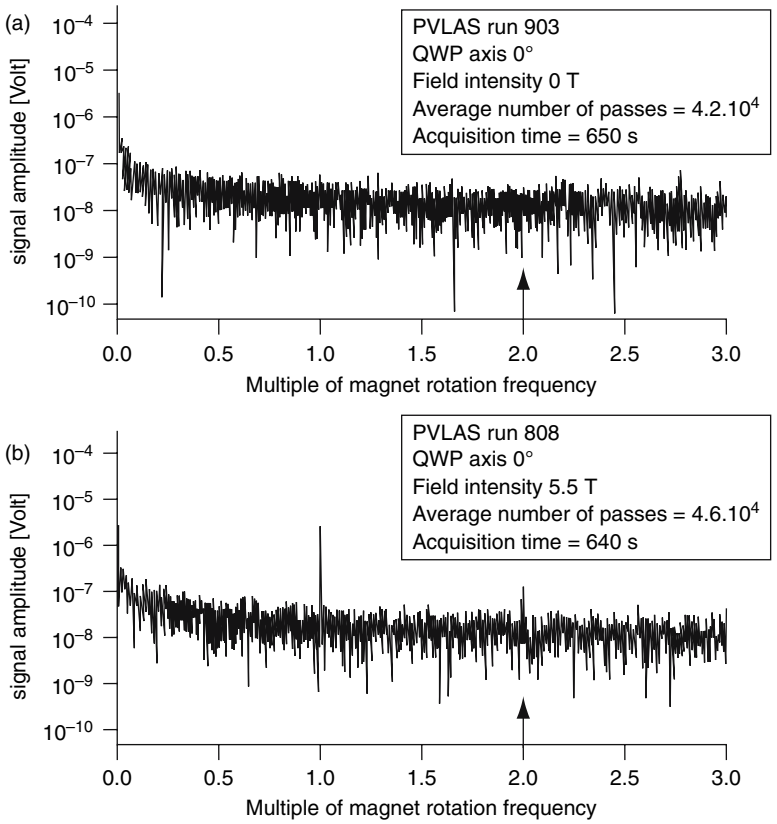

Fig. 9.14. Spectra of the demodulated photodiode signal showing vacuum rotation peaks with (**a**) field off, (**b**) field on (see text). The arrow points at the relevant signal peak at twice the magnet rotation frequency

rotation can only appear at the same frequency as that of the exciting field. This effect has been observed and measured in the past [14] and has also been re-checked for the mirrors presently used by PVLAS (G. Zavattini priv. com.). The estimates for the amplitude of the "1" peak from both sources give a value between 10^{-7} and 10^{-6}, which accounts well for a large part of the observed "1" peak amplitude.

Fringe fields at the mirror position have a measured component of a few Gauss, parallel to the mirror surface. Assume this parallel component has an intensity of 1×10^{-3} T. There is also a small component of the field normal to the mirror surface, which is due to the misalignment angle (about 10^{-3} rad) between the magnet rotation axis and the Fabry-Pérot cavity axis. Thus the Faraday-generating fringe field BF is conservatively estimated to be about 10^{-6} T. Reference [14] reports a rotation induced on a linearly polarized beam reflecting once off the surface of a multilayer

mirror of $3.7 \times 10^{-6}\,\mathrm{rad\,T^{-1}}$. The induced rotation at the "1"' frequency would in this case be $\alpha_{\mathrm{lit}} = (3.7 \times 10^{-6}\,\mathrm{rad\,T^{-1}})(10^{-6}\,\mathrm{T})(50,000\,\mathrm{passes}) \approx 2 \times 10^{-7}\,\mathrm{rad}$. Recent measurements (G. Zavattini priv. com.) done on the mirrors used in the PVLAS apparatus detected magnetically induced rotation on linearly polarized light traversing the mirror. A Verdet constant of about $V_{\mathrm{mir}} = 6.4 \times 10^{-3}\,\mathrm{rad\,T^{-1}\,cm^{-1}}$ was found. Assuming that the mirror coating layers exhibit the same Verdet constant and that the beam, upon reflection, enters the coating for a depth of about $10\,\mu\mathrm{m}$, one estimates $\alpha_{\mathrm{meas}} = \left(6.4 \times 10^{-3}\,\mathrm{rad\,T^{-1}\,cm^{-1}}\right)\left(10^{-6}\,\mathrm{T}\right)\left(10^{-3}\,\mathrm{cm}\right)(50,000\,\mathrm{passes}) \approx 3 \times 10^{-7}\,\mathrm{rad}$.

Considerable effort has been spent in trying to identify the nature and origin of the rotation peak in vacuum. The first step is to identify the signal as a "true" rotation, i.e., to prove that the peak stems form an actual rotation of the polarization plane of light traversing the ellipsometer. The second step is to localize, within the apparatus, the region where this rotation is induced. Finally, one must try to exclude all possible sources of instrumental artifacts. To establish the "true" rotation nature of the peak, one relies on three experimental facts

1. the signal, in order to be observed, must convert into an ellipticity via the QWP and must beat with the carrier ellipticity generated by the SOM;
2. the signal phase must change sign when the axes of the QWP are changed; and
3. the signal phase must, on average and within experimental uncertainties, lie near the "physical axis" direction identified on a polar plot by gas CME measurements.

The first point is given by the fact that the peak is actually observed as a sideband of the carrier ellipticity signal introduced by the SOM modulator. The second and third points are established from a statistical analysis of data taken in the course of several measurement runs. This analysis is briefly sketched below when discussing Fig. 9.15.

To localize the region where the rotation is induced, data runs were performed after removing the cavity mirrors and leaving the rest of the apparatus untouched. These data show no peak at the "2" frequency, down to the level of $10^{-9}\,\mathrm{rad}$, when the magnet is energized. This value is the background level that can be reached after $\sim 10,000\,\mathrm{s}$ of integration. Three main conclusions can be drawn from this fact regarding the origin of the "2" peak

1. it is not due to an electrical pick-up;
2. it is not generated either by the SOM modulator or by mechanical rotations of the QWP or of the entrance polarizer; and
3. it is generated within the Fabry-Pérot cavity, either in the interaction region or by some effect acting on the mirrors.

To further restrict the third point mentioned above, one observes that a direct effect of the fringe fields on the mirrors is excluded by known results on

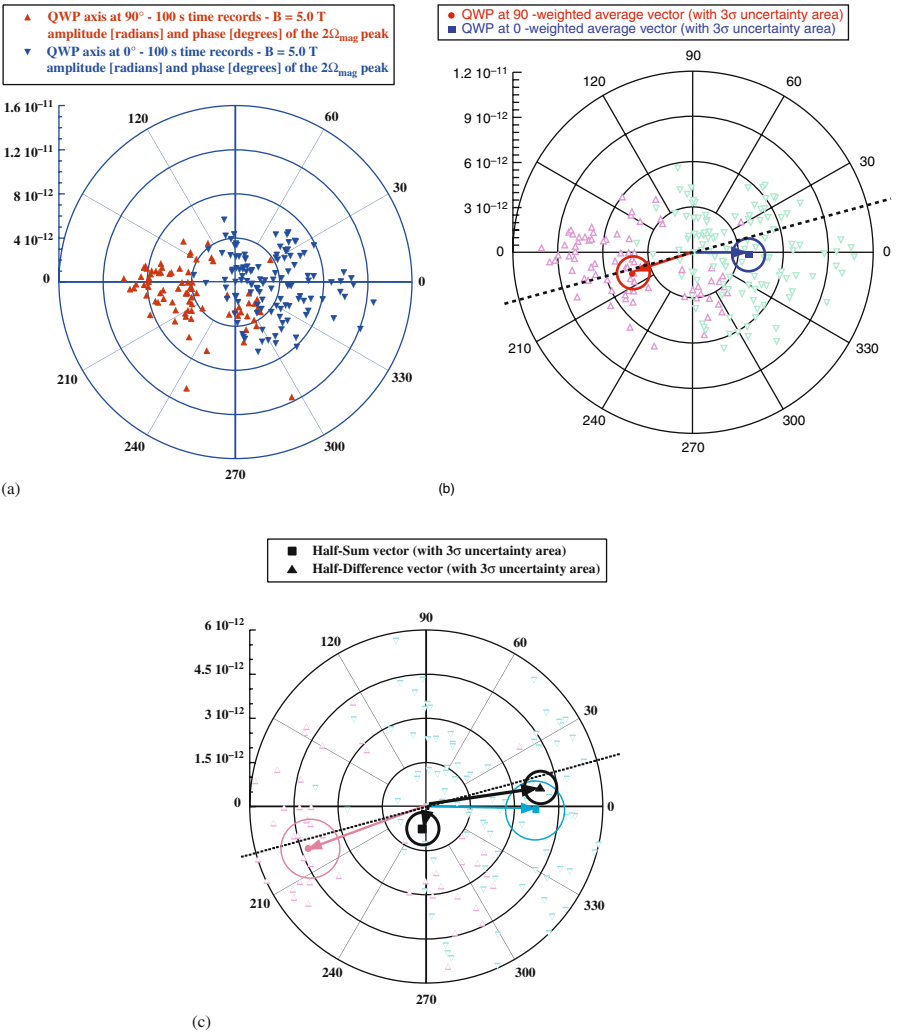

Fig. 9.15. Polar plot of phase and amplitude of vacuum rotation peaks for two orientations of the QWP (see also text). Data were taken at 1064 nm, 50,000 passes in the Fabry-Pérot, 5.0 T average field. Data points represent phase and amplitude of the $2\Omega_{mag}$ peak relative to a 100 s long time record. (**a**) data distributions for the two possible orientations of the axes of the QWP with respect to the initial polarization (labeled conventionally QWP90 and QWP0) (**b**) weighted average vectors are superimposed on the data distributions (scale is zoomed with respect to a)) (**c**) half-sum and half difference vectors are shown (scale is zoomed with respect to b))

magnetic-field-induced rotation on multilayer mirrors [14] coupled to direct measurements of the fringe field in the vicinity of the mirrors, which do not evidence the presence of a frequency component at twice the magnet rotation frequency. Even if it is not of relevance for the discussion of the rotation peak, we observe in passing that direct birefringence effects also are excluded by measurements found in the literature [15]. Thus, only an unknown indirect effect on the mirrors, or on the resonant cavity as global object, is left as a possible instrumental source of artifacts mimicking a physical rotation signal.

To complete the discussion let us now, finally, turn to the phase analysis of the signal. This is done by considering the detection photodiode current as a function of time, separately for each of the two possible orientations of the QWP axes, labeled "0" and "90" for convenience. Each of these two data sets is then subdivided into 100 s long time records (resulting in 121 records at "0" and 84 records at "90"). For each record, we perform a fit to determine the amplitude and phase of the component at twice the magnet rotation frequency ($2\Omega_{\mathrm{mag}}$). Amplitudes are quoted in units of $\mathrm{rad\,pass^{-1}}$. The result of this operation is a set of 121 amplitude-phase pairs for the "0" orientation of the QWP, and a set of 84 pairs for the "90" orientation. These data can be plotted on a polar graph and analyzed. Figure 9.15 (a) shows a polar plot where the two sets of data pairs just described have been plotted. Notice how the distributions for the two orientations of the QWP separate in different regions of the graph. Notice also the dispersions of the samples. We assume that this dispersion is due to some unidentified systematic source of uncertainty, which, however, has a Gaussian character. To obtain a weighted average vector, representing the global result for each orientation, we use the dispersion of this Gaussian distribution and add it in quadrature to the intrinsic uncertainty coming from the fit. As a guide, consider that the fit uncertainty for each point is about $0.07 \times 10^{-12}\,\mathrm{rad\,pass^{-1}}$, while the dispersion of the data sets is about $2 \times 10^{-12}\,\mathrm{pass^{-1}}$. Figure 9.15 (b) shows the weighted average vectors, obtained at the end of the above procedure, superimposed on the data distributions: one vector represents phase and amplitude of the rotation in vacuum observed when the QWP is at "0", while the other is relative to the "90" orientation. Circled regions at vector tips give 3σ uncertainty areas. The dotted straight line represents the physical axis. To derive a final figure for the rotation effect, one must combine the information from the two QWP orientations in the following way. Half the difference between the QWP-0 and the QWP-90 vectors gives the part of the signal changing sign under a QWP axis inversion. This is is the behavior as expected from a "true" rotation. The remaining part, i.e., the half-sum of the two vectors, can be considered as a residual spurious effect. Figure 9.15 (c) shows both the half-sum and half-difference vectors along with 3σ uncertainty areas at their tips. Notice how the half-difference vector lies in the direction of the physical axis. The amplitude of the half-difference vector then gives the magnitude of the rotation of the polarization plane of light traversing a 1 m long vacuum region where a 5.0 T transverse magnetic field is present as

$$\alpha = (3.9 \pm 0.5) \times 10^{-12}\,\mathrm{rad\,pass^{-1}}\ . \tag{9.25}$$

A list summarizing the possible sources of instrumental artifacts together with corresponding experimental tests is given in Tables 9.1.

Table 9.1. Summary of different experimental artifacts which could account for the observed signal and corresponding experimental tests which allow to identify and quantify them

Origin	Test	Comment
Magnetic rotation/birefringence from a residual gas	Measure the pressure and composition of the residual gas.	No rotation is generated by gases in a magnetic field. A birefringence is generated by the Cotton-Mouton effect; however, the Cotton-Mouton effect due to the worst contaminant is orders of magnitude below the observed effect.
Rotation/birefringence induced by fringe fields on the mirror coatings	Direct measurement of the effect (ultimate cure: eliminate fringe fields)	The rotation effect due to a field acting perpendicular to the mirror surface has been measured by [14]. Given an estimated fringe field component of 10^{-6} T at the Ω_{mag} frequency, this effect can account for the Ω_{mag} observed peak. No field component is measured at the $2\Omega_{\mathrm{mag}}$ frequency. The birefringence effect due to a field acting parallel to the mirror surface has been measured by [15]. The measured fringe field on the mirror surface (about 3–5 $\times 10^{-4}$ T) is not sufficient to account for the observed birefringence effect.
Electronic pick-up (rotation and birefringence)	Measure with field on and the cavity mirrors removed.	Pick-up is excluded by the fact that no peaks above the noise are observed in data runs with field on and cavity mirrors removed. This applies to both birefringence and rotation.

(Continued)

Table 9.1. Continued

Origin	Test	Comment
Diffused light from a magnetized inner surface of the cryostat bore	Change the geometrical acceptance of the light detection system.	A spatial filter is present before the detection photodiode. Data runs have been conducted with several different pinhole diameters down to 50 μm and no change has been observed in the signal.
Field-induced movement of the polarizer and/or the QWP (rotation)	Measure with field on and the cavity mirrors removed.	The effect is excluded by the fact that no peaks above the noise level are observed in data runs with the field on and the cavity mirrors removed.
Spurious, field-induced ellipticity generated by the SOM modulator	Measure with the field on and the cavity mirrors removed.	The effect is excluded by the fact that no peaks above the noise are observed in data runs with the field on and the cavity mirrors removed.
Beam pointing instability (birefringence and rotation)	Measure the beam movements and correlate them to the observed effect (ultimate cure: stabilize beam movements).	No correlation is observed between beam movements and observed effects.
Unknown field-polarization coupling	Eliminate the fringe fields.	Very hard to imagine a possible candidate effect. This however is not excluded.

9.5 Discussion

We discuss in this section the possible consequences of the experimental facts just described. The main result is the observation of an unexpected rotation of the polarization plane of linearly polarized light traversing a vacuum region in the presence of a transverse magnetic field. This empirical observation can have two origins

1. an instrumental artifact or
2. an underlying physical phenomenon.

The first origin cannot strictly be ruled out. There is always a non-zero probability that an hitherto unknown instrumental effect causes the observed

signal. This spurious effect, however, must mimic very closely the behavior of a real physical signal and, in addition, must come from a very indirect link between the magnetic field and the light polarization. A substantial part of the on-going efforts at PVLAS is directed towards identifying possible new sources of artifacts and devising ways to check them. Based on the above considerations, we make the hypothesis in the following that an underlying physical phenomenon is responsible for the presence of the observed rotation.

9.5.1 Possible Physical Origins of the Rotation Signal

We assume now that the observed rotation is actually an apparent rotation, caused by the vacuum behaving as a dichroic medium. In such a medium, photons are selectively absorbed according to the direction of their polarization with respect to a given anisotropy direction: this results in an overall apparent rotation of the polarization plane (see Fig. 9.4). The rotation is apparent since, due to absorption, the light intensity actually decreases. If, however, the number of absorbed photons is small compared to the total number of photons in the beam, then the intensity is practically unchanged and one will measure a rotation. We discuss two possible sources of selective absorption of photons: photon splitting and the oscillation of photons into neutral light bosons via the Primakoff effect.

Photon Splitting

To estimate the contribution of photon-splitting processes to the selective absorption of photons we follow [19] and use the following absorption coefficients for light polarized parallel and normal to the external magnetic field

$$\alpha_{\parallel} = 0.51\,(\omega/m_e)^5\,(B/B_{\rm cr})^6\ {\rm cm}^{-1}\ ,$$

$$\alpha_{\perp} = 0.24\,(\omega/m_e)^5\,(B/B_{\rm cr})^6\ {\rm cm}^{-1}\ , \tag{9.26}$$

where ω is the photon energy, m_e the electron mass, and $B_{\rm cr} = 4.41 \times 10^9\,{\rm T}$ is the critical field. With the experimental parameters of PVLAS ($\omega = 1.17\,{\rm eV}$ and $B = 5.0\,{\rm T}$) we obtain $\left(\alpha_{\parallel} - \alpha_{\perp}\right)_{\rm splitting} = 1.34 \times 10^{-82}\,{\rm cm}^{-1}$. From formula (1) of [13], taking into account a magnet length of 1 m and using the measured rotation of $3.9 \times 10^{-12}\,{\rm rad\,pass}^{-1}$, we can estimate $\left(\alpha_{\parallel} - \alpha_{\perp}\right)_{\rm PVLAS} = 7.8 \times 10^{-14}\,{\rm cm}^{-1}$. Clearly photon splitting alone cannot account for the observed rotation.

Photon-Boson Oscillation Model

According to the Primakoff effect, neutral particles can be produced from the interaction of two photons, one of which can be a virtual photon provided by an external field, and the other one a real photon from some photon

source [20]. In the present case, the virtual photon would be provided by the magnetic field and the real photon by the laser beam. Two types of production can occur: real production and virtual production (see Figs. 9.1 and 9.2 with the accompanying discussion). In a real production, a boson having a mass lower than the kinematic limit ($\sim 1\,\mathrm{eV}$ in this case) is produced and a photon disappears from the beam. In virtual production, a virtual boson is likewise produced by the two-photon interaction. It then subsequently decays back into a virtual photon and a real photon identical to the original incoming photon from the laser beam. If the incoming laser beam is linearly polarized, real production results in an apparent rotation (dichroism) of the polarization plane, while virtual production results in a linear birefringence acquired by the beam. In our case, where a magnetic field B_{ext} is present and a Fabry-Pérot cavity of finesse F is used to amplify the optical path, according to [20] and [21], the rotation and ellipticity amplitudes are given by

$$\alpha_b = \frac{1}{M_b^2}\frac{2FB_{\mathrm{ext}}^2\omega^2}{\pi m_b^4}\left[\sin\left(\frac{m_b^2 L}{2\omega}\right)\right]^2 ,$$

$$\psi_b = \frac{1}{M_b^2}\frac{FB_{\mathrm{ext}}^2\omega^2}{\pi m_b^4}\left[\frac{m_b^2 L}{2\omega} - \sin\left(\frac{m_b^2 L}{2\omega}\right)\right] . \tag{9.27}$$

In the above formulae, where naturalized Heaviside-Lorentz units are used[2], $M_b = 1/g_{b\gamma\gamma}$ is the inverse coupling constant to two photons [22, 23], m_b is the particle mass, ω is the incoming photon energy, and L is the length of the magnet (the angle θ between field and light initial polarization is set to 45°). One can solve the rotation formula for M_b, obtaining a function of α_b and of m_b. If one then directly measures α_b, the result can be plotted as a curve in the m_b–M_b plane. The meaning of this curve is obvious: all possible allowed values of the (m_b, M_b) pairs for a produced particle must belong to this curve. Figure 9.16 shows a portion of the m_b–M_b plane where the measured dichroism curve is plotted, along with 3σ uncertainty bands. The curve is calculated starting from the above model and using the measured rotation of $3.9 \times 10^{-12}\,\mathrm{rad\,pass^{-1}}$ for a cavity with $\sim 50,000$ passes and a field of 5.0 T. Photon energy is 1.17 eV (corresponding to the 1064 nm laser wavelength) and magnet length is taken as 1 m.

This exercise can be carried further, and one can actually estimate an interval for the allowed values of the mass and inverse coupling constant of the hypothetically produced particle. In order to do this, the PVLAS measured dichroism is combined with data obtained in a precursor experiment by the Brookhaven-Fermilab-Rochester-Trieste (BFRT) collaboration [22]. In this experiment, no signal was observed, either in rotation or in birefringence, and exclusion regions were set on the m_b–M_b plane based on the observed background. Figure 9.17 shows a portion of the m_b–M_b plane where exclusion regions obtained by BFRT are superimposed on the PVLAS measured

[2] In Heaviside-Lorentz units one sets $1\,\mathrm{T} = 195\,\mathrm{eV}^{-2}$ and $1\,\mathrm{m} = 5 \times 10^6\,\mathrm{eV}^{-1}$.

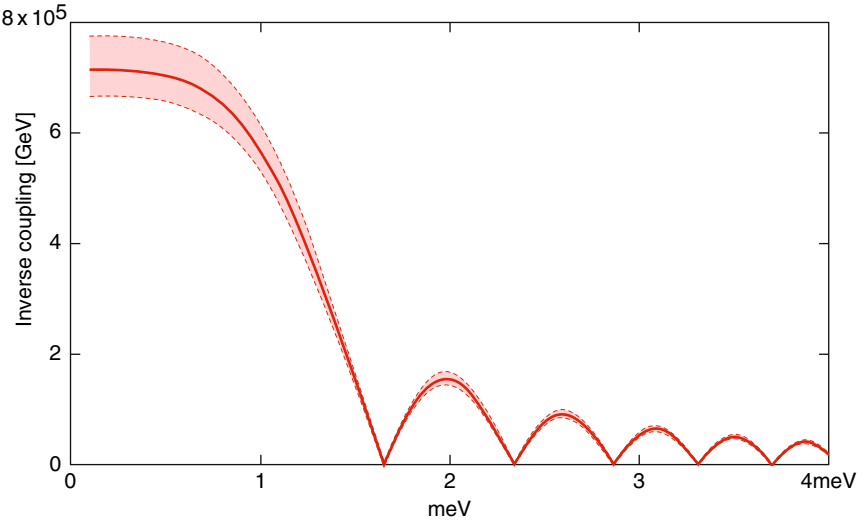

Fig. 9.16. Curve in the m_b–M_b plane resulting from PVLAS measured dichroism (see text)

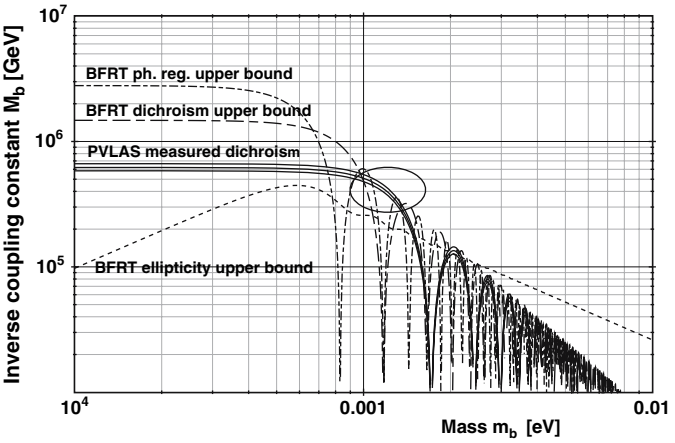

Fig. 9.17. Combined exclusion plot used for $g_{b\gamma\gamma}$ and m_b estimates (see text). The red curve represents the curve calculated from the measured PVLAS dichroism, including 3σ uncertainty bands. The green curve is the upper bound derived from the BFRT observed rotation background, while the blue curve gives the upper bound from the BFRT ellipticity background. Finally, the shaded area represents the portion of the plane excluded by the photon-regeneration experiment reported in [24]. The solid black oval evidences the main region where the PVLAS result is not excluded by BFRT

rotation curve. For completeness, we also include an exclusion region stemming from a pioneering photon regeneration type experiment also done at Brookhaven (see discussion below and [24]). Notice that there is at least one region where the PVLAS curve is not excluded by BFRT. Concentrating on this portion of the curve, one estimates the following allowed ranges for the hypothetical particle mass and for its inverse coupling to two photons

$$\begin{aligned} 1\,\mathrm{meV} \leq\ & m_b \ \leq 1.5\,\mathrm{meV} \\ 1.7\times10^{-6}\,\mathrm{GeV}^{-1} \leq\ & g_{b\gamma\gamma} \leq 1\times10^{-5}\,\mathrm{GeV}^{-1}\,. \end{aligned} \tag{9.28}$$

Notice, in Fig. 9.17, that the BFRT dichroism curve is apparently more sensitive than the PVLAS measured curve, especially for small mass values. This, however, is simply due to the fact that BFRT magnets were longer than the PVLAS magnet (8.8 m versus 1 m). Correspondingly, the BFRT curve has zeroes in a mass interval where the PVLAS curve is still sensitive. We mention here that the photon-to-boson oscillation model also predicts a birefringence effect coming from virtual boson production and that a birefringence of vacuum is actually observed in PVLAS. Finally, we remark that the estimates of particle parameters presented above are strongly model-dependent and should be considered with care.

9.5.2 Perspectives

The rotation signal observed by PVLAS is potentially an extremely important result, paving the way for a whole new field of physics. For this reason it is of utmost urgency to confirm its physical origin and to further investigate its consequences. This of course calls for independent experiments to be carried out as soon as possible.

Limited to testing the particle interpretation of the observed rotation, there also exist direct physical checks that can be executed using the present PVLAS apparatus. By "direct physical checks" we mean measurements attempting to detect phenomena directly linked to a possible particle origin of the rotation signal. One of these direct checks, the study of magnetically induced rotation in gases, is already underway at PVLAS, while another, a photon-regeneration type experiment, is being built in the existing apparatus and will be operative shortly. We will briefly describe both the study of magnetic rotation in gases and the photon-regeneration experiment and will remark on their relevance for the interpretation of the PVLAS rotation signal.

Anomalous Magnetically Induced Rotation in Gases

Gases do not exhibit the rotation equivalent of the CME; in other words, there is no magnetically induced rotation in gases. A photon-to-boson oscillation, on the other hand, can generate a rotation even in the presence of a gas. In

fact, the presence of a gas in the interaction region changes the refractive index of the medium through which the oscillation of photons into bosons takes place, also changing the coherence length of the oscillation itself. In other words, a given gas pressure will effectively change the mass of the photons and will shift the zeroes of the oscillating part in the dichroism formula given above. In practice, the said formula must be replaced with

$$\alpha(M_b, m_b, p_{\rm gas}) = \frac{F B_{\rm ext}^2 L^2}{8\pi M_b^2} \left(\frac{\sin x}{x}\right)^2 ,$$

$$x = \frac{L}{2}\left[\frac{p_{\rm gas}\,(n_{\rm stp}-1)\,\omega}{p_{\rm atm}} + \frac{m_b^2}{2\omega}\right] , \qquad (9.29)$$

where $p_{\rm gas}$ is the gas pressure, $p_{\rm atm}$ is the atmospheric pressure and $n_{\rm stp}$ is the index of refraction of the gas at STP. If a particle does exist, it will have some fixed values of M_b and m_b, thus the rotation will be a function of pressure with a characteristic oscillatory behavior. A measurement of the oscillatory dependence of observed rotation on the gas pressure in the interaction region would be a very strong signature of particle production within the PVLAS apparatus. We have therefore attempted to detect such a dependence by studying the rotation in gas, at fixed field, as a function of pressure. Figure 9.18 shows a preliminary example of such a study.

Figure 9.18 is a plot of rotation as a function of pressure for Ne gas measured at 5.0 T, with 50,000 passes in the Fabry-Pérot cavity at 1064 nm. The pressure-dependence of this set of data can be interpreted as consisting of a linear part plus an anomalous rotation responsible for the deviation from linearity. The linear part is not due to a rotation generated by the gas itself; rather, it must be ascribed to the birefringence due to the CME of the gas, which is transformed into a rotation by the action of the Fabry-Pérot.

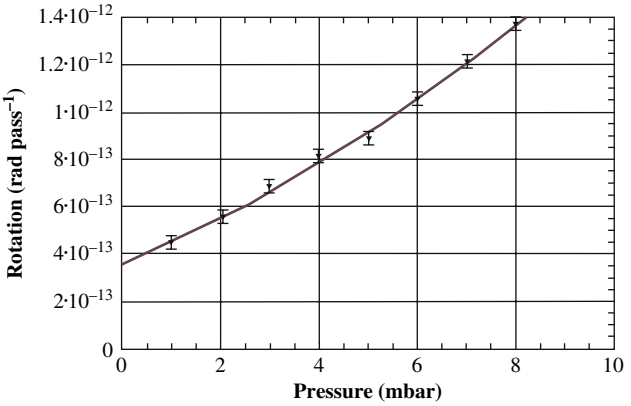

Fig. 9.18. Measured magnetic rotation as a function of Ne pressure (1064 nm and 5.0 T). Deviation from linearity could be due to particle production (see text)

It has in fact been recently found [25] that, due to the unavoidable intrinsic residual birefringence of the mirrors, a frequency-locked cavity will transform a birefringence generated within itself into a rotation and vice versa. For instance, it can generally be expected that about 10% of the birefringence present within the cavity will also appear as a rotation. The data of Fig. 9.18, can therefore be fitted with a function of the type

$$y(b, M_b, m_b, p_{\mathrm{gas}}) = bp_{\mathrm{gas}} + \alpha(M_b, m_b, p_{\mathrm{gas}}) \ , \tag{9.30}$$

to extract the parameters b, M_b, and m_b. These last two, in principle, should be related to the hypothetically produced particle. In the instance reported in Fig. 9.18, the above function gives the fitted curve shown in the graph, reproducing the observed anomalous behavior of the rotation. This gas-based technique is still at the preliminary stage, the chief difficulty lying in the fact that the anomalous part, containing the information on particle parameters, must be extracted as the difference between two nearly equal terms, the measured pressure-dependence of the data and the linearly dependent part inferred from cavity coupling. Errors are therefore large, and confidence level in the estimated particle parameters consequently low. The potential of the technique is however great, and efforts in near future will concentrate on lowering errors along two main directions: using gases with a low CME, resulting in a small linear part, and accumulating more statistics.

Photon Regeneration

A powerful test of the particle interpretation of the rotation result is the search for a positive detection in a photon-regeneration-type experiment (for the original concept see [26] and Sect. 9.6). In such an experiment, particles are produced from a two-photon interaction in a magnetic field region. The particles are then allowed to propagate in a second magnetic field region, blocked to the original photons, where the inverse process takes place and photons are produced apparently out of nothing. The regenerated photons, for kinematic reasons, will have the same wavelength as the original ones. Such an experiment is also poetically termed "shining light through a wall". Detection of regenerated photons would be a very robust signature of particle production.

Such an experiment is actually possible at PVLAS in a parasitic way, i.e., without perturbing the normal polarization measurements. Figure 9.19 shows how a regeneration setup can be built taking advantage of the fact that, in case of particle production, a beam of particles would leave the cavity in a downward direction and could be intercepted by a suitably placed magnet. In practice, a permanent dipole magnet can be placed below the lower optical bench with its bore aligned with the FP cavity axis. Particle production takes place within the main superconducting magnet, where one also takes advantage of the amplification provided by the cavity, while regeneration of

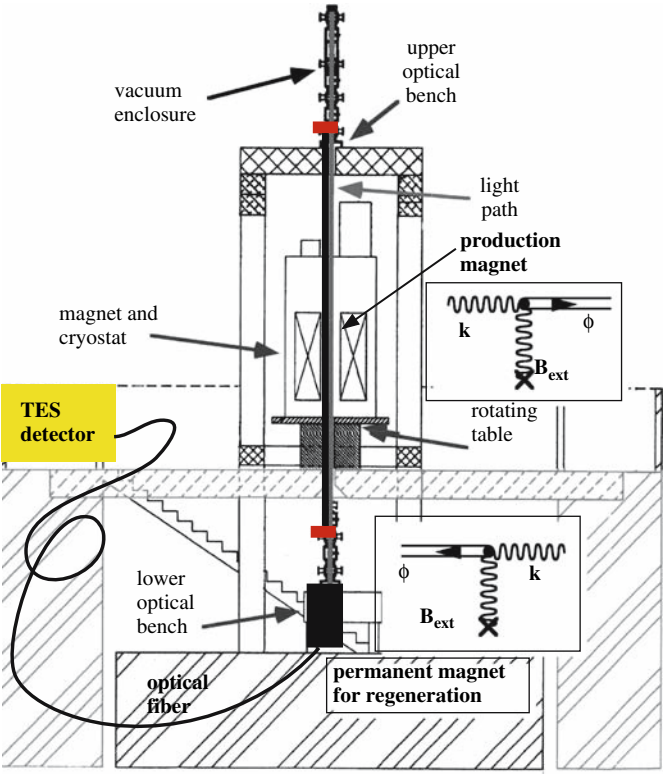

Fig. 9.19. Photon regeneration scheme implemented at PVLAS (see text)

photons takes place within the permanent magnet. These photons are then detected as excess counts over a background by a suitable detector (Transition Edge Sensor (TES) in Fig. 9.19, see also below) coupled to the regeneration chamber via an optical fiber.

If one assumes that the hypothetically produced particles have the parameters given above (namely $g_{b\gamma\gamma} \sim 2.5 \times 10^{-6}\,\mathrm{GeV}^{-1}$ and $m_b \sim 1$ meV), the estimated rate of regenerated photons in such a setup is small, but not negligible. Figure 9.20 shows a plot of the expected rate of regenerated photons as a function of laser power exiting the cavity assuming different possible configurations of the apparatus. The red spaced-dots curve is relative to the scheme of Fig. 9.19, with a 2.3 T strong and 0.5 m long permanent magnet. With a laser power of 25 mW at 1064 nm exiting the cavity, the regeneration rate is $\sim 0.3\,\mathrm{photons\,s}^{-1}$.

If one assumes detection efficiency of 50 and a detector with a 0.01 Hz background, then detection with a SNR ~ 1 becomes possible in about 10 s of measuring time. In other words, given a detector capable of detecting infrared photons at 1064 nm with a very low background, then the pho-

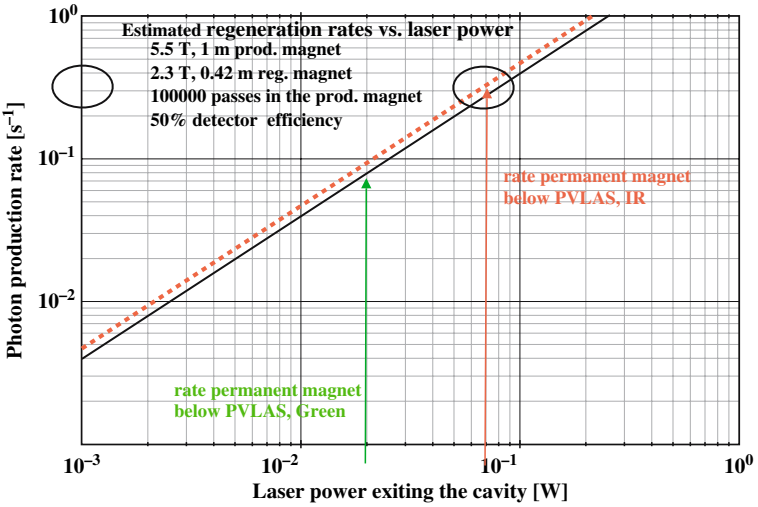

Fig. 9.20. Rate of regenerated photons vs. laser power exiting the cavity for several configurations of the apparatus and for two wavelengths. The scheme chosen in Fig. 9.19 is represented in this plot by the spaced-dots red curve ("rate permanent magnet below PVLAS, IR" in the legend). The right hand side solid black oval evidences the crossing point between the power figure and the relevant curve. The left hand side solid black oval gives the rate estimate of 0.3 photons s^{-1} (see also text)

ton regeneration test can be carried out at PVLAS in a matter of minutes, without perturbing the normal course of polarization measurements. Such a detector actually exists: Transition Edge Sensors [27] are basically resistors on the transition edge between superconduction and normal conduction. A small energy absorbed by the sensor causes a transition between the two regimes, which is then seen as a sharp change in the resistance of the sensor itself.

9.6 Conclusions

PVLAS is operating what amounts to a low-energy photon collider able to investigate the properties of the vacuum element. Detection of physical effects is made possible by the very high sensitivity of the optical ellipsometer which is at the core of PVLAS. Some of the interesting processes accessible with these low-energy measurements are, at the moment, photon-photon scattering and real or virtual particle production, where the particles involved are of some yet unknown type, possible dark matter constituent candidates. The observation by PVLAS of a magnetically induced rotation of vacuum is, if

confirmed, a result of a potentially revolutionary nature and would open up an entire new field of physics. For this reason, independent checks of this result are urgently needed and should be speedily undertaken without delay.

There is already the possibility of performing direct physical tests of the particle interpretation of the PVLAS observed rotation, and this is without actually perturbing the present configuration of the apparatus. One of these tests is based on measurements of the anomalous dependence on pressure of the magnetic rotation observed with a gas in the interaction region. This signature is very marked; however, the method is of difficult applicability and should be applied to a larger data set than that is available at present. The second direct test is based on the detection of photons regenerated from a beam of produced particles in the field of an additional magnet placed below the lower optical bench. A positive detection would be a definite confirmation of the particle interpretation of the rotation signal. The setup for this test is under construction, and the goal is to carry it to completion as soon as possible. As an added bonus, the presence of this setup in no way perturbs the normal operation of the ellipsometer. As a final remark, we want to point out that a negative result form both direct experimental tests described above would not disprove the physical origin of the PVLAS rotation signal; rather, it would simply put to rest the particle interpretation of these results in terms of a photon-to-boson oscillation phenomenon.

Note Added in Proof

G. Cantatore for the PVLAS Collaboration – Sunday, October 7, 2007

The rotation results published in 2006 in [13] regarded an empirical finding which was attributed to an effect originating in the Fabry-Pérot cavity with the magnetic field energized. The origin of this signal, whether physical or instrumental, was unknown; however, the diagnostic tests described in this article allowed one to localize the effect in the cavity and to exclude several spurious signal sources, such as those due to electromagnetic pick-ups or to a direct action of the fringe fields on the optical components. In fact, given that it was not possible to completely eliminate them, the fringe fields remained a plausible source of instrumental artifacts, albeit in conjunction with some yet-to-be-found indirect effect.

To further check against possible instrumental artifacts, several apparatus upgrades were designed and installed after this article was written. These upgrades had the main purpose of minimizing the supposed effects of the fringe fields. A new, higher power, laser emitting about 800 mW at 1064 nm was used, and the circuitry necessary for the electro-optic frequency-locking feedback loop was encased in μ-metal shielding. The old, mostly

iron, access structure was replaced with an aluminum one, and coaxial signal cables were substituted with better shielded ones. Two sets of three-axis Helmholtz coils were placed around the cavity mirrors and used to locally zero stray fields. Finally, the initial linear polarization of the laser beam was rotated to lie normal to the concrete beam supporting the magnet, and a new He gas compressor was put into service in the He gas recovery cycle, increasing the overall efficiency and therefore allowing longer data-taking periods.

After these substantial modifications, several measurement runs were carried out, both at the maximum field strength of 5 T and at the reduced field intensity of 2.3 T, when no measurable stray field is present. No rotation peaks were observed, neither at 2.3 T nor at 5 T (integrated background values were 10^{-8} rad and 1.2×10^{-8} rad, respectively). Also, no peak was observed at 2.3 T when measuring ellipticity (integrated background was 1.5×10^{-8}), while a tiny peak persisted at 5 T, albeit certainly of spurious nature. These new results, besides contradicting the earlier findings at 5 T, also completely exclude the particle interpretation of the previous PVLAS data.

One must remark that the original PVLAS signals, which have subsequently proven to be of instrumental origin, were in fact "true" optical signals, in the sense that they did correspond to actual modifications of the light polarization state. The actual mechanism which generated these signals (and which has disappeared in the upgraded apparatus) must have been a subtle in-phase combination of at least two different possible artifact sources, each one of which, when considered alone, could not have produced the effects reported in [13]. More details on these recent developments at PVLAS can be found in [28]. In addition we refer to the recent negative results of the light shining through the wall experiment carried out by the BMV collaboration [29].

The photon regeneration test sketched in the article will still be carried out at PVLAS with the double aim of testing through a direct physical process the negative result on particle production, and of setting new bounds on particle parameters. The main focus of the polarization measurements now must shift back to the original theme of the PVLAS experiment, which was built with the aim of measuring the photon–photon scattering in QED. The challenge, then, is to lower enough the present sensitivity to make such a measurement possible.

References

1. Euler, H., Kochel, K.: Über die Streuung von Licht an Licht nach der Diracschen Theorie. Naturwissenschaften **23**, 246 (1935);
Euler, H.: Über die Streuung von Licht an Licht nach der Diracschen Theorie. Ann. Phys. **26**, 39 (1936);
Heisenberg, W., Euler, H.: Folgerungen aus der Diracschen Theorie des Positrons. Z. Phys. **98**, 718 (1936);

Heisenberg, W., Euler, H.: Consequences of Dirac's theory of positrons. Z. Phys. **98**, 714 (1936) [physics/0605038];
Weisskopf, V.S.: Über die Elektrodynamik des Vakuums auf Grund der Quantentheorie des Elektrons. Mat. Phys. Medd.-K. Dan. Vidensk. Selsk. **14**, 6 (1936);
Schwinger, J.S.: On gauge invariance and vacuum polarization. Phys. Rev. **82**, 664 (1951);
Adler, S.L.: Photon splitting and photon dispersion in a strong magnetic field. Annals Phys. **67**, 599 (1971) 157, 161

2. Sikivie, P.: Experimental tests of the invisible axion. Phys. Rev. Lett. **51**, 1415 (1983), (E) ibid. **52**, 695 (1984);
Anselm, A.A.: Yad. Fiz 442, 1480 (1985);
Gasperini, M.: Axion production by electromagnetic fields. Phys. Rev. Lett. **59**, 396 (1987) 158
3. Iacopini, E., Zavattini, E.: Experimental method to detect the vacuum birefringence induced by a magnetic field. Phys. Lett. B **85**, 151 (1979);
Iacopini, E., Smith, B., Stefanini, G., Zavattini, E.: On a sensitive ellipsometer to detect the vacuum polarization induced by a magnetic field. Nuovo Cim. B **61**, 21 (1981);
Zavattini, E.: Magnetically induced optical activity of vacuum. Comments At. Mol. Phys. **33**, 83 (1996) 158
4. Maiani, L., Petronzio, R., Zavattini, E.: Effects of nearly massless, spin zero particles on light propagation in a magnetic field. Phys. Lett. B **175**, 359 (1986);
Raffelt, G., Stodolsky, L.: Mixing of the photon with low mass particles. Phys. Rev. D **37**, 1237 (1988) 158, 160
5. Bakalov, D., et al.: Production and detection of dark matter candidates: The PVLAS experiment. Prepared for 7th Marcel Grossmann Meeting on General Relativity (MG 7), Stanford, California, 24-30 Jul 1994, http://www.slac.stanford.edu/spires/find/hep/www?irn=5070643;
Bakalov, D., et al.: The measurement of vacuum polarization: The PVLAS experiment. Hyperfine Interactions 114, 103 (1998) 158, 159, 165
6. Bakalov, D., et al.: Experimental method to detect the magnetic birefringence of vacuum. Quantum Semiclass. Opt. 10, 239 (1998) 158
7. Pengo, R., et al.: Magnetic Birefringence of Vacuum: the PVLAS experiment. In: Zavattini, E., Bakalor, D., Rizzo, C Frontier Tests of QED and Physics of the Vacuum, p. 59. Heron Press, Sofia (1998) 169
8. Azzam, R.M.A., Bashara, N.M.: Ellipsometry and polarized light. North Holland Publishing Co. (1977) 161
9. Brandi, F., Polacco, E., Ruoso, G.: Stress-optic modulator: a novel device for high sensitivity linear birefringence measurements. Meas. Sci. Technol. **12**, 1503 (2001) 167
10. Born, M., Wolf, E.: Principles of Optics. Pergamon Press, Oxford 691 (1980) 168
11. Bregant, M., Cantatore, G., Della Valle, F., Ruoso, G., Zavattini, G.: Frequency locking to a high-finesse Fabry-Pérot cavity of a frequency doubled Nd:YAG laser used as the optical phase modulator. Rev. Sci. Instrum. **73**, 4142 (2002) [hep-ex/0202046];
Cantatore, G., et al.: Frequency locking of a Nd:YAG laser using the laser itself as the optical phase modulator. Rev. Sci. Instrum. **66**, 2785 (1995);

De Riva, A.M. et al.: Very high Q frequency-locked Fabry-Pérot cavity. Rev. Sci. Instrum. **67**, 2680 (1996) 172
12. Zavattini, E., et al.: Signal processing in the PVLAS experiment. In: WSEAS Trans. Syst. **11**, 1931 (2005) [hep-ex/0509029];
Milotti, E.: Sine-fit procedure for unevenly sampled, multiply clocked signals. J. Comp. Phys. **202**, 134 (2005) 174
13. Zavattini, E., et al. (PVLAS Collaboration) Experimental observation of optical rotation generated in vacuum by a magnetic field. Phys. Rev. Lett. **96**, 110406 (2006) [hep-ex/0507107] 174, 185, 193, 194
14. Iacopini, E., Stefanini, G., Zavattini, E.: Effects of a magnetic field on the optical properties of dielectric mirrors. Appl. Phys. A **32**, 63 (1983) 179, 182, 183
15. Bialolenker, G., Polacco, E., Rizzo, C., Ruoso, G.: First evidence for the linear magnetic birefringence of the reflecting surface of interferential mirrors. Appl. Phys. B **68**, 703 (1999) 182, 183
16. Rizzo, C., Rizzo, A., Bishop, D.M.: The Cotton-Mouton effect in gases: experiment and theory. Int. Rev. Phys. Chem. **16**, 81 (1997) 175
17. Carusotto, S., et al.: Measurement of the magnetic birefringence of noble gases. J. Opt. Soc. Am. B **1**, 635 (1984);
Cameron, R., et al.: First measurement of the magnetic birefringence of helium gas. Phys. Lett. A **157**, 125 (1991);
Cameron, R., et al.: Measurement of the magnetic birefringence of neon gas. J. Opt. Soc. Am. B **8**, 520 (1991) 175
18. Bregant, M., et al.: Measurement of the Cotton-Mouton effect in krypton and xenon at 1064 nm with the PVLAS apparatus. Chem. Phys. Lett. **392**, 276 (2004);
Bregant, M., et al.: A precise measurement of the Cotton-Mouton effect in neon. Chem. Phys. Lett. **410**, 288 (2005) 175, 176
19. Adler, S.L., et al.: Photon splitting in a strong magnetic field. Phys. Rev. Lett. **25**, 1061 (1970) 185
20. Maiani, L., Petronzio, R., Zavattini, E.: Effects of nearly massless, spin zero particles on light propagation in a magnetic field. Phys. Lett. B **175**, 359 (1986) 186
21. Raffelt, G., Stodolsky, L.: Mixing of the photon with low mass particles. Phys. Rev. D **37**, 1237 (1988) 186
22. Semertzidis, Y., et al.: Limits on the production of light scalar and pseudoscalar particles. Phys. Rev. Lett. **64**, 2988 (1990);
Cameron, R., et al.: Search for nearly massless, weakly coupled particles by optical techniques. Phys. Rev. D **47**, 3707 (1993) 160, 186
23. Masso, E., Toldra, R.: On a light spinless particle coupled to photons. Phys. Rev. D **52**, 1755 (1995) [hep-ph/9503293] 186
24. Ruoso, G., et al.: Search for photon regeneration in a magnetic field. Z. Phys. C **56**, 505 (1992) 187, 188
25. Zavattini, G., et al.: On measuring birefringences and dichroisms using Fabry-Pérot cavities. Appl. Phys. B **83**, 571 (2006) 190
26. Van Bibber, K., Dagdeviren, N.R., Koonin, S.E., Kerman, A., Nelson, H.N.: An experiment to produce and detect light pseudoscalars. Phys. Rev. Lett. **59**, 759 (1987) 190
27. Miller, A.J., et al.: Demonstration of a low-noise near-infrared photon counter with multiphoton discrimination. Appl. Phys. Lett. **83**, 791 (2003) 192

28. Zavattini E., et al. (PVLAS Collaboration): New PVLAS results and limits on magnetically induced optical rotation and ellipticity in vacuum, arXiv:0706.3419 [hep-ex] 194
29. Robilliard C., et al. (BMV Collaboration): No light shining through a wall, arXiv:0707.1296 [hep-ex] 194

10 Axion Searches in the Past, at Present, and in the Near Future

Rémy Battesti,[1] Berta Beltrán,[2] Hooman Davoudiasl,[3] Markus Kuster,[4,5,*] Pierre Pugnat,[6] Raoul Rabadán,[7] Andreas Ringwald,[8] Neil Spooner,[9] and Konstantin Zioutas[6,10]

[1] Laboratoire National des Champs Magnétiques Pulsés, CNRS/INSA/UPS, UMR 5147, 31400, Toulouse, France
[2] Department of Physics, University of Alberta, 11322-89 Av, Edmonton, AB, Canada
[3] Department of Physics, University of Wisconsin, Madison, WI 53706, USA
[4] Technische Universität Darmstadt, IKP, Schlossgartenstrasse 9, D-64289 Darmstadt, Germany
[5] Max-Planck-Institut für extraterrestrische Physik, Giessenbachstrasse, D-85748 Garching, Germany
[6] European Organization for Nuclear Research (CERN), CH-1211 Genève 23, Switzerland
[7] Institute for Advanced Study, Einstein Drive, Princeton, NJ 08540, USA
[8] Deutsches Elektronen-Synchrotron DESY, Notkestr. 85, D-22607 Hamburg, Germany
[9] University of Sheffield, Sheffield S3 7RH, UK
[10] University of Patras, Rio, 26500 Patras, Greece
[*] markus.kuster@cern.ch

Abstract. Theoretical axion models state that axions are very weakly-interacting particles. In order to experimentally detect them, the use of colorful and inspired techniques become mandatory. There are a wide variety of experimental approaches that were developed during the last 30 years; most of them make use of the Primakoff effect, by which axions convert into photons in the presence of an electromagnetic field. We review the experimental techniques used to search for axions and will give an outlook on experiments planned for the near future.

10.1 Searches for Dark Matter Axions

As described in the review by P. Sikivie on cosmological axions in Sect. 1.6, axions produced in the early universe with a mass ranging from μeV to meV could account for the cold dark-matter component of the universe and therefore an experimental evidence for axions in this mass range would be of great interest nowadays. Microwave resonant cavity experiments are the most sensitive detectors for cold dark-matter axions at present. The heart of such a device is a metallic conductor that acts as a cavity for electromagnetic fields such as photons. By tuning the size of the magnetic-field permeated cavity its resonant frequency can be shifted such that it matches the frequency of the axion field (which is related to the axion mass). In this case, axions will

R. Battesti et al.: *Axion Searches in the Past, at Present, and in the Near Future*, Lect. Notes Phys. **741**, 199–237 (2008)
DOI 10.1007/978-3-540-73518-2_10

convert resonantly into quasi-monochromatic photons, which could be detected with sensitive microwave receivers as an excess on the cavity power output. In Fig. 10.1 the schematic working principle of this kind of detectors is shown.

The signal obtained would carry information not only about the axion mass but also about the axion distribution in the galactic halo, as its width would represent the virial distribution of thermalized axions. Furthermore, the signal may also possess a finer substructure due to axions that have recently fallen into the galaxy and have not yet thermalized, as shown in Fig. 10.2. Again the reader is referred to Sikivie's review for a more detailed description of the axion distribution in the galactic halo.

Due to the very low mass range of the dark-matter axion, the expected signal is minuscule, and therefore the sensitivity of the experiment crucially depends on the quality of the microwave receivers (see Chap. 8 by Carosi and van Bibber). In the 1980s two pioneering experiments were carried out at Rochester-Brookhaven-Fermilab (RBF) [1] and the University of Florida (UF) [2] using small volume cavities ($\sim$1000 cm^3) and HFET amplifiers, but their sensitivities were lacking by two or three orders of magnitude the sensitivity necessary to probe the theoretically motivated region in the axion parametric space.

An improvement in the sensitivity lead to the second generation experiments, such as ADMX [3], which are currently taking data with a bigger resonant cavity compared to the preceding experiments, but still making use of the HFET amplifiers. Their results are compatible with the absence of any

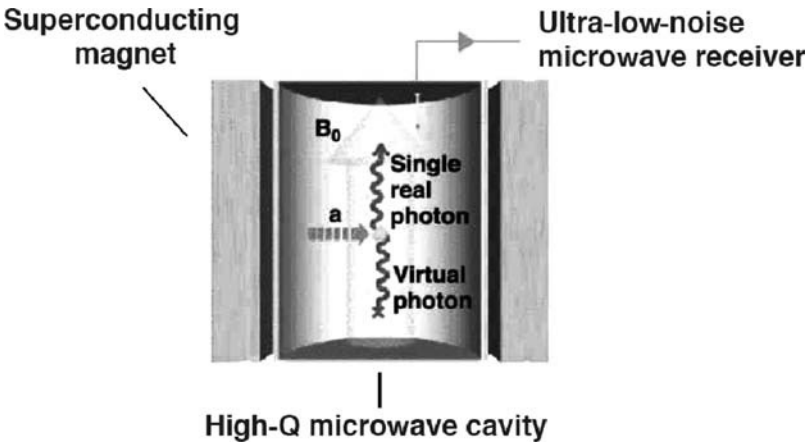

Fig. 10.1. Schematic principle of the microwave cavity experiment to look for cold dark-matter axions. First an axion would be resonantly converted into a quasi-monochromatic photon in the magnetic-field permeated microwave cavity. Then an ultra-low-noise receiver is set to detect this photon as an excess on the cavity power output

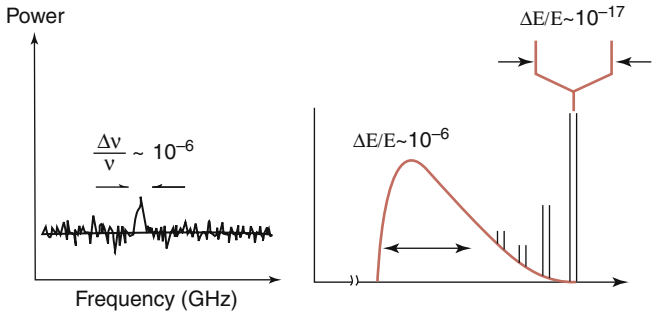

Fig. 10.2. *Left*: Representation of the signal expected in a microwave cavity experiment, where the photon signal appears as an excess over the noise in the power frequency spectrum. The width of the signal would be related to the predicted axion halo velocities. *Right*: Zoom showing the possible fine structure details in the expected signal

axion signal, providing the best upper limits for the axion to photon coupling constant $g_{a\gamma\gamma}$ in the lowest mass range ($m_a \approx 10^{-4} - 10^{-6}$ eV, see Fig. 10.26). A new amplifier technology based on Superconducting Quantum Interference Devices (SQUID), currently under development, can further improve the sensitivity of ADMX, such that it is possible to probe the theoretically favored axion parameter range (see Chap. 8 and Fig. 10.26).

Another second-generation experiment is the CARRACK experiment in Kyoto [4]. That also uses a resonant cavity to produce the axion-converted-photons, but the signal detection is based on a Rydberg-atom single-quantum detector, providing an extremely low-noise photon counting capability. This experiment is still in the development phase.

10.2 Solar Axions Searches

As seen from the Earth, the most important and strongest astrophysical source for axions is the core of the Sun. There, pseudoscalar particles like axions would be continuously produced in the fluctuating electric and magnetic fields of the plasma via their coupling (see Fig. 10.3 up) to two photons. After production the axions would freely stream out of the Sun without any further interaction (given that the axion mean free path in the Sun is $\approx g_{10}^{-2}\, 6 \times 10^{24}$ cm for 4 keV axions,[1] this is a valid assumption). The resulting differential solar axion flux on Earth would be [5]

$$\frac{\mathrm{d}\Phi_a}{\mathrm{d}E} = 6.02 \times 10^{10}\,\mathrm{cm}^{-2}\,\mathrm{s}^{-1}\,\mathrm{keV}^{-1} g_{10}^2\, E^{2.481} e^{-E/1.205}\,. \tag{10.1}$$

[1] Here we define $g_{10} = g_{a\gamma\gamma}/10^{-10}\,\mathrm{GeV}^{-1}$.

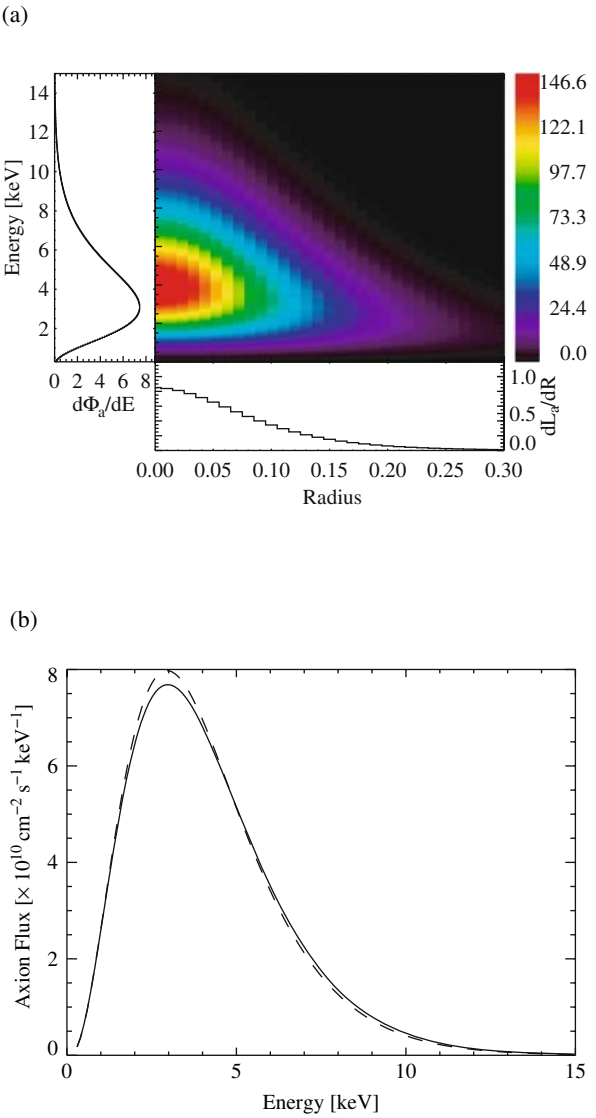

Fig. 10.3. *Up*: 2D representation of the axion surface luminosity seen from the Earth [5] as a function of the solar radius and the axion energy. *Down*: Comparison of the solar axion flux calculated using an older version of the standard solar model from 1982 (*dashed line*) and a more recent version from 2004 (*solid line*) [6]. Here an axion-photon coupling constant of $1 \times 10^{-10}\,\mathrm{GeV}^{-1}$ is assumed

The spectral energy distribution of the axions follows a thermal energy distribution between 1 and 10 keV, which peaks at ≈ 3 keV as shown in the top part of Fig. 10.3. For comparison two different solar axion spectra are shown in Fig. 10.3, calculated from different versions of the standard solar model (SSM): the solid line corresponds to a more recent implementation of the SSM from 2004, while the spectrum plotted as a dashed line is based on an older version published in 1982 [5, 6]. It is evident that small changes of the underlying SSM have only a small influence on the axion flux and the corresponding shape of the axion energy spectrum. In the following, we will summarize different techniques that aim to directly detect "solar axions".

10.2.1 Axion Helioscope

The most sensitive axion experiments, at present, in the mass range of $10^{-5}\,\mathrm{eV} \lesssim m_a \lesssim 1\,\mathrm{eV}$ are so-called "axion helioscopes," i.e., magnetic solar telescopes. The underlying physical principle of such a telescope is based on the idea proposed by P. Sikivie in 1983 [7] and is illustrated in Fig. 10.4. If we assume that axions are produced in the Sun, they would reach the Earth after about 500 s as an almost parallel axion beam (the apparent diameter of the axion emission region on the solar disk is $\approx 0.1°$). The apparatus for the detection on Earth uses the time reversed Primakoff effect, i.e., $a + \gamma_{\mathrm{virtual}} \rightarrow \gamma$, where the axion interacts with a virtual photon provided by a transversal magnetic field and reconverts into a real photon. These "reconverted" photons have the same energy and momentum as the axion, and therefore their energy distribution is identical to the energy spectrum of the solar axions shown in Fig. 10.3. An X-ray detector placed on the end side of the magnetic field would collect the photons and search for an axion signature above detector background. The expected number of reconverted photons reaching the detector for the given differential solar axion spectrum is

$$N = \int \frac{\mathrm{d}\Phi_a}{\mathrm{d}E} P_{a\rightarrow\gamma}\, S\, t\, \mathrm{d}E\ . \tag{10.2}$$

Here $\mathrm{d}\Phi_a/\mathrm{d}E$ is the differential axion flux at the Earth, S the magnet bore area, t the measurement time, and $P_{a\rightarrow\gamma}$ the conversion probability of an axion into a photon. To maximize t, the magnet is mounted in a similar way as conventional telescopes so that it can follow the track of the Sun on the sky.

The number of photons leaving the magnetic field toward the detector is determined by the probability that an axion converts back to an "observable" photon inside the magnetic field. Assuming that the conversion volume (magnetic field area) is evacuated, the probability is given by

$$P_{a\rightarrow\gamma} = \left(\frac{B g_{a\gamma\gamma}}{2}\right)^2 2L^2\, \frac{1-\cos(qL)}{(qL)^2}\ , \tag{10.3}$$

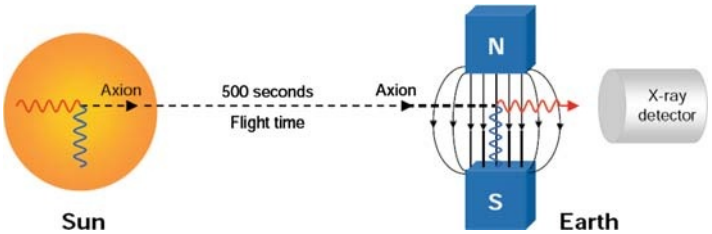

Fig. 10.4. Working principle of an axion helioscope. Axions produced in the Sun core by the Primakoff effect would be converted back into photons in a strong magnetic field. Eventually these photons, which have the same energy spectrum as the incoming axions, could be collected by an X-ray detector placed a the end of the magnet field area

where B and L are the magnet field strength and length of the field, and

$$q = m_a^2/2E_\gamma \,, \tag{10.4}$$

is the longitudinal momentum difference (or momentum transfer) between the axion and the photon of the energy E_γ. In order to achieve a maximum conversion probability $P_{a\to\gamma}$, the axion and photon fields must remain in phase over the length of the magnetic field; this sets the requirement that $qL < \pi$ [8, 9] (constructive interference). Thus, the sensitivity of a helioscope is limited to a specific axion mass range for a given q. For increasing axion masses the conversion is suppressed by the momentum mismatch between the axion and the photon, namely, due to the form factor $(1 - \cos(qL))/(qL)^2$ in (10.3).

Coherence can be restored for higher axion masses by filling the magnetic conversion region with a buffer gas [8] so that the photons inside the magnet pipe acquire an "effective mass" (which is equivalent to a refractive index n). Consequently the wavelength of the photon can match that of the axion for an appropriate gas pressure, and coherence will be preserved for a narrow axion-mass window. In this case the transition probability $P_{a\to\gamma}$ has to be recast into the more general equation [8]

$$P_{a\to\gamma} = \left(\frac{Bg_{a\gamma\gamma}}{2}\right)^2 \frac{1}{q^2 + \Gamma^2/4}[1 + e^{-\Gamma L} - 2e^{-\Gamma L/2}\cos(qL)] \,. \tag{10.5}$$

Here Γ is the absorption coefficient for the X-rays in the medium, and the momentum transfer becomes

$$q = \left|\frac{m_\gamma^2 - m_a^2}{2E_a}\right| \,, \tag{10.6}$$

with the effective photon mass

$$m_\gamma \simeq \sqrt{\frac{4\pi\alpha n_e}{m_e}} = 28.9\sqrt{\frac{Z}{A}\varrho} \,, \tag{10.7}$$

where n_e is the number density of electrons in the medium and m_e the electron mass. The second expression in (10.7) is a more convenient representation for m_γ giving the dependence of m_γ on the atomic number Z of the buffer gas, its mass A, and its density ϱ in $\mathrm{g\,cm^{-3}}$. As Helium is the type of gas commonly used for this purpose, (10.7) can be further simplified to

$$m_\gamma(\mathrm{eV}) \simeq \sqrt{0.02 \frac{P(\mathrm{mbar})}{T(\mathrm{K})}} \,, \tag{10.8}$$

where we use the corresponding parameters A, Z, and ϱ for Helium and treat Helium as an ideal gas. This equation directly relates m_γ to the measured experimental parameters, i.e., the pressure P and temperature T of the gas inside the magnetic field region. For a specific pressure P and temperature T, the coherence is restored for a narrow axion-mass window, for which the effective mass of the photon matches that of the axion such that

$$qL < \pi \implies \sqrt{m_\gamma^2 - \frac{2\pi E_a}{L}} < m_a < \sqrt{m_\gamma^2 + \frac{2\pi E_a}{L}} \,. \tag{10.9}$$

The differential energy spectrum of the photons from axion conversion follows from (10.1) and (10.3). Assuming full coherence, it can be approximated analytically [5] by

$$\begin{aligned} \frac{\mathrm{d}\Phi_\gamma}{\mathrm{d}E} &= \frac{\mathrm{d}\Phi_a}{\mathrm{d}E} P_{a\to\gamma} \\ &= 0.088\,\mathrm{cm^{-2}\,day^{-1}\,keV^{-1}}\, g_{10}^4 E^{2.481} e^{-E/1.205} \left(\frac{BL}{9.0\,\mathrm{T}\,9.26\,\mathrm{m}}\right)^2 \end{aligned} \tag{10.10}$$

It is obvious that the resulting low photon count rates from (10.10) require background-optimized detectors in order to achieve a reasonable detection sensitivity with an axion helioscope.

Helioscope Implementations

The first axion helioscope was built at the beginning of the 1990s [9], using a 1.8 m long magnet powered with a 2.2 T transverse magnetic field. As a detector, a proportional counter operating with a gas mixture of argon and methane (90% to 10%) was used to collect the photons from axion-to-photon conversion. The helioscope could be pointed to the Sun for a period of $\approx 15\,\mathrm{min\,day^{-1}}$. Two different regions of the axion mass range (with and without a gas in the conversion volume) were explored with this setup, setting the following limits on $g_{a\gamma\gamma}$ and m_a in the absence of a signal

$$\begin{aligned} g_{a\gamma\gamma} &< 3.6 \times 10^{-9}\ \mathrm{GeV^{-1}} \quad \text{for } m_a < 0.03\ \mathrm{eV} \,, \\ g_{a\gamma\gamma} &< 7.7 \times 10^{-9}\ \mathrm{GeV^{-1}} \quad \text{for } 0.03\ \mathrm{eV} < m_a < 0.11\ \mathrm{eV} \,. \end{aligned} \tag{10.11}$$

In the late 1990s a new helioscope with improved sensitivity (2.3 m long magnet, 4 T) was built in Tokyo [10]. For this experiment sixteen PIN photodiodes were used as X-ray detectors and the superconducting magnet was fixed on a polar mount, allowing the system to follow the Sun in a range from $-28°$ to $+28°$ in declination and 360° in right ascension. Due to the better tracking system, the Tokyo helioscope was able to follow the Sun for 24 h a day and the observation time of the Sun could be significantly improved. In total the Tokyo collaboration was able to use about 50% of the duty cycle of their instrument to track the Sun, while the rest of the time was devoted to background measurements. Similar to the first approach of [9], the experiment was divided into two phases: the first phase was finished in 1997 with an evacuated conversion region and the second phase in 2000 when the magnet pipe was filled with helium gas in order to extend the sensitive axion mass range. The resulting upper limits on $g_{a\gamma\gamma}$ from both data taking periods [11] are

$$\begin{aligned} g_{a\gamma\gamma} &< 6 \times 10^{-10}\ \mathrm{GeV}^{-1} \quad \text{for } m_a < 0.03\ \mathrm{eV}\ , \\ g_{a\gamma\gamma} &< 6.8\text{–}10.9 \times 10^{-10}\ \mathrm{GeV}^{-1} \quad \text{for } m_a < 0.3\ \mathrm{eV}\ . \end{aligned} \tag{10.12}$$

The most sensitive implementation of an axion helioscope is operating at present at CERN, the CERN Axion Solar Telescope (CAST). It was built in 2002 by refurbishing a 9.26 m long prototype of a twin aperture LHC dipole magnet. The two parallel pipes of the magnet, with a bore area of $A = 14.5\,\mathrm{cm}^2$ each, are homogeneously interspersed by a transverse dipole magnetic field (see Fig. 10.5, [12]). The maximum magnetic field that can be achieved with this prototype magnet is ≈ 9 T. The magnet is mounted on an azimuthal moving platform that allows to track the Sun for 1.5 h ($\pm 8°$ in height and $\approx 100°$ in azimuth) during sunrise and sunset. To detect the axions, three different types of detectors are attached to the ends of the magnet pipes: a gaseous detector with a novel MICROMEGAS readout [13],

Fig. 10.5. Experimental setup of the CAST experiment at CERN. From the left to the right the Helium cryogenic system, the CAST superconducting magnet, and the tracking system is shown. The tracking system allows to follow the Sun 1.5 h per day during sunrise and sunset

an X-ray telescope with a pn-CCD chip as focal plane detector [14] to detect axions during sunrise, and a Time Projection Chamber (TPC) that covers the opposite end of the magnet pipes, ready to collect axions during sunset [15].

CAST has taken data with the conversion region evacuated, during the years 2003 and 2004. In the absence of any axion signal, an upper limit on the axion to photon coupling constant has been established [5, 12] to

$$g_{a\gamma\gamma} < 0.88 \times 10^{-10}\ \mathrm{GeV}^{-1} \quad \text{for} \quad m_a < 0.02\ \mathrm{eV}\ , \tag{10.13}$$

at the 95% confidence level. This result is the best laboratory limit from a helioscope achieved so far. It covers a broad range of masses and supersedes the so far best limit from astrophysical considerations that was derived from the evolution of horizontal-branch stars in globular clusters [16, 17]. During 2005 the configuration, of the CAST experiment was upgraded, ready to jump into the second phase of the experiment, when the magnet pipes are filled with ^{4}He or ^{3}He gas. In this configuration, CAST will be able to expand its sensitivity to a maximum axion mass of ≈1.1 eV. CAST is scheduled to take data in this configuration during 2006 and 2007.

10.2.2 Bragg Diffraction

Another interesting and completely different approach to detect solar axions was proposed by E. A. Paschos and K. Zioutas [18]. This detection principle uses the intense Coulomb field of nuclei in a crystal lattice instead of an external magnetic field to convert axions to photons by the Primakoff effect. A crystal can be used either simultaneously as an axion converter and detector or to build a "reflective parabolic antenna" covered with a thin film of crystals that focus the resulting photons from axion-to-photon conversion on a detector in their focal plane. Background-optimized solid state detectors (e.g., NaI or Ge) generally used for WIMP searches or in double beta decay experiments provide excellent performance to implement the first type of crystalline axion detector.

To calculate the probability for axion conversion, the mass of the axion can be considered as negligibly small compared to the mass of the nuclei in the crystal; thus recoils of the nuclei can be neglected in a cystal during the conversion process. In this case the energy of the outgoing photon would be equal to the energy of the incident axion. The differential cross section for this conversion is given by [18]

$$\frac{\mathrm{d}\sigma}{\mathrm{d}\Omega} = \frac{g_{a\gamma\gamma}}{16\pi^2}\, F_a^2(\mathbf{q}) \sin^2(2\Theta)\ . \tag{10.14}$$

Here 2Θ is the scattering angle and F_a a form factor which describes the atomic structure of the crystal. The form factor F_a can be calculated from the Fourier transformation of the electrostatic field $\Phi(\mathbf{x})$ in the crystal [19]

$$F_a(\mathbf{q}) = k^2 \int \Phi(\mathbf{x})\, e^{\mathrm{i}\mathbf{q}\cdot\mathbf{x}}\, \mathrm{d}^3x \,, \tag{10.15}$$

with the transferred momentum $q = |\mathbf{q}| = 2k\sin(\Theta)$ and the axion momentum $k = |\mathbf{k}| \approx E_a$. Using the Sun as an axion source, the expected mean energy of the solar axions would be of the order of $\approx 4\,\mathrm{keV}$ (see Fig. 10.3). Thus the wave length of the axion λ is similar to the lattice spacing d of the crystal ($\approx$ few Å); consequently, we would expect a Bragg-reflection pattern. If a Bragg pattern arises, the intensity of the X-rays leaving the crystal has a maximum if the Bragg-condition

$$2\mathrm{d}\sin(\Theta_{\mathrm{Bragg}})\left(1 - \frac{1-n}{\sin^2(\Theta_{\mathrm{Bragg}})}\right) = m\lambda \quad \text{with} \quad m = 1, 2, 3, \ldots \,, \tag{10.16}$$

is fulfilled. Here n is the refractive index and d is the lattice spacing (compare Fig. 10.6). From (10.16) it is obvious that constructive interference will occur only if the waves reflected by different lattice layers are in phase. This is equivalent to the requirement that the path length of each photon wave leaving the crystal has to be equal to an integer multiple of its wavelength. The constructive interference then leads to an enhancement of the expected signal of the order of 10^4 compared to a scattering off a single atom in the crystal [18].

For a detector with a fixed orientation of its crystalline lattice relative to the Earth's surface the angle Θ, which is basically the angle between the line of sight towards the Sun and the crystalline lattice, would change during the course of the day when the Sun moves across the sky. Hence, the expected photon signal would have a well defined temporal signature as the Bragg condition is only satisfied for specific times during the day. This signature makes a potential signal clearly distinguishable from the detector background.

It was shown by [19] that the maximum achievable sensitivity for an upper limit on $g_{a\gamma\gamma}$ with this kind of detection technique is of the order of $g_{a\gamma\gamma} \lesssim 1 \times 10^{-9}\,\mathrm{GeV}^{-1}$ using a 100 kg DAMA-like NaI detector [20],

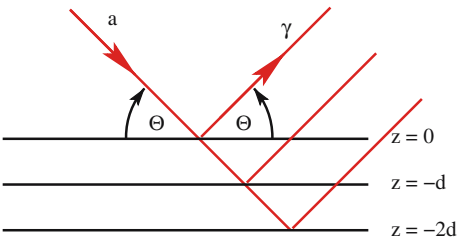

Fig. 10.6. Schematic view of different lattice layers in a crystal. The axion wave enters the crystal at the angle Θ. If the Bragg condition is fulfilled the outgoing photon waves reflected from different lattice layers would interfere constructively and enhance the expected signal

assuming an observation time of two years, and a detector background of $2\,\text{counts}\,\text{kg}^{-1}\,\text{day}^{-1}\,\text{keV}^{-1}$. It is obvious from this estimate, that axion detection with crystals based on Bragg reflection is not competitive to that with, e.g., axion helioscopes or astrophysical observations in terms of sensitivity with respect to $g_{a\gamma\gamma}$. An alternative and more effective detector configuration would be a large surface parabolic reflector ("mirror") or an array of reflectors covered with a thin crystalline layer [18]. In addition, polar crystal (ferroelectric) materials can improve the sensitivity because they provide stronger microscopic electric fields [18]. Nevertheless, the Bragg reflection technique has a major advantage; its sensitivity does not dependent on the mass of the axion, as long as nuclear recoils can be neglected.

Two different collaborations, COSME [21] and SOLAX [22], both using Germanium detectors with the main purpose of searching for dark matter WIMPs, analyzed their data looking for an axion signature. Both experiments were able to yield very similar mass-independent bounds to the axion-to-photon coupling in the absence of any signal

$$\begin{aligned} g_{a\gamma\gamma} &< 2.7 \times 10^{-9}\ \text{GeV}^{-1} \quad \text{(SOLAX)}\,, \\ g_{a\gamma\gamma} &< 2.8 \times 10^{-9}\ \text{GeV}^{-1} \quad \text{(COSME)}\,. \end{aligned} \tag{10.17}$$

The DAMA collaboration [23] achieved a similar limit

$$g_{a\gamma\gamma} < 1.7 \times 10^{-9}\ \text{GeV}^{-1} \quad \text{(DAMA)}\,, \tag{10.18}$$

using NaI(Tl) crystals as detector material.

10.2.3 Geomagnetic Axion Conversion

It has recently been shown by [24] that Geomagnetic Conversion of Solar Axions to X-rays (GECOSAX) can yield a photon flux which is measurable by a satellite based X-ray observatory on the dark side of the Earth. A key ingredient of this idea is using the Earth as an X-ray shield and looking for axions on its dark side. Using the Earth as a "shield" towards the Sun, effectively removes the solar X-ray background (see Fig. 10.7 for a schematic representation of this setup). In the following section, the feasibility of such an experiment will be demonstrated, based on recent measurements of the dark-Earth X-ray background by the Suzaku satellite.

The radius of the Earth is $R_\oplus \approx 6.4 \times 10^3\,\text{km}$, and its magnetic field is well approximated by a dipole for distances less than 1000 km above the surface. The magnetic field strength at the equator is $B_\oplus \simeq 3 \times 10^{-5}\,\text{T}$, and it drops as $\propto 1/r^3$ [25]. However, over distances $L \ll R_\oplus$ above the Earth's surface, it can be assumed that $B_\oplus = \text{const}$. As we are interested in low Earth orbits ($L < 1000\,\text{km}$), this is a valid assumption [24]. The influence of the atmosphere of the Earth is negligible because for $L > 150\,\text{km}$ solar axions

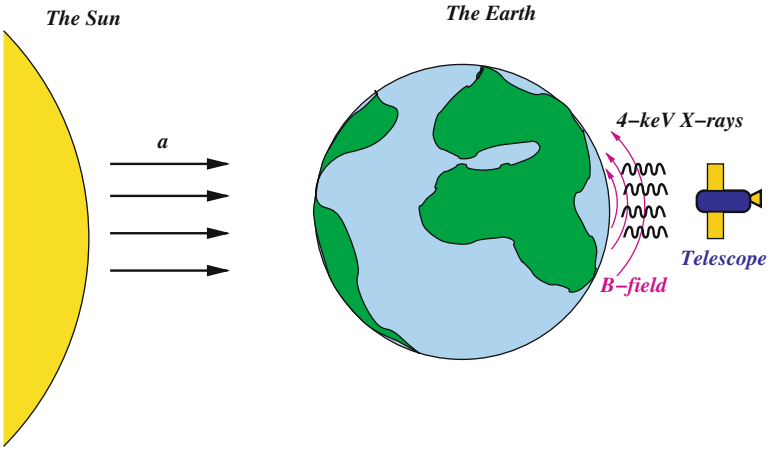

Fig. 10.7. The observational setup to detect geomagnetic converted axions (GECOSAX). The Sun is used as an axion source and a satellite based X-ray observatory to detect the photons from geomagnetically converted axions. The Earth acts as a shield for direct X-rays coming from the Sun and other X-ray sources in the sky

essentially travel in vacuum. For an axion mass $m_a \leq 10^{-4}\,\mathrm{eV}$, a mean axion energy $E_a = 4\,\mathrm{keV}$, and a satellite orbit of $L_\oplus \simeq 600\,\mathrm{km}$, the axion-to-photon conversion probability can be approximated as

$$P_{a\to\gamma}(L) = \frac{1}{4}\left(g_{a\gamma\gamma}BL\right)^2 \ , \tag{10.19}$$

where $g_{a\gamma\gamma}$ is the coupling strength of the axion to the photon. To be able to compare the expected axion flux in a specific energy range with available data, the spectrum given by (10.1) is integrated over the energy range of 2–7 keV to find the solar axion flux at Earth to be

$$\Phi_a \approx 2.7 \times 10^{11}(g_{a\gamma\gamma}/10^{-10}\,\mathrm{GeV}^{-1})^2\,\mathrm{cm}^{-2}\,\mathrm{s}^{-1} \ . \tag{10.20}$$

Thus, using (10.19) the expected flux of X-rays from axion-to-photon conversion at an altitude of $L_\oplus$ near the equator for $g_{a\gamma} = 10^{-10}\,\mathrm{GeV}^{-1}$ and $B = B_\oplus$ is

$$\Phi_\gamma(L_\oplus) \equiv \Phi_a\, P_{a\to\gamma}(L_\oplus) \approx 3 \times 10^{-7}\,\mathrm{cm}^{-2}\,\mathrm{s}^{-1} \ . \tag{10.21}$$

Based on the published technical specifications [26] of the Rossi X-ray timing explorer (RXTE), [24] has estimated that the flux given by (10.21) can be detected on the dark side of the Earth.

However, recently the Suzaku X-ray satellite team has measured the dark-Earth X-ray background in the range of 2–7 keV for calibration purposes [27].

Suzaku has a circular orbit at 575 km with an inclination of 33°. Unfortunately, the Suzaku satellite does not provide a fast slew rate and thus cannot perform this kind of measurement. However, as will be shown below, a telescope, capable of tracking the solar core on the dark side of the Earth and with similar X-ray detection capabilities will be sensitive to axion-photon couplings $g_{a\gamma\gamma}$ far below the current existing laboratory and astrophysical bounds for axion masses $m_a < 10^{-4}\,\mathrm{eV}$.

The expected signal from axion to photon conversion has several distinct features that will allow to clearly distinguish it from the detector background. These features are

1. a thermal-like spectral distribution of X-rays, peaking at approximately 4 keV, on the night side of the Earth,
2. the X-rays would only come from the center of the Sun, which subtends approximately 3′ on the sky,
3. the observed X-ray intensity would vary with the magnetic field strength and thus with the orbital position of the satellite and its orientation relative to the Earth's magnetic field (pointing direction of the satellite), and
4. the signal would be modulated by the Sun-Earth distance, resulting in an annual modulation of the intensity of the signal.

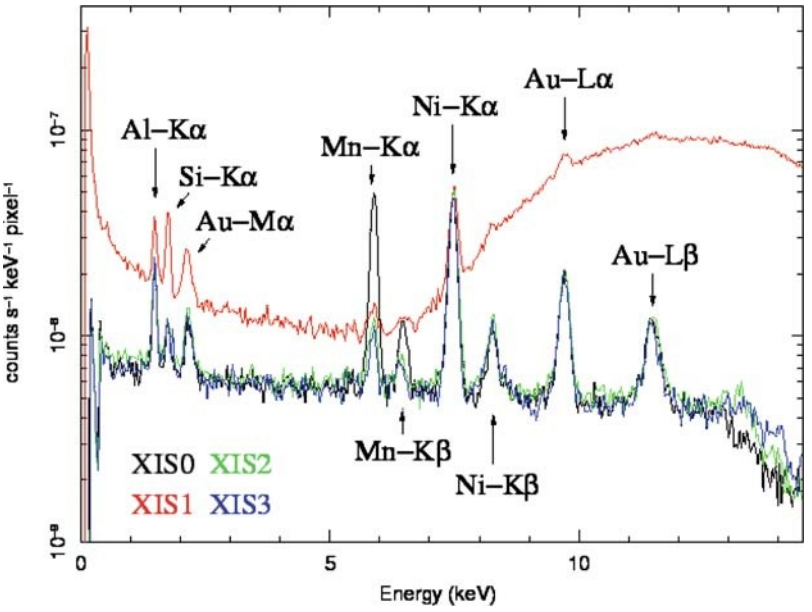

Fig. 10.8. Dark-Earth background measured by Suzaku based on a 800 ksec long observation. Individual fluorescent emission lines originating in detector materials are marked [28]

To estimate the sensitivity of Suzaku for solar axion detection, the effective area of the Suzaku detector was assumed to be ≈300 cm^2 in the 2–7 keV range [27]. The expected dark-Earth background of the Suzaku XIS detector per unit area is presented in Fig. 10.8 [28]. Given the above effective area, the $\approx 1'$ resolution of the X-ray telescope, and the Suzaku dark-Earth background data, the measurement of the X-ray flux from solar axion conversion is clearly feasible. The Suzaku team estimates that with 3×10^5 s of data, a 4σ bound $g_{a\gamma\gamma} < 10^{-10}\,\mathrm{GeV}^{-1}$ would have been possible [27]. Based on the Suzaku background data [27], the sensitivity of a solar-core-tracking X-ray telescope is plotted as a function of m_a in Fig. 10.9. The Earth-occulted background can in general be measured in situ, by pointing the X-ray telescope away from the direction of the core of the Sun. The observation of such a signal amounts to viewing an X-ray image of the solar core through the Earth. Therefore, this method can achieve an unambiguous detection of solar axions. In summary, for solar axions with $m_a < 10^{-4}$ eV, an orbiting X-ray telescope, with an effective area of a few 10^3 cm^2, can probe solar axion $g_{a\gamma\gamma}$ well beyond the sensitivity of current laboratory experiments.

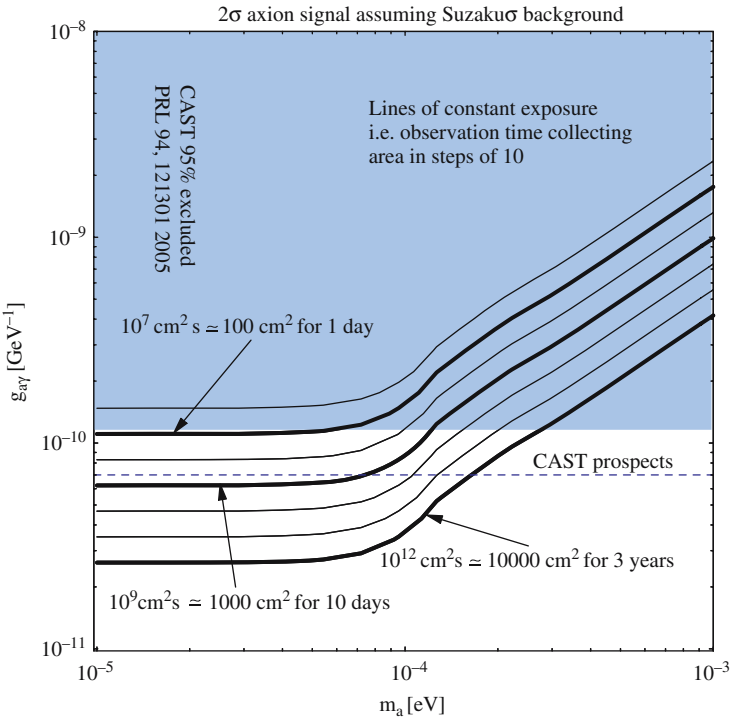

Fig. 10.9. The shaded area schematically depicts the CAST 95% C.L. excluded region [5]. The lines show sensitivities obtainable with the background measured by Suzaku

10.3 Searches for Laser Induced Axions

In this section, a new generation of purely laboratory based experiments that are able to provide complementary results to solar axions searches, will be briefly introduced. Whereas the solar axion experiments, described in the previous sections, probe axions that would escape from the Sun, the experiments presented in the following are supposed to produce axions from polarized laser beams, propagating in a transverse magnetic field. Yet the mechanism for both, the production and detection, is the same as in the previously described experiments: the Primakoff effect.

Searches for laser-induced axions provide a fully model-independent approach, as they do not rely on the physical processes and conditions in the Sun and how axions or axion-like particles could be produced under these conditions. They can be viewed as fixed target type experiments, with low energy polarized photon beams colliding with virtual photons provided by the magnetic field, i.e., $\gamma + \gamma_{\text{virtual}} \rightarrow \ a$. By pushing the optical detection techniques up to the present state-of-art, a significant enlarged domain of axion mass and axion di-photon coupling constant, not yet explored with laser based experiments, is expected to be probed with photons, typically in the energy range of a few eV. In addition, laser based experiments are not only focused on the axion search, but also offer a broad band of scientific interests, starting from a precise new test of QED up to the search of any scalar, pseudo-scalar, or other particles like paraphotons or millicharged particles that can couple to photons. In general, laser based experiments can be divided into two categories,

- the so called "photon regeneration" or "light shining through a wall" experiments and
- experiments that probe the magneto-optical properties of the vacuum.

10.3.1 Light Shining Through a Wall

The light shining through a wall or photon regeneration principle was first proposed by [29] in 1987 (for an independent proposal of this type, see [30]). The basic idea of this experiment is shown in Fig. 10.10. A polarized laser beam propagates inside a transverse magnetic field (with $\mathbf{E} \parallel \mathbf{B}$). The laser is blocked by a wall at some point on its path so that only weakly-interacting pseudoscalar or scalar particles created before will be able to pass through this absorber. The conversion probability for the production of an axion-like particle in this case is given by

$$P_{\gamma \rightarrow a} \propto \frac{1}{4}(g_{a\gamma\gamma}BL)^2\, F(qL)\ , \tag{10.22}$$

where $F(qL)$ is the form factor given by (10.3). A fraction of these weakly-interacting particles will reconvert into detectable photons after they have

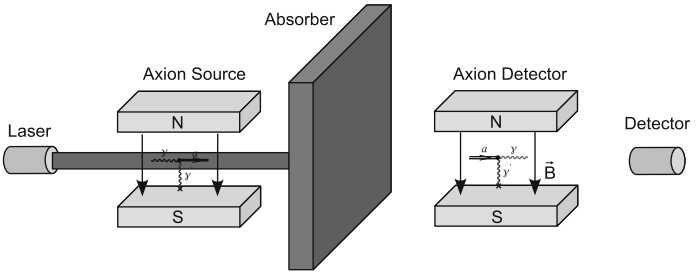

Fig. 10.10. Schematic view of a photon regeneration or light shining through a wall experiment. A polarized laser beam enters a transverse magnetic field from the left. A small fraction of the laser photons can be transmuted to, e.g., axions. While the laser light is blocked by a thick absorbing wall, the axions would pass it. A second magnetic field behind the wall is used to reconvert the axions to photons which are finally detected [29]

passed the wall and entered the second magnetic field, called "Axion Detector" in Fig. 10.10. The total probability of observing a regenerated photon with a detector located at the end of the second magnetic field is

$$P_{\gamma\to a\to\gamma} = P^2_{\gamma\to a} \,. \tag{10.23}$$

The expected counting rate depends on the power of the laser P and can be enhanced by an optical cavity installed on the production side. If the total number of reflections in the primary magnet is N_r and the detection efficiency is η, then the total number of counts expected from reconversion calculates from [31]

$$\frac{\mathrm{d}N_\gamma}{\mathrm{d}t} = \frac{1}{16}\frac{\langle P\rangle}{\omega}\frac{N_\mathrm{r}+2}{2}\,\eta\,(g_{a\gamma\gamma}BL)^4\sin^2\left(\frac{m_a^2L}{4\omega}\right)\Big/\left(\frac{m_a^2L}{4\omega}\right)^4 \tag{10.24}$$

$$\approx \frac{1}{16}\frac{\langle P\rangle}{\omega}\frac{N_\mathrm{r}+2}{2}\,\eta\,(g_{a\gamma\gamma}BL)^4 \,, \tag{10.25}$$

where the approximation (10.25) is valid only for $m_a \ll \sqrt{2\pi\omega/L}$.

The pioneering experiment based on this technique was performed by the Brookhaven-Fermilab-Rutherford-Trieste (BFRT) collaboration. They used two superconducting dipole magnets of length $L = 4.4\,\mathrm{m}$ which were able to provide a magnetic field of $B = 3.7\,\mathrm{T}$. The optical laser with a wavelength of $\lambda = 514\,\mathrm{nm}$ had an average power of $\langle P\rangle = 3\,\mathrm{W}$ and was operated in an optical cavity providing 200 reflections. As no signal from photon regeneration was found, the BFRT collaboration was able to set an upper limit on $g_{a\gamma\gamma}$ of [32]

$$g_{a\gamma\gamma} < 6.7\times10^{-7}\,\mathrm{GeV}\ (95\%\,\mathrm{C.L.})\,, \tag{10.26}$$

for axion-like pseudoscalars with a maximum mass of

$$m_a < 10^{-3}\,\mathrm{eV}\,. \tag{10.27}$$

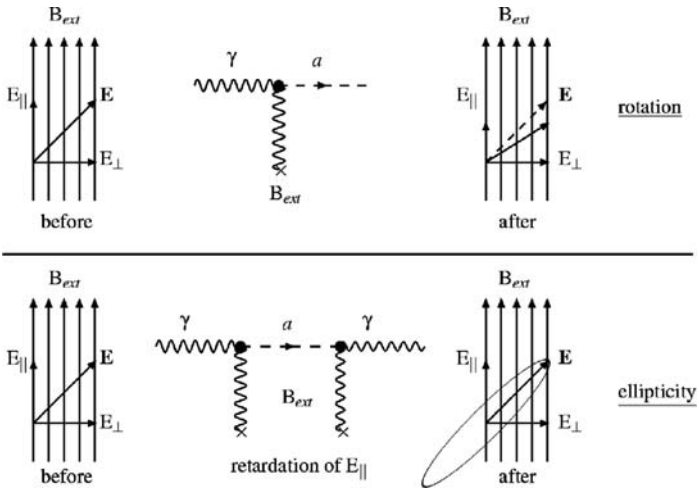

Fig. 10.11. *Up*: Linear Dichroism or rotation of the polarization vector by an angle ε. *Down*: Linear Birefringence or induction of an ellipticity Ψ in an initially linearly polarized beam

10.3.2 Probing the Magneto-Optical Properties of the Vacuum

The second of the purely laboratory experimental approaches to search for axions and axion-like particles is of indirect detection type. It is based on the theoretical prediction that scalar or pseudo-scalar particles can affect the polarization of light propagating in vacuum through a transverse magnetic field $\mathbf{B}$ because of their coupling to photons [33] (see also Sect. 8.7). A light beam initially linearly polarized at an angle θ with respect to $\mathbf{B}$ is expected to acquire a small ellipticity Ψ and a small apparent rotation Θ due to dispersive and absorptive processes induced by the production of spinless particles see Fig. 10.11. These effects are usually referred to as birefringence and linear dichroism of the vacuum, respectively, and are characterized by

$$\Psi \approx N \, \frac{B^2 L^3 m_a^2}{96 \omega M^2} \, \sin(2\theta) \, , \tag{10.28}$$

$$\Theta \approx N \, \frac{B^2 L^2}{16 \, M^2} \, \sin(2\theta) \, , \tag{10.29}$$

in the limit $m_a^2 L/4\omega \ll 1$. Here m_a is the axion mass, $M = 1/g_{a\gamma\gamma}$ the inverse coupling constant to two photons, ω the photon energy, L and N the effective path lengths and the number of paths the light travels in the transverse magnetic field. The polarization state of the light beam leaving the magnetic field, characterized by (10.28) and (10.29), would manifest itself as a sizable deviation from the pure QED prediction [34, 35] for which no measurable linear dichroism is expected.

The photon splitting effect can also produce a differential absorption [36], giving rise to an apparent angular rotation of the polarization of the order of 10^{-34} rad in a 9.5 T magnetic field over a length of 25 km. This angular rotation angle is far from being measurable under laboratory conditions, except if the coupling with scalar or pseudo-scalar particles would significantly enhance this effect [37].

The vacuum magnetic birefringence predicted by the QED, corresponds to the dispersive effect produced by virtual electron-positron pairs as was already stated by Heisenberg and Euler in 1936 [34]: "Even if electromagnetic fields are not strong enough to create matter, they will, due to the virtual possibility of creating matter, polarize the vacuum and therefore change the Maxwell's equations". This ellipticity constitutes the background signal for a measurement that aims to detect a birefringence or dichroism induced by a spinless particle. The ellipticity expected from vacuum-polarization can be expressed from one loop calculation as [34, 35]

$$\Psi_{\mathrm{QED}} \approx N \, \frac{B^2 L \alpha^2 \omega}{15\,\mathrm{m}^4} \sin(2\theta) \; , \tag{10.30}$$

where $\alpha \approx 1/137$ is the fine-structure constant, ω is the photon energy and m_e the electron mass. The maximum ellipticity a laser beam with a wavelength $\lambda = 1550\,\mathrm{nm}$ propagating in a 9.5 T field over a length $NL = 25\,\mathrm{km}$ would acquire is equal to 2×10^{-11} rad.

A search for both effects, birefringence and dichroism, was carried out with the same magnets used in the BFRT experiment [32], setting a bound on the axion-to-photon coupling constant of

$$g_{a\gamma\gamma} < 3.6 \times 10^{-7}\,\mathrm{GeV}^{-1} \; , \tag{10.31}$$

for masses

$$m_a < 5 \times 10^{-4}\,\mathrm{eV} \; , \tag{10.32}$$

at the 95% CL.

Very recently the Italian PVLAS experiment [38] (see Sect. 8.7) has been taking data to test the vacuum birefringence in the presence of a magnetic field with a 1 m long dipole magnet operated at a maximum field of 5.5 T, therefore improving on the sensitivity of the previous experimental setups. For the first time the PVLAS collaboration has measured a positive value for the amplitude of the rotation ε of the polarization plane in vacuum with $B \approx 5\,\mathrm{T}$ (quoted with a 3σ uncertainty interval) [38]

$$\varepsilon = (3.9 \pm 0.5) \times 10^{-12}\,\mathrm{rad\,pass}^{-1} \; . \tag{10.33}$$

This signal can be translated to an allowed range for the mass m_b and the coupling constant to two photons $g_{b\gamma\gamma}$ of a neutral light pseudoscalar boson

$$1\,\mathrm{meV} \leq \; m_b \; \leq 1.5\,\mathrm{meV} \; ,$$

$$1.7 \times 10^{-6}\,\mathrm{GeV}^{-1} \leq g_{b\gamma\gamma} \leq 1 \times 10^{-5}\,\mathrm{GeV}^{-1}\,. \tag{10.34}$$

Several new experiments are planned and already in progress with the goal to verify this signal. They are based on any or a combination of both experimental techniques: the light shining through the wall principle and the principle to test the properties of the quantum vacuum. In Table 10.1, a summary of actually planned or already operating experiments is given together with their performance parameters. A more detailed introduction to some of the experiments quoted in Table 10.1 is given in the following sections.

Axion-Like Particle Search – ALPS

A collaboration of DESY, Laser Zentrum Hannover and Sternwarte Bergedorf is presently setting up the Axion-Like Particle Search (ALPS) photon regeneration experiment that exploits the photon beam of high-power optical lasers, sent along the transverse magnetic field of a superconducting HERA dipole magnet [39]. This experiment, which has been approved by the DESY directorate on January 11, 2007, and is expected to take data in summer of 2007, offers a window of opportunity for a rapid firm establishment or exclusion of the axion-like particle interpretation of the anomaly published by PVLAS. In case of confirmation, it would also allow for the measurement of mass, parity, and coupling strength of this particle.

Table 10.1. Planned laser-based experiments to detect axion-like particles. The most important magnet and laser parameters are shown. PVLAS, and later also OSQAR, will use optical cavities to enhance the number of generated ALPs. $P_{\gamma\Phi\gamma}$ (PVLAS) denotes the probability for a photon-ALP-photon conversion for the different experimental setups based on the coupling constant derived from the PVLAS measurement and the BFRT limits. The last column gives the expected signal rate of reconverted photons

Name	Location	Laser	Magnet	$P_{\gamma\phi\gamma}$ (PVLAS)	γ Flux
ALPS	DESY/D	$\lambda = 1064\,\mathrm{nm}$ $P = 200\,\mathrm{W}$	$B = 5\,\mathrm{T}$ $L = 4.21\,\mathrm{m}$	$\sim 10^{-19}$	$10^{1}\,\mathrm{s}^{-1}$
BMV	LULI/F	$\lambda = 1053\,\mathrm{nm}$ $P = 500\,\mathrm{W}$	$B = 11\,\mathrm{T}$ $L = 0.25\,\mathrm{m}$	$\sim 10^{-21}$	$10\,\mathrm{pulse}^{-1}$
LIPSS	Jlab/USA	$\lambda = 900\,\mathrm{nm}$ $P = 10\,\mathrm{kW}$	$B = 1.7\,\mathrm{T}$ $L = 1\,\mathrm{m}$	$\sim 10^{-23.5}$	$10^{-1}\,\mathrm{s}^{-1}$
OSQAR	CERN/CH	$\lambda = 514\,\mathrm{nm}$ $P = 1\,\mathrm{kW}$	$B = 9.5\,\mathrm{T}$ $L_1 = 1\,\mathrm{m}$ $L_2 = 13.3\,\mathrm{m}$	$\sim 10^{-20}$	$10\,\mathrm{s}^{-1}$
PVLAS	Legnaro/I	$\lambda = 1064\,\mathrm{nm}$ $P = 0.8\,\mathrm{W}$	$B_1 = 5\,\mathrm{T}$ $B_2 = 2.2\,\mathrm{T}$ $L_1 = 4.21\,\mathrm{m}$ $L_2 = 0.5\,\mathrm{m}$	$\sim 10^{-23}$	$10^{-1}\,\mathrm{s}^{-1}$

Fig. 10.12. Superconducting HERA dipole magnet exploited by ALPS for conversion of laser photons into axion-like particles, as well as for the reconversion of axion-like particles into photons

The photon regeneration experiment ALPS is built around a spare dipole of the HERA proton storage ring at the DESY magnet test stand (see Fig. 10.12). Both parts of the experiment, i.e., axion-like particle production and reconversion into photons are accommodated in one single magnet, as the test stand architecture in its present configuration forbids to place two fully functional magnets in line. The general layout of the experiment is depicted in Fig. 10.13. A high intensity laser beam is placed on one side of the magnet traversing half of its length. In the middle of the magnet, the laser beam is reflected back to its entering side, and an optical barrier prevents any photons from reaching the second half of the magnet. Axion-like particles would penetrate the barrier, eventually reconverting into photons inside the second half of the magnet. Reconverted photons are then detected with a pixeled semi-conductor detector outside the magnet.

The magnetic field will be produced by a spare dipole magnet of the HERA proton storage ring (see Fig. 10.12). At a nominal current of 6000 A, the magnet reaches a field of 5.4 T over a total magnetic length of 8.82 m. In the first stage, ALPS will exploit a laser system delivering a linearly polarized photon beam with an average power of 50 W at a wavelength of 532 nm

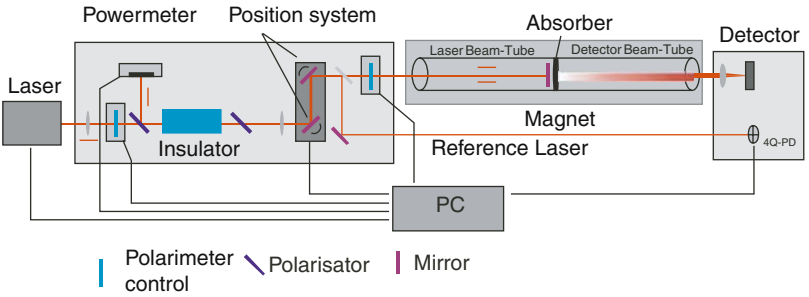

Fig. 10.13. Schematic view of the experimental setup with the laser on the left, followed by the laser injector/extractor system, the magnet and the detector table. An intensity-reduced reference beam of the laser is guided parallel to the magnet for constant alignment monitoring between laser and detector

and a low-noise, high-quantum-efficiency commercial CCD camera. Already with this configuration, the axion-like particle interpretation of PVLAS can be clarified: in this case, the expected counting rate is about 2 Hz. In the second stage, it is planned to use a commercial fiber laser (Nd:YAG) at 1064 nm, which is able to deliver 200 W linearly polarized photons, together with an InGaAs pixel detector normally used in infrared astronomy. This configuration will enable ALPS to explore also "new territory" in the coupling vs. mass plot.

The BMV Project

The BMV (Birefringence Magnetique du Vide) project [40], which is being built in Toulouse, France, combines very intense pulsed magnetic fields, developed at LNCMP, and a very sensitive optical device to detect the effects induced on a laser beam by such fields. This device is developed at LCAR-IRSAMC in collaboration with LMA-VIRGO from IN2P3 in Lyon, France. The goal was to assemble a first version of the experiment in 2006 and to obtain first results in 2007. In particular, the setup will be able to test the results published by the PVLAS collaboration [38].

The BMV project is based on a Fabry-Pérot cavity with a finesse of about 1×10^6 and a pulsed magnetic field as high as 25 T over the length of about one meter. The sensitivity limit for the measured ellipticity is about 4×10^{-9}, more than 100 times the one expected with the PVLAS apparatus. In the final stage, the experiment will have the sensitivity to measure the vacuum birefringence as predicted by QED.

The experimental setup of the optical apparatus is shown in Fig. 10.16. The light provided by a Nd:YAG laser ($\lambda = 1064$ nm) is polarized and is injected in a Fabry-Pérot cavity containing the magnetic field region. The light exiting the cavity is analyzed by a polarizer and detected by a photodiode. Light reflected back by the cavity is collected, and this signal is used to drive the locking electronics that changes the laser frequency to keep the Fabry-Pérot resonating. The measurement will be performed by phase detection as the magnetic field is pulsed.

To achieve a maximum in sensitivity, the project demands a transverse magnetic field as high as possible. This can only be obtained using pulsed magnet techniques. Moreover, a magnetic field region of maximum possible length is required, as the QED effect depends on the product B^2L, where L is the length of the magnetic field region. The goal is to realize a pulsed magnet delivering a transverse magnetic field approaching 25 T. Due to the high field value, the structure of the magnet is very constrained. In particular, at this field level, the magnetic pressure corresponds to 250 MPa (2.5 t cm^{-2}). Pulsed magnets that can provide such high fields have already been developed and tested, based on the X-coil geometry shown in Fig. 10.14. The length of the coil is 0.25 m, providing a peak field of 14.3 T corresponding to about 28 T^2 m (see Fig. 10.15). This is one of the highest field strengths ever reached with

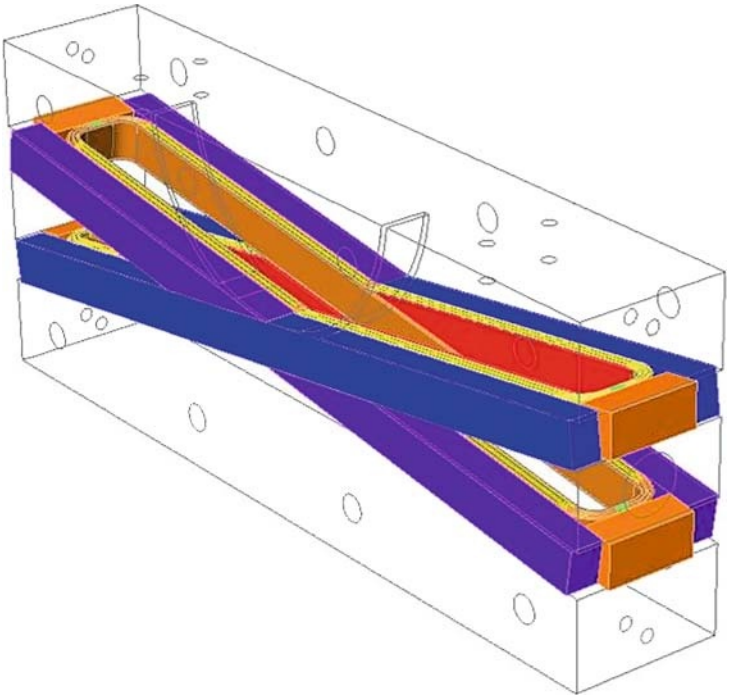

Fig. 10.14. Schematic view of the X-coil used in BMV

such a configuration. One of the prototype coils has been aged at a duty cycle of about 5 pulses per hour. It has delivered 100 pulses at a peak field of 11.5 T and 100 pulses at a peak field of 12.5 T, corresponding to about 21 T^2 m. The magnet will be supplied by a pulsed generator based on a bank of 12 capacitors. In particular, this generator will be able to produce a single pulse or to give a field that oscillates.

As far as the optical system is concerned, a system of high precision mechanical translators and rotators for the Fabry-Pérot cavity mirrors and for the polarizers has been designed and assembled at LCAR in Toulouse. The piezoelectric stacks of the mirrors' orientation system as well as the mechanism allowing their rotation are adapted to ultra-high vacuum. Tests have been carried out with a vertical 3.6 m long Fabry-Pérot cavity based on the LMA mirrors, made to reach a finesse of $\sim 5 \times 10^5$. Figure 10.16 shows a schematic drawing of the experiment with the Fabry-Pérot resonator, the magnetic field region, and two cryostats. The chambers for the optics operated at a ultra-high vacuum, are fixed on an optical table with a length of 3.6 m. The length of the cavity is about 2 m.

The year 2006 was a crucial one for the project. In May that year the experiment started to be set up at LNCMP. First with just one magnet in

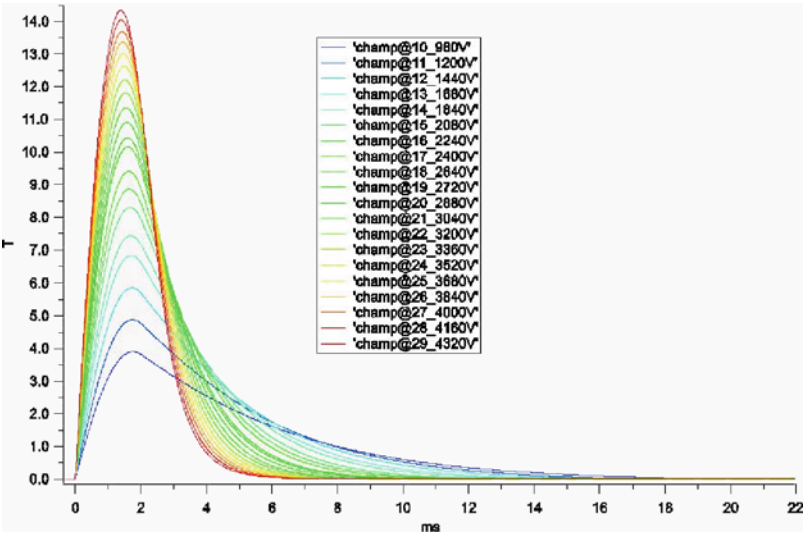

Fig. 10.15. Magnetic field delivered by the X-coil depending on time and for different supply voltages

place, then, when test runs were completed, with two magnets in place. This configuration corresponds to $40\,\mathrm{T}^2\,\mathrm{m}$. A new set of mirrors is in preparation at LMA. The clean environments, already used at LCAR, moved in the experimental clean room at LNCMP will allow to exploit these new mirrors at their best. Finesse $> 2 \times 10^5$ is expected. The sensitivity should also be at least $10^{-8} \times 1/\sqrt{(Hz)}$, thanks to the high central frequency of the modulated effect.

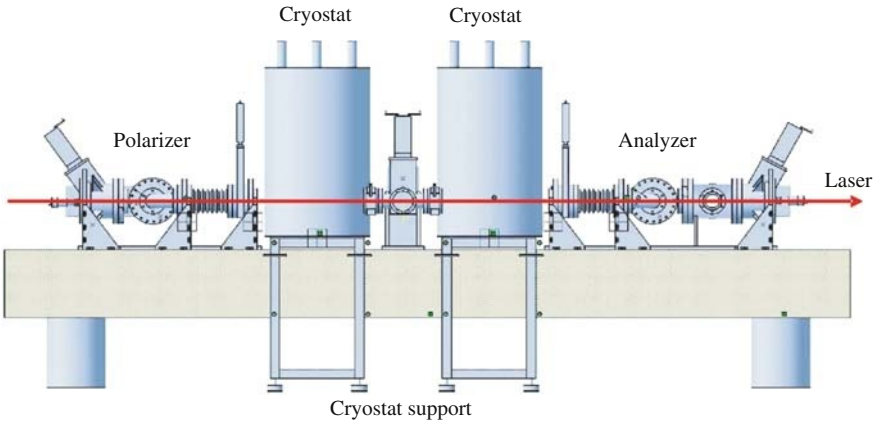

Fig. 10.16. Schematic view of the experimental setup of the BMV project

Figure 10.17 represents the exclusion region in the m_a vs. the inverse coupling constant M_a plane, given for one day of operation (20 magnet pulses) and assuming a zero ellipticity measurement, based on the experimental parameters given above. The red curves indicate the Brookhaven (BFRT) result [32]; the blue line, the BMV projected result; and finally, the black cross, the region of values that could explain the PVLAS results. This interpretation would thus be excluded by a zero-ellipticity measurement with the BMV setup.

The OSQAR Experiment at CERN (2-in-1 Experiment)

Because of the strong transverse magnetic field required to obtain measurable effects, an ideal implementation, to investigate simultaneously the magneto-optical properties of the quantum vacuum and the photon regeneration effect, is within long superconducting accelerator dipolar magnets, such as the ones developed and manufactured for the Large Hadron

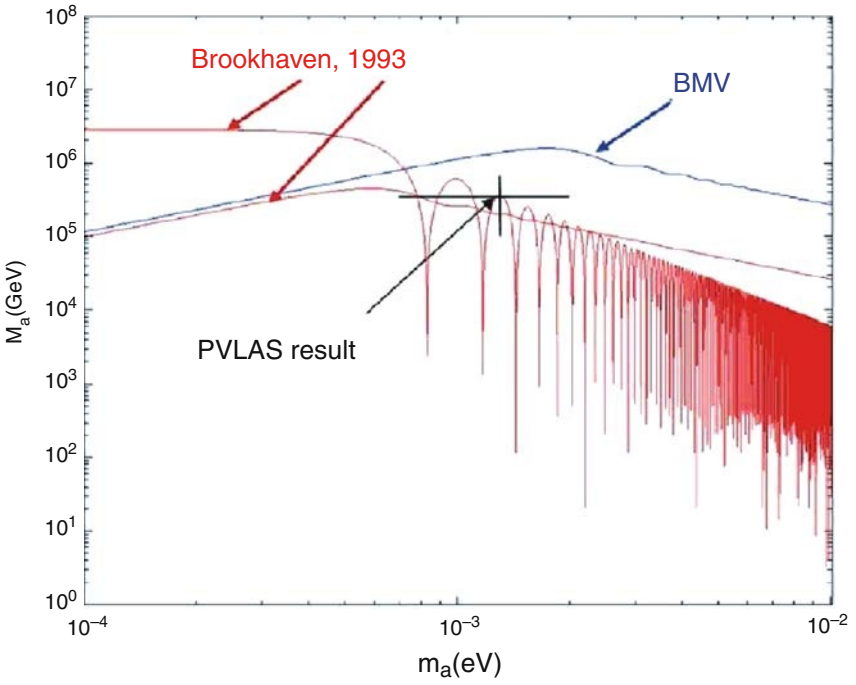

Fig. 10.17. Limits on the inverse coupling constant M_a in the m_a vs. M_a plane for an axion-like particle given for one day of operation (20 magnet pulses) assuming a zero ellipticity measurement

Collider (LHC). The re-use of recently decommissioned 15 m long twin aperture LHC superconducting magnet prototypes, providing a transverse magnetic field $B = 9.5\,\mathrm{T}$, offers a unique opportunity for the construction of a new powerful 2-in-1 experiment, based on optical techniques [41]. The cross section of such a dipole magnet is shown in Fig. 10.18.

Linearly polarized laser light beams will be used as probes inside vacuum chambers housed inside superconducting magnet apertures. One of the apertures will be dedicated to the measurement of the Vacuum Magnetic Birefringence (VMB) and optical absorption anisotropy whereas the other one will be used to detect the photon regeneration from axions or axion-like particles using an invisible light shining through a wall. The availability of several decommissioned LHC superconducting magnet prototypes at CERN offers the opportunity of possible upgrades for the proposed experiments, each of them improving the sensitivity by increasing the vacuum light pass in the transverse magnetic field with the connection of additional magnets.

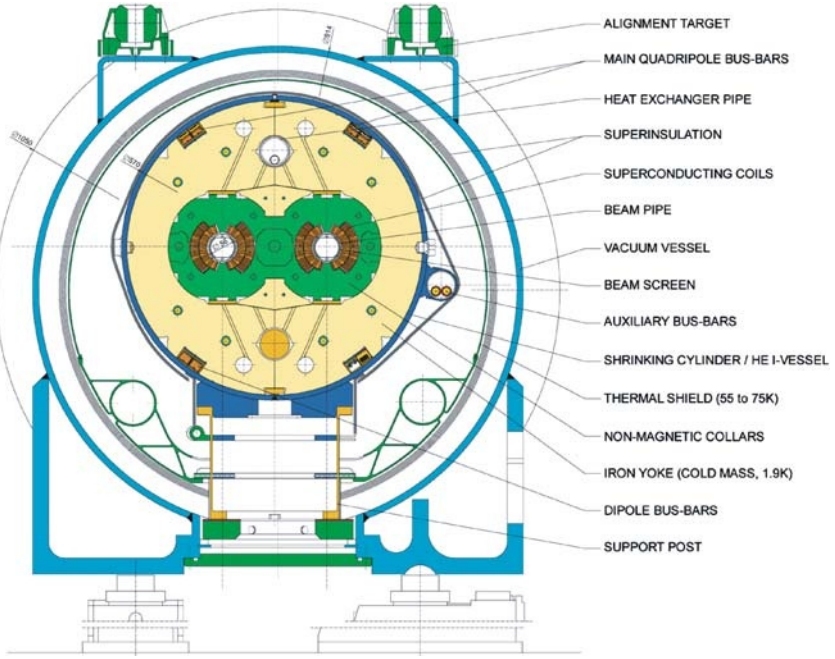

Fig. 10.18. Cross section of a LHC superconducting main dipole magnet housed inside its cryostat

Measurement of the Vacuum Magnetic Birefringence (VMB)

A first version of the experimental configuration, to measure very small optical birefringence, was proposed by [41] and is shown in Fig. 10.19. It is based on a Fabry-Pérot cavity of finesse equal to 10^3–10^4 and a novel measurement method, using a double path of light through a half-wave plate, mounted in a high-speed rotation stage. The initial linear polarization state of the laser beam can be modulated typically in the kHz range. After the second pass through the half-wave plate, the laser beam will retrieve to the first order, its linear polarization state with the small VMB rotation angle, induced by the vacuum and submitted to the transverse B field inside the optical cavity. Then a quarter-wave plate will convert the quasi-linear polarized laser beam coming out from the cavity into a quasi-circular one. Finally, a polarizer will ensure a linear and optimal conversion of the induced ellipticity into a power modulation of the laser beam. By replacing the half-wave rotating plate with an electro-optic modulator, it can be expected to work in the MHz range for the modulation and the detection. This constitutes one of the alternative solutions studied at present to improve the VMB measurements. For the phase-1 of this project, the sensitivity is expected to reach the state of the art, i.e., 10^{-9}–10^{-8} rad $\mathrm{Hz}^{-1/2}$. An improvement of at least two orders of magnitude of the present reference results given by the BFRT collaboration [32], concerning the VMB and absorption anisotropy, is expected together with the measurement, for the first time, of the QED prediction [41].

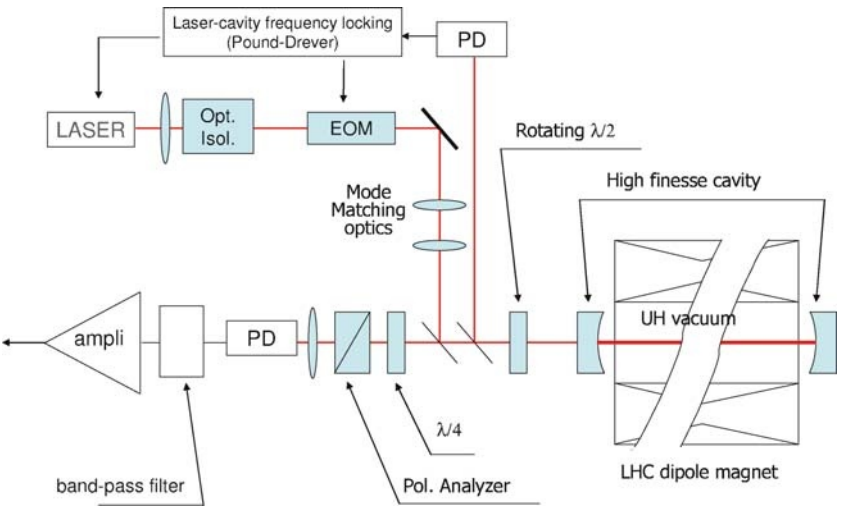

Fig. 10.19. Optical scheme for the measurements of the vacuum magnetic birefringence adapted from [41] with inputs from D. Romanini and L. Duvillaret

The Photon Regeneration Experiment

To complement and cross-check the VMB measurements, the photon regeneration experiment will be integrated in the second aperture of the 15 m long LHC superconducting magnet. The principle of this experiment is schematized in Fig. 10.20. A high finesse Fabry-Pérot cavity, inserted inside a part of the dipole magnetic field region, is used as an axion source, and a photomultiplier with a proper magnetic shield, or an avalanche photodiode, as an optical detection system. The optical barrier will intercept all photons not converted into axions and the detection of any photon at the same wavelength as the laser beam can be interpreted as an axion-to-photon reconversion inside the regeneration region. A chopper can be used for a synchronous photon counting, with the chopped laser beam, to improve the background rejection. When the magnetic field is switched off, the same measurements can be repeated to detect the possible mixing effect between photons and paraphotons.

With an Nd:YAG laser, an optical beam power as large as 100–1000 W can be obtained at the wavelength $\lambda = 1064$ nm. The optimum for the photon regeneration experiment is obtained for an optical cavity and a regeneration region both immersed in the same magnetic field integral. Assuming, as a first step, the use of a single LHC dipole with a 7 m long regeneration region and an optical cavity with a finesse of 10^4–10^5 of the same length, the photon counting rate given by the BFRT collaboration [32] can be improved by a factor of about 10^8. This corresponds to a limit for the coupling constant to two photons $1/M$ of about $10^{-9}\,\mathrm{GeV}^{-1}$, i.e., an improvement by more than 2 orders of magnitude with respect to the BFRT results. The loss of coherence in the axion-to-photon conversion will prevent the probe of axions with a mass typically larger than 0.4 meV at the lower values of $1/M$. During the preparatory phase of this photon regeneration experiment, the focus will be on the checking of PVLAS results [38]. Preliminary estimates show that this objective can be achieved at 95% confidence level with an integration time of about 1 hour, assuming 1000 reflections in a cavity of 1 m length in a 9 T field and an optical power of about 1 W.

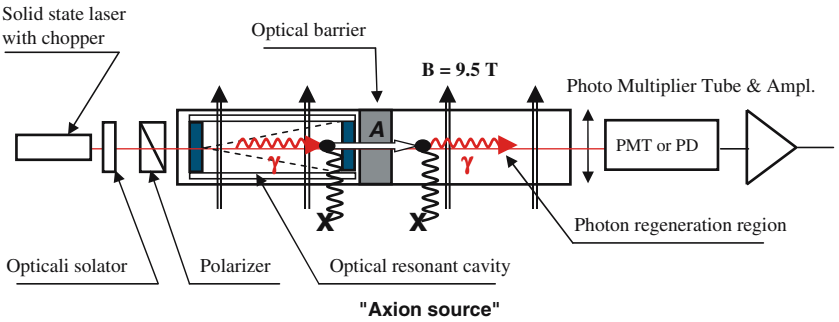

Fig. 10.20. Scheme of the photon regeneration experiments

10.4 Search for Kaluza-Klein Axions with TPCs

Higher-dimensional axionic theories that include δ extra spatial dimensions to the $(3+1)$ dimensions of the Minkowski space-time predict that the axion field can propagate in these additional dimensions (see Sect. 3.7 for an introduction). An important consequence of such so-called Kaluza-Klein (KK) axion models would be that the axion field would decouple from the Peccei-Quinn energy scale and aquire an infinite tower of mass eigenstates. The mass spacing between individual eigenstates would then be $\propto 1/R$, where R is the compactification radius of the extra dimensions. The corresponding axion-mass eigenvalues then follow

$$m_{a0} \approx m_{\mathrm{PQ}} \quad \text{and} \quad m_{an} \approx \frac{n}{R} \quad \text{with} \quad n = 1, 2, 3, \ldots \,. \tag{10.35}$$

Taking actual limits on the Peccei-Quinn scale into account, the lifetime of the Peccei-Quinn axion with respect to a $a \rightarrow \gamma\gamma$ decay is calculated from

$$\tau_a = \frac{64\pi}{g_{a\gamma\gamma}^2 m_a^3} \,, \tag{10.36}$$

to 10^{27} years $\lesssim \tau_a \lesssim 10^{42}$ years, which is several orders of magnitude longer compared to the age of our universe (13.7×10^9 years [42]). Particles that decay with such long lifetimes are not observable with actual experimental techniques. Taking (10.35) and (10.36) into account and setting $m_a = m_{a0}$, it is obvious that the lifetime of the more massive KK-axion states is significantly shorter, e.g., we get a lifetime of 2.7×10^7 years $\lesssim \tau_a \lesssim 2.7 \times 10^{14}$ years for the 10 keV mode. In this case, the experimental observation of the axion di-photon decay becomes feasible, as will be shown in the following sections.

10.4.1 Gravitationally Trapped Solar KK-Axions

A potential source of KK-axion would be the hot plasma of the Sun, where axions can be produced by either the Primakoff conversion or photon coalescence (see Fig. 10.21). The total solar axion luminosity from both contributions is given by [43]

$$L_a = A L_\odot \left(\frac{g_{a\gamma\gamma}}{10^{-10}\,\mathrm{GeV}^{-1}} \right)^2 \left(\frac{R}{\mathrm{keV}^{-1}} \right)^\delta \,, \tag{10.37}$$

with a normalization factor A ($A = 0.067$ and 0.12, respectively, for axions produced by photon coalescence and Primakoff effect), the solar luminosity $L_\odot$, and the number of extra dimensions δ. Most of these axions would freely stream out of the Sun and leave the solar system before they decay. Nevertheless, a small fraction of axions would have velocities smaller than the escape velocity v_{esc} and could be trapped in the gravitational potential of the Sun. These trapped KK-axions would revolve the Sun on Keplerian

orbits as shown in Fig. 10.22 until they decay. Since axions produced by the Primakoff effect are relativistic ($v \gg v_{\rm esc}$), their contribution to the overall number density of trapped axions is smaller, by a factor of 10^3, compared to axions produced by photon coalescence. Depending on the KK-axion lifetime τ_a the number density of trapped axions would evolve with time according to [43]

$$N_a(t) = R_a \tau_a (1 - \exp^{-t/\tau_a}) \,, \tag{10.38}$$

where R_a is the axion production rate. From (10.38) the present KK-axion number density can be calculated depending on the distance to the Sun, as well as the axion number density we would expect on Earth today. The resulting mass spectrum of trapped KK-axions is shown in the left part of Fig. 10.23 for both production processes. Assuming that KK-axions decay into two coincident photons with identical energy $E_\gamma = m_a/2$, the decay spectrum is given by [44]

$$\frac{{\rm d}R}{{\rm d}m_a} = \frac{g_{a\gamma\gamma}^2}{64\pi} n_0 m_a^3 f(m_a) \,, \tag{10.39}$$

where $f(m_a)$ is the trapped axion mass spectrum and n_0 the present total KK-axion number density. The right part of Fig. 10.23 shows the axion decay spectrum resulting from (10.39) on Earth depending on energy. Integration over all energies, yields a total KK-axion decay rate of

$$R = 2.5 \times 10^{11} \left(\frac{g_{a\gamma\gamma}}{{\rm GeV}^{-1}} \right)^2 \left(\frac{n_0}{{\rm m}^{-3}} \right) \, {\rm m}^{-3} \, {\rm day}^{-1} \,. \tag{10.40}$$

10.4.2 KK-Axion Detection with Large TPCs

The possibility that such a local axion population exists, motivates an experimental search for KK-axions. To estimate the minimum sensitivity necessary

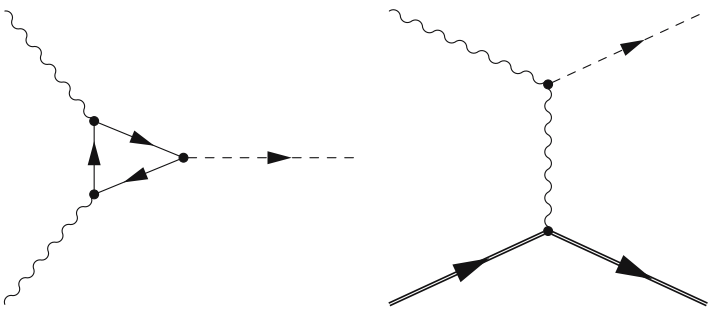

Fig. 10.21. Feynman diagram for axion production by photon coalescence (*left*) and the Primakoff effect (*right*)

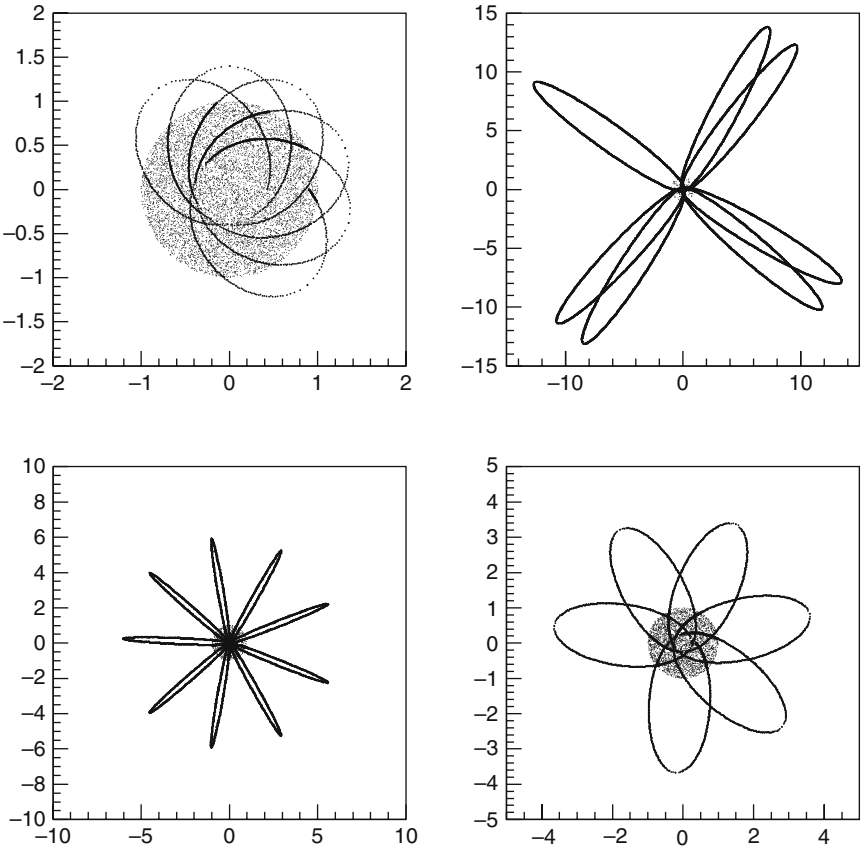

Fig. 10.22. Keplerian orbits of Kaluza-Klein axions trapped in the gravitational potential of the Sun. The x- and y-axis indicate the distance from the Sun in units of solar radii (adapted from [43] with permission)

to be able to observe KK-axion decays, the expected axion di-photon decay rate can be calculated from (10.40). Assuming a local axion number density of $n_0 = 10^{14}\,\mathrm{m}^{-3}$ and $g_{a\gamma\gamma} = 9.2 \times 10^{-14}\,\mathrm{GeV}^{-1}$ (see [43, 45] for details), an axion decay rate of $R = 0.21\,\mathrm{m}^{-3}\,\mathrm{day}^{-1}$ is expected. It is obvious from this estimate that a detector with a large sensitive volume and low background is required in order to be sensitive to the resulting low count rates. In addition, the detector must be able to separate the two coincident axion decay photons with an energy of $E_\gamma = m_a/2 \approx$ few keV, which are emitted back to back. Solid and liquid state detectors like NaI, Ge, or Xe are disfavored for this purpose. The mean free path of X-rays in, e.g., Ge is of the order of a few μm; consequently, the decay photons would be indistinguishable from

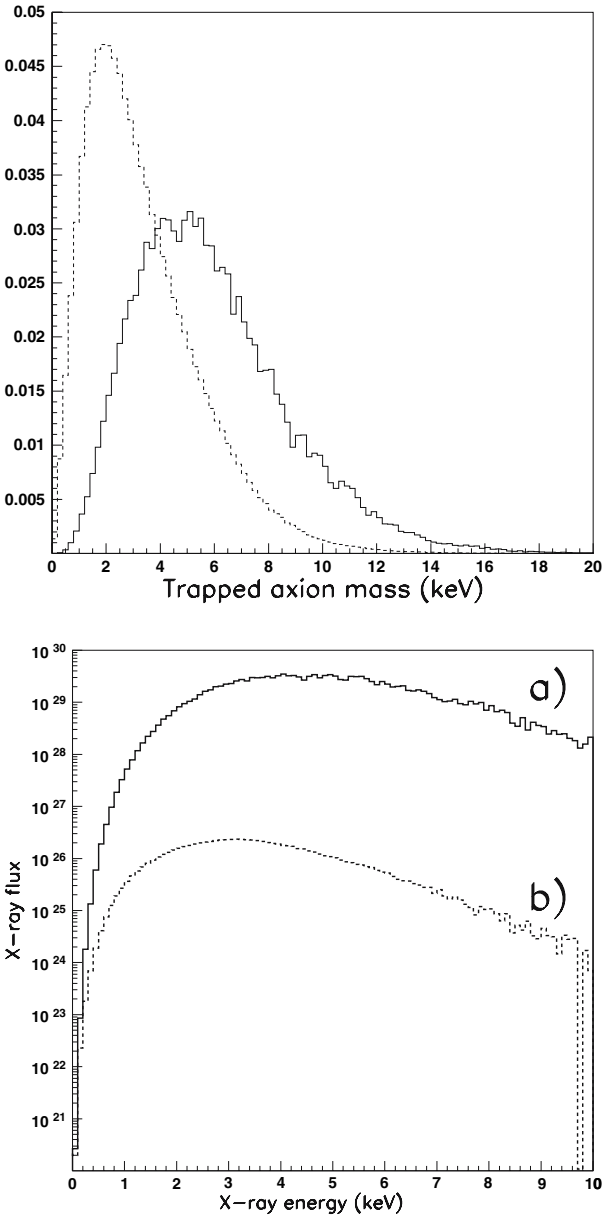

Fig. 10.23. *Left*: Mass spectra of KK-axions trapped in the gravitational potential of the Sun which crosses the orbit of the Earth. The solid line represents the mass distribution for axions produced via photon coalescence and the dashed line the mass distribution for axions produced via the Primakoff effect. Please note that the area of both distributions is normalized to unity. *Right*: The corresponding X-ray spectra resulting from axion to two photon decay of axions produced via (**a**) photon coalescence and (**b**) the Primakoff effect (adapted from [43])

the detector background. Instead, a large volume Time Projection Chamber (TPC) operated underground and at low pressure similar to the DRIFT II detectors [46] would be an ideal system for such an experiment. In [44], the sensitivity and background rejection efficiency has been estimated based on Monte-Carlo simulations for a $1\,m^3$ DRIFT II type detector operated with CS_2 as detection gas. The resulting sensitivity is shown in Fig. 10.24 for realistic KK-axion model parameters and for different detector configurations. According to these results, a DRIFT II type TPC detector shielded with 15 cm Pb would be sufficient, to fully probe the predicted parameter range of the model presented by [43] (the range of the model parameters is indicated as a black box in Fig. 10.24). At present, it seems feasible to realize a detector system at moderate cost by upgrading a DRIFT II detector similar to the one shown in Fig. 10.25. This would require additional shielding and a better spatial resolution of the detector in order to reduce the detector background and to be able to spatially resolve the secondary electrons produced by the two KK-axion decay photons.

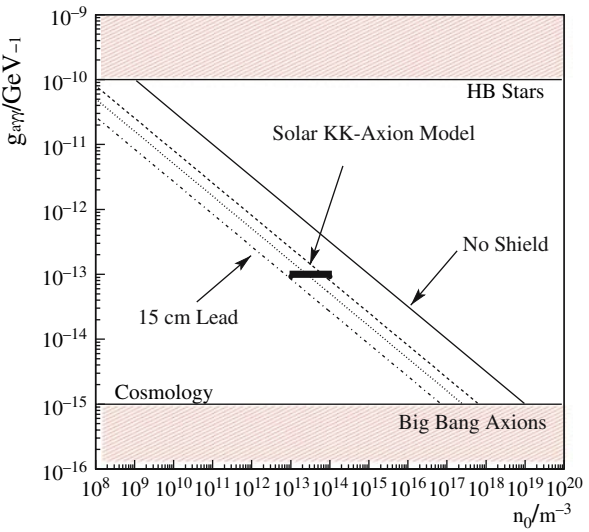

Fig. 10.24. Sensitivity estimate for a $1\,m^3$ TPC detector operated with CS_2 as gas for different detector shield configurations. In addition exclusion contours from astrophysical considerations are shown. The parameter range predicted from the solar KK-axion model of [43] is marked by the black box (adopted from [44])

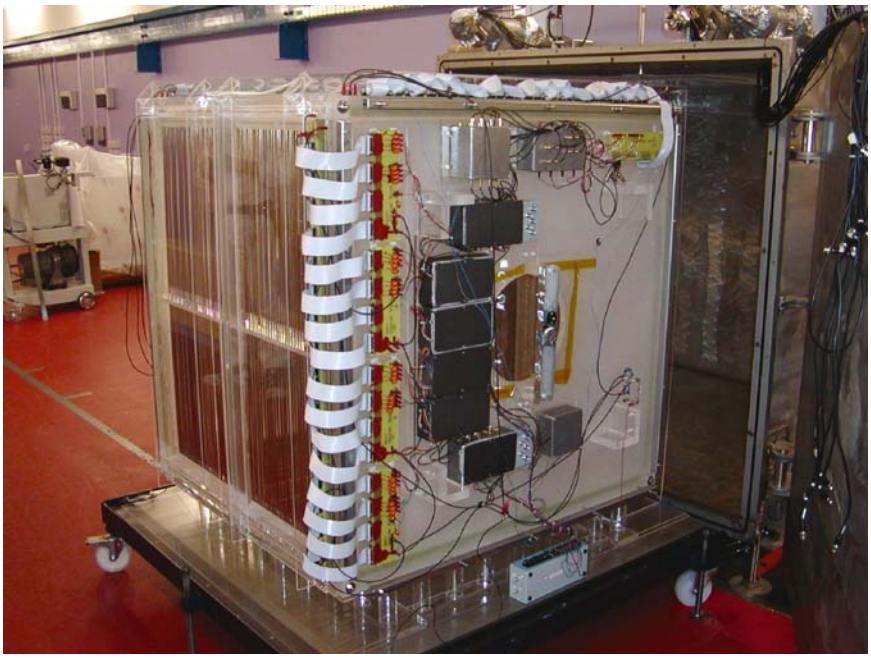

Fig. 10.25. Image of the DRIFT II detector during installation in the Boulby underground laboratory

10.5 Collider Bounds on Scalars and Pseudoscalars

If pseudoscalar particles couple to photons and gluons, it is possible to constrain their couplings and mass by looking at processes where a pseudoscalar particle is involved. The processes we consider here are $e^+e^- \to \gamma + E_T$ for e^+e^- colliders, and pp or $p\bar{p} \to$ single jet $+E_T$ for hadron colliders. One characteristic of the dimension five amplitudes considered here is that the cross section is independent of the center of mass energy at high energies. This follows from a dimensional analysis: the interaction $g\phi F \wedge F$, where ϕ is the pseudoscalar field, has a coupling constant g with a dimension of inverse mass. Therefore $2 \to 2$ processes, involving the production of a single ϕ particle, will have a cross section

$$\frac{\mathrm{d}\sigma}{\mathrm{d}\Omega} = g^2 f(s/t)\,, \tag{10.41}$$

where $f(s/t)$ is a function which depends only on the angle. Specifically, the couplings we are interested in are the following

$$L \propto \frac{\alpha_s}{16\pi f}\phi\, G^b_{\mu\nu}\tilde{G}^{b\mu\nu}\,, \tag{10.42}$$

for gluons, and

$$L \propto \frac{g_{a\gamma\gamma}}{8} \phi \, F_{\mu\nu} \tilde{F}^{\mu\nu} \, , \tag{10.43}$$

for photons. Hadron colliders are more effective in providing limits for axion-gluon couplings and e^+e^- colliders, for axion-photon couplings.

10.5.1 Bounds from Hadron Colliders

Here the results from two experiments in hadron colliders are summarized; for a more detailed analysis refer to [47]. Using the data from the DØ experiment at Fermilab a bound on f can be set to

$$f > 35 \, \text{GeV} \, . \tag{10.44}$$

As for future and ongoing experiments, the Large Hadron Collider (LHC) at CERN is expected to improve the bound on f to

$$f_{\text{LHC}} > 1300 \ \text{GeV} \, . \tag{10.45}$$

10.5.2 Bounds from e^+e^- Colliders

More interesting are the limits that can be obtained for the photon coupling to axions in e^+e^- colliders. Several experiments during the past and planned for future have been analyzed to determine the bound that could be obtained assuming the data are consistent with the standard-model backgrounds. A bound $g_{a\gamma\gamma} < 5.5 \times 10^{-4} \, \text{GeV}^{-1}$ was obtained using e^+e^- collider data from ASP [49, 50]. As the amplitudes are independent of energy, the bounds can be improved mainly by increasing the total luminosity. An analysis of the combined data from LEP at ALEPH, OPAL, L3, and DELPHI would yield the more restrictive bound:

$$g_{a\gamma\gamma} < 1.5 \times 10^{-4} \, \text{GeV}^{-1} \, , \tag{10.46}$$

for $m_\phi < 65 \, \text{MeV}$. For the PEP-II e^+e^- collider, current integrated luminosity gives

$$g_{a\gamma\gamma}(\text{PEPII}) < 8.9 \times 10^{-6} \, \text{GeV}^{-1} \, , \tag{10.47}$$

for $m_\phi < 0.12 \, \text{GeV}$. A similar bound can be obtained from KEKB e^+e^- collider. With the current integrated luminosity the bound would be

$$g_{a\gamma\gamma}(\text{KEKB}) < 8.2 \times 10^{-6} \, \text{GeV}^{-1} \, , \tag{10.48}$$

for $m_\phi < 0.13 \, \text{GeV}$. The expected total luminosity for KEKB is at least twice the current total, which would improve the bound to $g_{a\gamma\gamma} < 5.9 \times 10^{-6} \, \text{GeV}^{-1}$. Finally, for the Super KEKB upgrade to KEKB is expected to produce $10^7 \, \text{pb}^{-1}$ per year. After two years, this would improve the bound to

$$g_{a\gamma\gamma}(\text{KEKB}) < 1.9 \times 10^{-6} \, \text{GeV}^{-1} \, , \tag{10.49}$$

which would rule out most of the parameter space favored by PVLAS.

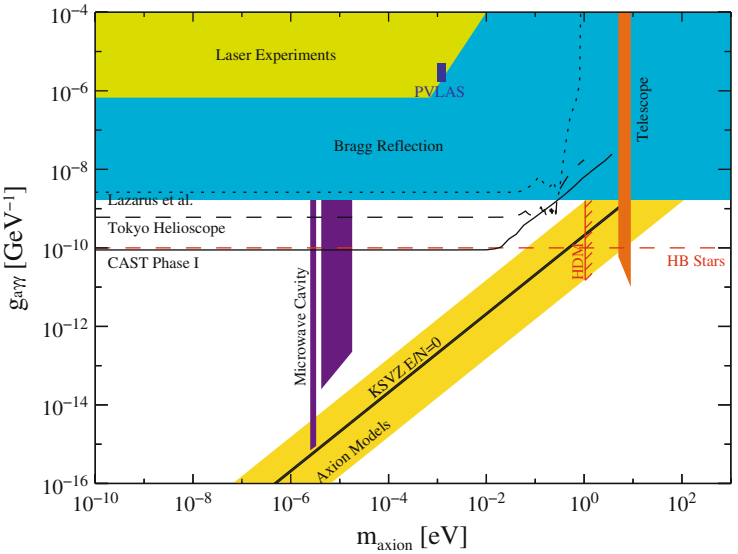

Fig. 10.26. Exclusion plots in the $g_{a\gamma\gamma}$ vs. m_a parameter space. Limits derived with different experimental techniques are shown. Limits from DAMA, SOLAX, and COSME are denoted as "Bragg Reflection" [21, 22, 23]. In addition, the best limits from laser experiments, microwave cavity experiments, telescope searches, helioscope searches marked as "Lazarus et al.," "Tokyo Helioscope," and "CAST Phase I" [5, 9, 10, 11], and the best astrophysical limits are shown [16, 17]. The region predicted by theoretical models is marked as "Axion Models". The vertical line "HDM" indicates the hot dark matter limit for hadronic axions [48]

10.6 Summary and Outlook

In this chapter we reviewed different experimental searches for axions and axion-like particles that are actually running or planned to take place in the near future. Already existing upper limits on the axion-to-photon coupling strength $g_{a\gamma\gamma}$, in the mass range of $1 \times 10^{-10}\,\text{eV} \lesssim m_a \lesssim 1 \times 10^{2}\,\text{eV}$, derived with different experimental techniques, are summarized in Fig. 10.26. In addition, the parameter range that can be derived from the PVLAS result is indicated by a rectangular box marked as "PVLAS".

It was not our intention to give a complete review of all existing experimental techniques to search for axions; this would be beyond the scope of this chapter. Instead, we focused on the topics that were addressed during the Joint ILIAS-CAST-CERN Axion Training at CERN. The common factor of all experiments is the inspired techniques used, which are extremely challenging and innovative.

The fact that the PVLAS collaboration has reported a positive signal that could be interpreted as a signature of an axion-like particle has boosted

a race, to build a new set of laser-based experiments. We are convinced that the years that follow are going to be very exciting.

Acknowledgment

We acknowledge support from the Virtuelles Institut für Dunkle Materie und Neutrinophysik – VIDMAN (Germany). Furthermore, the authors acknowledge the helpful discussions within the network on direct dark matter detection of the ILIAS integrating activity of the European Union (contract number: RII3-CT-2003-506222). Parts of this work has been performed in the CAST collaboration, and we thank our colleagues for their support. The CAST project was supported by the Bundesministerium für Bildung und Forschung (BMBF) under the grant number 05 CC2EEA/9 and 05 CC1RD1/0.

References

1. De Panfilis, S., et al.: Limits on the abundance and coupling of cosmic axions at $4.5\,\mu\text{eV} < M(A) < 5.0\,\mu\text{eV}$. Phys. Rev. Lett. **59**, 839 (1987);
   Wuensch, W.U., et al.: Results of a laboratory search for cosmic axions and other weakly coupled light particles. Phys. Rev. D **40**, 3153 (1989) [200]
2. Hagmann, C., Sikivie, P., Sullivan, N.S., Tanner, D.B.: Results from a search for cosmic axions. Phys. Rev. D **42**, 1297 (1990) [200]
3. Asztalos, S.J., et al.: An improved RF cavity search for halo axions. Phys. Rev. D **69**, 011101 (2004) [astro-ph/0310042] [200]
4. Tada, M., et al.: CARRACK II: A new large-scale experiment to search for axions with Rydberg-atom cavity detector. Nucl. Phys. Proc. Suppl. **72**, 164 (1999) [201]
5. Andriamonje S. [CAST Collaboration]: An improved limit on the axion - photon coupling from the CAST experiment. J. Cosmol. Astropart. Phys. 010 (2007), [hep-ex/0702006] [201, 202, 203, 205, 207, 212, 233]
6. Bahcall, J.N., Pinsonneault, M.H.: What do we (not) know theoretically about solar neutrino fluxes. Phys. Rev. Lett. **92**, 121301(1) (2004), [astro-ph/0402114] [202, 203]
7. Sikivie, P.: Experimental tests of the invisible axion. Phys. Rev. Lett. **51**, 1415 (1983);
   (E) ibid. **52**, 695 (1984) [203]
8. van Bibber, K., McIntyre, P.M., Morris, D.E., Raffelt, G.G.: A practical laboratory detector for solar axions. Phys. Rev. D **39**, 2089 (1989) [204]
9. Lazarus, D.M., Smith, G.C., Cameron, R., Melissinos, A.C., Ruoso, G., Semertzidis, Y.K., Nezrick, F.A.: A search for solar axions. Phys. Rev. Lett. **69**, 2333 (1992) [204, 205, 206, 233]
10. Moriyama, S., Minowa, M., Namba, T., Inoue, Y., Takasu, Y., Yamamoto, A.: Direct search for solar axions by using strong magnetic field and X-ray detectors. Phys. Lett. B **434**, 147 (1998) [hep-ex/9805026] [206, 233]

11. Inoue, Y., Namba, T., Moriyama, S., Minowa, M., Takasu, Y., Horiuchi, T., Yamamoto, A.: Search for sub-electronvolt solar axions using coherent conversion of axions into photons in magnetic field and gas helium. Phys. Lett. B **536**, 18 (2002) [astro-ph/0204388] 206, 233
12. Zioutas, K., et al. [CAST Collaboration]: First results from the CERN axion solar telescope (CAST). Phys. Rev. Lett. **94** (2005) 121301 [hep-ex/0411033] 206, 207
13. Abbon, P., et al.: The Micromegas detector of the CAST experiment. New. J. Phys. 9 (2007) 170 [physics/0702190] 206
14. Kuster, M., et al.: The X-ray Telescope of CAST. New. J. Phys. 9 (2007) 169 [physics/0702188] 207
15. Autiero, D., et al.: The CAST time projection chamber. New. J. Phys. 9 (2007) 171 [physics/0702189] 207
16. Raffelt, G.G.: Astrophysical axion bounds. [hep-ph/0611350] 207, 233
17. Raffelt, G.G: *Stars as Laboratories for Fundamental Physics*. University of Chicago Press, Chicago (1996) 207, 233
18. Paschos, E.A., Zioutas, K.: A proposal for solar axion detection via Bragg scattering. Phys. Lett. B **323**, 367 (1994) 207, 208, 209
19. Cebrían, S., et al.: Prospects of solar axion searches with crystal detectors. Astropart. Phys. **10**, 397 (1999) 207, 208
20. Bernabei, R., et al.: Performance of the 100 kg NaI(Tl) setup of the DAMA experiment at Gran Sasso. Nuovo Cim. **112**, 545 (1999) 208
21. Morales, A., et al. [COSME Collaboration]: Particle dark matter and solar axion searches with a small germanium detector at the Canfranc underground laboratory. Astropart. Phys. **16**, 325 (2002) [hep-ex/0101037] 209, 233
22. Avignone, F.T., et al. [SOLAX Collaboration]: Experimental search for solar axions via coherent Primakoff conversion in a germanium spectrometer. Phys. Rev. Lett. **81**, 5068 (1998) [astro-ph/9708008] 209, 233
23. Bernabei, R., et al.: Search for solar axions by Primakoff effect in NaI crystals. Phys. Lett. B **515**, 6 (2001) 209, 233
24. Davoudiasl, H., Huber, P.: Detecting solar axions using earth's magnetic field. Phys. Rev. Lett. **97**, 121302 (2006) [hep-ph/0509293] 209, 210
25. Landolt-Börnstein, New Series, Vol. 2b, *Geophysics of the Solid Earth, the Moon and the Planets*, pp. 31–99, Springer, Berlin (1985) 209
26. Jahoda, K., et al.: Proc. SPIE Vol. 2808, p. 59–70, EUV, X-Ray, and Gamma-Ray Instrumentation for Astronomy VII, In: Siegmund, Oswald H., Gummin, Mark A. (eds.) 210
27. The Suzaku team, private communication 210, 212
28. Porter, F.S., the Suzaku Team (2005), `http://www.astro.isas.ac.jp/suzaku/doc/suzaku_td/node9.html` 211, 212
29. Van Bibber, K., Dagdeviren, N.R., Koonin, S.E., Kerman, A., Nelson, H.N.: An experiment to produce and detect light pseudoscalars. Phys. Rev. Lett. **59**, 759 (1987) 213, 214
30. Anselm, A.A.: Arion ↔ Photon oscillations in a steady magnetic field. (In Russian), Yad. Fiz. **42**, 1480 (1985) 213
31. Cameron, R., et al.: Search for nearly massless, weakly coupled particles by optical techniques. Phys. Rev. D **47**, 3707 (1993) 214
32. Ringwald, A.: Axion interpretation of the PVLAS data? J. of Phys. Conf. Ser. **39**, 197 (2005) [hep-ph/0511184] 214, 216, 222, 224, 225
33. Maiani, L., Petronzio, R., Zavattini, E.: Effects of nearly massless, spin-zero particles on light propagation in a magnetic field. Phys. Lett. **175B**, 359 (1986) 215

34. Heisenberg, W., Euler, H.: Folgerungen aus der Diracschen Theorie des Positrons. Z. Phys. **98**, 718 (1936);
Weisskopf, V.S., Über die Elektrodynamik des Vakuums auf Grund der Quantentheorie des Elektrons. Mat. Phys. Medd.-K. Dan. Vidensk. Selsk. **14**, 6 (1936);
Schwinger, J.S.: On gauge invariance and vacuum polarization. Phys. Rev. **82**, 664 (1951) 215, 216
35. Adler, S.L.: Photon splitting and photon dispersion in a strong magnetic field. Annals Phys. **67**, 599 (1971) 215, 216
36. Adler, S.L., et al.: Photon splitting in a strong magnetic field. Phys. Rev. Lett. **25**, 1061 (1970) 216
37. Gabrielli, E., et al.: Photon propagation in magnetic and electric fields with scalar/pseudoscalar couplings: new look. Phys. Rev. D74, 073002 (2006) [hep-ph/0604143] 216
38. Zavattini, E., et al. [PVLAS Collaboration]: Experimental observation of optical rotation generated in vacuum by a magnetic field. Phys. Rev. Lett. **96**, 110406 (2006) [hep-ex/0507107] 216, 219, 225
39. Ehret, K., et al.: Production and detection of axion-like particles in a HERA dipole magnet: Letter-of-intent for the ALPS experiment. Letter of Intent [hep-ex/0702023] 217
40. Bailly, G., Battesti, R., Batut, S., Faure, S., Ganau, P., Mackowski, J.-M., Michel, C., Nardone, M., Pinard, L., Polizzi, L., Pinto Da Souza, B., Portugall, O., Remilleux, A., Rikken, G.L.J.A., Rizzo, C., Robillard, C., Trénec, G., Vigué, J.: [The BMV Collaboration] 219
41. Pugnat, P., et al.: Feasibility study of an experiment to measure the Vacuum Magnetic Birefringence. Czech J. of Phys. 55 A389 (2005) http://doc.cern.ch/archive/electronic/cern/preprints/at/at-2005-009.pdf;
Pugnat. P., et al.: QED Test and Axion Search by means of Optical Techniques, Letter of Intent submitted to the CERN SPSC, CERN-SPSC-2005-034, 17 October 2005, http://doc.cern.ch//archive/electronic/cern/preprints/spsc/public/spsc-2005-034.pdf;
Pugnat, P., et al.: QED test and axion search in LHC superconducting dipoles by means of optical techniques. Czech J. of Phys. 56 C193 (2006); 223, 224
42. Spergel, D.N., et al. (WMAP Collaboration): First year Wilkinson Microwave Anisotropy Probe (WMAP) observations: determination of cosmological parameters. Astrophys. J. Suppl. **148**, 175 (2003) [astro-ph/0302209] 226
43. DiLella, L., Zioutas, K.: Observational evidence for gravitationally trapped massive axion(-like) particles. Astropart. Phys. **19**, 145 (2003) [astro-ph/0207073] 226, 227, 228, 229, 230
44. Morgan, B., et al.: Searches for Kaluza-Klein axions with gas TPCs. Astropart. Phys. **23**, 287 (2005) 227, 230
45. Morgan, B.: Dark matter detection with gas time projection chambers. The University of Sheffield – Department of Physics and Astronomy, PhD Thesis (2004) 228
46. Alner, G.J., et al.: The DRIFT-II dark matter detector: design and commissioning. Nucl. Instr. Meth. Phys. Res. A **555**, 173 (2005) 230
47. Kleban, M., Rabadán, R.: Collider bounds on pseudoscalars coupling to Gauge bosons. [hep-ph/0510183] 232
48. Hannestad, S., Mirizzi, A., Raffelt, G.: New cosmological mass limit on thermal relic axions. JCAP 0507, 002 (2005) [hep-ph/0504059] 233

49. Masso, E., Toldra, R.: On a light spinless particle coupled to photons. Phys. Rev. D **52**, 1755 (1995) [hep-ph/9503293] 232
50. Hearty, C., et al.: Search for the anomalous production of single photons in e^+ e^- annihilation at $\sqrt{s} = 29\,\mathrm{GeV}$. Phys. Rev. D **39**, 3207 (1989) 232

Acronyms and Abbreviations

ADC	analog digital converter
ADMX	Axion Dark Matter eXperiment, USA
AGB	asymptotic giant branch
AGS	alternating gradient synchrotron
ALP	axion-like particle
BBN	big bang nucleosynthesis
BFRT	Brookhaven-Fermilab-Rochester-Trieste
BNL	Brookhaven National Laboratory, USA
BR	branching ratio
BSMM	beyond the SM model
CAST	CERN Axion Solar Telescope, CERN Geneva
CCD	charge coupled device
CDM	cold dark matter
CKM	Cabbibo-Kobayashi-Maskawa
CKT	Csáki-Kaloper-Terning
CL	confidence level
CMB	cosmic microwave background
CMBR	cosmic microwave background radiation
CMD	cryogenic magnetic detector
CME	Cotton-Mouton effect
COBE	Cosmic Background Explorer, NASA
COMPASS	Common Muon Proton Apparatus for Structure and Spectroscopy, CERN Geneva
CP	charge conjugation transformation followed by parity transformation
DAMA	Dark Matter Experiment, Laboratori Nationali del Gran Sasso, Italy
DAQ	data acquisition
DFSZ	Dine-Fischler-Schrednicki-Zhitnisky
DM	dark matter
DRIFT	Directional Recoil Identification From Tracks, Boulby Underground Laboratory, UK
EDM	electric dipole moment
EoS	equation of state

FCNC	flavour changing neutral current
FET	field-effect transistor
FFT	fast Fourier transform
FIRAS	Far Infrared Absolute Spectrophotometer, NASA
FP	Fabry-Pérot
GECOSAX	Geomagnetic Conversion of Solar Axions
HEP	high energy physics
HERA	Hadron-Electron Ring Accelerator Facility, DESY Hamburg
HERMES	HERA meausurement of spin, DESY Hamburg
HFET	heterostructure field-effect transistor
IF	intermediate frequency
IGM	intergalactic medium
ILC	International Linear Collider
ILIAS	Integrated Large Infrastructures for Astroparticle Science
INFN	Istituto Nazionale di Fisica Nucleare, Italy
KEK	National Laboratory for High Energy Physics, Japan
KSVZ	Kim-Shifman-Vainshtein-Zakharov
LHC	Large Hadron Collider, CERN Geneva
LHe	liquid helium
LHS	left hand side
LLNL	Lawrence Livermore National Laboratory, USA
LOI	letter of intent
MDM	magnetic dipole moment
MICROMEGAS	Micromesh Gaseous Structure
NRAO	National Radio Astronomy Observatory, USA
OSQAR	Optical search for QED vacuum magnetic birefringence, Axions and photon regeneration; CERN Geneva
P	parity transformation
PAC	program advisory committee
PQ	Peccei-Quinn
pQCD	Perturbative Quantum Chromodynamics
PVLAS	Polarizzazione del Vuoto con Laser, INFN, Italy
QCD	quantum chromodynamics
QED	quantum electrodynamics
QM	quantum mechanics
QSO	quasi stellar object – quasar
QWP	quarter-wave-plate
RGB	red giant branch
RHS	right hand side
RXTE	Rossi X-ray Timing Explorer
SM	standard model
SN	supernova
SNOC	SuperNova Observation Calculator

SNR	signal to noise ratio
SNS	spallation neutron source
SOLAX	Solar Axion Experiment, Sierra Grande, Argentinia
SOM	stress optical modulator
SQUID	superconducting quantum interference devices
SREDM	Storage Ring EDM collaboration
SSB	spontaneous symmetry breaking
SSM	standard solar model
SUSY	supersymmetry
T	time reversal transformation
TE	transverse electric
TES	transition edge sensor
TM	transverse magnetic
TPC	time projection chamber
UCN	ultra cold neutron
VEV	vacuum expectation value
WIMP	weakly interacting massive particle
WMAP	Wilkinson Microwave Anisotropy probe
XIS	X-ray Imaging Spectrometer

Index